

**APPLIED
COMPUTATIONAL
ELECTROMAGNETICS
SOCIETY
JOURNAL**

December 2018
Vol. 33 No. 12
ISSN 1054-4887

The ACES Journal is abstracted in INSPEC, in Engineering Index, DTIC, Science Citation Index Expanded, the Research Alert, and to Current Contents/Engineering, Computing & Technology.

The illustrations on the front cover have been obtained from the research groups at the Department of Electrical Engineering, The University of Mississippi.

THE APPLIED COMPUTATIONAL ELECTROMAGNETICS SOCIETY

<http://aces-society.org>

EDITORS-IN-CHIEF

Atef Elsherbeni

Colorado School of Mines, EE Dept.
Golden, CO 80401, USA

Sami Barmada

University of Pisa, ESE Dept.
56122 Pisa, Italy

ASSOCIATE EDITORS-IN-CHIEF: REGULAR PAPERS

Mohammed Hadi

Kuwait University, EE Dept.
Safat, Kuwait

Antonio Musolino

University of Pisa
56126 Pisa, Italy

Marco Arjona López

La Laguna Institute of Technology
Torreon, Coahuila 27266, Mexico

Alistair Duffy

De Montfort University
Leicester, UK

Abdul A. Arkadan

Colorado School of Mines, EE Dept.
Golden, CO 80401, USA

Paolo Mezzanotte

University of Perugia
I-06125 Perugia, Italy

Wenxing Li

Harbin Engineering University
Harbin 150001, China

Salvatore Campione

Sandia National Laboratories
Albuquerque, NM 87185, USA

Luca Di Rienzo

Politecnico di Milano
20133 Milano, Italy

Maokun Li

Tsinghua University
Beijing 100084, China

Wei-Chung Weng

National Chi Nan University, EE Dept.
Puli, Nantou 54561, Taiwan

Rocco Rizzo

University of Pisa
56123 Pisa, Italy

Mauro Parise

University Campus Bio-Medico of Rome
00128 Rome, Italy

Alessandro Formisano

Seconda Università di Napoli
81031 CE, Italy

Lei Zhao

Jiangsu Normal University
Jiangsu 221116, China

Yingsong Li

Harbin Engineering University
Harbin 150001, China

Piotr Gas

AGH University of Science and Technology
30-059 Krakow, Poland

Sima Noghianian

University of North Dakota
Grand Forks, ND 58202, USA

ASSOCIATE EDITORS-IN-CHIEF: EXPRESS PAPERS

Lijun Jiang

University of Hong Kong, EEE Dept.
Hong, Kong

Amedeo Capozzoli

Univerita di Napoli Federico II, DIETI
I-80125 Napoli, Italy

Shinichiro Ohnuki

Nihon University
Tokyo, Japan

Steve J. Weiss

US Army Research Laboratory
Adelphi Laboratory Center (RDRL-SER-M)
Adelphi, MD 20783, USA

Yu Mao Wu

Fudan University
Shanghai 200433, China

Kubilay Sertel

The Ohio State University
Columbus, OH 43210, USA

Jiming Song

Iowa State University, ECE Dept.
Ames, IA 50011, USA

Maokun Li

Tsinghua University, EE Dept.
Beijing 100084, China

EDITORIAL ASSISTANTS

Matthew J. Inman

University of Mississippi, EE Dept.
University, MS 38677, USA

Shanell Lopez

Colorado School of Mines, EE Dept.
Golden, CO 80401, USA

EMERITUS EDITORS-IN-CHIEF

Duncan C. Baker

EE Dept. U. of Pretoria
0002 Pretoria, South Africa

Allen Glisson

University of Mississippi, EE Dept.
University, MS 38677, USA

Ahmed Kishk

Concordia University, ECS Dept.
Montreal, QC H3G 1M8, Canada

Robert M. Bevensee

Box 812
Alamo, CA 94507-0516, USA

Ozlem Kilic

Catholic University of America
Washington, DC 20064, USA

David E. Stein

USAF Scientific Advisory Board
Washington, DC 20330, USA

EMERITUS ASSOCIATE EDITORS-IN-CHIEF

Yasushi Kanai Niigata Inst. of Technology Kashiwazaki, Japan	Mohamed Abouzahra MIT Lincoln Laboratory Lexington, MA, USA	Alexander Yakovlev University of Mississippi, EE Dept. University, MS 38677, USA
Levent Gurel Bilkent University Ankara, Turkey	Sami Barmada University of Pisa, ESE Dept. 56122 Pisa, Italy	Ozlem Kilic Catholic University of America Washington, DC 20064, USA
Erdem Topsakal Mississippi State University, EE Dept. Mississippi State, MS 39762, USA	William O'Keefe Coburn US Army Research Laboratory Adelphi, MD 20783, USA	Fan Yang Tsinghua University, EE Dept. Beijing 100084, China

EMERITUS EDITORIAL ASSISTANTS

Khaled ElMaghoub Trimble Navigation/MIT Boston, MA 02125, USA	Christina Bonnington University of Mississippi, EE Dept. University, MS 38677, USA
Anne Graham University of Mississippi, EE Dept. University, MS 38677, USA	Mohamed Al Sharkawy Arab Academy for Science and Technology, ECE Dept. Alexandria, Egypt

DECEMBER 2018 REVIEWERS: REGULAR PAPERS

Ugur Alkasi	William Kefauver
Stamatios Amanatiadis	Jean-Fu Kiang
Abd Arkadan	George Kyriacou
Zsolt Badics	Alberto Leggieri
Toure Baidy	Maokun Li
Sami Barmada	Wen-Jiao Liao
Adalbert Beyer	Zi-Liang Liu
Robert Burkholder	Djordje Mirkovic
Kalaivani C. T.	Masood Molimoli
Fangyuan Chen	Ozlem Ozgun
Zhe Chen	M. Periyasamy
Hsi-Tseng Chou	Andrew Peterson
Klaus Debes	Daniele Pinchera
Manohar Deshpande	Mohammd Pourbagher
Said El-Khamy	C.J. Reddy
Ibrahim Elshafiey	Mustafa Secmen
Martins Ezuma	Ashish Singh
Ian Flintoft	Mohamed Talaat
Glauco Fontgalland	Fernando Teixeira
Amin Gorji	Christopher Trueman
Zhengwei Hao	Marsellas Waller
Mehedi Hasan	Chao-Fu Wang
Nan Hu	Fan Yang
Niamat Hussain	Tara Yousefi
Shian Hwu	Huan Zhang
Arkom Kaewrawang	Bo Zhu
Yasushi Kanai	

TABLE OF CONTENTS – REGULAR PAPERS

On the Numerical Dispersion of the Radial Point Interpolation Meshless (RPIM) Method in Lossy Media
Xiaoyan Zhang, Zhizhang (David) Chen, and Yiqiang Yu..... 1332

Eigenvalue Decomposition Approach for Beampattern Synthesis
Jie Chen and Yingzeng Yin..... 1340

Discontinuous Galerkin Finite Element Time Domain Method for Analysis of Ferrite Circulator with Non-conforming Meshes
Min Li, Xiadong Ye, F. Xu, and N. M. Luo..... 1346

Time Domain Parabolic Equation Method for Scattering Analysis of Electrically Large Coated Objects by using Impedance Boundary Condition
Ling Guan and Shifei Tao 1352

Fast Wideband Electromagnetic Analysis Using the Interpolation Technique and Fast Generating Matrix Method
Wei Bin Kong, Xiao Fang Yang, Feng Zhou, Jia Ye Xie, Ru Gang Wang, and Kai Lai Zheng..... 1360

A Study on Upper Limit Frequency of Symmetric Extended TEM Cells
Chunjiang Song, Xinkai Fu, and Fei Dai 1368

On the Correction of the Probe Positioning Errors in a Non-Redundant Bi-Polar Near to Far-Field Transformation
Francesco D’Agostino, Flaminio Ferrara, Claudio Gennarelli, Rocco Guerriero, and Massimo Migliozzi..... 1374

Far Field Reconstruction based on Compressive Sensing with Prior Knowledge
Baozhu Li, Wei Ke, Huali Lu, Shuming Zhang, and Wanchun Tang..... 1383

A Review of the Modal Decomposition Matrix for Calculating the Far Field of an Infinitely Flanged Rectangular Waveguide
Gregory A. Mitchell and Wasyl Wasykiwskyj 1390

Using Superformula to Miniaturize CPW Rat Race Coupler
Amjad A. Omar and Nihad I. Dib 1397

A Miniaturized Antenna with Optimum Q-Factor and High NFD for UWB Microwave Imaging M. Tarikul Islam, Md. Samsuzzaman, Iskandar Yahya, and Mohammad T. Islam.....	1402
Powering Sensors in IoT System by Using Compact Seven Band PIFA Rectenna Nermeen A. Eltresy, Dalia M. Elsheakh, Esmat A. Abdallah, and Hadia M. Elhennawy.....	1411
Linearization of S-Parameter Cascading for Analysis of Multiple Reflections Richard J. Allred and Cynthia M. Furse.....	1420
Biomimetic Radar Target Recognition Based on Hypersausage Chains Huan-Huan Zhang and Pei-Yu Chen.....	1429
SAR Electromagnetic Image Conditioning Using a New Adaptive Particle Swarm Optimization B. Malakonda Reddy and Md. Zia Ur Rahman.....	1439
A Study on the Distribution and Uniformity of Symmetric Extended TEM Cells Chunjiang Song, Yuntao Jin, and Fei Dai.....	1447
Air Plasma Key Parameters for Electromagnetic Wave Propagation at and Out of Thermal Equilibrium: Applications to Electromagnetic Compatibility Pascal André, Géraldine Faure, Ali Mahfouf, and Sébastien Lalléchère.....	1453
Fast Calculation of the Filamentary Coil Impedance Using the Truncated Region Eigenfunction Expansion Method Grzegorz Tytko and Leszek Dzikowski.....	1461
Analytical Modeling of Magnetic Field Considering the Saturation in Switched Reluctance Motor Shenglong Hu and Shuguang Zuo.....	1467
Characterizations of Magnetic Field Distributions inside Buckling Pipelines Yu Zhang, Yameng Xue, Xinjing Huang, Jian Li, and Shili Chen.....	1475
A Novel Approach for Intruder Localization Based on Leaky Coaxial Cable Sensor with IQ Demodulation and Synchronous Subtraction Qiao Guan, Hongmin Lu, Kunbo Wang, and Chongchong Chen.....	1483
Calculation and Analysis of an Analytical Model for Magnetic Field Monitoring Based on TREE in Eddy Current Testing Feng Jiang and Shulin Liu.....	1489

On the Numerical Dispersion of the Radial Point Interpolation Meshless (RPIM) Method in Lossy Media

Xiaoyan Zhang^{1,2}, Zhizhang (David) Chen^{3*}, and Yiqiang Yu^{1,3}

¹ School of Information Engineering
East China Jiaotong University, Nanchang, 330013, China

² State Key Laboratory of Millimeter Waves, Nanjin, 210096, China
xy_zhang3129@ecjtu.jx.cn

³ Department of Electrical and Computer Engineering
Dalhousie University, NS B3J 2X4, Canada
*zz.chen@ieee.org, yiqiang.yu@dal.ca

Abstract — A general formula for numerical dispersion of the two-dimensional time-domain radial point interpolation meshless (2-D RPIM) method is analytically derived. Numerical loss and dispersion characteristics of the RPIM method with both Gaussian and multiquadric basis functions are investigated. It is found that numerical loss and dispersion errors of the RPIM vary with types of basis functions used and associated parameters, number of the nodes, and medium conductivities. In addition, condition numbers of the moment matrix of the meshless methods can also increase numerical dispersion errors. With a reasonable condition number of the moment matrix, the radial point interpolation meshless methods perform generally better than the FDTD method in terms of numerical dispersion errors.

Index Terms — Gaussian basis function, multiquadric basis function, numerical dispersion, radial point interpolation method (RPIM).

I. INTRODUCTION

Meshless or mesh-free methods present alternative methods to replace the mesh/grid based methods for electromagnetic field modeling. Time-domain radial point interpolation meshless (RPIM) method is one of the typical meshless methods. References [1, 2] show that it may be equivalent to the finite-difference time-domain (FDTD) method under certain conditions. But in a general case, it promises better accuracy and computational efficiency in solving the problems of irregular or multiscale structures [3, 4]. The numerical results show that the RPIM approach can reduce about 80% of the number of unknowns and about 70% of the computational time in comparison with the FDTD method. The RPIM can not only save more than 60% of the memory required by the FDTD method, but also run

100% faster.

Recently, the RPIM method was successfully applied to solve various electromagnetic problems. Rodrigo *et al.* proposed an improved Lennard-Jones discretization method for the RPIM and validated it with a scattering problem [5]. Tanaka *et al.* investigated a unique meshless method using the RPIM and applied it to an eddy current problem [6]. Khalef combined a Crank–Nicolson scheme with the RPIM and utilized it to model waveguide problems [7]. However, when radial basis functions (RBFs) and interpolating points are not properly chosen for solving Maxwell’s equations, the meshless methods can become erroneous and even divergent, which limits further engineering applications of the RPIM [8, 9]. Therefore, it is important to investigate errors of the meshless methods. One of the errors of main concerns is numerical dispersion of a meshless method.

In 2008, Lai *et al.* derived a numerical dispersion relationship for the RPIM method in lossless media [10], but it is only for one-dimensional structure and the dispersion characteristics of the RPIM method have not been well studied. In 2013, Ansarizadeh and Movahhedi investigated dispersion error of the RPIM method by tracing the propagation of the electromagnetic wave [11]. Their work also focused on the lossless media and they did not derive a general formula for the numerical dispersion of the RPIM method. In 2014, we studied the numerical dispersion of the RPIM method and its relationship to the finite-difference time-domain (FDTD) approach [1], but it is only for the Gaussian basis function with two adjacent points in lossless media. In 2017, we derived a general formula for numerical dispersion of the RPIM method in lossless media [12]. Since then, no more numerical dispersion analysis of the RPIM method has been reported. Important issues such as node density, other non-Gaussian basis functions [6,

13] and their impacts on numerical dispersions in lossy media have not been studied.

In this paper, we address the above issues: we first develop the general numerical dispersion relation of the RPIM method for both lossless and lossy medium, verify it with the FDTD method when its node distributions are made to be the same as that of the FDTD, and then investigate numerical dispersion properties of the RPIM method with different basis functions, number of nodes and conductivities. To our best knowledge, these issues have not been reported in the past.

It is worth to mention here that the meshless method is expected to have smaller numerical dispersion errors than the conventional FDTD method; this is because the meshless methods use high-order basis functions to expand the fields than the roof-top basis functions used in the FDTD method [14]. Our investigations presented here show that it is true in general but not so under certain conditions because of the meshless methods involve more complex matrix operations.

II. NUMERICAL DISPERSION FORMULATION

For simplicity, a two-dimensional (2-D) TM_z wave propagating in a lossy and isotropic source-free medium of permittivity ε , conductivity σ , and permeability μ is considered. Maxwell's equations in time domain can be written in a matrix form as:

$$\begin{bmatrix} \varepsilon \frac{\partial}{\partial t} + \sigma & \frac{\partial}{\partial y} & -\frac{\partial}{\partial x} \\ \frac{\partial}{\partial y} & \mu \frac{\partial}{\partial t} & 0 \\ \frac{\partial}{\partial x} & 0 & -\mu \frac{\partial}{\partial t} \end{bmatrix} \begin{bmatrix} E_z \\ H_x \\ H_y \end{bmatrix} = 0. \quad (1)$$

Take E_z for an inspection. As Fig. 1 shows, E_z at node k can be interpolated with field values at the neighboring nodes j that is within the support domain centered at node k . Its node-based expansion can be expressed as [3]:

$$E_z(X_k) = \sum_{j=1}^N \Psi_j(X_k) \cdot E_z(X_j) = \mathbf{\Psi}(X_k) \mathbf{E}_z(X_j), \quad (2)$$

where $X_k = (x_k, y_k)$ represents spatial position of node k , $\mathbf{X}_j = (X_1, X_2, \dots, X_N)$ stores all the node locations, and N is the total number of nodes within the support domain. Then, vector $\mathbf{\Psi}(X_k) = [\Psi_1(X_k), \Psi_2(X_k), \dots, \Psi_N(X_k)]$ is a shape function, which is determined by:

$$\mathbf{\Psi}(X_k) = \mathbf{r}(X_k)^T \mathbf{G}^{-1}. \quad (3)$$

Here $\mathbf{r}(X_k) = [r_1(X_k), r_2(X_k), \dots, r_N(X_k)]$ is a basis function. For Gaussian function, $r_j(X_k)$ has the following form [3, 4]:

$$r_j(X_k) = \exp(-\alpha_c \frac{|X_j - X_k|^2}{d_c^2}), \quad (4)$$

where α_c is the shape parameter, d_c is the minimum distance between two nodes. For a multi-quadric basis function with shape parameters of C and q , $r_j(X_k)$ has the following form [6]:

$$r_j(X_k) = \left(\frac{|X_j - X_k|^2}{d_c^2} + C^2 \right)^q. \quad (5)$$

Then, the moment matrix \mathbf{G} in (3) is:

$$\mathbf{G} = \begin{bmatrix} 1 & r_2(X_1) & \cdots & r_N(X_1) \\ r_1(X_2) & 1 & \cdots & r_N(X_2) \\ \vdots & \vdots & \ddots & \vdots \\ r_1(X_N) & r_2(X_N) & \cdots & 1 \end{bmatrix}. \quad (6)$$

Let X_E and X_H denote the spatial positions of the nodes at which electric field and magnetic field are located, respectively. By substituting these formulas into (1), we can get:

$$\varepsilon \frac{\partial \mathbf{E}_z(X_E)}{\partial t} + \sigma \mathbf{E}_z(X_E) = -\mathbf{\Psi}'_y(X_E) \mathbf{H}_x(X_H) + \mathbf{\Psi}'_x(X_E) \mathbf{H}_y(X_H), \quad (7a)$$

$$\frac{\partial \mathbf{H}_x(X_H)}{\partial t} = -\frac{1}{\mu} \mathbf{\Psi}'_y(X_H) \mathbf{E}_z(X_E), \quad (7b)$$

$$\frac{\partial \mathbf{H}_y(X_H)}{\partial t} = \frac{1}{\mu} \mathbf{\Psi}'_x(X_H) \mathbf{E}_z(X_E). \quad (7c)$$

Here $\mathbf{\Psi}'_\xi = \partial \mathbf{\Psi} / \partial \xi$ ($\xi = x, y, z$).

By following the Fourier analysis approach [15], the numerical dispersion relation can be obtained. That is, first, the field components in (7) are assumed to have the following form:

$$f(\mathbf{r}, t) = f_0 \exp(-j\mathbf{k} \cdot \mathbf{r}) \exp(j\omega t), \quad (8)$$

where ω is angular frequency, f_0 is the amplitude. $\mathbf{k} = k_x \mathbf{a}_x + k_y \mathbf{a}_y = (\beta + j\alpha)(\mathbf{a}_x \cos \phi + \mathbf{a}_y \sin \phi)$, with β being the phase shift constant, α being the attenuation constant and ϕ being the propagation angle with respect the x -axis. \mathbf{r} is the displacement vector.

We then apply the time-average (TA) scheme [16] to the lossy term of (7a) and use the central finite-difference to approximate the time derivatives. Then, substitution of (8) into (7) reads:

$$E_{z0} e^{-j\mathbf{k} \cdot \mathbf{r}_E} \boldsymbol{\varphi}_1 \boldsymbol{\varphi}_t = \mathbf{\Phi}(X_E) \begin{bmatrix} H_{x0} \\ H_{y0} \end{bmatrix} e^{-j\mathbf{k} \cdot \mathbf{r}_H}, \quad (9a)$$

$$H_{x0} e^{-j\mathbf{k} \cdot \mathbf{r}_H} \boldsymbol{\varphi}_2 \boldsymbol{\varphi}_t = -\frac{1}{\mu} \mathbf{\Psi}'_y(X_H) E_{z0} e^{-j\mathbf{k} \cdot \mathbf{r}_E}, \quad (9b)$$

$$H_{y0} e^{-j\mathbf{k} \cdot \mathbf{r}_H} \boldsymbol{\varphi}_2 \boldsymbol{\varphi}_t = \frac{1}{\mu} \mathbf{\Psi}'_x(X_H) E_{z0} e^{-j\mathbf{k} \cdot \mathbf{r}_E}. \quad (9c)$$

Here Δt is the time step and is set as $d_c/2v_0$ to be consistent with FDTD method. v_0 is the speed of light. ϕ_1 , ϕ_2 , ϕ_t , and $\Phi(X_E)$ are defined as:

$$\phi_1 = \begin{bmatrix} 1 & 1 \\ -1 & 1 \end{bmatrix} \begin{bmatrix} \varepsilon/\Delta t \\ \sigma/2 \end{bmatrix}, \phi_2 = [1 \quad -1], \phi_t = \begin{bmatrix} e^{j\omega\Delta t/2} \\ e^{-j\omega\Delta t/2} \end{bmatrix}, \quad (10)$$

$$\Phi(X_E) = \begin{bmatrix} -\Psi'_y(X_E) & \Psi'_x(X_E) \end{bmatrix}. \quad (11)$$

After some manipulations, the following equations are obtained:

$$\begin{bmatrix} \varepsilon^{TA}c_0 & \Psi'_y(X_E)\mathcal{Q}_E & -\Psi'_x(X_E)\mathcal{Q}_E \\ \frac{\Psi'_y(X_H)\mathcal{Q}_H}{\mu c_0} & 1 & 0 \\ -\frac{\Psi'_x(X_H)\mathcal{Q}_H}{\mu c_0} & 0 & 1 \end{bmatrix} \begin{bmatrix} E_{z0} \\ H_{x0} \\ H_{y0} \end{bmatrix} = 0, \quad (12)$$

with

$$\mathcal{Q}_E = \begin{bmatrix} e^{-jk\cdot\Delta r_1^E} & e^{-jk\cdot\Delta r_2^E} & \dots & e^{-jk\cdot\Delta r_N^E} \end{bmatrix}^T, \quad (13a)$$

$$\mathcal{Q}_H = \begin{bmatrix} e^{-jk\cdot\Delta r_1^H} & e^{-jk\cdot\Delta r_2^H} & \dots & e^{-jk\cdot\Delta r_N^H} \end{bmatrix}^T. \quad (13b)$$

Here, $\Delta r_j^E = \mathbf{r}_j^H - \mathbf{r}^E$, $\Delta r_j^H = \mathbf{r}_j^E - \mathbf{r}^H$, \mathbf{r}^H and \mathbf{r}^E are the displacement vectors of magnetic field and electric field respectively. $c_0 = 2j \sin \theta_t / \Delta t$, $i = \sqrt{-1}$ and $\theta_t = \omega\Delta t / 2$. $\varepsilon^{TA} = \varepsilon - j\sigma\Delta t / 2 \tan \theta_t$.

By setting the determinant of the coefficient matrix of (12) to zero, and with some manipulations, numerical dispersion relation can be obtained as:

$$\varepsilon^{TA} \mu c_0^2 = \Psi'_y(X_E)(\Psi'_y(X_H)\mathcal{Q}_H)\mathcal{Q}_E + \Psi'_x(X_E)(\Psi'_x(X_H)\mathcal{Q}_H)\mathcal{Q}_E. \quad (14)$$

This equation is solved with Newton iteration method.

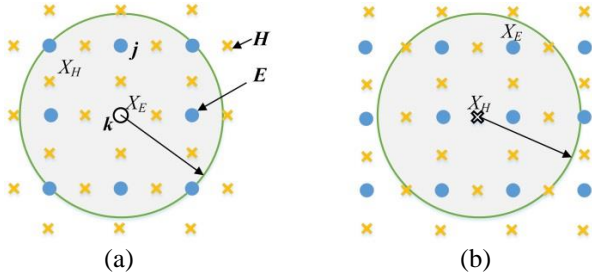


Fig. 1. The support domain centered at node k and used in formulas (7a) (a) and of (7b) and (7c) (b).

III. DISPERSION ANALYSIS OF THE MESHLESS METHODS

In the following paragraphs, we conduct numerical dispersion analysis of the meshless methods. To do so, we define numerical loss error (NLE), numerical phase

error (NPE) as follows [17]:

$$NLE = \left| \frac{\alpha_{num} - \alpha_0}{\alpha_0} \right| \times 100\%, \quad (15a)$$

$$NPE = \left| \frac{\beta_{num} - \beta_0}{\beta_0} \right| \times 100\%. \quad (15b)$$

β_{num} and α_{num} are the phase shift and attenuation constants of the meshless methods computed with (14), respectively. β_0 and α_0 are the theoretical phase shift and attenuation constants, respectively. With the above definitions, the dispersion errors of the meshless methods are studied as follows.

A. Effects of basis functions and their parameters

First, N is set to 4 and the distance between adjacent nodes is $\Delta s = \lambda/20$. Such a setting is comparable to the conventional finite-difference time-domain (FDTD) method where a field component at a grid point is related to the field components at the surrounding four grid points. The dielectric constant of the medium under consideration is $\varepsilon_r = 1$ and the conductivity is $\sigma = 0.001$ S/m.

Figure 2 shows the $NLEs$ and $NPEs$ of the RPIM and the FDTD methods. The RPIM method uses Gaussian basis function with different α_c values. It can be seen that when $\alpha_c = 10^{-4}$, the dispersion errors of the RPIM method are almost the same as those of the FDTD method, which is consistent with the phenomenon described in [1]; when $\alpha_c = 10^{-3}$, the $NLEs$ and $NPEs$ of the RPIM method are both less than the errors of the FDTD method; however, when $\alpha_c = 10^{-2}$, their $NLEs$ and $NPEs$ are sharply increased. This means that using a large α_c will result in a large error or even solution divergence.

Figure 3 shows the condition number of the moment matrix \mathbf{G} in (6) versus different α_c . As α_c decreases, the condition number of \mathbf{G} increases rapidly. It implies that \mathbf{G} can become an ill-conditioned matrix and unstable solutions are more likely to occur with a small α_c . In other words, choosing a smaller α_c does not necessarily lead to smaller errors because of potential large condition numbers of the moment matrix. To ensure both the stability and accuracy of the RPIM method, we select α_c at the range of 10^{-3} in the following studies.

We now turn to the RPIM method with the multiquadric basis function of (5). First, we set the parameter $q=0.01$ and let C change from 0.3 to 10. Figure 4 shows the numerical dispersion errors with changing C . Then, we let the value of q change with a fixed $C=1$. Figure 5 shows the numerical dispersion errors with changing q .

From Fig. 4 (a), we can see that the $NLEs$ of the

RPIM method with the multiquadric basis function are approximately equal to or less than those of FDTD method in most of the propagation angles. With small C , however, the NPE s can be larger than those of FDTD approach at some propagation angles (see Fig. 4 (b)).

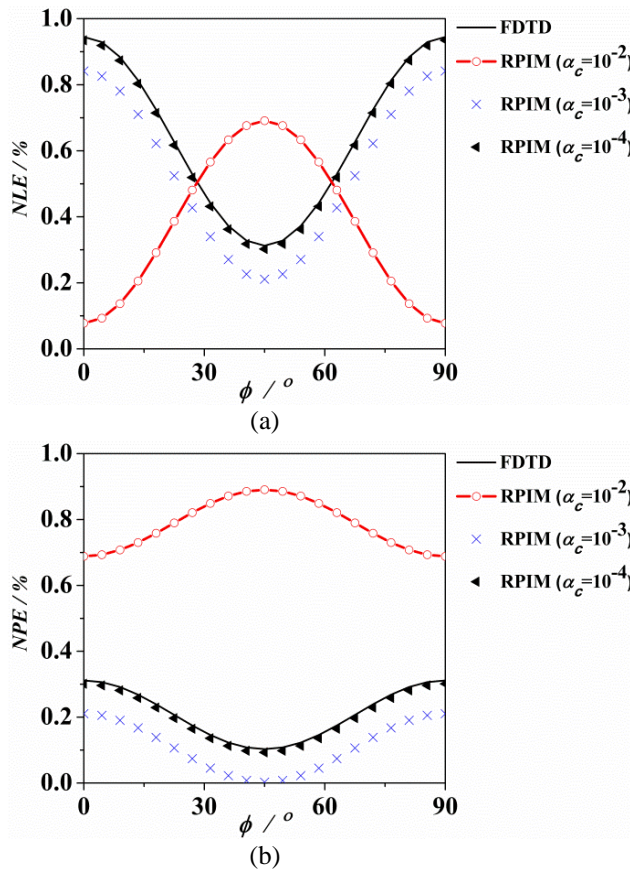


Fig. 2. Numerical dispersion of the RPIM method: (a) NLE and (b) NPE versus the angle of propagation in a medium of $\epsilon_r=1$ and $\sigma=0.001S/m$.

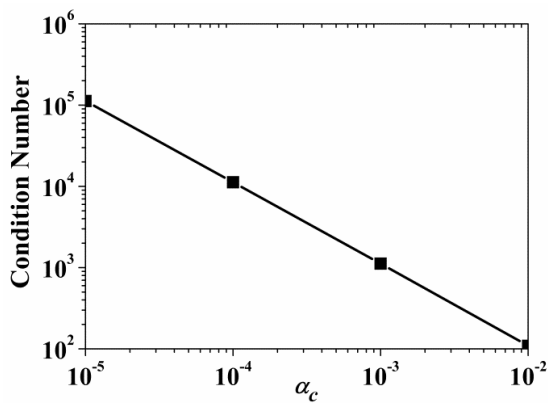


Fig. 3. Condition number of the moment matrix G versus different α_c of Gaussian basis function.

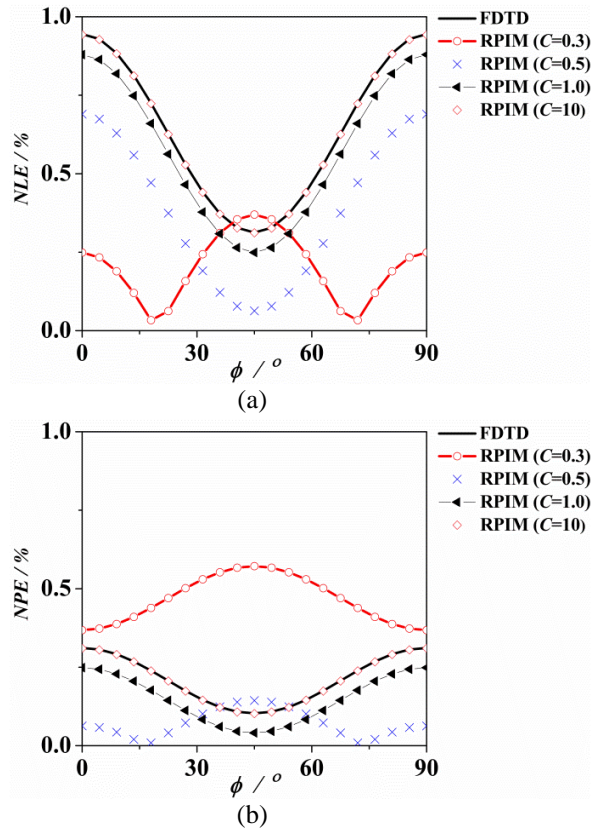


Fig. 4. Numerical dispersion of the RPIM method using the multiquadric basis function: (a) NLE and (b) NPE of the RPIM method versus the angle of propagation. $q=0.01$. C is changed from 0.3 to 10. $N=4$ and $\sigma=0.001 S/m$.

From Fig. 5, we can see that q has little effect on the NLE s and NPE s of the algorithm. Therefore, numerical dispersion errors of the RPIM method with the multiquadric basis function are mainly determined by C .

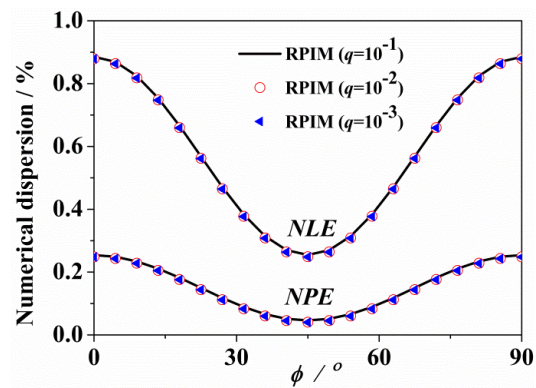


Fig. 5. Numerical dispersion of the RPIM method using the multiquadric basis function of the RPIM method versus the angle of propagation with $q=0.01$, 0.01 and 0.001 , respectively. In all cases, $C=1$, $N=4$, and $\sigma=0.001 S/m$.

Figure 6 gives the condition numbers of the moment matrix G versus different C . Comparing Fig. 6 with Fig. 3, we can clearly see that the condition numbers of G based on multiquadric function are far greater than that of G with Gaussian function; in other words, when the RPIM uses the multiquadric function as basis function, its coefficient matrix is more prone to be system singularity or numerical instability than that with Gaussian basis function.

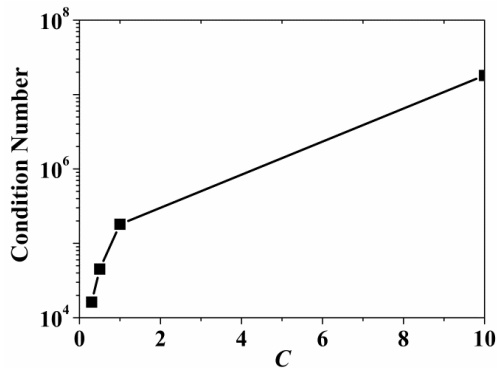


Fig. 6. Condition number of the moment matrix G versus different C of multiquadric basis function.

Hence, based on the above analyses, in balancing between the modeling accuracy and the matrix condition number, it can be concluded that Gaussian basis function is a better choice for the RPIM approach for electromagnetic modeling. Therefore, in the following investigation, we use Gaussian basis function.

B. Effects of numbers of the nodes within a support domain

In this subsection, we investigate the effect of the number N of the nodes within a support domain. This is an important study as the results may provide a practical guideline on how to choose the number of nodes that can provide the best accuracy with least possible computational expenditure. The numbers of the node points are $N=4$, 12 ($\alpha_c=0.001$) and 16 ($\alpha_c=0.003$, for solution stability), respectively, with the change of the size of the support domain. The conductivity of the medium is $\sigma=0.1$ S/m.

Figure 7 shows the numerical dispersions. As seen, when $N=4$, the numerical dispersion errors approximately equal to those of the FDTD method; when $N=12$, the NLE s and the NPE s of the algorithm are also less than the errors of the FDTD approach; however, when $N=16$, although the NPE s of the meshless method are smaller than those of the FDTD method, almost all of the NLE s are far greater than them. The reason is that the condition number of G is significantly increased when $N=16$ (see Fig. 8). Although we can increase the value of α_c to reduce the condition number of the moment matrix, only

the NPE s of the algorithm will decrease but not necessarily NLE . Clearly, the NLE is more sensitive than the NPE to the singularity of the moment matrix. In weighting all the above factors, we conclude that only when the moment matrix becomes nonsingular, numerical dispersion errors of the RPIM method can be reduced by increasing the number of the nodes.

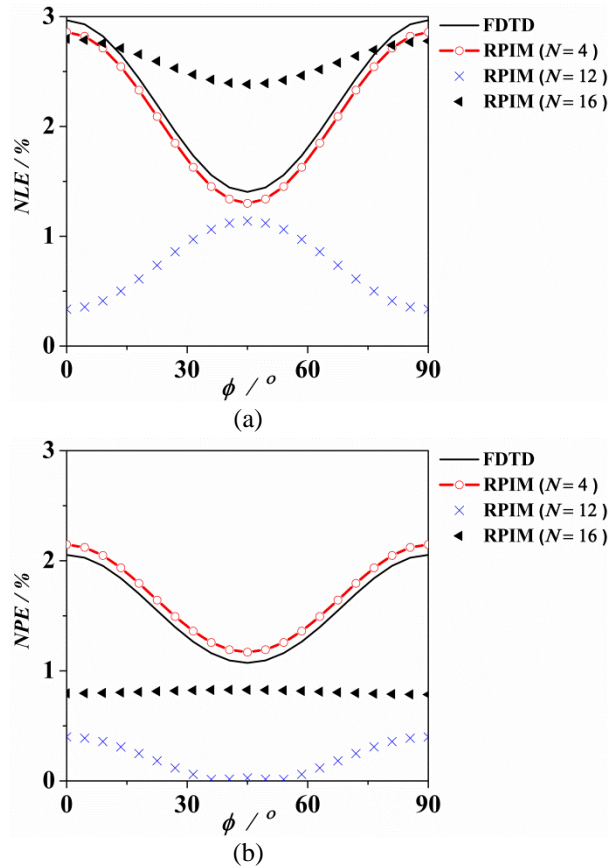


Fig. 7. Numerical dispersion of the RPIM method with Gaussian basis function: (a) NLE and (b) NPE versus N . $\Delta s=\lambda/20$ and $\sigma=0.1$ S/m.

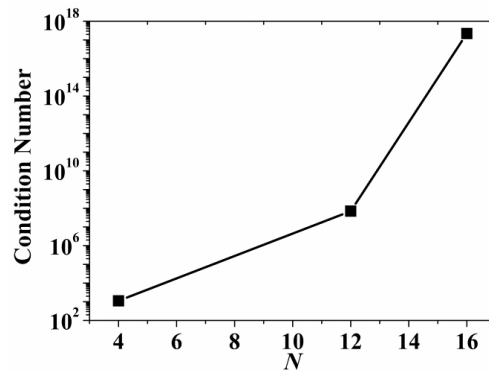


Fig. 8. Condition number of the moment matrix G versus different N .

C. Effects of media's conductivity

In this subsection, we investigate the effect of conductivity of the medium. $\sigma=0.001$ S/m, 0.1 S/m, and 1 S/m are used as the conductivity of the medium under consideration, respectively. For obtaining a stable solution, N is set to 4 with $\alpha_c=0.001$.

Figure 9 shows the $NLEs$ and $NPEs$ of the RPIM method. The $NLEs$ and the $NPEs$ of the method increase with the increase of σ . And the increase of the $NPEs$ is much larger than that of the $NLEs$. Therefore, the electromagnetic wave propagation in lossy dielectric may lead to greater numerical dispersion error than in free space.

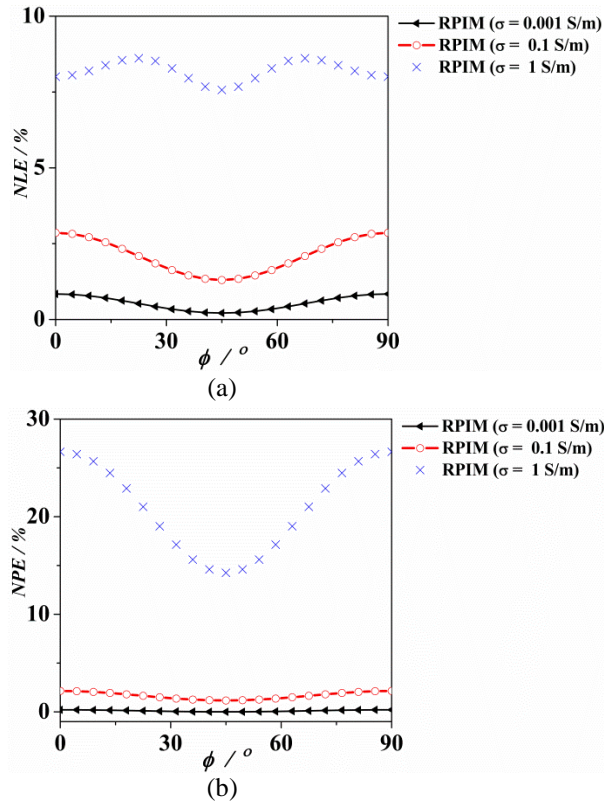


Fig. 9. Numerical dispersion of the RPIM method with Gaussian basis function: (a) NLE and (b) NPE versus conductivity. $N=4$, $\Delta s=\lambda/20$, and $\alpha_c=0.001$.

IV. CONCLUSION

The general relation for numerical dispersion of the RPIM method is derived and analyzed for both lossless and lossy media in this paper. It was shown that only when the moment matrix is nonsingular, the numerical dispersion error of the RPIM can be less than that of the FDTD method. Solution stability and accuracy of the RPIM method are also influenced by the types of the basis functions and the number of nodes. The moment matrix of the RPIM with multiquadric basis function is more prone to be ill-conditioned than Gaussian function.

Moreover, the NLE of the meshless method is more sensitive than the NPE to the singularity of the moment matrix; therefore, the balances between the solution stability (as a result of the ill-condition) and solution accuracy should be considered when choosing the modeling parameters. Another finding is that increase of medium conductivity leads to increase of numerical dispersion error.

Finally, it is noted that the FDTD method can be considered as a special case of the meshless methods with low-order roof-top functions as the basis functions [14], [18], [19], [20]. As a result, the meshless methods are expected to have smaller numerical errors in general but not always due to the conditions and complexity of the moment matrix. This is shown in this paper.

ACKNOWLEDGMENT

The authors wish to acknowledge the supports of National Natural Science Foundation of China through Grant #61471107, #61761017, Open Project of State Key Laboratory of Millimeter Waves through Grant #K201829 and the Natural Science and Engineering Research Council (NSERC) of Canada through its discovery program.

REFERENCES

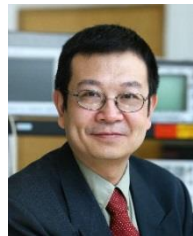
- [1] S. Yang, Z. Chen, Y. Yu, and S. Ponomarenko, "On the numerical dispersion of the radial point interpolation meshless method," *IEEE Microwave And Wireless Components Letters*, vol. 24, no. 10, pp. 653-655, Oct. 2014.
- [2] T. Kaufmann, C. Fumeaux, and R. Vahldieck, "The meshless radial point interpolation method for time-domain electromagnetics," *2008 IEEE MTT-S International Microwave Symposium Digest*, Atlanta, USA, pp. 61-64, Sep. 2008.
- [3] Y. Yu, F. Jolani, and Z. Chen, "An efficient meshless approach to multi-scale modeling in the time-domain," *The Applied Computational Electromagnetics Society*, vol. 27, no. 6, pp. 466-474, June 2012.
- [4] Y. Yu and Z. Chen, "A 3-D radial point interpolation method for meshless time-domain modeling," *IEEE Transactions on Microwave Theory and Techniques*, vol. 57, no. 8, pp. 2015-2020, Aug. 2009.
- [5] R. M. S. de Oliveira, W. C. B. Sousa, and W. R. M. Rabelo, "A meshless discretization methodology based on lennard-jones forces," *IEEE Antennas and Wireless Propagation Letters*, vol. 16, pp. 1492-1495, June 2017.
- [6] Y. Tanaka, S. Watanabe, and T. Oko, "Study of eddy current analysis by a meshless method using RPIM," *IEEE Transactions on Magnetics*, vol. 51, no. 3, pp. 7201404, Mar. 2015.
- [7] R. Khalef, M. T. Benhabiles, F. Grine, and M. L.

- Riabi, "An unconditionally stable radial point interpolation meshless method based on the Crank–Nicolson scheme solution of wave equation," *IEEE Transactions on Microwave Theory and Techniques*, vol. 66, no. 8, pp. 3705–3713, Aug. 2018.
- [8] T. Kaufmann, C. Engström, C. Fumeaux, and R. Vahldieck, "Eigenvalue analysis and longtime stability of resonant structures for the meshless radial point interpolation method in time domain," *IEEE Transactions on Microwave Theory and Techniques*, vol. 58, no. 12, pp. 3399–3408, Dec. 2010.
- [9] Y. Zhang, K. R. Shao, Y. Guo, J. Zhu, D. X. Xie, and J. D. Lavers, "A comparison of point interpolative boundary meshless method based on PBF and RBF for transient eddy-current analysis," *IEEE Transactions on Magnetics*, vol. 43, no. 4, pp. 1497–1500, Apr. 2007.
- [10] S. J. Lai, B. Z. Wang, and Y. Duan, "Meshless radial basis function method for transient electromagnetic computations," *IEEE Trans. Magnetics*, vol. 44, no. 10, pp. 2288–2295, Oct. 2008.
- [11] F. Ansarizadeh and M. Movahhedi, "Unconditionally-stable meshless methods using different split-step techniques and their phase velocity considerations," *The Applied Computational Electromagnetics Society*, vol. 28, no. 9, pp. 788–794, Sep. 2013.
- [12] X. Zhang, P. Ye, Z. Chen, and Y. Yu, "Numerical dispersion analysis of radial point interpolation meshless method," *2017 Progress in Electromagnetics Research Symposium*, Singapore, pp. 717–719, Nov. 2015.
- [13] Z. Shaterian, T. Kaufmann, and C. Fumeaux, "On the choice of basis functions for the meshless radial point interpolation method with small local support domains," *IEEE International Conference on Computational Electromagnetics*, Hong Kong, China, pp. 288–290, Feb. 2015.
- [14] Z. Chen and S. Luo, "Generalization of the finite-difference-based time-domain methods using the method of moments," *IEEE Transactions on Microwave Theory and Techniques*, vol. 54, no. 9, pp. 2515–2524, Sep. 2006.
- [15] G. Sun and C. W. Trueman, "Numerical dispersion and numerical loss in explicit finite-difference time-domain methods in lossy media," *IEEE Transactions on Antennas and Propagation*, vol. 53, no. 11, pp. 3684–3690, Nov. 2005.
- [16] J. A. Pereda, O. García, A. Vegas, and A. Prieto, "Numerical dispersion and stability analysis of the FDTD technique in lossy dielectrics," *IEEE Microwave and Guided Wave Letters*, vol. 8, no. 7, pp. 245–247, July 1998.
- [17] G. Sun, X. Ma, and Z. Bai, "Numerical stability and dispersion analysis of the precise-integration time-domain method in lossy media," *IEEE Transactions on Microwave Theory and Techniques*, vol. 60, no. 9, pp. 2723–2729, Sep. 2012.
- [18] Z. Chen and M. Ney, "Method of weighted residuals: a general approach to deriving time- and frequency-domain numerical methods," *IEEE Antennas and Propagation Magazines*, vol. 51, no. 1, pp. 51–70, Feb. 2009.
- [19] Z. Chen, "How can we unify numerical methods with a single mathematic framework?," *Proceedings of 2014 Asia-Pacific Conference on Antennas and Propagation*, Harbin, China, pp. 1392–1395, July 2014.
- [20] J. Wang, Z. Chen, J. Li, Y. Yu, and J. Liang, "Towards a unifying computational platform with the node-based meshless method," *Proceedings of 2018 IEEE International Microwave Symposium*, Pennsylvania, USA, pp. 1017–1020, June 2018.



Xianyan Zhang received the B.S. degree in Applied Physics and M.S. degree in Physical Electronics from Yunnan University, Kunming, China, in 2001 and 2004 respectively, and the Ph.D. degree in Electromagnetic Field and Microwave Technology from Institute of Electronics, Chinese Academy of Sciences in 2007.

Her research interests include electromagnetic computation, antenna design and wireless power transmission structure design.



Zhizhang (David) Chen received the bachelor's degree from Fuzhou University, the Master degree in Radio Engineering from Southeast University, P. R. China, the Ph.D. degree in Electrical Engineering from the University of Ottawa, Canada. He was a NSERC Post-doctoral Fellow with McGill University, Montreal, Canada. He is currently a Professor with Dalhousie University, Halifax, Nova Scotia, Canada, where he has served as the Head of the Department of Electrical and Computer Engineering. He has been an Adjunct or Visiting Professor with the University of Nottingham of UK, École Nationale Supérieure des Télécommunications de Bretagne of France, Shanghai Jiaotong University,

Beihang University, Fuzhou University and the University of Electronic Science and Technology of China.

Chen has authored and coauthored over 350 journal and conference papers in computational electromagnetics, RF/microwave electronics, antennas, and wireless technologies. His current research interests are in time-domain electromagnetic modeling techniques, ultra-wideband wireless communication systems and wireless power transfer technology. He received the 2005 Nova Scotia Engineering Award, a 2006 Dalhousie Graduate Teaching Award, the 2007 & 2015 Dalhousie Faculty of Engineering Research Award and the 2013 IEEE Canada Fessenden Medal. He is the Fellow of the IEEE, the Canadian Academy of Engineering and the Engineering Institute of Canada.



Yiqiang Yu received the M.S. degree in Communication Systems in 2003 and the Ph.D. in Microwave Communications Engineering in 2007 from Swansea University, U.K.

He is an Associate Professor with East China Jiaotong University.

He is also an Adjunct Professor with the University of Electronic Science and Technology of China and Dalhousie University, Halifax, Canada. He is also the CEO of Chengdu Sprouting Technology Co. Ltd. His primary interest is in applications of computational electromagnetics. His interests also include wireless power transmission structure design, antennas design and measurement, EMI/EMC analysis and testing.

Eigenvalue Decomposition Approach for Beampattern Synthesis

Jie Chen¹ and Yingzeng Yin²

¹School of Electronic Engineering
Xi'an Aeronautical University, Xi'an, 710077, China
chenbinglin88888@163.com

²National Key Laboratory of Antenna and Microwave Technology
School of Electronic Engineering, Xidian University, Xi'an, 710071, China
yyzeng@mail.xidian.edu.cn

Abstract — The relation between the manifold matrix of the array and the synthesized beampattern is investigated. The synthesized beampattern can be obtained by eigenvalue decomposition of the projection matrix of the array manifold matrix, while the least square error reaches the minimum. For an antenna array whose manifold matrix has been determined, the projection matrix can be derived easily from the array manifold matrix. Then, eigenvalue decomposition of the projection matrix is implemented to obtain the synthesized beampattern. The antenna element excitations can be obtained by an ameliorated least square method. The results of the simulations compared with the traditional least square method show that the matching degree between the targeted beampattern and the synthesized beampattern of the new method is higher and that the new method is more efficient.

Index Terms — Array manifold matrix, beampattern synthesis, eigenvalue decomposition, least square method, projection matrix.

I. INTRODUCTION

Beampattern synthesis of the antenna array and beamforming technology have been broadly studied and used in the domains of multiple-input multiple-output (MIMO) radar and smart antenna for several decades. In the early phase of development, beamforming was accomplished in the radio frequency front end by phase shifters and radio amplifiers weighting the antenna element excitations. This structure is cumbersome, sizable, and inflexible. As microelectronic and digital technology develop, beamforming is achieved by digital signal processing techniques. The most researched topic is the receiving beamforming, in which the received antenna element signals are weighted to form the expected beampattern. Many approaches for beamforming have been developed by researchers. One method is the well-known capon beamforming [1,16].

Another approach views beamforming as a nonlinear optimization problem to obtain the antenna element excitations or the weighting vector. This method has been used in several recent studies [2-7]. However, it is well known that convex optimization approach is an iterative method for pattern synthesis in most cases.

Currently, with the development of signal processing technology, many articles have been published. In the literature [8], an optimization method of an arbitrary side-lobe attenuation level was provided. The literature [9] discussed a beamforming approach for wideband use in MIMO systems. In the literature [10], a compressed sensing method was applied for beamforming. An ameliorated difference genetic algorithm for beamforming was proposed in the literature [11]. In the literature [12], the beamforming method under the constraint of l_1 -norm minimization was investigated. Phased array beam steering through serial control of the phase shifters was presented in another article [13].

The least square (LS) method is a classic approach that has been used broadly in many areas [14]. A steerable least square approach was presented in a further article [15]. Reference [17] studied the phase and pattern characteristics of a sub-wavelength broadband reflectarray unit element based on triple concentric circular-rings.

In the methods mentioned above, the expected beampatterns are often presumed in advance as a determined vector to lower the complexity of beamforming and to reduce the computing amount. However, none of these methods investigates the relation between the manifold matrix of array and the targeted beampattern. In this paper, the relation between the manifold matrix of array and the targeted beampattern is investigated. The synthesized beampattern can be obtained by eigenvalue decomposition of the projection matrix of the array manifold matrix, while the least square error reaches the minimum. Then, the

antenna element excitations can be obtained through an ameliorated least square method. Compared with the traditional least square method, the synthesized outcomes of the new approach are more efficient and have better agreement with the expected beampattern. In addition, the new method is a non-iterative approach for pattern synthesis.

The rest of this paper is organized as follows: Section II presents the beampattern synthesis paradigm; Section III provides the eigenvalue decomposition method for beampattern synthesis; Section IV shows the solution of the array excitation by an ameliorated least square method; Section V discusses the new approach and compares the results with the traditional least square method; and Section VI draws a conclusion.

II. BEAMPATTERN SYNTHESIS PARADIGM

Consider an N -element d -spaced uniform linear antenna array, where all the elements are isotropic. Assume all the antenna elements transmit a narrow-band beam with a central wave length λ . We investigate the far-field scenario. The antenna elements are arranged as shown in Fig. 1, numbered from 1 to N .

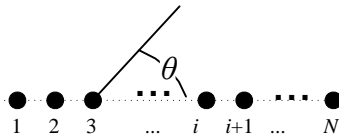


Fig. 1. Arrangement of the uniform linear antenna array.

In Fig. 1, the angle between the signal and the axis of the array is denoted as θ , in the far field, the formed beampattern can be written as:

$$s = \sum_{i=0}^{N-1} W_i e^{j2\pi i d \cos \theta / \lambda}. \quad (1)$$

In equation (1), W_i is the $i+1$ th antenna element's current excitation.

Let $\mathbf{a}(\theta) = [1, e^{j2\pi d \cos \theta / \lambda}, \dots, e^{j2\pi d(N-1) \cos \theta / \lambda}]^T$ be the steering vector with superscript T denoting the transpose operation. Denote the antenna element excitation vector as $\mathbf{W} = [W_0, W_1, \dots, W_{i-1}, \dots, W_{N-1}]^T$. Thus, equation (1) can be expressed as:

$$s = \mathbf{a}^T(\theta) \mathbf{W}. \quad (2)$$

Set θ in the interval of $[0^\circ, 180^\circ]$. Denote its discrete value as $\theta_1, \theta_2, \dots, \theta_k, \dots, \theta_K$. If the targeted beampattern vector is:

$$\begin{aligned} \mathbf{P} &= [P(\theta_1), P(\theta_2), \dots, P(\theta_k), \dots, P(\theta_K)]^T \\ &= [P_1, P_2, \dots, P_k, \dots, P_K]^T, \end{aligned} \quad (3)$$

then, the objective of the beampattern synthesis is to obtain the weighting vector by solving the equation:

$$\text{abs}([\mathbf{a}(\theta_1), \mathbf{a}(\theta_2), \dots, \mathbf{a}(\theta_k), \dots, \mathbf{a}(\theta_K)]^T \mathbf{W}) = \mathbf{P}, \quad (4)$$

where abs denotes the absolute value operation.

Let $\mathbf{A} = [\mathbf{a}(\theta_1), \mathbf{a}(\theta_2), \dots, \mathbf{a}(\theta_k), \dots, \mathbf{a}(\theta_K)]$, where \mathbf{A} is the array manifold matrix; therefore, equation (4) can be expressed as:

$$\text{abs}(\mathbf{A}^T \mathbf{W}) = \mathbf{P}. \quad (5)$$

It is difficult to solve this equation directly because this equation is considered an overdetermined equation in most cases.

To solve this equation, traditional practice is to transform equation (5) into either:

$$\mathbf{A}^T \mathbf{W} = \mathbf{P}, \quad (6)$$

or

$$\min \|\mathbf{A}^T \mathbf{W} - \mathbf{P}\|^2. \quad (7)$$

In equation (7), $\|\cdot\|$ denotes the vector length operation.

Compared with equation (5), equations (6) and (7) remove the absolute value operation and simplify the solving process. There are many traditional methods to solve equations (6) and (7). Obviously, removing the absolute operation of equation (5) largely simplifies the process, however, it also causes less agreement between the synthesized beampattern and the expected beampattern. Hence, in the following sections of this paper, a novel approach is presented to solve equation (5).

III. BEAMPATTERN SYNTHESIS BY EIGENVALUE DECOMPOSITION

To solve equation (5), an intermediate vector \mathbf{F} is used to satisfy:

$$\mathbf{A}^T \mathbf{W} = \mathbf{F}, \quad (8)$$

$$\text{abs}(\mathbf{F}) = \mathbf{P}. \quad (9)$$

First, equation (9) can be solved; its solution is:

$$\begin{aligned} \mathbf{F} &= \text{diag}(e^{j\phi_1}, e^{j\phi_2}, \dots, e^{j\phi_K}) \mathbf{P} \\ &= [P_1 e^{j\phi_1}, P_2 e^{j\phi_2}, \dots, P_K e^{j\phi_K}]^T. \end{aligned} \quad (10)$$

In this equation, diag denotes the diagonal matrix, and ϕ_k ($k=1, 2, \dots, K$) is an arbitrary angle variable. Therefore, we can obtain:

$$\text{diag}(\mathbf{F}^*) = \text{diag}[P_1 e^{-j\phi_1}, P_2 e^{-j\phi_2}, \dots, P_K e^{-j\phi_K}]^T, \quad (11)$$

where $*$ denotes the conjugate operation.

Then, equation (9) can be transformed into:

$$\begin{aligned} \text{diag}(\mathbf{F}^*) \mathbf{F} &= \text{diag}[P_1 e^{-j\phi_1}, P_2 e^{-j\phi_2}, \dots, P_K e^{-j\phi_K}]^T \mathbf{F} \\ &= [P_1^2, P_2^2, \dots, P_K^2]^T = \text{diag}[P_1, P_2, \dots, P_K]^T \mathbf{P} \\ &= \text{diag}(\mathbf{P}) \mathbf{P}. \end{aligned} \quad (12)$$

Hence, equation (8) can be transformed into:

$$\text{diag}(\mathbf{F}^*) \mathbf{A}^T \mathbf{W} = \text{diag}(\mathbf{F}^*) \mathbf{F} = \text{diag}(\mathbf{P}) \mathbf{P}. \quad (13)$$

Denote $\mathbf{G} = \text{diag}(\mathbf{F}^*) \mathbf{A}^T$ and $\mathbf{M} = \text{diag}(\mathbf{P}) \mathbf{P}$. Then, equation (13) can be rewritten as:

$$\mathbf{G} \mathbf{W} = \mathbf{M}. \quad (14)$$

Its least square solution is:

$$\mathbf{W}_{LS} = (\mathbf{G}^H \mathbf{G})^{-1} \mathbf{G}^H \mathbf{M}. \quad (15)$$

In equation (15), superscript H denotes the conjugate transpose operation.

According to the projection theory, equation (15) means that while \mathbf{M} is projected into the column vector space of the \mathbf{G} matrix, the error between the synthesized beampattern obtained by \mathbf{W}_{LS} and \mathbf{M} reaches the minimum [14]. It is easy to determine that the projection vector from \mathbf{M} to matrix \mathbf{G} 's column vector space is [14]:

$$\mathbf{P}_G = \mathbf{G}(\mathbf{G}^H \mathbf{G})^{-1} \mathbf{G}^H \mathbf{M}. \quad (16)$$

Its error vector is [14]:

$$\mathbf{E}_G = (\mathbf{E} - \mathbf{G}(\mathbf{G}^H \mathbf{G})^{-1} \mathbf{G}^H) \mathbf{M}, \quad (17)$$

where \mathbf{E} is a unit matrix.

Obviously, the minimum of the error is $\mathbf{0}$ vector, i.e., $\mathbf{E}_G = \mathbf{0}$. Hence, in this situation:

$$\mathbf{E}_G = (\mathbf{E} - \mathbf{G}(\mathbf{G}^H \mathbf{G})^{-1} \mathbf{G}^H) \mathbf{M} = \mathbf{0}. \quad (18)$$

Taking a step forward, we can obtain:

$$\mathbf{G}(\mathbf{G}^H \mathbf{G})^{-1} \mathbf{G}^H \mathbf{M} = \mathbf{E} \mathbf{M} = \mathbf{1} \times \mathbf{M}. \quad (19)$$

Equation (19) means \mathbf{M} is the eigenvector of the matrix $\mathbf{G}(\mathbf{G}^H \mathbf{G})^{-1} \mathbf{G}^H$ to the eigenvalue of 1.

Therefore, the synthesized beampattern \mathbf{Q} can be obtained from the eigenvalue decomposition of the matrix $\mathbf{G}(\mathbf{G}^H \mathbf{G})^{-1} \mathbf{G}^H$. \mathbf{Q} is the eigenvector to the eigenvalue of 1. From \mathbf{Q} , the array element excitation vector can be obtained.

IV. THE SOLUTION OF THE ELEMENT CURRENT EXCITATIONS

After eigenvector \mathbf{Q} is substituted into equation (14), the following equation can be obtained:

$$\mathbf{G} \mathbf{W} = \mathbf{Q}. \quad (20)$$

Substituting $\mathbf{G} = \text{diag}(\mathbf{F}^*) \mathbf{A}^T$ into equation (20), we can obtain:

$$\mathbf{G} \mathbf{W} = \text{diag}(\mathbf{F}^*) \mathbf{A}^T \mathbf{W} = \mathbf{Q}. \quad (21)$$

From equation (21), we can obtain:

$$\mathbf{A}^T \mathbf{W} = (\text{diag}(\mathbf{F}^*))^{-1} \mathbf{Q}. \quad (22)$$

Let $\mathbf{D} = \text{diag}((\text{diag}(\mathbf{F}^*))^{-1} \mathbf{Q})$ and $\mathbf{B} = \mathbf{A}^T$; then, the steerable least square solution \mathbf{W} of equation (22) can be obtained as [15]:

$$\mathbf{W} = (\mathbf{B}^H (\mathbf{D}^{-1})' \mathbf{B})^{-1} \mathbf{B}^H (\text{diag}(\mathbf{F}^*))^{-1} \mathbf{Q}, \quad (23)$$

where l is an integer variable.

V. THE SIMULATIONS AND RESULTS

In this section, three examples are conducted to demonstrate the new approach's performance.

Consider an N -element d -spaced uniform linear antenna array, where all the elements are isotropic. Assume all the antenna elements transmit a narrow-band beam with a central wave length λ . We investigate the far-field scenario. The antenna elements are arranged as shown in Fig. 1, numbered from 1 to N . Let $d = \lambda/2$.

Given that the beampattern is a periodic function of θ , we set θ in a cycle interval of $[0^\circ, 180^\circ]$. Let θ 's discrete value $\theta_1, \theta_2, \dots, \theta_k, \dots, \theta_K$ be $0^\circ, 1^\circ, \dots, 179^\circ, 180^\circ$, in sequence. These settings are consistent with real practice and facilitate digital processing.

In the first example, let $N=21$, and the expected beampattern is created by uniform element excitation. The targeted beampattern can be obtained by:

$$s = \sum_{i=0}^{N-1} I e^{j2\pi i d (\cos \theta - \cos \theta_0) / \lambda}, \quad (24)$$

where θ is the signal transmitting angle as shown in Fig. 1, $\theta_0 = \pi/2$ is the scan angle, and I is the amplitude of the antenna element current excitation.

Let $\mathbf{F} = \mathbf{P}$; the simulation outcomes are shown in Fig. 2. In the legend column of Fig. 2, the target denotes the expected beampattern created by equation (24); LS refers to the traditional least square solution of equation (6); eigen marks the synthesized beampattern that is the eigenvector to the eigenvalue of 1 obtained from eigenvalue decomposition of the matrix $\mathbf{G}(\mathbf{G}^H \mathbf{G})^{-1} \mathbf{G}^H$; the beampattern of eigen is substituted into equation (23) to obtain the array element excitation and $l=0, l=1, l=2, l=3, l=4$ indicate the beampatterns created by the element excitation of equation (23), while l has different values.

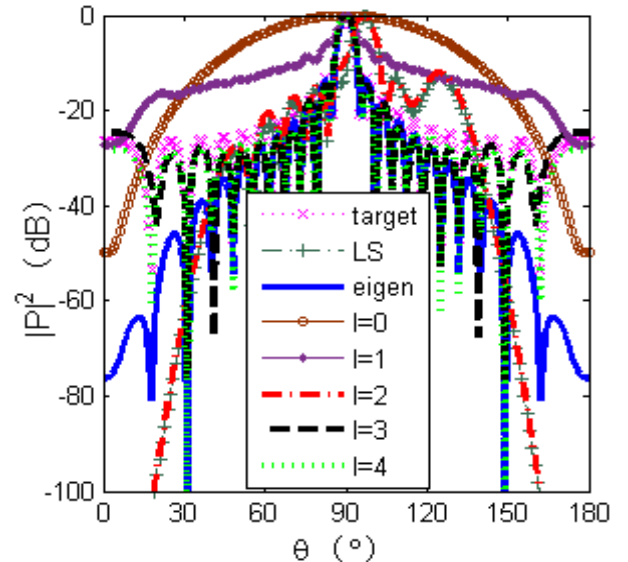


Fig. 2. The outcomes of the first simulation ($N=21$).

In Fig. 2, the main-lobe of the targeted beampattern is in the range $[84^\circ, 96^\circ]$, with the highest level at $\theta=90^\circ$. Its first side-lobe peak level is -13.6 dB. The main-lobe of the least square method is in the range $[84^\circ, 106^\circ]$, with the highest level at $\theta=97^\circ$. Its side-lobe peak level is -12.5 dB at $\theta=126^\circ$. The beampattern of the eigenvalue decomposition method and the targeted beampattern overlap in range from the left second side-

lobe to the right second side-lobe. In the other range, while θ is moving farther away from $\theta=90^\circ$, the gain of the eigenvalue decomposition beampattern gradually decreases more than that of the targeted beampattern. The beampattern created by equation (23), while $l=0$, has no apparent main-lobe or side-lobe. The beampattern, created by equation (23) while $l=1$, has an apparent main-lobe but no side-lobe. Its main-lobe is in the range of $[85^\circ, 95^\circ]$, with the highest level at $\theta=90^\circ$. Its first side-lobe peak level is -5.5 dB. While $l=2$, the beampattern created by equation (23) nearly overlaps with the beampattern of the least square method. The beampatterns created by equation (23), while $l=3$ and $l=4$, nearly overlap with the targeted beampattern.

It can be seen from Fig. 2 that the synthesized beampattern from eigenvalue decomposition, and the outcomes, while $l=3$, $l=4$, all have better agreement with the targeted beampattern than the outcome produced by the traditional least square method.

In the second example, let $N=15$, where all other conditions are the same as those in the first example. The expected beampattern is created by equation (24), with uniform element excitation. The simulation outcomes are shown in Fig. 3. In the legend column of Fig. 3, the target denotes the expected beampattern created by equation (24); LS refers to the traditional least square solution of equation (6); eigen marks the synthesized beampattern that is the eigenvector to the eigenvalue of 1 obtained from eigenvalue decomposition of the matrix $\mathbf{G}(\mathbf{G}^H\mathbf{G})^{-1}\mathbf{G}^H$; the beampattern of eigen is substituted into equation (23) to obtain the array element excitation and $l=0$, $l=1$, $l=2$, $l=3$, $l=4$ indicate the beampatterns created by the element excitation of equation (23), while l has different values.

In Fig. 3, the main-lobe of the targeted beampattern is in the range $[82^\circ, 98^\circ]$, with the highest level at $\theta=90^\circ$. Its first side-lobe peak level is -13.2 dB. The main-lobe of the least square method is in the range $[90^\circ, 106^\circ]$, with the highest level at $\theta=97^\circ$. Its side-lobe peak level is -1.5 dB at $\theta=82^\circ$. The beampattern of the eigenvalue decomposition method and the targeted beampattern overlap in the main-lobe range. In the other range, while θ is moving farther away from $\theta=90^\circ$, the gain of the eigenvalue decomposition beampattern gradually decreases more than that of the targeted beampattern. The beampattern created by equation (23), while $l=0$, has no apparent main-lobe or side-lobe. The beampattern created by equation (23), while $l=1$, has an apparent main-lobe but no side-lobe. Its main-lobe is in the range $[82^\circ, 98^\circ]$, with the highest level at $\theta=90^\circ$. Its first side-lobe peak level is -5.3 dB. While $l=2$, the beampattern created by equation (23) nearly overlaps with the beampattern of the least square method. While $l=3$ and $l=4$, the beampatterns created by equation (23) nearly overlap with the targeted

beampattern.

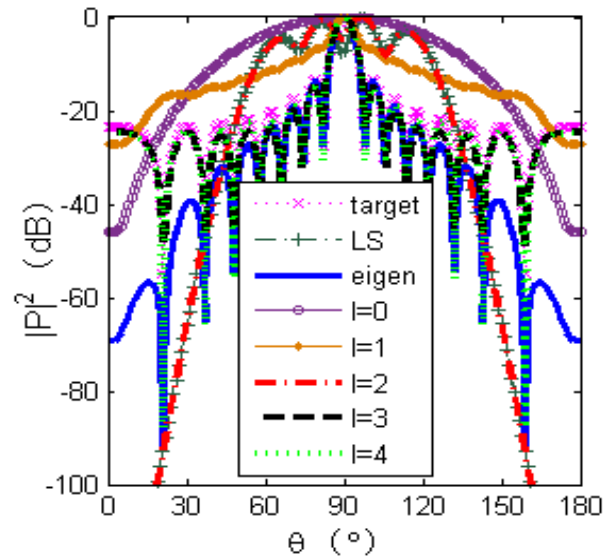


Fig. 3. The outcomes of the second simulation ($N=15$).

It can be seen from Fig. 3 that, once again, the synthesized beampattern of eigenvalue decomposition, and the outcomes, while $l=3$, $l=4$, all have better agreement with the targeted beampattern than the outcome produced by the traditional least square method.

In the third example, let $N=23$, and in the targeted beampattern, there exists a null beam, where θ is in the scope from 116° to 123° , with a lowest attenuation of -81 dB at $\theta=116^\circ$. Except for these values, other conditions are the same as those in the first example. The expected beampattern is still created by equation (24), with uniform element excitation. The simulation outcomes are shown in Fig. 4. In the legend column of Fig. 4, the target denotes the expected beampattern created by equation (24); LS refers to the traditional least square solution of equation (6); eigen marks the synthesized beampattern that is the eigenvector to the eigenvalue of 1 obtained from eigenvalue decomposition of the matrix $\mathbf{G}(\mathbf{G}^H\mathbf{G})^{-1}\mathbf{G}^H$; the beampattern of eigen is substituted into equation (23) to obtain the array element excitation and $l=0$, $l=1$, $l=2$, $l=3$, $l=4$ indicate the beampatterns created by the element excitation of equation (23), while l has different values.

In Fig. 4, the main-lobe of the targeted beampattern is in the range $[85^\circ, 95^\circ]$, with the highest level at $\theta=90^\circ$. Its first side-lobe peak level is -13.5 dB. The main-lobe of the least square method is in the range $[81^\circ, 95^\circ]$, with the highest level at $\theta=88^\circ$. Its side-lobe peak level is -6.1 dB at $\theta=113^\circ$. The beampattern of the eigenvalue decomposition method and the targeted beampattern overlap in range from the left first side-

lobe to the right first side-lobe and null beam scope. In the other range, while θ is moving farther away from $\theta=90^\circ$, the gain of the eigenvalue decomposition beampattern gradually decreases more than that of the targeted beampattern. The beampattern, created by equation (23), while $l=0$, has no apparent main-lobe or side-lobe. The beampattern, created by equation (23), while $l=1$, has an apparent main-lobe but no side-lobe. Its main-lobe is in the range $[85^\circ, 95^\circ]$, with the highest level at $\theta=90^\circ$. Its first side-lobe peak level is -6.7 dB. While $l=2$, the beampattern created by equation (23) nearly overlaps with the beampattern of the least square method. While $l=3$ and $l=4$, the beampatterns created by equation (23) nearly overlap with the targeted beampattern in the range where the null beam is not located. Only the targeted beampattern, the beampattern of the eigenvalue decomposition approach, and the beampattern created by equation (23), while $l=4$, have null beams in the same range; other beampatterns all have no null beam. The beampattern created by equation (23), while $l=4$, has a null beam with the lowest level, -79 dB at $\theta=116^\circ$.

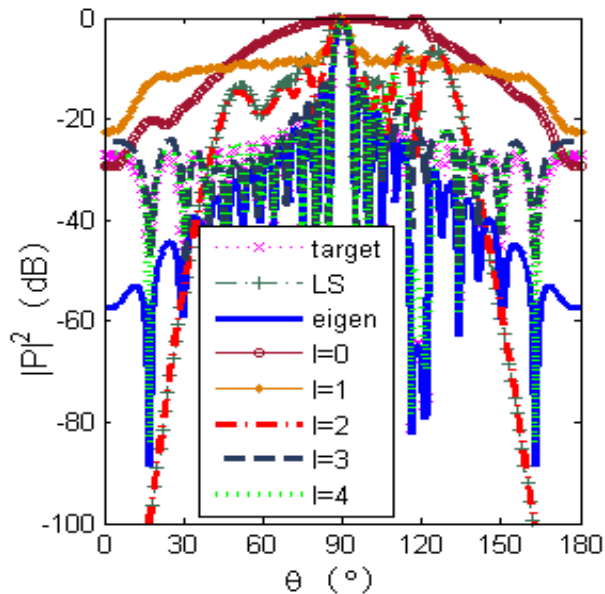


Fig. 4. The outcomes of the third simulation ($N=23$).

It can be seen from Fig. 4 that, once again, both the synthesized beampattern from eigenvalue decomposition and the outcome, while $l=4$, have better agreement with the targeted beampattern than the outcome produced by the traditional least square method. In particular, at the null beam zone, both the beampattern synthesized from eigenvalue decomposition and the outcome, while $l=4$, have much better agreement with the targeted beampattern, and the outcome produced by the traditional least square method has no apparent null beam.

From these examples, we can learn that the new method has better performance than the traditional least square method, and while l increases from 1 to 4, the beampattern created by the element excitation of equation (23) gradually matches the targeted pattern better and better. We simulate the new approach using the MATLAB software platform on an HP notebook PC with a core i5-5200U CPU and a 4G memory. All simulations in this paper take approximately less than one second to obtain the final outcomes.

VI. CONCLUSION

The synthesized beampattern can be obtained by eigenvalue decomposition of the projection matrix of the array manifold matrix, while the least square error reaches the minimum. For an antenna array whose manifold matrix has been determined, the projection matrix can be derived easily from the array manifold matrix. Then, eigenvalue decomposition of the projection matrix is conducted to obtain the synthesized beampattern, and the antenna element excitations can be solved by an ameliorated least square method. The results of the simulations compared with the traditional least square method show that the matching degree between the targeted beampattern and the synthesized beampattern of the new method is higher and that the new method is more efficient.

ACKNOWLEDGMENT

This work has been supported in part by the Chinese Government under the grant No. 61501340 of the National Natural Science Foundation, and Education Department of Shaanxi Province under the grant No. 17JK0397 of the Special Research Plan of Science and Technology Foundation.

REFERENCES

- [1] T. K. Sarkar, J. Koh, R. Adve, et al., "A pragmatic approach to adaptive antennas," *IEEE Acoust., Speech, and Signal Processing Mag.*, vol. 42, no. 2, pp. 39-55, 2000.
- [2] P. Lopez, J. A. Rodriguez, F. Ares, and E. Moreno, "Subarray weighting for difference patterns of monopulse antennas: Joint optimization of subarray configurations and weights," *IEEE Trans. Antennas Propag.*, vol. 49, no. 11, pp. 1606-1608, 2001.
- [3] S. Caorsi, A. Massa, M. Pastorino, and A. Randazzo, "Optimization of the difference patterns for monopulse antennas by a hybrid real/integer coded differential evolution method," *IEEE Trans. Antennas Propag.*, vol. 53, no. 1, pp. 372-376, 2005.
- [4] M. D'Urso, T. Isernia, and E. F. Meliaddò, "An effective hybrid approach for the optimal synthesis of monopulse antennas," *IEEE Trans.*

- Antennas Propag.*, vol. 55, no. 4, pp. 1059-1066, 2007.
- [5] L. Manica, P. Rocca, A. Martini, and A. Massa, "An innovative approach based on a tree-searching algorithm for the optimal matching of independently optimum sum and difference excitations," *IEEE Trans. Antennas Propag.*, vol. 56, no. 1, pp. 58-66, 2008.
- [6] Y. Chen, S. Yang, and Z. Nie, "The application of a modified differential evolution strategy to some array pattern synthesis problems," *IEEE Trans. Antennas Propag.*, vol. 56, no. 7, pp. 1919-1927, 2008.
- [7] L. Manica, P. Rocca, M. Benedetti, and A. Massa, "A fast graph-searching algorithm enabling the efficient synthesis of sub-arrayed planar monopulse antennas," *IEEE Trans. Antennas Propag.*, vol. 57, no. 3, pp. 652-663, 2009.
- [8] A. Morabito and P. Rocca, "Optimal synthesis of sum and difference patterns with arbitrary sidelobes subject to common excitations constraints," *IEEE Antennas Wireless Propag. Lett.*, vol. 9, pp. 623-626, 2010.
- [9] H. He, P. Stoica, and J. Li, "Wideband MIMO systems: Signal design for transmit beampattern synthesis," *IEEE Trans. Signal Processing*, vol. 59, no.2, pp. 618-628, 2011.
- [10] G. Oliveri and A. Massa, "Bayesian compressive sampling for pattern synthesis with maximally sparse non-uniform linear arrays," *IEEE Trans. Antennas Propag.*, vol. 59, no. 2, pp. 467-481, 2011.
- [11] X. Li, W. T. Li, and X. W. Shi, "Modified differential evolution strategy for antenna array pattern synthesis," *Progr. Electromagn. Res.*, vol. 137, no. 2, pp. 371-388, 2013.
- [12] H. Chen, Q. Wang, and R. Fan, "Beampattern synthesis using reweighted l_1 -norm minimization and array orientation diversity," *Radioengineering*, vol. 22, no. 2, pp. 602-609, 2013.
- [13] R. L. Haupt, "Phased array beam steering through serial control of the phase shifters," *Appl. Comput. Electrom. Society Journal*, vol. 32, no. 12, pp. 1140-1143, 2017.
- [14] L. I. Vaskelainen, "Constrained least-squares optimization in conformal array antenna synthesis," *IEEE Trans. Antennas Propag.*, vol. 55, no. 3, pp. 859-867, 2007.
- [15] J. Chen, Y. Z. Yin, and Y. Jiao, "A steerable least square approach for pattern synthesis," *Progr. Electromagn. Res. M*, vol. 59, pp. 181-191, 2017.
- [16] J. Capon, "High resolution frequency-wave number spectrum analysis," *Proceedings of the IEEE*, vol. 57, pp. 1408-1418, 1969.
- [17] J. Nourinia, C. Ghobadi, B. Mohammadi, and F. Alizadeh, "Study of phase and patterns

characteristics of a sub-wavelength broadband reflectarray unit element based on triple concentric circular-rings," *Appl. Comput. Electrom. Society Journal*, vol. 33, no. 6, pp. 714-718, June 2018.



Jie Chen is now an Associate Professor of School of Electronic Engineering, Xi'an Aeronautical University, No.259 Xi'an West Second Ring Road, Xi'an, 710077, China. He received his bachelor and master degree in Electronic Science and Technology major from School of Electronic and Information, Xi'an Jiaotong University in 1997 and 2004, respectively. In 2013, he achieved his doctor degree in Electromagnetic Theory and Microwave Technique major from School of Electronic Engineering, Xidian University. His research interests are in the areas of smart antenna, antenna array, microwave circuit design, wireless communication and RFID technique.



Yingzeng Yin is now a Professor of Xidian University. He works in National Key Laboratory of Antenna and Microwave Technology, School of Electronic Engineering, Xidian University, Xi'an, 710071, China. His research activities are in the fields of microwave circuit design, antenna design, smart antenna design and RFID technique.

Discontinuous Galerkin Finite Element Time Domain Method for Analysis of Ferrite Circulator with Non-conforming Meshes

M. Li^{1,2}, X. D. Ye³, F. Xu¹, and N. M. Luo³

¹School of Electronic Science and Engineering
Nanjing University of Posts and Telecommunications, Nanjing, 210003, China

²Department of Electronic Information Engineering
Suqian College, Suqian, 223800, China
18800608557@163.com

³Department of Communication Engineering
Nanjing University of Science and Technology, Nanjing, 210094, China
yexiaodong@njjust.edu.cn

Abstract —In this paper, a Discontinuous Galerkin finite element time-domain method (DG-FETD) based on non-conforming hybrid meshes is presented for analysis of the ferrite device. The DG-FETD method with explicit difference scheme is firstly used to analyze the electromagnetic characteristics of complex medium such as ferrite material to reduce memory requirement and computational time. The recursive convolution (RC) method is applied into DG-FETD to deal with the constitutive relation of ferrite material. What's more, the non-conforming hybrid mesh method with tetrahedron-hexahedron is employed to improve the flexibility and accuracy in mesh processing and reduce the number of unknowns. Numerical results show the efficiency of the proposed method.

Index Terms —Discontinuous Galerkin finite element time-domain method, ferrite device, non-conforming hybrid meshes.

I. INTRODUCTION

Nowadays, the analysis of the electromagnetic properties for complex medium has received much attention. The ferrite material which is regarded as complex medium is widely used for the ultra-miniature and ultra-wideband device with characteristic of non-reciprocity such as circulator and isolator. For these ferrite device, both the finite element time-domain method (FETD) [1] and the finite-difference time-domain method (FDTD) [2] can be used to analyze electromagnetic characteristics. Although the FDTD method is simple, it suffers from serious degradation when modeling curved and fine geometrical features, because staircase approximation introduces large discretization errors even when the grid size is very

small. The conventional FETD method with the characteristic of flexible modeling can not form the block diagonal which must calculate a large sparse matrix inversion via solver. Fortunately, discontinuous Galerkin method has been proposed and combined with the FETD method called discontinuous Galerkin finite element time-domain (DG-FETD) method [3]-[5]. Numerical fluxes are introduced to impose the tangential continuity of the electrical and magnetic fields at the interfaces between adjacent elements. Central flux [6] and upwind flux [7] are the common ways and a comparative study of these two schemes can be found in [8]. The DG-FETD has enhanced flexibility of FETD and can support irregular non-conforming meshes constituted of various types and shapes. It also supports various basis functions in different sub-domains. Furthermore, the resulting mass matrix is a block diagonal matrix and the method can lead to a fully explicit time-marching scheme. To improve the accuracy of modeling and reduce the number of unknowns, the non-conforming meshes based on hexahedron-tetrahedron is introduced into DG-FETD [9], [10] and the information between neighboring elements is exchanged through central flux [11], [12]. To treat the ferrite material in the time-domain analysis, we usually use the recursive convolution (RC), piecewise linear RC (PLRC) and the trapezoidal RC (TRC) techniques [13]-[15]. In this letter, we introduce RC technique into DG-FETD to deal with the constitutive relation of ferrite material for the first time and further introduce the non-conforming mesh technique to RC-DGFETD which can reduce computational time, memory requirement and number of unknowns effectively. It can also improve flexibility of modeling. We will also try to implement PLRC and TRC as a future venue of research.

The theory of the non-conforming RC-DGFETD is presented in Section II. The numerical results are discussed in Section III, and the conclusion is drawn in Section IV.

II. THEORY AND IMPLEMENTATION OF THE NON-CONFORMING DG-FETD

A. Ferrite material

Permeability of the ferrite is a tensor that varies with frequency when an external magnetic field exists. We assume that an alternating magnetic field \mathbf{H} and constant bias magnetic field H_0 in direction \mathbf{y} is imposed on the ferrite, the total magnetization \mathbf{M}_t and the total magnetic intensity \mathbf{H}_t are then expressed as:

$$\mathbf{H}_t = H_0 \mathbf{y} + \mathbf{H}, \quad (1)$$

$$\mathbf{M}_t = M_s \mathbf{y} + \mathbf{M}. \quad (2)$$

Where \mathbf{M} denotes alternating magnetization due to \mathbf{H} ($|\mathbf{H}| \ll H_0$). In frequency domain, when the external magnetic field is parallel to the Y axis, the permeability [16] can be expressed as:

$$\mu_r(\omega) = \begin{pmatrix} 1 + \frac{\omega_0 \omega_m}{\omega_0^2 - \omega^2} & 0 & -\frac{j\omega \omega_m}{\omega_0^2 - \omega^2} \\ 0 & 1 & 0 \\ \frac{j\omega \omega_m}{\omega_0^2 - \omega^2} & 0 & 1 + \frac{\omega_0 \omega_m}{\omega_0^2 - \omega^2} \end{pmatrix}. \quad (3)$$

Where $\mu_r(\omega)$ and γ denote relative magnetic permeability and gyromagnetic ratio respectively.

$$\omega_0 = \gamma H_0, \omega_m = \gamma 4\pi M_s, \gamma = 1.76 \times 10^7 \text{ rad} / (s \times Oe),$$

\bar{M}_s denotes saturation magnetization.

The Eq. (3) can be transformed into time domain expression with Inverse Fast Fourier Transforms (IFFT) method, then μ_r can be expressed as:

$$\mu_r(t) = \begin{pmatrix} \delta(t) + \omega_m \sin \omega_0 t \cdot u(t) & 0 & -\omega_m \cos \omega_0 t \cdot u(t) \\ 0 & \delta(t) & 0 \\ \omega_m \cos \omega_0 t \cdot u(t) & 0 & \delta(t) + \omega_m \sin \omega_0 t \cdot u(t) \end{pmatrix}. \quad (4)$$

B. RC-DGFETD for Ferrite material

Considering the area of the ferrite device, one can use the following Maxwell's curl equations to describe the distribution of electromagnetic fields:

$$\varepsilon_0 \varepsilon_r \otimes \frac{\partial \mathbf{E}}{\partial t} = \nabla \times \mathbf{H}, \quad (5)$$

$$\mu_0(\mu_r(t)) \otimes \frac{\partial \mathbf{H}}{\partial t} = -\nabla \times \mathbf{E}. \quad (6)$$

Because the relative permittivity ε_r is independent to frequency, we focus on the derivation of (6), and (5) will be derived with formula of domain containing PML, which is introduced to truncate the boundary. We use the basis function \mathbf{f}_i^h to test (6), and covert it by

vector identical equation and divergence theorem.

The (6) can then be changed into:

$$\begin{aligned} & \iiint_V \mathbf{f}_i^h \cdot \mu_0(\mu_r(t)) \otimes \mathbf{f}_j^h \frac{\partial h}{\partial t} dV \\ & = -\iiint_V \nabla \times \mathbf{f}_i^h \cdot \mathbf{f}_j^e dV - \iint_{\partial V} \mathbf{f}_i^h \cdot \mathbf{n} \times \mathbf{f}_j^e dS \end{aligned} \quad (7)$$

The Central-flux is employed between elements and has the following forms:

$$\mathbf{n} \times \mathbf{H}|_{\partial V} = \frac{1}{2} \mathbf{n} \times (\mathbf{H} + \mathbf{H}^+) \Big|_{\partial V}, \quad (8)$$

$$\mathbf{n} \times \mathbf{E}|_{\partial V} = \frac{1}{2} \mathbf{n} \times (\mathbf{E} + \mathbf{E}^+) \Big|_{\partial V}. \quad (9)$$

Where \mathbf{E} and \mathbf{H} represent the electrical and magnetic fields within sub-domain V , \mathbf{E}^+ and \mathbf{H}^+ represent the electrical and magnetic fields from the adjacent elements. Applying (9) into (7) leads to:

$$\begin{aligned} & \iiint_V \mathbf{f}_i^h \cdot \mu_0(\mu_r(t)) \otimes \mathbf{f}_j^h \frac{\partial h}{\partial t} dV \\ & = -\iiint_V \nabla \times \mathbf{f}_i^h \cdot \mathbf{f}_j^e dV e - \frac{1}{2} \iint_{\partial V} \mathbf{f}_i^h \cdot \mathbf{n} \times \mathbf{f}_j^e dS e \\ & \quad - \frac{1}{2} \iint_{\partial V} \mathbf{f}_i^h \cdot \mathbf{n} \times \mathbf{f}_j^{e+} dS e^+ \end{aligned} \quad (10)$$

Insertion of (4) into (10) and further use of recursive convolution leads to:

$$\begin{aligned} & \frac{df_1(t)}{dt} \otimes f_2(t) = f_1(t) \otimes \frac{df_2(t)}{dt} \\ & \mu_0 \iiint_V \mathbf{f}_i^h \cdot \mathbf{f}_j^h dV \frac{\partial h}{\partial t} \\ & + \mu_0 \iiint_V \mathbf{f}_i^h \cdot (\bar{x}\bar{x} + \bar{z}\bar{z}) \mathbf{f}_j^h dV \text{Re}[\omega_m \omega_0 e^{-j\omega_0 t} u(t) \otimes h] \\ & + \mu_0 \iiint_V \mathbf{f}_i^h \cdot (-\bar{x}\bar{z} + \bar{z}\bar{x}) \mathbf{f}_j^h dV \text{Re}[-j\omega_m \omega_0 e^{-j\omega_0 t} u(t) \otimes h] \\ & + \mu_0 \iiint_V \mathbf{f}_i^h \cdot (-\bar{x}\bar{z} + \bar{z}\bar{x}) \mathbf{f}_j^h dV \omega_m h \\ & = -\iiint_V \nabla \times \mathbf{f}_i^h \cdot \mathbf{f}_j^e dV e - \frac{1}{2} \iint_{\partial V} \mathbf{f}_i^h \cdot \mathbf{n} \times \mathbf{f}_j^e dS e \\ & \quad - \frac{1}{2} \iint_{\partial V} \mathbf{f}_i^h \cdot \mathbf{n} \times \mathbf{f}_j^{e+} dS e^+ \end{aligned} \quad (11)$$

The (11) can be converted into a matrix equation:

$$\begin{aligned} & [T_h] \frac{\partial h}{\partial t} + [F1]\Omega(t) + [F2]\Gamma(t) + [Tb]h \\ & = [P_h]e + [S_h]e + [S_h]e^+ \end{aligned} \quad (12)$$

In this paper, the perfect matched layer (PML) is constructed to truncate the computation region, DG-FETD for PML domain is also given:

$$\varepsilon(\Lambda(t)) \otimes \frac{\partial \mathbf{E}}{\partial t} = \nabla \times \mathbf{H}, \quad (13)$$

$$\mu(\Lambda(t)) \otimes \frac{\partial \mathbf{H}}{\partial t} = -\nabla \times \mathbf{E}. \quad (14)$$

Here, $\Lambda(t)$ is diagonal tensor:

$$\begin{aligned} \Lambda(t) &= \bar{x}\bar{x} \left[\delta(t) + \frac{1}{2} \frac{\sigma_z}{\varepsilon_0} \text{sgn}(t) \right] + \bar{y}\bar{y} \left[\delta(t) + \frac{1}{2} \frac{\sigma_z}{\varepsilon_0} \text{sgn}(t) \right] \\ &\quad + \bar{z}\bar{z} \left[\delta(t) - \frac{\sigma_z}{\varepsilon_0} e^{-\frac{\sigma_z t}{\varepsilon_0}} u(t) \right] \\ &= (\bar{x}\bar{x} + \bar{y}\bar{y} + \bar{z}\bar{z}) \delta(t) + (\bar{x}\bar{x} + \bar{y}\bar{y}) \frac{1}{2} \frac{\sigma_z}{\varepsilon_0} \text{sgn}(t) - \bar{z}\bar{z} \frac{\sigma_z}{\varepsilon_0} e^{-\frac{\sigma_z t}{\varepsilon_0}} u(t) \end{aligned}$$

Using the basis function \mathbf{f}_i^e and \mathbf{f}_j^h to test (13) and (14) respectively and the central-flux conditions is applied between neighboring elements. Then the convolution theorem and divergence theorem is applied, (13) and (14) can be changed into:

$$\begin{aligned} &\varepsilon \iiint_V \mathbf{f}_i^e \cdot \mathbf{f}_j^e dV \frac{\partial e}{\partial t} + \varepsilon \frac{\sigma_z}{\varepsilon_0} \iiint_V \mathbf{f}_i^e \cdot (\bar{x}\bar{x} + \bar{y}\bar{y} - \bar{z}\bar{z}) \mathbf{f}_j^e dV e \\ &+ \varepsilon \frac{\sigma_z}{\varepsilon_0} \iiint_V \mathbf{f}_i^e \cdot \bar{z}\bar{z} \mathbf{f}_j^e dV \frac{\sigma_z}{\varepsilon_0} e^{-\frac{\sigma_z t}{\varepsilon_0}} \mu(t) \otimes e \\ &= \iiint_V \nabla \times \mathbf{f}_i^e \cdot \mathbf{f}_j^e dV h + \frac{1}{2} \oint_{\partial V} \mathbf{f}_i^e \cdot \bar{\mathbf{n}} \times \mathbf{f}_j^e dS h + \frac{1}{2} \oint_{\partial V} \mathbf{f}_i^e \cdot \bar{\mathbf{n}} \times \mathbf{f}_j^{h+} dS h^+ \end{aligned} \quad (15)$$

$$\begin{aligned} &\mu \iiint_V \mathbf{f}_i^h \cdot \mathbf{f}_j^h dV \frac{\partial h}{\partial t} - \mu \frac{\sigma_z}{\varepsilon_0} \iiint_V \mathbf{f}_i^h \cdot (\bar{x}\bar{x} + \bar{y}\bar{y} - \bar{z}\bar{z}) \mathbf{f}_j^h dV h \\ &+ \mu \frac{\sigma_z}{\varepsilon_0} \iiint_V \mathbf{f}_i^h \cdot \bar{z}\bar{z} \mathbf{f}_j^h dV \frac{\sigma_z}{\varepsilon_0} e^{-\frac{\sigma_z t}{\varepsilon_0}} \mu(t) \otimes h \\ &= - \iiint_V \nabla \times \mathbf{f}_i^h \cdot \mathbf{f}_j^e dV e - \frac{1}{2} \oint_{\partial V} \mathbf{f}_i^h \cdot \bar{\mathbf{n}} \times \mathbf{f}_j^e dS e - \frac{1}{2} \oint_{\partial V} \mathbf{f}_i^h \cdot \bar{\mathbf{n}} \times \mathbf{f}_j^{e+} dS e^+ \end{aligned} \quad (16)$$

Because parameter ω_0 and ω_m have no value in non-ferrite material region, so we can couple the matrix equations of PML region and ferrite region as follows:

$$[T_e] \frac{\partial e}{\partial t} + [T_{ep1}] e + [T_{eq1}] \phi(t) = [P_e] h + [S_e] h + [S_s] h^+, \quad (17)$$

$$\begin{aligned} &[T_h] \frac{\partial h}{\partial t} + [T_{hp1}] h + [T_{hq1}] \phi(t) + [F1] \Omega(t) + [F2] \Gamma(t) + [Tb] h \\ &= [P_h] e + [S_h] e + [S_s] e^+ \end{aligned} \quad (18)$$

Where

$$\begin{aligned} [F_1] &= \mu_0 \iiint_V \mathbf{f}_i^h \cdot (\bar{x}\bar{x} + \bar{z}\bar{z}) \mathbf{f}_j^h dV \\ [F_2] &= \mu_0 \iiint_V \mathbf{f}_i^h \cdot (-\bar{x}\bar{x} + \bar{z}\bar{z}) \mathbf{f}_j^h dV \\ [T_b] &= \mu_0 \omega_m \iiint_V \mathbf{f}_i^h \cdot (-\bar{x}\bar{x} + \bar{z}\bar{z}) \mathbf{f}_j^h dV \\ \phi(t) &= \frac{\sigma_z}{\varepsilon_0} e^{-\frac{\sigma_z t}{\varepsilon_0}} u(t) \otimes e \\ \phi(t) &= \frac{\sigma_z}{\varepsilon_0} e^{-\frac{\sigma_z t}{\varepsilon_0}} u(t) \otimes h \\ \Omega(t) &= \text{Re}[\omega_m \omega_0 e^{-j\omega_0 t} u(t) \otimes h] \\ \Gamma(t) &= \text{Re}[-j\omega_m \omega_0 e^{-j\omega_0 t} u(t) \otimes h] \end{aligned}$$

$$[T_e] = \varepsilon \int_V \mathbf{f}_i^e \cdot \mathbf{f}_j^e dV, \quad [T_{eq}] = \varepsilon \frac{\sigma_z}{\varepsilon_0} \int_V \mathbf{f}_i^e \cdot \bar{z}\bar{z} \cdot \mathbf{f}_j^e dV$$

$$[T_{ep}] = \varepsilon \frac{\sigma_z}{\varepsilon_0} \int_V \mathbf{f}_i^e \cdot (\bar{x}\bar{x} + \bar{y}\bar{y} - \bar{z}\bar{z}) \mathbf{f}_j^e dV$$

$$[T_h] = -\mu \int_V \mathbf{f}_i^h \cdot \mathbf{f}_j^h dV, \quad [T_{hq}] = \mu \frac{\sigma_z}{\mu_0} \int_V \mathbf{f}_i^h \cdot \bar{z}\bar{z} \cdot \mathbf{f}_j^h dV$$

$$[T_{hp}] = \mu \frac{\sigma_z}{\mu_0} \int_V \mathbf{f}_i^h \cdot \bar{z}\bar{z} \cdot \mathbf{f}_j^h dV$$

(17) and (18) is discretized using leap-frog in time:

$$\begin{aligned} &([T_e] + \frac{\Delta t}{2} [T_{ep1}]) e^{n+1} \\ &= \Delta t ([P_e] + [S_e] + [S_s]) h^{n-1/2} - \Delta t [T_{eq1}] \frac{\phi^{n+1} + \phi^n}{2} \\ &+ ([T_e] - \frac{\Delta t}{2} [T_{ep1}]) e^n \end{aligned} \quad (19)$$

$$\begin{aligned} &([T_h] + \frac{\Delta t}{2} ([T_{hq1}] + [Tb])) h^{n+1/2} \\ &= \Delta t ([P_h] + [S_h] + [S_s]) e^{n+1} - \Delta t [T_{hp1}] \frac{\phi^{n+1} + \phi^n}{2} \\ &- \Delta t [F1] \frac{\Omega^{n+1} + \Omega^n}{2} - \Delta t [F2] \frac{\Gamma^{n+1} + \Gamma^n}{2} \\ &+ ([T_h] - \frac{\Delta t}{2} ([T_{hq1}] + [Tb])) h^{n-1/2} \end{aligned} \quad (20)$$

C. Non-conforming hybrid interfaces matrix calculation

The implementation of the DG-FETD method on hybrid meshes mainly focuses on the computation of the matrix involving integrals over a hybrid interface between current elements in V and neighboring elements in V+ of the different type, it has no relationship with other matrix involving integrals over an element or an interface between two elements of the same type. So we concentrate on the calculation of such integrals of (11) as follows:

$$\frac{1}{2} \oint_{\partial V} \mathbf{f}_i^e \cdot \bar{\mathbf{n}} \times \mathbf{f}_j^{h+} dS h^+, \quad (21)$$

$$\frac{1}{2} \oint_{\partial V} \mathbf{f}_i^h \cdot \bar{\mathbf{n}} \times \mathbf{f}_j^{e+} dS e^+. \quad (22)$$

Where \mathbf{f}_j^{h+} and \mathbf{f}_j^{e+} denote basis functions of neighboring elements. There are several cases of non-conforming interfaces, two complex cases will be considered as follow. Case (a) as shown in Fig. 1 (a) corresponds to the situation where current element in V is a hexahedron and the neighboring elements in V+ are six tetrahedrons. The curved hexahedron basis function is employed in current element and edge basis functions of tetrahedral element is employed in neighboring elements [17]. One hexahedron and six tetrahedrons form the interfaces in which one quadrangular and six

triangulars intersect into six non-conforming surfaces, when we calculate the integrals of [Sse] and [Ssh] in (17) and (18) of hexahedron hybrid interface, for example, [Sse] can be calculated as:

$$\begin{aligned} & \frac{1}{2} \int_s \mathbf{f}_i^e \cdot \mathbf{n} \times \mathbf{f}_j^{h+} dS h^+ \\ &= \frac{1}{2} \int_s \mathbf{f}_i^e \cdot \mathbf{n} \times \mathbf{f}_j^{h+} dS_1 h^+ + \frac{1}{2} \int_s \mathbf{f}_i^e \cdot \mathbf{n} \times \mathbf{f}_j^{h+} dS_2 h^+ \\ &+ \frac{1}{2} \int_s \mathbf{f}_i^e \cdot \mathbf{n} \times \mathbf{f}_j^{h+} dS_3 h^+ + \frac{1}{2} \int_s \mathbf{f}_i^e \cdot \mathbf{n} \times \mathbf{f}_j^{h+} dS_4 h^+ \\ &+ \frac{1}{2} \int_s \mathbf{f}_i^e \cdot \mathbf{n} \times \mathbf{f}_j^{h+} dS_5 h^+ + \frac{1}{2} \int_s \mathbf{f}_i^e \cdot \mathbf{n} \times \mathbf{f}_j^{h+} dS_6 h^+ \end{aligned} \quad (23)$$

where \mathbf{f}_i^e is curved hexahedron basis function, \mathbf{f}_j^{h+} is Whitney vector basis function of the neighboring tetrahedral cells. $S_1 S_2 S_3 S_4 S_5 S_6$ denote the hybrid interfaces of the hexahedron and the integrals in Eq. (23) are stored for each hybrid interface.

Case (b) as shown in Fig. 1 (b) corresponds to the situation where the current element in V is a tetrahedron and the neighboring elements in V^+ are hexahedrons. For this situation, \mathbf{f}_i^e represents Whitney vector basis function and \mathbf{f}_j^{h+} represents curved hexahedron basis function.

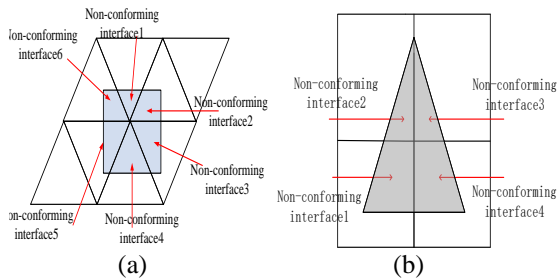


Fig. 1. (a), (b) Non-conforming hybrid interfaces formed by one hexahedron and six tetrahedrons and one tetrahedron and four hexahedrons

III. NUMERICAL RESULTS AND DISCUSSION

The numerical results are presented in this section to show the accuracy and efficiency of non-conforming RC-DGFETD for analyzing the ferrite material. Figure 2 shows the model of the Y-junction circulator, the size of the wave guide aperture is $22.86\text{mm} \times 10.16\text{mm}$ and the ferrite cylinder of the model with a radius of 3.5mm and a height of 10.16mm . Twenty layers PML are employed with a thickness of 2.5mm for each layer. The hybrid hexahedral-tetrahedral meshes and tetrahedral meshes are employed respectively as shown in Fig. 3. In the first case, the simulation domain is firstly discretized with tetrahedral grid of 1.5mm for the domain of air and hybrid hexahedral-tetrahedral grid of 0.3mm

for the ferrite part. In the second case, the model is discretized with tetrahedral grid of 1.5mm . Constant magnetic field is imposed in the direction of \mathbf{y} , which is perpendicular to the propagating direction of the microwave. The magnetic intensity is 200 Oe , saturation magnetization is $1317\text{G}/4\pi$, the relative permittivity of the ferrite material is 11.7 . The excitation source used in the simulation is a Gaussian pulse with center frequency of 10GHz and bandwidth of 4GHz . The comparison of the results between different methods is shown in Figs. 4-7 and the comparison of the detailed parameters of Y-junction circulator is also listed in Table 1.

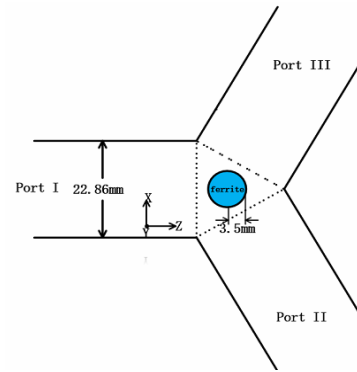


Fig. 2. Geometry of the Y-junction circulator.

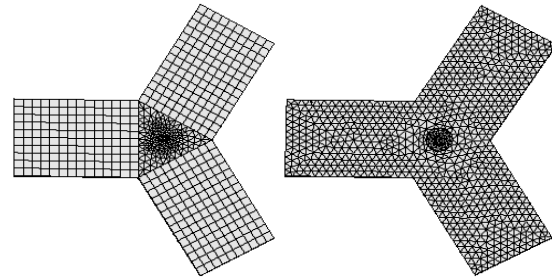


Fig. 3. Hybrid and tetrahedral meshes of the Y-junction circulator.

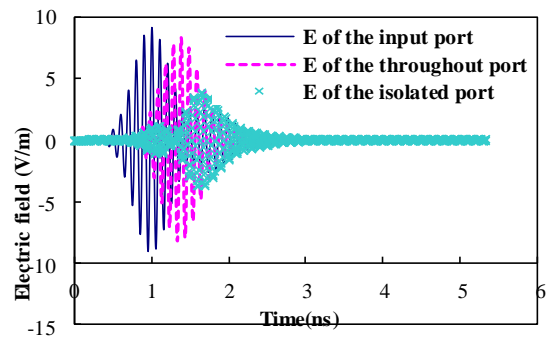


Fig. 4. Time domain waveforms of electric field in different port of Y-junction circulator with hybrid.

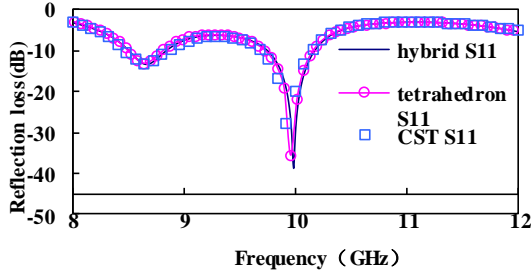


Fig. 5. Reflection loss of input port with hybrid DG-FETD and tetrahedral mesh DG-FETD and CST.

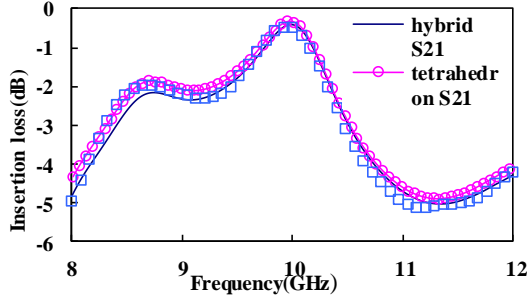


Fig. 6. Insertion loss of the throughout port with hybrid DG-FETD, and DG-FETD with tetrahedral grid and CST.

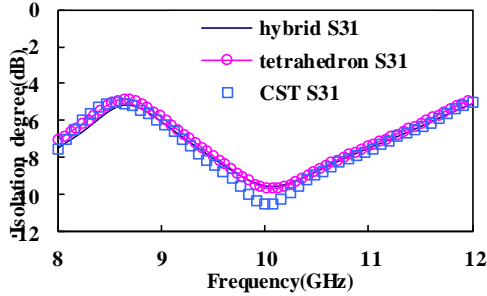


Fig. 7. Isolated degree of isolation port with hybrid DG-FETD and tetrahedral mesh DG-FETD and CST.

Table 1: Parameters of Y-junction circulator with different decomposition method

Method	Element Number	Un-knowns	Δt (ns)	Number of Time Steps	CPU Time(s)
Hybrid	21379	280259	80	18750	4049
Tetrahedral	39064	397613	50	30000	15516

From Fig. 5 to Fig. 7, a good agreement of the results between the DG-FETD and CST can be observed. The number of unknowns for the hybrid mesh is reduced compared with the tetrahedral mesh for simulations with comparable accuracy levels as shown in Table 1. What's more, the iterative time of the hybrid mesh method is much less than that of the tetrahedral mesh.

Finally, The comparison between the SETD [18] method and the DG-FETD is also given in Fig. 2 and Table 2. Both of the methods are applied to analyze the same model in the first example. A good agreement of the results between SETD and DG-FETD can be found in Fig. 8. The memory requirement and unknowns for the DG-FETD are reduced compared with the SETD as shown in Table 2. What's more, the memory requirement of the DG-FETD is also much less than that of the standard SETD.

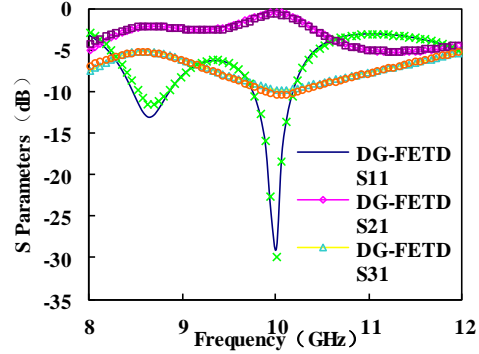


Fig. 8. The scattering parameters of Y-junction circulator with DG-FETD and SETD.

Table 2: Computational cost of the two methods

Method	Unknowns	CPU Time(s)	Memory (GB)
DG-FETD	89992	973	171MB
SETD	94971	3940	197MB

IV. CONCLUSION

This paper proposes a DG-FETD based on non-conformal meshes for the analysis of the ferrite circulator. The Discontinuous Galerkin method is presented to solve time-domain Maxwell's equation and the central-flux is used. Furthermore, the non-conformal mesh method is utilized in the DG-FETD to reduce the memory requirement and the number of unknowns. Numerical results show the efficiency of the non-conformal DG-FETD, especially for the memory requirement and iterative time.

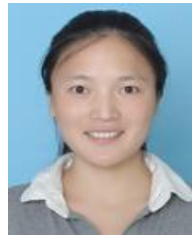
ACKNOWLEDGMENT

We would like to thank the support of Postgraduate Research & Practice Innovation Program of Jiangsu Province under Grant No. KYCX18_0865.

REFERENCES

- [1] W. H. Reed, "Triangular mesh methods for the neutron transport equation," *Los Alamos Scientific Laboratory Report LA-UR*, 1973.
- [2] J. Chen and Q. H. Liu. "Discontinuous Galerkin time-domain methods for multiscale electromagnetic simulations: A review," *Proc. IEEE*, vol.

- 101, no. 2, pp. 242-254, Feb. 2013.
- [3] S. D. Gedney, C. Luo, J. A. Roden, R. D. Crawford, B. Guernsey, J. A. Miller, T. Kramer, and E. W. Lucas, "The discontinuous Galerkin finite-element time-domain method solution of Maxwell's equations," *Appl. Comput. Electromag. Society J.*, vol. 24, no. 2, pp. 129-142, Apr. 2009.
- [4] T. Lu, P. Zhang, and W. Cai, "Discontinuous Galerkin methods for dispersive and lossy Maxwell's equations and PML boundary conditions," *J. Comput. Phys.*, vol. 200, no. 2, pp. 549-580, Nov. 2004.
- [5] J. Chen and Q. H. Liu, "Discontinuous Galerkin time domain methods for multiscale electromagnetic simulations: A review," *Proc. IEEE*, vol. 101, no. 2, pp. 242-254, Feb. 2013.
- [6] S. D. Gedney, C. Luo, J. A. Roden, R. D. Crawford, B. Guernsey, J. A. Miller, T. Kramer, and E. W. Lucas, "The discontinuous Galerkin finite-element time-domain method solution of Maxwell's equations," *Appl. Comput. Electromag. Society J.*, vol. 24, no. 2, pp. 129-142, Apr. 2009.
- [7] J. H. Lee and Q. H. Liu, "A 3-D discontinuous spectral element time-domain method for Maxwell's equations," *IEEE Trans. Antennas Propag.*, vol. 57, no. 9, pp. 2666-2674, Sep. 2009.
- [8] X. Li and J. M. Jin, "A comparative study of three finite element-based explicit numerical schemes for solving Maxwell's equations," *IEEE Trans. Antennas Propag.*, vol. 60, no. 3, pp. 1450-1457, Mar. 2012.
- [9] S. Dosopoulos, B. Zhao, and J. F. Lee, "Non-conformal and parallel discontinuous Galerkin time domain method for Maxwell's equations: EM analysis of IC packages," *J. Comput. Phys.*, vol. 238, pp. 48-70, Dec. 2012.
- [10] S. Dosopoulos and J. F. Lee, "Interior penalty discontinuous Galerkin finite element method for the time-dependent first order Maxwell's equations," *IEEE Trans. Antennas Propag.*, vol. 58, no. 12, pp. 4085-4090, Dec. 2010.
- [11] E. Montseny and X. Ferrières, "Dissipative terms and local time-stepping improvements in a spatial high order Discontinuous Galerkin scheme for the time-domain Maxwell's equations," *J. Comput. Phys.*, vol. 227, no. 14, pp. 6795-6820, Dec. 2008.
- [12] H. Xu, D. Z. Ding, and R. S. Chen, "A hybrid explicit-implicit scheme for spectral-element time-domain analysis of multiscale simulation," *J. ACES*, vol. 31, no. 4, pp. 77-82, Apr. 2016.
- [13] R. J. Luebbers, "FDTD for th-order dispersive media," *IEEE Trans. Antennas Propag.*, vol. 40, no. 11, pp. 1297-1301, Nov. 1992.
- [14] D. F. Kelley and R. J. Luebbers, "Piecewise linear recursive convolution for dispersive media using FDTD," *IEEE Trans. Antennas Propag.*, vol. 44, no. 6, pp. 792-797, June 1996.
- [15] J. Shibayama and A. Nomura, "Simple trapezoidal recursive convolution technique for the frequency-dependent FDTD analysis of a Drude-Lorentz model," *IEEE Photonics Technology Letters*, vol. 21, no. 2, pp. 100-102, Apr. 2009.
- [16] D. M. Pozar, *Microwave Engineering*. John Wiley & Sons, 2009.
- [17] J. M. Jin, *The Finite Element Method in Electromagnetics*. 2nd ed., New York: Wiley, 2002.
- [18] P. Shen, "Time domain spectral element analysis of complex medium microwave devices," [D] *Nanjing: Nanjing University of Science and Technology*, pp. 36-37, 2013.



Min Li was born in Shandong, China. She is currently working toward the Ph.D. degree in Nanjing University of Posts and Telecommunications. Her research interests include semiconductor simulation, RF-integrated circuits and computational electromagnetic.



Xiaodong Ye was born in Jiangsu, China. He is currently an Associate Professor with the Electronic Engineering of NJUST. His current research interests include computational electromagnetics, electromagnetic scattering and radiation.

Time Domain Parabolic Equation Method for Scattering Analysis of Electrically Large Coated Objects by using Impedance Boundary Condition

Ling Guan and Shifei Tao

School of Electronic and Optical Engineering
Nanjing University of Science and Technology, Nanjing, Jiangsu Province 210094, China
s.tao@njust.edu.cn

Abstract — The time domain parabolic equation method (TDPE) is an efficient tool for analyzing electromagnetic (EM) scattering by electrically large objects. It reduces the cost of computational resources by dividing three-dimensional solution space into multiple two-dimensional transverse planes for calculating scattered fields one by one. For thin coated perfectly electrically conducting (PEC) objects, the efficiency of TDPE method will decrease if dielectric is considered to be meshed. As an approximate method, Leontovich impedance boundary condition (IBC) handles this problem by modeling a surface impedance on the outer surface of coating dielectric, instead of solving Maxwell's equations in the dielectric domain. Thus in this paper, TDPE method based on Leontovich IBC is proposed to analyze broadband scattering problems of large-scale coated PEC objects. Numerical results have validated the accuracy and efficiency of the proposed method.

Index Terms — Coated objects, impedance boundary condition, time domain parabolic equation, wideband electromagnetic scattering.

I. INTRODUCTION

Recently, accurate and efficient prediction of wide-band electromagnetic (EM) scattering characteristic for electrically large objects has been required increasingly in many regions, because the broadband detection and stealth of targets are applied widely. The radar cross sections (RCS) evaluation of objects is a vital tool for the target identification and the optimization of objects' shape or coating. However, the coated material for stealth and camouflage will increase the complexity and reduce the efficiency in the EM scattering analysis. Therefore, it is necessary to develop an accurate and efficient numerical method to handle this problem. The parabolic equation (PE) method has been widely used to analyze the propagation of acoustic wave [1,2], light wave [3,4] and seismic wave [5], because it modules the wave propagating along the paraxial direction. The method is firstly proposed by Leontovich and Fock in [6], where the electromagnetic (EM) wave diffraction

on the earth's surface is researched. After then, the EM wave propagation over obstacle surface [7], irregular terrain [8] and even expressway [9] is also modeled, calculated and analyzed. The PE method converts a three-dimensional (3D) problem to multiple two-dimensional (2D) problems by marching the solving plane. In this way, the computational resources can be reduced dramatically [10-13]. Recently, more attention is focused on the solution in time domain since the requirement for broadband or transient analysis becomes more urgent [14]. The 2D time domain parabolic equation (TDPE) developed by Murphy is utilized to analyze ocean acoustic propagation [16]. Later, a 3D vector TDPE is proposed for solving wide-band EM scattering problems of perfectly conducting (PEC) objects with high efficiency [17].

However, less work reports on the wide-band analysis of composite objects, especially for coated objects [18,19]. In traditional rigorous methods, e.g., surface integral equation (SIE) [20-24] and volume-surface integral equation (VSIE) [25], the number of unknowns will increase significantly if coating dielectric is meshed because thickness is usually small compared to the wavelength. Leontovich impedance boundary condition (IBC) which prescribes on the outer surface of coating materials can overcome this problem [26]. It avoids the dense grids and costly solution inside the coating by constituting a local relationship between the tangential components of the electric field and magnetic field. In [27], IBC is introduced into time-domain integral equation (TDIE) to analyze transient scattering from coated bodies. Both unknown electric and magnetic currents are considered and modeled independently to guarantee the continuity of normal components across mesh edges. The method is free of spurious resonant solutions and exact fields can be obtained. TDIE presents obvious advantages when analyzing open boundary problems of homogeneous scatterers because it automatically satisfies the radiation condition. Only scatterers need a discretization rather than the whole solution space. This results in a sharp decrease on the number of unknowns. However, huge

computational resources will be cost on solving dense matrix equations in TDIE, even if it is accelerated by the plane-wave time-domain algorithm and multilevel fast multipole algorithm which restricts its application on analyzing large-scale scattering and radiation problems.

In this paper, we propose TDPE with Leontovich IBC to solve wide-band EM scattering from coated objects. The dielectric region is described by IBC, which leads to a great reduction in computing times and memory requirements. The implicit finite difference (FD) scheme of Crank–Nicolson (CN) type is employed to solve the parabolic equation. The transient scattered fields can be computed plane by plane along the forward wave propagation direction. Additionally, the complete scattering field in all directions can be obtained by the rotating TDPE method.

II. THREE-DIMENSIONAL TIME DOMAIN PARABOLIC EQUATION METHOD

A. Vector three-dimensional TDPE formulations

Parabolic equation is an approximate form of the wave equation in paraxial direction. The wave equation in source-free region can be written as:

$$\frac{\partial^2 \psi}{\partial x^2} + \frac{\partial^2 \psi}{\partial y^2} + \frac{\partial^2 \psi}{\partial z^2} + k^2 \psi = 0, \quad (1)$$

where ψ denotes the scattered field component and k is the wave number.

Assuming the x axis is the paraxial direction of the parabolic equation, the reduced scattered field can be defined as:

$$u(x, y, z) = e^{-ikx} \psi(x, y, z). \quad (2)$$

Substitute (2) to (1) and factorize it, the forward and backward parabolic equation can be obtained:

$$\begin{cases} \frac{\partial u_+}{\partial x} = -ik(1 - \sqrt{Q})u_+ \\ \frac{\partial u_-}{\partial x} = -ik(1 + \sqrt{Q})u_- \end{cases}, \quad (3)$$

where $Q = \frac{1}{k^2} \left(\frac{\partial^2}{\partial y^2} + \frac{\partial^2}{\partial z^2} \right) + n^2$ denotes the pseudo

differential operator. u_+ and u_- represent the forward and backward components of the reduced scattered field.

With the first order Taylor series expansion, Q can be approximated as:

$$\sqrt{Q} \approx 1 + \frac{Q-1}{2}. \quad (4)$$

Thus, the standard parabolic equation can be obtained:

$$\frac{\partial u}{\partial x} = \frac{i}{2k} \left(\frac{\partial^2}{\partial y^2} + \frac{\partial^2}{\partial z^2} \right) u. \quad (5)$$

The vector PE is composed of three scalar parabolic equations in three dimensions. The standard vector PE in free space can be written as:

$$\begin{cases} \frac{\partial^2 u_x}{\partial y^2} + \frac{\partial^2 u_x}{\partial z^2} + 2ik \frac{\partial u_x}{\partial x} = 0 \\ \frac{\partial^2 u_y}{\partial y^2} + \frac{\partial^2 u_y}{\partial z^2} + 2ik \frac{\partial u_y}{\partial x} = 0 \\ \frac{\partial^2 u_z}{\partial y^2} + \frac{\partial^2 u_z}{\partial z^2} + 2ik \frac{\partial u_z}{\partial x} = 0 \end{cases}. \quad (6)$$

Define a Fourier transform as:

$$\tilde{\Pi}(x, y, z, s) = \frac{1}{2\pi} \int_{-\infty}^{\infty} \tilde{F}(k) u(x, y, z, k) e^{-iks} dk, \quad (7)$$

where $\tilde{F}(k) = \int_0^{\infty} \mathbf{E}' e^{i\omega t} dt$ is a spectrum function, \mathbf{E}' represents the incident plane wave, $s = ct - x$ is the distance from the paraxial wave-front ct and c is the light speed.

Using the Fourier transform in (7), the three dimensional vector PE in time domain is obtained:

$$\frac{\partial^2 \Pi_{\xi}}{\partial y^2} + \frac{\partial^2 \Pi_{\xi}}{\partial z^2} - 2 \frac{\partial^2 \Pi_{\xi}}{\partial x \partial s} = 0 \quad \xi = x, y, z, \quad (8)$$

where Π_{ξ} ($\xi = x, y, z$) denotes the components of transient reduced scattered field for $x-$, $y-$ and $z-$ directions, respectively.

Applying central difference scheme to (8), the semi-discretized form of the time-domain PE can be derived:

$$\begin{aligned} \frac{8}{\Delta x \Delta s} \left(\begin{matrix} \Pi_{\xi, l+1}^{m+1} - \Pi_{\xi, l+1}^m \\ -\Pi_{\xi, l}^{m+1} + \Pi_{\xi, l}^m \end{matrix} \right) = \\ \frac{1}{\Delta z^2} \nabla_z^2 \left(\begin{matrix} \Pi_{\xi, l+1}^{m+1} + \Pi_{\xi, l+1}^m \\ + \Pi_{\xi, l}^{m+1} + \Pi_{\xi, l}^m \end{matrix} \right) + \frac{1}{\Delta y^2} \nabla_y^2 \left(\begin{matrix} \Pi_{\xi, l+1}^{m+1} + \Pi_{\xi, l+1}^m \\ + \Pi_{\xi, m+1, l}^{m+1} + \Pi_{\xi, m, l}^m \end{matrix} \right), \end{aligned} \quad (9)$$

in which $\Pi_{\xi, l}^m$ ($\xi = x, y, z$) is the unknown, $\Delta x, \Delta y, \Delta z$ are the spatial range steps in three dimensions and Δs is the time step. ∇_y^2 and ∇_z^2 denote the second-order difference operator along the y - and z -axes, respectively:

$$\begin{aligned} & -\frac{1}{\Delta z^2} \Pi_{\xi, l+1}^{m+1, p, q-1} - \frac{1}{\Delta y^2} \Pi_{\xi, l+1}^{m+1, p-1, q} - \frac{1}{\Delta z^2} \Pi_{\xi, l+1}^{m+1, p, q+1} - \frac{1}{\Delta y^2} \Pi_{\xi, l+1}^{m+1, p+1, q} + \left(\frac{8}{\Delta x \Delta s} + \frac{2}{\Delta z^2} + \frac{2}{\Delta y^2} \right) \Pi_{\xi, l+1}^{m+1, p, q} \\ & = \frac{1}{\Delta y^2} \Pi_{\xi, l+1}^{m, p-1, q} + \frac{1}{\Delta z^2} \Pi_{\xi, l+1}^{m, p, q-1} + \frac{1}{\Delta y^2} \Pi_{\xi, l+1}^{m, p+1, q} + \frac{1}{\Delta z^2} \Pi_{\xi, l+1}^{m, p, q+1} + \frac{1}{\Delta y^2} \Pi_{\xi, l}^{m+1, p-1, q} + \frac{1}{\Delta z^2} \Pi_{\xi, l}^{m, p, q+1} + \left(\frac{8}{\Delta x \Delta s} - \frac{2}{\Delta z^2} - \frac{2}{\Delta y^2} \right) \Pi_{\xi, l+1}^{m, p, q} + \left(\frac{8}{\Delta x \Delta s} - \frac{2}{\Delta z^2} - \frac{2}{\Delta y^2} \right) \Pi_{\xi, l}^{m+1, p, q} \\ & + \frac{1}{\Delta z^2} \Pi_{\xi, l}^{m+1, p, q-1} + \frac{1}{\Delta y^2} \Pi_{\xi, l}^{m, p+1, q} + \frac{1}{\Delta y^2} \Pi_{\xi, l}^{m+1, p+1, q} + \frac{1}{\Delta z^2} \Pi_{\xi, l}^{m+1, p, q+1} + \frac{1}{\Delta y^2} \Pi_{\xi, l}^{m, p-1, q} + \frac{1}{\Delta z^2} \Pi_{\xi, l}^{m, p, q-1} + \left(\frac{8}{\Delta x \Delta s} - \frac{2}{\Delta z^2} - \frac{2}{\Delta y^2} \right) \Pi_{\xi, l}^{m, p, q} \quad \xi = x, y, z \end{aligned} \quad (10)$$

By using the CN FD scheme to solve (9), the discrete form of vector TDPE can be derived as (10), where $\Pi_{\xi,l}^{m,p,q}$ represents the reduced transient scattered field at the location of $(m\Delta x, p\Delta y, q\Delta z)$ at the time step of $l\Delta t$. As observed in (10), the unknown on the $(m+1)$ th transverse plane at the $(l+1)$ th time step can be calculated from the values on the m th transverse plane at the $(l+1)$ th time step and those at the l th time step. The computation process of CN FD scheme is shown in Fig. 1. The calculation can be taken plane by plane with marching along the paraxial direction for each time step. As a result, the computational resources reduce because it converts a 3D problem into several 2D problems. As seen in Fig. 2, every plane consists of 4 parts which need to be mesh: 1) the truncation boundary, 2) free space, 3) the scatterer boundary, and 4) the interior of scatterers. In this paper, the perfect matching layers (PML) are employed to truncate transverse plane and the IBC is adopted according to the thin coat of scatterers. It will be introduced in Section III detailedly. In each solution plane, the fields at the boundary grids of scatterers are computed by IBC and the fields at other grids can be obtained by (10), i.e., the CN FD scheme.

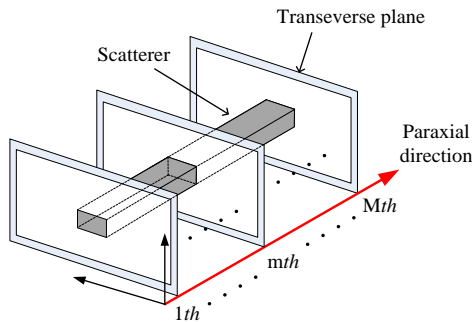


Fig. 1. Computation process of CN FD scheme in TDPE method.

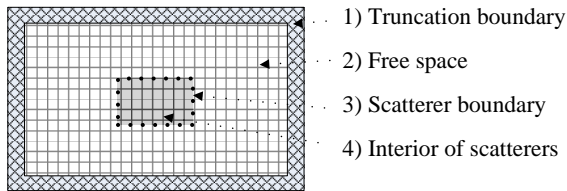


Fig. 2. Computation regions and mesh grids in a transverse plane.

B. Rotating TDPE method

The standard PE gets a good accuracy only in the range of smaller than $\pm 15^\circ$ around the paraxial direction, as shown in Fig. 3 (a), because the error of first order Taylor series expansion for pseudo differential operator

in (4) is proportional to $\sin^4 \alpha$, where α is the angle between the observed direction and the paraxial direction. To obtain full-angle scattering fields, the rotating TDPE method is used. In Fig. 3 (b), the paraxial direction is fixed at x-axis while the scatterer and incident wave are rotated by a specified angle to make the observed area around the paraxial direction. After rotation, the grids of targets can be regenerated directly by the coordinate transformation and repartitioned into a new series of transverse planes to be solved. Accordingly, for an irregular and asymmetric target, the full bistatic RCS can be calculated by rotating at least 12 times.

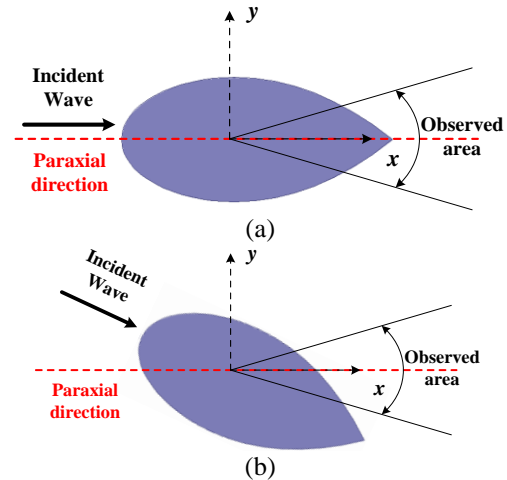


Fig. 3. Scheme of rotating TDPE method. (a) A narrow-angle scattering pattern around the paraxial direction can be obtained accurately by a single TDPE run. (b) Results of other angles can be obtained by rotating the objects and incident waves.

III. IMPLEMENTATION OF THE TDIBC IN THE TDPE FORMULATION

Leontovich IBC is an approximate boundary condition in the electromagnetic. It constructs a relationship between the the tangential components of the electric field \mathbf{E} and the magnetic field \mathbf{H} . The relation is defined on the outer surface Γ of the thin homogeneous dielectric and the equivalent impedance depends on the coating materials.

Leontovich IBC can be written as follows:

$$\hat{n} \times \mathbf{E}(P) = Z [\hat{n} \times (\hat{n} \times \mathbf{H}(P))], \quad (11)$$

where \hat{n} is the outward directed normal of point P on the Γ . Z represents the surface impedance of point P , which is given by:

$$Z(\omega) = -i \sqrt{\frac{\mu_0 \mu_r}{\epsilon_0 \epsilon_r}} \tan(\omega \sqrt{\mu_0 \mu_r \epsilon_0 \epsilon_r} d), \quad (12)$$

where μ_0, ϵ_0 is the permeability and permittivity in

free space, μ_r, ε_r is the relative permeability and permittivity of the dielectric and d denotes the thickness of the coating.

As seen from (12), it is difficult to obtain the time-domain expression of Z analytically by using a Fourier transform. Thus we utilize the vector fitting method [28] to solve this problem. $Z(\omega)$ in frequency domain is approximated by the rational fraction in Laplace domain ($s = j\omega$):

$$Z(s) = \frac{a_0 + a_1 s + \dots + a_N s^N}{b_0 + b_1 s + \dots + b_N s^N}. \quad (13)$$

Using partial-fraction expansion, (13) can be rewritten as:

$$Z(s) = c_0 + \sum_{i=1}^N \frac{c_i}{s - p_i}, \quad (14)$$

where p_i is the pole and c_i is the residue. In this way, the expression of Z in time domain can be easily obtained:

$$Z(t) = c_0 \delta(t) + \sum_{i=1}^N c_i e^{p_i t}. \quad (15)$$

By substituting $\nabla \times \mathbf{E} = i\omega\mu\mathbf{H}$ to (11), the IBC can be expressed only by electric field \mathbf{E} :

$$\hat{n} \times \mathbf{E} = \frac{Z}{ikZ_0} [\hat{n} \cdot (\nabla \times \mathbf{E}) \hat{n} - \nabla \times \mathbf{E}]. \quad (16)$$

It can be transformed into a scalar form:

$$\begin{aligned} & (n_x, n_y, n_z) \times (E_x, E_y, E_z) \\ &= \frac{Z}{ikZ_0} \left[\begin{array}{c} (n_x, n_y, n_z) \cdot \left(\frac{\partial E_z}{\partial y} - \frac{\partial E_y}{\partial z}, \frac{\partial E_x}{\partial z} - \frac{\partial E_z}{\partial x}, \frac{\partial E_y}{\partial x} - \frac{\partial E_x}{\partial y} \right) \\ - \left(\frac{\partial E_z}{\partial y} - \frac{\partial E_y}{\partial z}, \frac{\partial E_x}{\partial z} - \frac{\partial E_z}{\partial x}, \frac{\partial E_y}{\partial x} - \frac{\partial E_x}{\partial y} \right) \end{array} \right] \cdot (n_x, n_y, n_z). \end{aligned} \quad (17)$$

The total electric field \mathbf{E} in (16) is the sum of the incident field and scattering field, i.e., $\mathbf{E} = \mathbf{E}^s + \mathbf{E}^i$, where $\mathbf{E}^s = e^{ikx}\mathbf{u}$ in PE method. So the scalar form of \mathbf{E} can be written as:

$$(E_x, E_y, E_z) = (E_x^i + e^{ikx}u_x, E_y^i + e^{ikx}u_y, E_z^i + e^{ikx}u_z). \quad (18)$$

By substituting (20) into (17) and separating the incident field and scattering field, three scalar equations can be derived as:

$$\begin{aligned} & n_y u_z - n_z u_y - \frac{Z}{ikZ_0} \left[\begin{array}{c} (n_x^2 - 1) \left(\frac{\partial u_z}{\partial y} - \frac{\partial u_y}{\partial z} \right) + n_x n_y \left(\frac{\partial u_x}{\partial z} - \frac{\partial u_z}{\partial x} - iku_x \right) \\ + n_x n_z \left(iku_y + \frac{\partial u_y}{\partial x} - \frac{\partial u_x}{\partial y} \right) \end{array} \right] \\ &= (-n_y E_z^i + n_z E_y^i) e^{-ikx} + \frac{Z e^{-ikx}}{ikZ_0} \left[\begin{array}{c} (n_x^2 - 1) \left(\frac{\partial E_z^i}{\partial y} - \frac{\partial E_y^i}{\partial z} \right) \\ + n_x n_y \left(\frac{\partial E_x^i}{\partial z} - \frac{\partial E_z^i}{\partial x} \right) + n_x n_z \left(\frac{\partial E_y^i}{\partial x} - \frac{\partial E_x^i}{\partial y} \right) \end{array} \right], \end{aligned} \quad (19)$$

$$\begin{aligned} & n_z u_x - n_x u_z - \frac{Z}{ikZ_0} \left[\begin{array}{c} n_x n_y \left(\frac{\partial u_x}{\partial y} - \frac{\partial u_y}{\partial z} \right) + (n_y^2 - 1) \left(\frac{\partial u_x}{\partial z} - \frac{\partial u_z}{\partial x} - iku_x \right) \\ + n_y n_z \left(iku_y + \frac{\partial u_y}{\partial x} - \frac{\partial u_x}{\partial y} \right) \end{array} \right] \\ &= (-n_x E_x^i + n_x E_z^i) e^{-ikx} + \frac{Z e^{-ikx}}{ikZ_0} \left[\begin{array}{c} n_x n_y \left(\frac{\partial E_x^i}{\partial y} - \frac{\partial E_y^i}{\partial z} \right) + (n_y^2 - 1) \left(\frac{\partial E_x^i}{\partial z} - \frac{\partial E_z^i}{\partial x} \right) \\ + n_y n_z \left(\frac{\partial E_y^i}{\partial x} - \frac{\partial E_x^i}{\partial y} \right) \end{array} \right], \end{aligned} \quad (20)$$

$$\begin{aligned} & n_x u_y - n_y u_x - \frac{Z}{ikZ_0} \left[\begin{array}{c} n_x n_z \left(\frac{\partial u_z}{\partial y} - \frac{\partial u_y}{\partial z} \right) + n_y n_z \left(\frac{\partial u_x}{\partial z} - \frac{\partial u_z}{\partial x} - iku_x \right) \\ + (n_z^2 - 1) \left(iku_y + \frac{\partial u_y}{\partial x} - \frac{\partial u_x}{\partial y} \right) \end{array} \right] \\ &= (-n_x E_y^i + n_y E_x^i) e^{-ikx} + \frac{Z e^{-ikx}}{ikZ_0} \left[\begin{array}{c} n_x n_z \left(\frac{\partial E_z^i}{\partial y} - \frac{\partial E_y^i}{\partial z} \right) + n_y n_z \left(\frac{\partial E_x^i}{\partial z} - \frac{\partial E_z^i}{\partial x} \right) \\ + (n_z^2 - 1) \left(\frac{\partial E_y^i}{\partial x} - \frac{\partial E_x^i}{\partial y} \right) \end{array} \right]. \end{aligned} \quad (21)$$

Therefore, the time-domain IBC can be derived from (19)~(21) by using Fourier transforms. It should be noted that the convolution operation $Z(t) * \Pi(t)$ can be expanded by [29]:

$$\begin{aligned} Z(t) * \Pi(t) \Big|_{t=n\Delta t} &= \left(c_0 \delta(t) + \sum_{i=1}^N c_i e^{p_i t} \right) * \Pi(t) \Big|_{t=n\Delta t} \\ &= c_0 \Pi^{(n)} + \sum_{i=1}^N c_i e^{p_i t} * \Pi(t) \Big|_{t=n\Delta t}, \quad (22) \\ &\approx c_0 \Pi^{(n)} + \sum_{i=1}^N \left[\chi_i^{(0)} \Pi^{(n)} + \sum_{k=1}^n \chi_i^{(k)} \Pi^{(n-k)} \right] \end{aligned}$$

where $\chi_i^{(0)} = \int_0^{\Delta t/2} c_i e^{p_i \tau} d\tau$, $\chi_i^{(k)} = \int_{(k-1/2)\Delta t}^{(k+1/2)\Delta t} c_i e^{p_i \tau} d\tau$, n denotes the number of time steps and Δt denotes the time increment.

Let $\psi_i^{(n)} = \sum_{k=1}^n \chi_i^{(k)} \Pi^{(n-k)}$ and it can be computed by the recursion convolution:

$$\psi_i^{(n)} = -\frac{c_i}{p_i} (1 - e^{p_i \Delta t}) e^{p_i \Delta t / 2} \Pi^{(n-1)} + e^{p_i \Delta t} \psi_i^{(n-1)}. \quad (22)$$

By substituting (24) to (23), $Z(t) * \Pi(t)$ can be calculated quickly. This approach avoids numerous integral operations in the convolution and saves computational time.

IV. NUMERICAL RESULTS

All the numerical results are tested on Lenovo personal computer of Inter Q9500 (2.83GHz) with RAM of 8G. The incident source for all the examples in this paper is the modulated Gaussian pulse, and it can be written as:

$$\mathbf{E}^i(\mathbf{r}, t) = \hat{n} \exp\left(-\frac{(t - \mathbf{r} \cdot \hat{k}/c - \tau_p)^2}{2\sigma^2}\right), \quad (23)$$

where \hat{n} is the unit vector of electrical field, \hat{k} is the wave vector, $\tau_p = 10\sigma$ is the time delay, $\sigma = 3 / (\pi f_{bw})$ is the pulse width and f_{bw} is the bandwidth.

A. Wide-band scattering from a coated PEC cylinder

We firstly analyze a coated PEC cylinder with radius of $2m$ and height of $2m$ by using the proposed method and the time domain integral equation (TDIE) method with IBC, which is computed by in-house code. The relative complex permittivity of the coating material is $\epsilon_r = \epsilon' - j\epsilon'' = 2 - j$ and the relative permeability is $\mu_r = 1$. The thickness of coating material is $0.01m$. As shown in the inset of Fig. 4, a y -polarization plane wave illuminates along the center axis of the cylinder. Both the incident direction and paraxial direction of TDPE method are along the $+x$ axis. The bandwidth of the modulated Gaussian pulse in this example is $600MHz$. The bistatic RCS calculated by TDIE and TDPE at $200MHz$, $300MHz$ and $400MHz$ are shown in Figs. 4 (a)-(c). It can be found that there is a good agreement between them. The bistatic RCS for all azimuthal angles is obtained by rotating TDPE. In order to evaluate the error in the TDPE method, the root mean square errors (RMSE) of RCS changing with the azimuthal angle φ are defined as:

$$RMSE = \sqrt{\frac{1}{N} \sum_{i=1}^N |\sigma_i - \sigma_i^{IE}|^2}, \quad (24)$$

where N is the number of frequency points, σ_i and σ_i^{IE} are the RCS values computed by TDPE and TDIE with IBC at the i th frequency point, respectively. Figure 5 compares the errors of RCS ranging from $\varphi = 0^\circ$ to 45° which are obtained by a single TDPE run and rotating TDPE method. It can be observed that the RMSE of a single TDPE run stays lower than $1dB$ within 15° along the paraxial direction and increases as angle becomes larger. It proves the fact that the standard TDPE only gets a good accuracy only within a narrow-angle range around the paraxial direction and the full bistatic RCS can be obtained by using rotating TDPE method, as described in Section II. In this example, 7 rotating TDPE runs are used to obtain the final results. Figure 6 gives the comparison between the two methods on the magnitudes of reduced transient scattered fields at the point of $(2m, 2.6m, 0m)$. It also verifies the accuracy of the proposed method and the late-time behavior is stable because of the CN FD scheme. To discuss the influence of dielectric loss on the proposed method, three different kinds of coated materials with $\epsilon_r = 2 - 0.1j$, $\epsilon_r = 2 - 0.5j$ and $\epsilon_r = 2 - 1.0j$ are analyzed and compared. Table 1 shows the average

RMSE with respect to the TDIE results, defined as $\sum_{i=1}^M RMSE / M$ (M is the number of calculated angles).

It can be seen that the errors for all three materials achieve a low level lower than $1dB$ and are almost independent of frequencies. The proposed method has a high accuracy when the thickness of coated material is small.

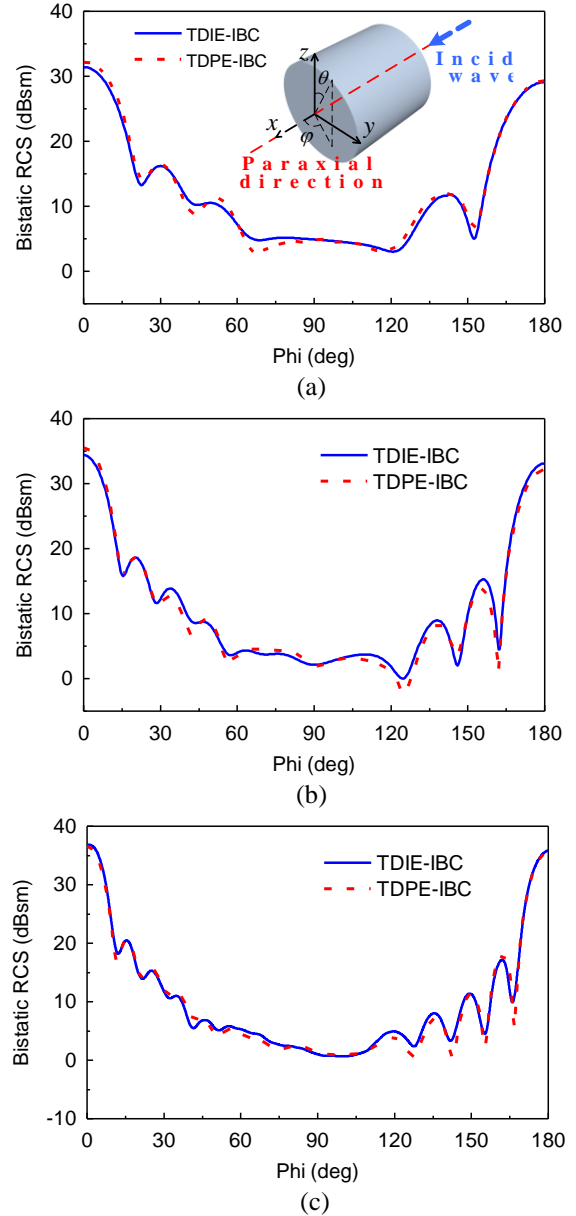


Fig. 4. Bistatic RCS of a coated PEC cylinder at different frequencies: (a) $f = 200$ MHz, (b) $f = 300$ MHz, and (c) $f = 400$ MHz. The incident direction of the plane wave is shown in the inset of (a).

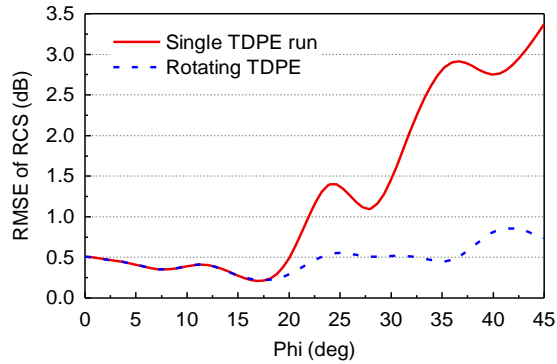


Fig. 5. Comparison of RMSE for bistatic RCS calculated by a single TDPE run and the rotating TDPE method.

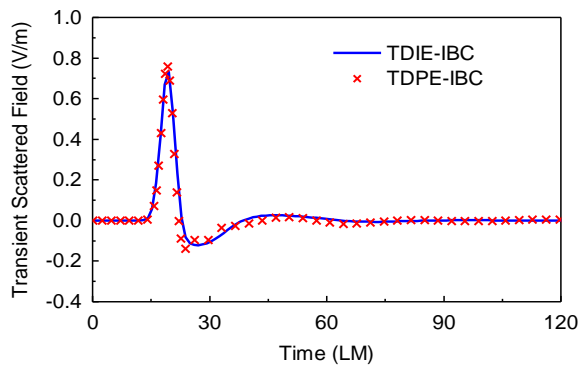


Fig. 6. Transient scattered field at the point (2m, 2.6m, 0m). The unit LM represents light meter and 1LM = 1/c, where c is the light speed in free space.

Table 1: Average RMSE calculated for different coated materials with different permittivity

Material Constant	Average RMSE(dB)
$\epsilon_r = 2 - 0.1j$	0.60
$\epsilon_r = 2 - 0.5j$	0.61
$\epsilon_r = 2 - 1.0j$	0.58

B. Wide-band scattering from a coated PEC spherical cone

To discuss the accuracy and efficiency of the proposed method further, the broadband scattering of a coated PEC spherical cone is analyzed. The cone is coated with dielectric of $\epsilon_r = 2 - j$, $\mu_r = 1$ and the thickness is 0.01m. The radius of the hemisphere is 4m and the height of the cone is 6m. The simulated scenario is shown in the inset of Fig. 7. A y-polarization plane wave illuminates from the top of the cone. Both the incident direction and paraxial direction of TDPE method are also along the +x axis. The bandwidth of the modulated Gaussian pulse in this example is 1GHz. The full bistatic RCS results computed by rotating TDPE at 200MHz, 500MHz and 800MHz achieve a good agreement with the results of TDIE in Figs. 7 (a)-(c).

This demonstrates that the proposed method is still accurate when the frequency band is further broadened. The transient forward-scattered field values are presented in Fig. 8, where a remarkable consistence is achieved between the two methods. Additionally, the computational resources of the two methods are compared in Table 2. It can be found that both the memory requirement and the time consumption reduce significantly for the proposed method. Therefore, it is an efficient tool to analyze the wideband scattering from electrically large coated objects.

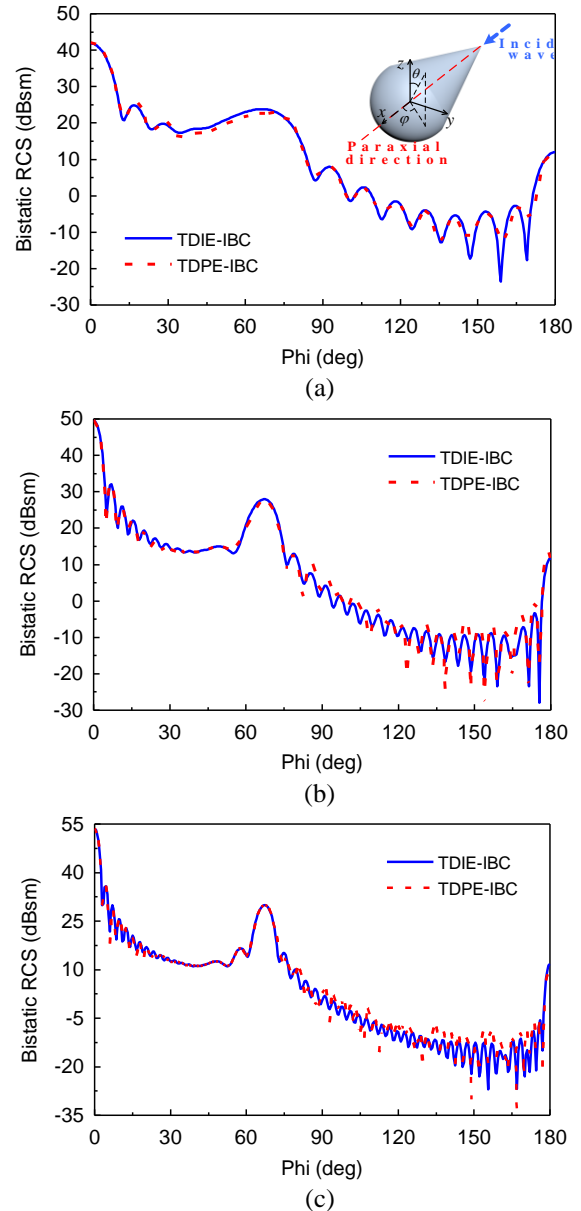


Fig. 7. Bistatic RCS of a coated PEC spherical cone at different frequencies: (a) $f = 200$ MHz, (b) $f = 500$ MHz, and (c) $f = 800$ MHz. The incident direction of the plane wave is shown in the inset of (a).

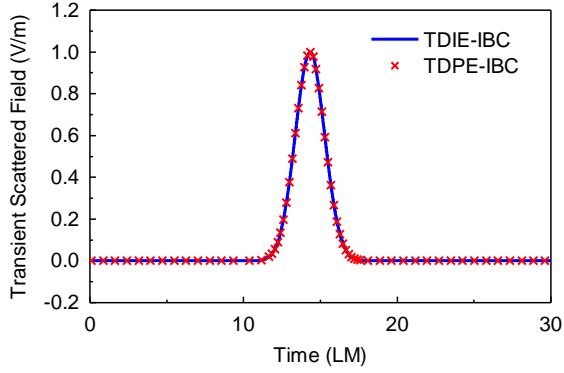


Fig. 8. Transient scattered field at the point (10m, 2m, 0m). The unit LM represents light meter and 1LM = 1/c, where c is the light speed in free space.

Table 2: Comparison of the computational resources for the TDIE with IBC method and the proposed method

Methods	Peak Memory Requirement (MB)	Total CPU Time (h)
TDIE-IBC	8562	18.9
TDPE-IBC	352	10.8

VI. CONCLUSION

In this paper, we propose the time-domain parabolic equation method with impedance boundary condition to analyze the wideband scattering from electrically large coated objects. The TDPE method increases the efficiency by converting the three-dimensional problem to multiple two-dimensional problems. And additionally, most of the computational resources do not need to be consumed on the dielectric regions due to the impedance boundary condition. The accurate bistatic RCS for all directions can be obtained by the rotating TDPE method. Numerical results have validated the accuracy and efficiency of this method.

ACKNOWLEDGMENT

This work was supported by the Natural Science Foundation under Grant 61701240, Fundamental Research Funds for the Central Universities with No. 30918011317, and State Key Laboratory of Millimeter Waves under Grant K201920.

REFERENCES

[1] A. C. Rappaport, "On the parabolic equation method for water-wave propagation," *J. Fluid. Mech.*, vol. 95, no. 1, pp. 159-176, 1979.
 [2] R. A. Dalrymple and P. A. Martin, "Perfect boundary conditions for parabolic water-wave models," *Proc. R. Soc. London A*, vol. 437, pp. 41-54, 1992.
 [3] M. D. Feit and J. A. Fleck, Jr., "Light propagation in graded-index fibers," *Appl. Opt.*, vol. 17, pp.

3990-3998, 1978.
 [4] D. Yevick, "A guide to electric field propagation techniques for guided-wave optics," *Opt. Quantum Electron.*, vol. 26, pp. 185-197, 1994.
 [5] F. Collino and P. Joly, "Splitting of operators, alternate directions, and paraxial approximations for the three-dimensional wave equation," *SIAM J. Sci. Comput.*, vol. 16, pp. 1019-1048, 1995.
 [6] M. Leontovich and V. Fock, "Solution of the problem of propagation of electromagnetic waves along the earth's surface by the method of parabolic equation," *Acad. Sci. Ussr. J. Phys.*, vol. 7, pp. 557-573, 1946.
 [7] Q. F. Wei, C. Y. Yin, and W. Wu, "Research and verification for an improved two-way parabolic equation method in obstacle environment," *IET Microwaves, Antennas & Propag.*, vol. 12, no. 4, pp. 576-582, 2018.
 [8] M. F. Levy, "Parabolic equation modeling of propagation over irregular terrain," *Electron. Lett.*, vol. 26, pp. 1153-1155, 1990.
 [9] Z. He, H. Zeng, and R. S. Chen, "Two way propagation modeling of expressway with vehicles by using the three-dimensional ADI-PE method," *IEEE Trans. Antennas Propag.*, vol. 66, no. 4, pp. 2156-2160, Apr. 2018.
 [10] Z. He, Z. H. Fan, D. Z. Ding, and R. S. Chen, "Efficient radar cross-section computation of electrically large targets with ADI-PE method," *Electron. Lett.*, vol. 51, no. 4, pp. 360-362, 2015.
 [11] Z. He and R. S. Chen, "A vector meshless parabolic equation method for three-dimensional electromagnetic scatterings," *IEEE Trans. Antennas Propag.*, vol. 63, no. 6, pp. 2595-2603, 2015.
 [12] Z. He and R. S. Chen, "A novel parallel parabolic equation method for electromagnetic scatterings," *IEEE Trans. Antennas Propag.*, vol. 64, no. 11, pp. 4777-4784, 2016.
 [13] Z. He, Z. H. Fan, D. Z. Ding, and R. S. Chen, "GPU-accelerated ADI-PE method for the analysis of EM scatterings," *Electron. Lett.*, vol. 51, pp. 1652-1654, 2015.
 [14] Z. He and R. S. Chen, "A novel marching-on-in-degree solver of time domain parabolic equation for transient EM scattering analysis," *IEEE Trans. Antennas Propag.*, vol. 61, no. 11, pp. 4905-4910, 2016.
 [15] Z. He and R. S. Chen, "Frequency-domain and time-domain solvers of parabolic equation for rotationally symmetric geometries," *Comput. Phys. Commun.*, vol. 220, pp. 181-187, 2017.
 [16] J. E. Murphy, "Finite-difference treatment of a time-domain parabolic equation: Theory," *J. Acoust. Soc. Am.*, vol. 77 no. 5 pp. 1958-1960, 1985.
 [17] Z. He, R. S. Chen, "Fast analysis of wide-band scattering from electrically large targets with

- time-domain parabolic equation method,” *Comput. Phys. Commun.*, vol. 200, pp. 139-146, 2016.
- [18] Z. He, D. Z. Ding, and R. S. Chen, “An efficient marching-on-in-degree solver of surface integral equation for multilayer thin medium-coated conductors,” *IEEE Antennas & Wireless Propag. Lett.*, vol. 15, pp. 1458-1461, 2016.
- [19] Z. He and R. S. Chen, “A fast marching-on-in-degree solution for analysis of conductors coated with thin dispersive dielectric,” *IEEE Trans. Antennas Propag.*, vol. 65, no. 9, pp. 4751-4758, 2017.
- [20] Z. He, Z. H. Fan, D. Z. Ding, and R. S. Chen, “Solution of PMCHW integral equation for transient electromagnetic scattering from dielectric body of revolution,” *IEEE Trans. Antennas Propag.*, vol. 63, no. 11, pp. 5124-5129, 2015.
- [21] Z. He, R. S. Chen, and W. Sha, “An efficient marching-on-in-degree solution of transient multi-scale EM scattering problems,” *IEEE Trans. Antennas Propag.*, vol. 64, no. 7, pp. 3039-3046, 2016.
- [22] Z. H. Fan, Z. He, and R. S. Chen, “Marching-on-in-degree solution of the transient scattering from multiple bodies of revolution,” *IEEE Trans. Antennas Propag.*, vol. 64, no. 1, pp. 321-326, 2015.
- [23] Z. He and R. S. Chen, “An efficient high-order marching-on-in-degree solver for conducting and dielectric bodies of revolution,” *Trans. Antennas Propag.*, vol. 65, no. 8, pp. 4374-4378, 2017.
- [24] Z. He, H. H. Zhang, and R. S. Chen, “Parallel marching-on-in-degree solver of time-domain combined field integral equation for bodies of revolution accelerated by MLACA,” *IEEE Trans. Antennas Propag.*, vol. 63, no. 8, pp. 3705-3710, 2015.
- [25] T. K. Sarkar and E. Arvas, “An integral equation approach to the analysis of finite microstrip antennas: Volume/surface formulation,” *IEEE Trans. Antennas Propag.*, vol. 38, no. 3, pp. 305-312, Mar. 1990.
- [26] T. B. A. Senior, “Impedance boundary conditions for imperfectly conducting surfaces,” *Appl. Sci. Res.*, vol. 8, no. 1, pp. 418, 1960.
- [27] Q. Chen, M. Lu, and E. Michielssen, “Integral equation based analysis of transient scattering from surfaces with impedance boundary condition,” *IEEE Antennas and Propag. Society Symp., 2004*, Monterey, CA, USA, vol., 4, pp. 3891-3894, 2004.
- [28] B. Gustavsen and A. Semlyen, “Rational approximation of frequency domain responses by vector fitting,” *IEEE Trans. Power Delivery*, vol. 14, no. 3, pp. 1052-1061, 1999.
- [29] J. M. Jin, *The Finite Element Method in Electromagnetics*. John Wiley & Sons, 2015.



Ling Guan was born in Nanjing, China. He received the B.S. degree in Communication Engineering from the School of Electrical Engineering and Optical Technique, Nanjing University of Science and Technology, Nanjing, China, in 2014. He is currently pursuing his Ph.D. degree in Electronic Engineering at Nanjing University of Science and Technology.

His research interests are antennas, metamaterials and computational electromagnetics.



Shifei Tao was born in Anhui, China, in 1987. He received the B.Sc. degree in Communication Engineering and Ph.D. degree in EM Field and Microwave Technique from Nanjing University of Science and Technology (NJUST), Nanjing, Jiangsu, China, in 2008 and 2014, respectively.

Since 2017, he has been with Nanjing University of Science and Technology, where he works as an Assistant Professor. From 2015 to 2016, he was a Postdoctoral Research Associate in Electric and Computer Engineering in Northeastern University, Boston, USA. His current research interests are in the computational electromagnetics, antennas, electromagnetic scattering and radiation.

Fast Wideband Electromagnetic Analysis Using the Interpolation Technique and Fast Generating Matrix Method

Wei Bin Kong^{1,2}, Xiao Fang Yang¹, Feng Zhou¹, Jia Ye Xie³, Ru Gang Wang¹,
and Kai Lai Zheng⁴

¹ College of Information Engineering
Yancheng Optical Fiber Sensing and Application Engineering Technology Research Center
Yancheng Institute of Technology, Jiangsu Yancheng, 224051, China
kongweibin2007@sina.com,

² State Key Laboratory of Millimeter Waves
Southeast University, Jiangsu Nanjing, 210096, China

³ Industrial Center
Nanjing Institute of Technology, Jiangsu Nanjing, 211167, China

⁴ College of Electronic and Optical Engineering & College of Microelectronics
Nanjing University of Posts and Telecommunications, Jiangsu Nanjing, 210023, China

Abstract — A fast wideband electromagnetic scattering analysis method based on the interpolation technique and fast generating matrix method is proposed. By factoring out the dominant phase term, the matrix element is transformed into the element which fluctuates slowly with frequency. The matrices over the frequency band are fast generated via interpolation technique. Instead of employing different meshing grids at different frequencies, this new method requires only one mesh generated at the highest frequency of the given bandwidth. This approach not only saves much work in geometrical modeling but also leads to less time for wideband scattering problem. The proposed algorithm is implemented in the platform of FGG-FG-FFT, which is not sensitive to both the grid spacing and the expansion order. A method for fast generating matrix also is introduced to speed up filling the near matrix. Consequently, it can not only reduce the impedance matrix filling time in the whole frequency band but also accelerate the matrix filling process at frequency interpolation sampling points. Several numerical examples are provided to demonstrate the correctness and the efficiency of the proposed method for the wideband scattering analysis.

Index Terms — Electromagnetic scattering, FGG-FG-FFT, frequency sweeps, interpolation technique, near matrix.

I. INTRODUCTION

Wideband electromagnetic (EM) scattering analysis has been widely applied to the area of noncooperative

radar target identification and radar imaging. Since frequency sweep is always needed in these applications, one has to calculate the scattering at a number of frequency sample points in a given bandwidth. For the analysis of electrically large objects, even a single calculation is very time-consuming, let alone one has to calculate many times. Therefore, it is urgent to accelerate the process of wideband electromagnetic analysis.

Integral equation combined with the method of moments (MoM) is one of the most popular method in computational electromagnetic [1]. In order to overcome the shortcomings of the method of moments in both computation time and storage memory, many fast algorithms have been developed, such as the fast multipole method (FMM) [2], the multilevel fast multipole algorithm (MLFMA) [3]-[6], and the FFT-based methods (Adaptive integral method (AIM), Precorrected-FFT method (P-FFT), IE-FFT, Fitting the Green's function method (FGG-FG-FFT), etc. [7]-[12]). When analyzing broad-band electromagnetic characteristics of the target, the features of the fast algorithms are different. The FMM is based on the addition theorem of Green's function. Therefore, there exists the sub-wavelength breakdown [13]. The FFT-based methods can be applied to all over frequency band [8], [9]. However, one still has to calculate the scattering at each frequency sample point for frequency sweep. Besides the computational load, different meshes are required for different frequencies. This leads to tremendous work in geometrical modeling. In order to save time for preliminary treatment, the surface of the PEC object

is discretized with triangular patches at the highest frequency. The discrete grid is scale-changing in the whole frequency band. Therefore, a single fast multipole method is difficult to complete computation of frequency sweep.

The promising and interesting approach to the broadband electromagnetic response over a frequency band without the direct calculation is the data reconstruction method. Asymptotic waveform estimation (AWE) [14], [15], model-based parameter estimation (MBPE) [16]-[18], model order reduction [19], interpolation methods [20]-[24], extrapolation methods [25], and Stoer-Bulirsch algorithm [26], etc., have been developed. However, on the one hand, the above methods in the formulation-domain modeling are based on the fully filled impedance matrix. On the other hand, the methods in the solution-domain modeling suffer from the difficulty of keeping accuracy due to the fast oscillating of the data. For example, AWE is accurate only around the frequency of expansion and is difficult to adaptively choose the expansion points. Furthermore, its accuracy deteriorates beyond a certain bandwidth [27], [28]. Some of these methods in the solution-domain are not suitable for the electrically large targets, nor are they suitable for general targets with complex structure in the real world.

In this paper, a method based on the interpolation technique and fast generating matrix method is developed to solve the wideband scattering problem. In this method, only one fixed mesh grid of the target at the highest frequency is required for all frequency samples at which the scattering will be calculated. The proposed algorithm is implemented in the platform of FGG-FG-FFT to enhance its capability for large problems. Furthermore, the near matrix of FGG-FG-FFT over the frequency band are fast generated via interpolation technique, denoted by FGG-FG-FFT-NMI. In order to fast generate the modified matrices at the three normalized frequency samples and the derivative of the modified matrix at the internal sample, a method for fast filling the near matrix is adopted. It can not only reduce the impedance matrix filling time in the whole frequency band but also accelerate the matrix filling process at frequency interpolation sampling points. Therefore, the speed of the wideband scattering analysis is greatly accelerated.

II. FORMULATIONS AND EQUATIONS

A. Impedance matrix form of the normalized frequency

The radiation and scattering problem of an arbitrary shaped perfectly electric conducting (PEC) object can be formulated by the SIEs such as the electric field integral equation (EFIE) and the magnetic field integral equation (MFIE). Assume that the surface current is expanded in

terms of the Rao-Wilton-Glisson (RWG) functions [29]. After applying the Galerkin's procedure, the SIEs are converted into the matrix systems.

The frequency range is $[f_l, f_h]$, i.e., the lowest frequency f_l and the highest frequency f_h . The object surface is supposed to be discretized at f_h . λ_h is the wavelength at f_h . The element with the normalized frequency of the impedance matrix for the EFIE and MFIE is, respectively, expressed as:

$$Z_{ij}^E(f_r) = \int_{S_i(\lambda_h)} ds \int_{S_j(\lambda_h)} ds' \left[\vec{J}_i(\vec{r}) \cdot \vec{J}_j(\vec{r}') k_r - \nabla_h \cdot \vec{J}_i(\vec{r}) \nabla_h' \cdot \vec{J}_j(\vec{r}') \frac{1}{k_r} \right] G(\vec{r}, \vec{r}') j \eta_0 \lambda_h^2, \quad (1)$$

$$Z_{ij}^M(f_r) = \left[\frac{1}{2} \int_{S_i(\lambda_h)} ds \vec{J}_i(\vec{r}) \cdot \vec{J}_j(\vec{r}') - \int_{S_i(\lambda_h)} ds \vec{J}_i(\vec{r}) \cdot \hat{n} \times \int_{S_j(\lambda_h)} ds' \nabla_h G(\vec{r}, \vec{r}') \times \vec{J}_j(\vec{r}') \right] \lambda_h^2, \quad (2)$$

where, $G(\vec{r}, \vec{r}')$ denotes the Green's function of free space, which can be expressed as:

$$G(\vec{r}, \vec{r}') = \frac{e^{-jk_r|\vec{r}-\vec{r}'|}}{4\pi|\vec{r}-\vec{r}'|}, \quad (3)$$

where $k_r = 2\pi f_r$. The normalized frequency $f_r = f / f_h$ varies within $[f_l / f_h, 1]$.

Usually, S_i consists of two triangle subdomains; that is, $S_i = S_i^+ \cup S_i^-$ and, $\vec{J}_i(\vec{r})$ is defined on a pair of triangles as:

$$\vec{J}_i(\vec{r}) = \begin{cases} \vec{J}_i^+(\vec{r}) = \frac{l_i}{2A_i^+} (\vec{r} - \vec{r}_{io}^+), & \vec{r} \in S_i^+ \\ \vec{J}_i^-(\vec{r}) = \frac{l_i}{2A_i^-} (\vec{r}_{io}^- - \vec{r}), & \vec{r} \in S_i^- \end{cases}. \quad (4)$$

For more details of RWG basis functions, readers can refer to the literature [29].

The element for the combined field integral equation (CFIE) can be expressed as:

$$Z_{ij}^C = \alpha Z_{ij}^E + (1 - \alpha) \eta_0 Z_{ij}^M, \quad (5)$$

where, $0 \leq \alpha \leq 1$.

Here, the following modified matrix element is adopted:

$$\tilde{Z}_{ij}^S = \begin{cases} Z_{ij}^S f_r e^{jk_r R_{ij}} & S_i \cap S_j = 0 \\ Z_{ij}^S f_r & S_i \cap S_j \neq 0 \end{cases}, \quad (6)$$

where, the superscript $S = E, M, C$ represents EFIE, MFIE and CFIE. $R_{ij} = |\vec{r}_i - \vec{r}_j|$ is the distance between the centers of the RWG elements S_i and S_j . The interpolation scheme requires three frequency samples within $[f_l, f_h]$, i.e., the lowest frequency f_l , the highest

frequency f_h , and an internal frequency f_{in} .

For the integrity of this paper, the interpolation method is introduced briefly [22]. For convenience, let x_0, x_1, x_2 , and x denote the normalized frequencies $f_l/f_h, f_{in}/f_h, 1$, and f/f_h , respectively. $y(x_i)$ denotes the modified matrix elements at $x_i, i=0,1,2$; $y'(x_1)$ is the first order derivative of $y(x_1)$ with respect to the normalized frequency. The modified matrices for any normalized intermediate frequencies x are then approximated by a cubic polynomial:

$$y(x) = \sum_{i=0}^2 y(x_i)\phi_i(x) + y'(x_1)\varphi_1(x), \quad (7)$$

where,

$$\phi_0(x) = \left(\frac{x-x_2}{x_0-x_2} \right) \left(\frac{x-x_1}{x_0-x_1} \right)^2, \quad (8)$$

$$\phi_1(x) = \Theta(x) \left(1 - \frac{x-x_1}{x_1-x_0} - \frac{x-x_1}{x_1-x_2} \right), \quad (9)$$

$$\phi_2(x) = \left(\frac{x-x_0}{x_2-x_0} \right) \left(\frac{x-x_1}{x_2-x_1} \right)^2, \quad (10)$$

$$\varphi_1(x) = (x-x_1)\Theta(x), \quad (11)$$

$$\Theta(x) = \left(\frac{x-x_0}{x_1-x_0} \right) \left(\frac{x-x_2}{x_1-x_2} \right). \quad (12)$$

B. The frame of the FGG-FG-FFT

Impedance matrix can be split into two parts:

$$Z^S = (Z^{S-near} - Z^{S-far}) + Z^{S-far} \approx Z^{S-corr} + Z^{S-far}, \quad (13)$$

where Z^{S-corr} is a sparse matrix, which is obtained by letting the ‘‘far elements’’ of $Z^{S-near} - Z^{S-far}$ become zero. The detail of the matrix Z^{S-far} can be written as:

$$Z^{EFIE-far} = j\eta_0\lambda_h^2(k_r\bar{\Pi} \cdot G\bar{\Pi}^T - \frac{1}{k_r}\Pi_d G\Pi_d^T), \quad (14)$$

$$Z^{MFIE-far} = \lambda_h^2\bar{\Pi}_g \cdot G\bar{\Pi}^T, \quad (15)$$

where $\bar{\Pi}$, Π_d and $\bar{\Pi}_g$ are all sparse matrices, where the head mark ‘‘ $\bar{\cdot}$ ’’ implies matrix elements being 3D vectors; G is a triple Toeplitz matrix related to the Green’s function and may be simply called the discrete Green’s function; the superscript ‘‘T’’ indicates the matrix transpose. The detail of choice for (14) and (15) in the literatures [11], [12].

C. Fast filling the near matrix

As can be seen from the above, in the FFT-based methods, near matrix elements are calculated directly. It is well known that the calculation of the near matrix accounts for most of solution time for large-scale EM problems. When the RWG function is adopted, it can be

found that every integral in (1) and (2) for a matrix element Z_{ij}^S includes a lot of calculations shared by other matrix elements. As is shown in Fig. 1, since a RWG function is defined on a pair of triangles with a common edge, the interaction between the two triangles is in close relation to 9 matrix elements. In the widely used RWG-RWG interaction scheme [29], 9 RWG-RWG interactions over a pair of triangles are independently calculated for generating the corresponding 9 matrix elements. Therefore, that leads to repeated calculations, because the triangle-triangle interactions already calculated are not reusable for the RWG-RWG interactions. Removing these redundant calculations can greatly improve the efficiency of generating matrix. A triangle-triangle scheme was proposed to accelerate filling MoM matrix [30]. However, the method adopted by this paper is different from the method in the literature [30].

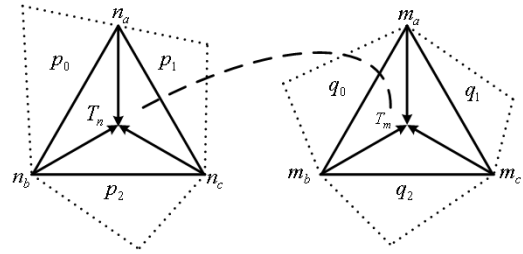


Fig. 1. Triangle-triangle interactions of RWG functions.

The matrix elements of (1) and (2) are both in form of the RWG-RWG interaction. The triangle-triangle interactions of the matrix element of (1) and (2) can be calculated as:

$$Z_{ij} = Z_{S_i^+, S_j^+} + Z_{S_i^+, S_j^-} + Z_{S_i^-, S_j^+} + Z_{S_i^-, S_j^-}. \quad (16)$$

For convenience, the calculation formulae of the four terms in the right hand of (16) are very analogous, so only one needs to be provided. Here, we present a detailed expression of the main parts:

$$\int_{S_i} ds \bar{J}_i(\vec{r}) \cdot \int_{S_j} \bar{J}_j(\vec{r}') G(\vec{r}, \vec{r}') ds', \quad (17)$$

$$= \frac{l_i l_j}{4} (Q_1 - \vec{r}_{io} \cdot \vec{Q}_2 - \vec{r}_{jo}' \cdot \vec{Q}_3 + \vec{r}_{io} \cdot \vec{r}_{jo}' Q_4)$$

where,

$$Q_1 = \frac{1}{A_i A_j} \int_{S_i} \int_{S_j} \vec{r} \cdot \vec{r}' G(\vec{r}, \vec{r}') ds ds', \quad (18)$$

$$\vec{Q}_2 = \frac{1}{A_i A_j} \int_{S_i} \int_{S_j} \vec{r}' G(\vec{r}, \vec{r}') ds ds', \quad (19)$$

$$\vec{Q}_3 = \frac{1}{A_i A_j} \int_{S_i} \int_{S_j} \vec{r} G(\vec{r}, \vec{r}') ds ds', \quad (20)$$

$$Q_4 = \frac{1}{A_i A_j} \int_{S_i} \int_{S_j} G(\vec{r}, \vec{r}') ds ds', \quad (21)$$

$$\int_{S_i} ds \vec{J}_i(\vec{r}) \cdot \hat{n} \times \int_{S_j} ds' \nabla G(\vec{r}, \vec{r}') \times \vec{J}_j(\vec{r}') \quad (22)$$

$$= \frac{I_{ij}}{4} (P_1 - \vec{r}_{io} \times \hat{n} \cdot \vec{P}_2 - \vec{r}'_{jo} \cdot \vec{P}_3 + \vec{r}'_{jo} \times (\vec{r}_{io} \times \hat{n}) \cdot \vec{P}_4)$$

where,

$$P_1 = \frac{1}{A_i A_j} \int_{S_i} ds \vec{r} \times \hat{n} \cdot \int_{S_j} ds' \nabla G(\vec{r}, \vec{r}') \times \vec{r}', \quad (23)$$

$$\vec{P}_2 = \frac{1}{A_i A_j} \int_{S_i} ds \int_{S_j} ds' \nabla G(\vec{r}, \vec{r}') \times \vec{r}', \quad (24)$$

$$\vec{P}_3 = \frac{1}{A_i A_j} \int_{S_i} ds (\vec{r} \times \hat{n}) \times \int_{S_j} ds' \nabla G(\vec{r}, \vec{r}'), \quad (25)$$

$$\vec{P}_4 = \frac{1}{A_i A_j} \int_{S_i} ds \int_{S_j} ds' \nabla G(\vec{r}, \vec{r}'). \quad (26)$$

Note that basic integral terms of (17) and (22) which include $Q_1, \bar{Q}_2, \bar{Q}_3, Q_4, P_1, \bar{P}_2, \bar{P}_3, \bar{P}_4$ are irrelevant with information of common edge. These integral items can be easily obtained by Gaussian triangle quadrature, and can be shared by multiple matrix elements, which is the reason why the redundant calculations can be removed. Generally, the interactions between a pair of triangles associate with up to 9 matrix elements.

III. NUMERICAL RESULTS

In this section, several numerical examples are given to demonstrate the efficiency and accuracy of FGG-FG-FFT-NMI. The grid spacings are selected to be equal, i.e., $h_x = h_y = h_z = 0.25\lambda_h$ at the highest frequency f_h . The expansion order is $M = 2$. When necessary, the direct (no interpolation) FGG-FG-FFT, MoM with out-of-core LU solver and IE-ODDM [31] are also employed as the reference.

Example A: A PEC Rectangular Block

Here, we consider the electromagnetic scattering by a PEC rectangular block with dimensions $10\lambda_h(x) \times 3\lambda_h(y) \times 0.5\lambda_h(z)$, as shown in Fig. 2. The incidence angle is $\theta^{in} = 0^\circ, \phi^{in} = 0^\circ$. In such cases, the frequency varies from 6 to 30 GHz. The rectangular block surface is modeled by with 16,644 triangle patches with the average edge size of $0.1\lambda_h$, yielding 24,966 unknowns. The frequency increment of $\Delta f = 1$ GHz is considered.

Plotted in Fig. 3 are the RCS results at the scattering direction $(\theta^s, \phi^s) = (60^\circ, 0^\circ)$ obtained from FGG-FG-FFT-NMI, direct FGG-FG-FFT, and MoM, respectively. It is also worth mentioning that MoM is used. The result at each frequency point is calculated rigorously. It shows that the RCS results computed by FGG-FG-FFT-NMI agree very well with those by direct FGG-FG-FFT and MoM.

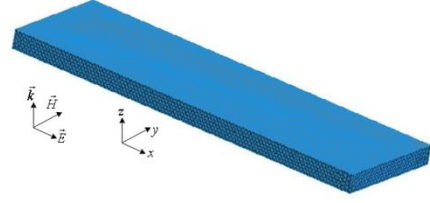


Fig. 2. Geometry of a PEC rectangular block with $10\lambda_h(x) \times 3\lambda_h(y) \times 0.5\lambda_h(z)$.

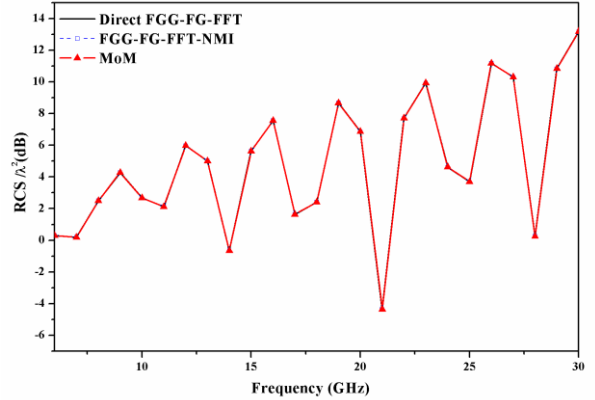


Fig. 3. The RCS of the PEC rectangular block at the scattering direction $(\theta^s, \phi^s) = (60^\circ, 0^\circ)$ at different frequencies.

As observed from Table 1, the triangle-triangle scheme reduces the CPU time to 12.89% of the time required by the RWG-RWG scheme at 30 GHz. The statistics on the filling time of near matrix are listed in Table 2 at 20 GHz. As shown in Table 2, the CPU time to fill this matrix is cut down. In this example, it costs about 1.27 hours using FGG-FG-FFT-NMI at the whole frequency band, and 3.23 hours using direct FGG-FG-FFT.

Table 1: CPU time for directly calculating the near matrix for the three examples at 30 GHz (in seconds)

Ex.	Method	Time Cost	Time Ratio	Reduced By
A	RWG-RWG	300.3	7.76	87.11%
	Triangle-Triangle	38.7		
B	RWG-RWG	310.3	8.36	88.03%
	Triangle-Triangle	37.1		
C	RWG-RWG	1092.1	7.94	87.41%
	Triangle-Triangle	137.5		

Table 2: CPU time spent of the filling time (in seconds)

Ex.	Method	Z^{near}	Near part In Z^{far}
A	Direct Calculation	300.3	25.5
	Interpolation Scheme	0.24	24.3
B	Direct Calculation	304.7	26.3
	Interpolation Scheme	8.02	26.6
C	Direct Calculation	1130.6	70.4
	Interpolation Scheme	10.3	72.2

Example B: A Metallic 90° Dihedral Corner Reflector

The example deals with a flat metallic structure. The scattering from a metallic 90° dihedral corner reflector as shown in Fig. 4 is considered in a bandwidth from 6 GHz to 30 GHz. The two plates, with the sharing edge being $16\lambda_h$ long in z-direction, are $8\lambda_h$ long in both x- and y-directions. The RCS is computed for a plane wave incident from $\theta^{in} = 0^\circ$ and $\phi^{in} = 0^\circ$ with the electric field x-direction polarized as is shown in Fig. 4. The surface of the metallic 90° dihedral corner reflector is discretized with about 10 elements per wavelength, yielding 88,045 unknowns. The frequency increment of $\Delta f = 1$ GHz is considered.

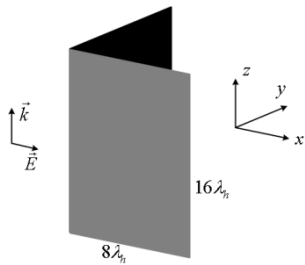
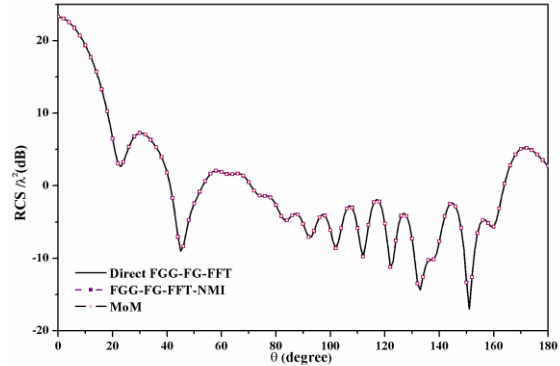


Fig. 4. Geometry of a metallic 90° dihedral corner reflector.

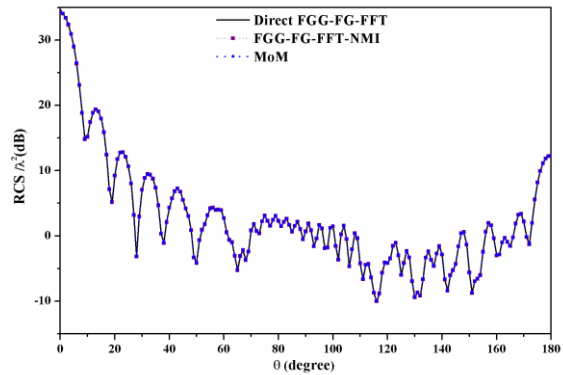
The bistatic RCS at 11 GHz and 25 GHz are compared to the results from direct FGG-FG-FFT, FGG-FG-FFT-NMI and MoM in Fig. 5, respectively. The good agreement in these two figures shows the accuracy of the proposed method in this paper. The variation of RCS with frequency at the scattering direction $\theta^S = 150^\circ$, $\phi^S = 0^\circ$, as shown in Fig. 6. It shows that the RCS results computed by FGG-FG-FFT-NMI agree very well with those by direct FGG-FG-FFT and MoM.

Seen from Table 1, the triangle-triangle scheme reduces the CPU time to 11.97% of the time required by the RWG-RWG scheme at 30 GHz. The statistics on the filling time of near matrix are listed in Table 2 at 20 GHz.

As shown in Table 2, the CPU time to fill this matrix is cut down by a factor of 37.99. In this example, it costs about 8.17 hours using FGG-FG-FFT-NMI at the whole frequency band, and 10.2 hours using direct FGG-FG-FFT.



(a) The bistatic RCS curves at 11 GHz



(b) The bistatic RCS curves at 25 GHz

Fig. 5. The bistatic RCS curves of a metallic 90° dihedral corner reflector.

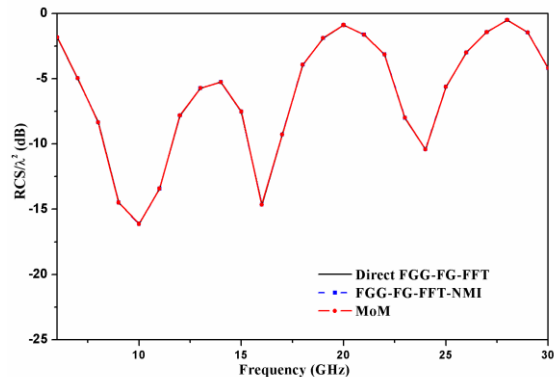


Fig. 6. The RCS of the metallic 90° dihedral corner reflector at the scattering direction $(\theta^S, \phi^S) = (150^\circ, 0^\circ)$ at different frequencies.

Example C: A Missile Model

At last, as an example, we consider a missile model. The missile model, $41\lambda_h$ long and $12\lambda_h$ width in the largest dimension as shown in Fig. 7, is simulated using 102,282 unknowns. The frequency is swept from 6 GHz to 30 GHz under the stepping of $\Delta f = 1$ GHz.

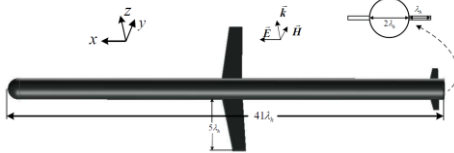
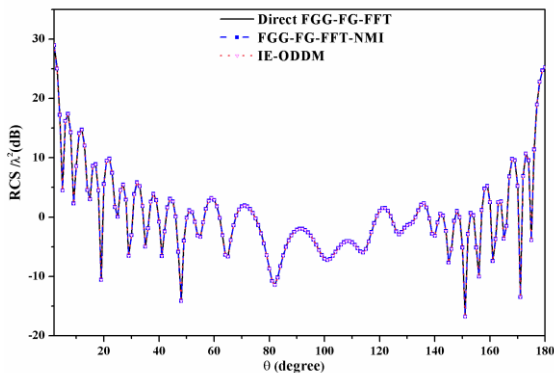
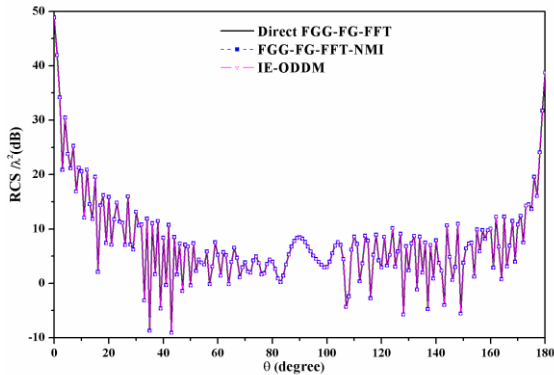


Fig. 7. The PEC missile model.



(a) The bistatic RCS curves at 9 GHz



(b) The bistatic RCS curves at 27 GHz

Fig. 8. The bistatic RCS curves of the missile model.

The bistatic RCS at 9 GHz and 27 GHz are compared to the results from direct FGG-FG-FFT, FGG-FG-FFT-NMI and IE-ODDM in Fig. 8, respectively. The good agreement in these two figures shows the accuracy of the proposed method. Figure 9 presents the RCS results at the direction of $(\theta^s, \phi^s) = (80^\circ, 0^\circ)$ at different frequencies. It shows that the RCS results computed by FGG-FG-FFT-NMI agree very well with those by direct FGG-FG-FFT. Table 1 lists the CPU time for calculating

the near matrix required by the triangle-triangle scheme and RWG-RWG scheme, respectively. At 30GHz, the triangle-triangle scheme reduces the CPU time to 12.59% of that required by the RWG-RWG scheme. The statistics on the filling time of near matrix are listed in Table 2 at 20 GHz. As shown in Table 2, the CPU time to fill this matrix is cut down by a factor of 109.77. In this example, it costs about 7.87 hours using FGG-FG-FFT-NMI at the whole frequency band, and 15.5 hours using direct FGG-FG-FFT. If the frequency increments are smaller, the difference between efficiency of the two methods will be greater. This can also be verified from Table 2.

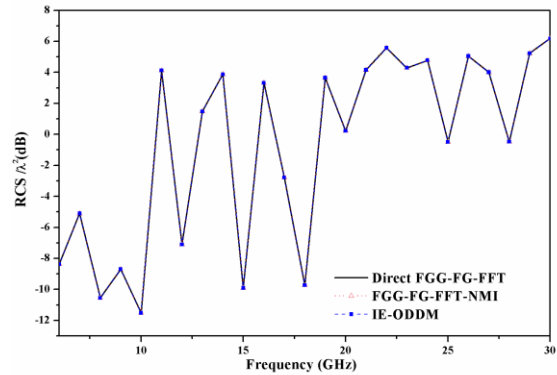


Fig. 9. The RCS of the missile model at the scattering direction $(\theta^s, \phi^s) = (80^\circ, 0^\circ)$ at different frequencies.

VI. CONCLUSION

A new fast frequency sweeps method using both the interpolation technique and the fast generating matrix method is proposed. It fuses both the benefits of FGG-FG-FFT and the fast frequency sweeping method based on the interpolation technique and the triangle-triangle scheme. It can not only reduce time in geometrical modeling, but also accelerate the impedance matrix filling process. Thus, it can efficiently accelerate the process of frequency sweeps. The proposed algorithm is not sensitive to both the grid spacing and the expansion order. Numerical experiments validate the accuracy and efficiency.

ACKNOWLEDGMENT

This work was supported by Open Research Program of State Key Laboratory of Millimeter Waves in Southeast University K201718, K201731 and K201928, The Natural Science Foundation of China 61673108, 11801492, The Colleges and Universities Natural Science Foundation in Jiangsu Province 18KJD510010, The Open Project Program of the Key Laboratory of Underwater Acoustic Signal Processing, Ministry of Education UASP1801, The Fundamental Research Funds for the Central Universities 2242016K30013, and

The Natural Science Foundation of Jiangsu Province BK20181050.

REFERENCES

- [1] R. F. Harrington, *Field Computation by Moment Methods*. The MacMillian, New York, 1968.
- [2] N. Engheta, W. D. Murphy, V. Rokhlin, and M. S. Vassiliou, "The fast multipole method (FMM) for electromagnetic scattering problems," *IEEE Trans. Antennas Propag.*, vol. 40, no. 6, pp. 634-641, June 1992.
- [3] J. M. Song, C. C. Lu, and W. C. Chew, "Multilevel fast multipole algorithm for electromagnetic scattering by large complex objects," *IEEE Trans. Antennas Propag.*, vol. 45, no. 10, pp. 1488-1493, Oct. 1997.
- [4] W. B. Kong, H. X. Zhou, K. L. Zheng, and W. Hong, "Analysis of multiscale problems using the MLFMA with the assistance of the FFT-Based method," *IEEE Trans. Antennas Propag.*, vol. 63, no. 9, pp. 4184-4188, Sep. 2015.
- [5] W. B. Kong, H. X. Zhou, W. D. Li, G. Hua, and W. Hong, "The MLFMA equipped with a hybrid tree structure for the multiscale EM scattering," *International Journal of Antennas and Propagation*, vol. 2014, Article ID 281303, 2014.
- [6] X. M. Pan, J. G. Wei, Z. Peng, and X. Q. Sheng, "A fast algorithm for multiscale electromagnetic problems using interpolative decomposition and multilevel fast multipole algorithm," *Radio Sci.*, vol. 47, RS1011, 2012.
- [7] E. Bleszybski, M. Bleszynski, and T. Jaroszewicz, "AIM: Adaptive integral method for solving large-scale electromagnetic scattering and radiation problems," *Radio Sci.*, vol. 31, pp. 1225-1251, 1996.
- [8] J. R. Phillips and J. K. White, "A precorrected-FFT method for electrostatic analysis of complicated 3-D structures," *IEEE Trans. Computer-Aided Design of Integrated Circuits and Systems*, vol. 16, 1059-1072, 1997.
- [9] W. J. Yu, C. H. Yan, and Z. Y. Wang, "Fast multi-frequency extraction of 3-D impedance based on boundary element method," *Microw. Opt. Tech. Lett.*, vol. 50, no. 8, pp. 2191-2197, Aug. 2008.
- [10] S. M. Seo and J. F. Lee, "A fast IE-FFT algorithm for solving PEC scattering problems," *IEEE Trans. Magn.*, vol. 41, no. 5, pp. 1476-1479, May 2005.
- [11] J. Y. Xie, H. X. Zhou, W. B. Kong, J. Hu, Z. Song, W. D. Li, and W. Hong, "A novel FG-FFT method for the EFIE," in *Int. Conf. Comput. Problem-Solving (ICCP)*, 2012.
- [12] J. Y. Xie, H. X. Zhou, W. Hong, W. D. Li, and G. Hua, "A highly accurate FGG-FG-FFT for the combined field integral equation," *IEEE Trans. Antennas Propag.*, vol. 6, no. 9, pp. 4641-4652, Sep. 2013.
- [13] L. J. Jiang and W. C. Chew, "A mixed-form fast multipole algorithm," *IEEE Trans. Antennas Propag.*, vol. 53, no. 12, pp. 4145-4156, Dec. 2005.
- [14] C. J. Reddy, M. D. Deshpande, C. R. Cockrell, and F. B. Beck, "Fast RCS computation over a frequency band using method of moments in conjunction with asymptotic waveform evaluation technique," *IEEE Trans. Antennas Propag.*, vol. 46, no. 8, pp. 1229-1233, Aug. 1998.
- [15] R. Bao, A. Q. Wang, and Z. X. Huang, "Fast simulations of electromagnetic scattering from rough surface over a frequency band using asymptotic waveform evaluation technique: horizontal polarization," *J. Electromagn. Waves Appl.*, vol. 32, no. 11, pp. 1379-1388, 2018.
- [16] E. K. Miller, "Model-based parameter estimation in electromagnetics: Part I. Background and theoretical develop," *IEEE Antennas Propag. Mag.*, vol. 40, no. 1, pp. 42-52, Feb. 1998.
- [17] E. K. Miller, "Model-based parameter estimation in electromagnetics: Part II. Applications to EM observables," *IEEE Antennas Propag. Mag.*, vol. 40, no. 2, pp. 51-65, Apr. 1998.
- [18] E. K. Mille, "Model-based parameter estimation in electromagnetics: Part III. Applications to EM integral equations," *IEEE Antennas Propag. Mag.*, vol. 40, no. 3, pp. 49-66, June 1998.
- [19] V. V. S. Prakash, "RCS computation over a frequency band using the characteristic basis and model order reduction method," in *Proc. IEEE Antennas Propag. Soc. Int. Symp.*, vol. 4, pp. 89-92, 2003.
- [20] E. H. Newman, "Generation of wide-band data from the method of moments by interpolating the impedance matrix," *IEEE Trans. Antennas Propag.*, vol. 36, no. 12, pp. 1820-1824, Dec. 1988.
- [21] J. Yeo and R. Mittra, "An algorithm for interpolating the frequency variations of method-of-moments matrices arising in the analysis of planar microstrip structures," *IEEE Trans. Microw. Theory Tech.*, vol. 51, no. 3, pp. 1018-1025, Apr. 2003.
- [22] W. D. Li, H. X. Zhou, W. Hong, and T. Weiland, "An accurate interpolation scheme with derivative term for generating MoM matrices in frequency sweeps," *IEEE Trans. Antennas Propag.*, vol. 57, no. 8, pp. 2376-2385, June 2009.
- [23] W. D. Li, J. X. Miao, J. Hu, Z. Song, and H. X. Zhou, "An improved cubic polynomial method for interpolating/extrapolating MoM matrices over a frequency band," *Progress in Electromagnetics Research*, vol. 117, pp. 267-281, 2011.
- [24] Y. L. Xu, H. Yang, X. Liu, and R. J. Shen, "An interpolation scheme for Green's function and its application in method of moment," *Applied Computational Electromagnetics Society*, vol. 33,

- no. 7, July 2018.
- [25] Y. Wang, H. Ling, J. Song, and W. C. Chew, "A frequency extrapolation algorithm for FISC," *IEEE Trans. Antennas Propag.*, vol. 45, no. 12, pp. 1891-1893, Dec. 1997.
- [26] A. Karwowski, A. Noga, and T. Topa, "Computationally efficient technique for wide-band analysis of grid-like spatial shields for protection against LEMP effects," *Applied Computational Electromagnetics Society*, vol. 32, no. 1, pp. 87-92, Jan. 2017.
- [27] H. H. Zhang, Z. H. Fan, and R. S. Chen, "Fast wideband scattering analysis based on Taylor expansion and higher-order hierarchical vector basis functions," *IEEE Antennas Wireless Propag. Lett.*, vol. 14, pp. 579-582, 2015.
- [28] G. H. Wang and Y. F. Sun, "Broadband adaptive RCS computation through characteristic basis function method," *Journal of Electrical & Computer Engineering*, vol. 2014, pp. 1-5, 2014.
- [29] S. M. Rao, D. R. Wilton, and A. W. Glisson, "Electromagnetic scattering by surfaces of arbitrary shape," *IEEE Trans. Antennas Propag.*, vol. 30, no. 3, pp. 409-418, May 1982.
- [30] Y. Zhang, *Electromagnetic Field Parallel Computation*. XDUP, Xi An, 2006. (Chinese).
- [31] W. D. Li, W. Hong, and H. X. Zhou, "Integral equation-based overlapped domain decomposition method for the analysis of electromagnetic scattering of 3D conducting objects," *Microw. Opt. Tech. Lett.*, vol. 49, no. 2, pp. 265-274, Dec. 2007.

A Study on Upper Limit Frequency of Symmetric Extended TEM Cells

Chunjiang Song¹, Xinkai Fu², and Fei Dai^{2,*}

¹ Department of Engineering Physics
Tsinghua University, Beijing, 100084, China

² School of Electronic and Information Engineering
Beihang University, Beijing, 100191, China
*daphige@buaa.edu.cn

Abstract — TEM Cells is a commonly used electromagnetic field test device. The upper limit frequency of the TEM Cells is limited to the first resonant frequency. Through the electromagnetic numerical simulation, this paper analyzes the resonant frequency law of high-order modes and studies the resonant frequency characteristics and the upper limit of the frequency of symmetrically extended TEM Cells. Studies have shown that there is an error in the estimated value of the X_{mn} parameter used in the conventional standard TEM Cells resonant frequency calculation method, which may lead to errors in the order of the resonant modes. Symmetrically extended TEM Cells do not change the original resonant frequency, but because of the coupling modes of even mode and odd mode between two cell units, each of the original resonant frequencies will split two close resonant frequency.

Index Terms — Resonant frequency, resonant modes, TEM Cells, upper limit frequency.

I. INTRODUCTION

TEM Cells was originally proposed by Crawford in 1974 [1], which is a transverse electromagnetic (TEM) wave transmission structure like coaxial lines, mainly composed of an intermediate transmission section and a transition section.

The working frequency of the TEM Cells is limited to the first resonant frequency. Above this frequency, electromagnetic waves in the TE mode or TM mode will be generated in the TEM Cells, affecting the distribution of the electromagnetic field in the TEM mode, thereby affecting the test accuracy. Hill pointed out that the TE₀₁ mode is the first higher-order mode to propagate in the intermediate transmission section of TEM Cells, followed by TE₁₀ mode [2]. The calculation method for the cutoff frequency of TE₀₁ mode and TE₁₀ mode respectively proposed by Wilson and Ma [3] and Crawford and Workman [4] were recommended in IEEE STD 1309-2005 [5]. Chen found that Wilson's method

leads to erroneous conclusions in the calculation of higher-order modes. Then he gives a computer code to compute higher-order modes and a fitting curve for the first higher-order mode cutoff frequency of 50 Ω TEM Cells [6]. Chen's method was recommended by IEEE STD 1309-2013 [7] to replace the original method. To expand the bandwidth of TEM Cells, Deng et al. proposed some methods, such as slitting the outer wall, placing magnetic rings or ferrite components, and attaching absorbing materials [8,9].

In order to extend the test space, Wilson and Ma proposed asymmetric TEM Cells [3]. Malathi studied the extended characteristic impedance of asymmetric TEM Cells [10]. Virginie proposed a three-dimensional TEM cell [11]. Dai and Song et al. proposed TEM Cells with dual and quadruple symmetric extensions [12,13]. When expanding the space, the higher-order mode cutoff frequencies of TEM Cells are not expected to be reduced. This paper will further study the upper limit of the use frequency of symmetric extended TEM Cells.

II. THE LAW OF HIGH-ORDER MODE RESONANCE FREQUENCY OF TEM CELLS

In Fig. 1, the bottom walls/plates of two identical TEM Cells are bonded together first and removed then. By applying an ideal differential excitation to the input ports, a virtual electric wall can be formed at the overlapping walls. Therefore, it will not change the electromagnetic field distribution when removing the overlapping plates, thereby multiplying the test area.

Hill proposed two models with the same structure but different dimensions [2]. The basic TEM Cells used these two models to analyze the high-order mode resonant frequency. Figure 2 shows the Radial diagram of the TEM Cell model. The size of model I is $a=b=3\text{m}$, $g=0.26\text{m}$, $L_C=L_E=3.0\text{m}$; the size of the model II is $a=6.1\text{m}$, $b=7.32\text{m}$, $g=1.02\text{m}$, $L_C=6.1\text{m}$, $L_E=6.86\text{m}$. Hill, Wilson, and Chen calculated that the cut-off frequencies and resonant frequencies of the first few higher-order

modes of the two models are basically the same [2,3,6], as shown in Table 1 and Table 2. Hill gives the relationship between resonant frequency and cut-off frequency [2]:

$$f_{R(mnp)} = \sqrt{f_{c(mn)}^2 + \left(\frac{pc}{2L_{mn}}\right)^2}, \quad (1)$$

$$L_{mn} = L_c + X_{mn}L_E. \quad (2)$$

Where

c is the speed of light ($\approx 3 \times 10^8$ m/s),

m, n, p are mode numbers,

L_{mn} is the equivalent electrical length of the TEM Cells,

L_c is the length of the central section,

L_E is the sum of the lengths of the two tapered sections,

X_{mn} is a mode-dependent fraction.

Approximate values of $X_{01} = 0.77$ and $X_{10} = 0.47$ can be used [7].

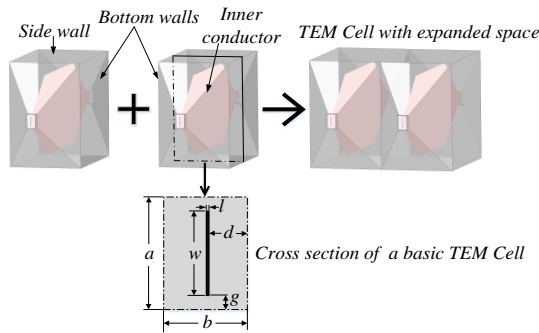


Fig. 1. Symmetrically extended TEM Cells.

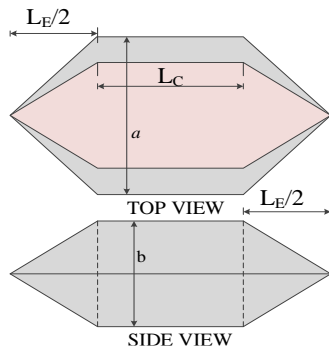


Fig. 2. Radial diagram of a basic TEM Cell.

Table 1: Cutoff frequencies and resonant frequencies of Model I ($a=b=3$ m, $g=0.26$ m, $L_c=L_E=3.0$ m)

Mode	$f_{C(m,n)}$ (MHz)	Mode	$f_{R(m,n,p)}$ (MHz)
TE01	29.0	TE011	40
TE10	50	TE101	60
TE01	29.0	TE012	63
TE11	63.5	TE111	73
TE10	50	TE102	84
TE01	29.0	TE013	89

Table 2: Cutoff frequencies and resonant frequencies of Model II ($a=6.1$ m, $b=7.32$ m, $g=1.02$ m, $L_c=6.1$ m, $L_E=6.86$ m)

Mode	$f_{C(m,n)}$ (MHz)	Mode	$f_{R(m,n,p)}$ (MHz)
TE01	15.2	TE011	20.7
TE10	24.6	TE101	30.01
TE01	15.2	TE012	31.51
TE11	31.3	TE111	36.08
TE10	24.6	TE102	40.98
TE01	15.2	TE013	42.06

Hill gives a description of the field distribution of higher-order modes in TEM Cells [2], as shown in Fig. 3.

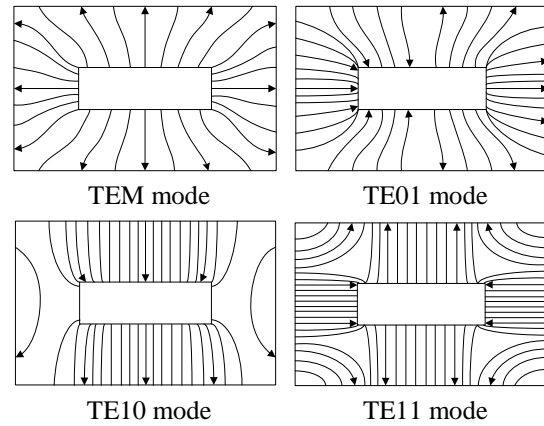


Fig. 3. The TEM mode and the first three high-order modes on cross section of a TEM Cell.

The quality factor is a quality indicator that represents the ratio of stored energy to lost energy. When the material is an ideal metal, its loss energy is zero, so the quality factor is infinite. To compare the difference between the real metal boundary and the ideal boundary, the simulations of the two cases were simulated respectively. Model I and Model II were analyzed in the eigenmode of HFSS where simulations were performed for both models. In the first case, walls and septum are set to PEC. In the other case, walls are set to aluminum and septum is set to copper. The simulation results are shown in Table 3.

Table 3 shows that the resonant frequency is not affected by the material, and the quality factor is dependent only on the structural geometry. Comparing Table 1, Table 2, and Table 3, the resonant frequencies in the grey part of Table 3 are the higher-order mode frequencies appearing in Tables 1 and 2. However, Table 3 has more higher-order modes than Tables 1 and 2. They are given in the 1st line, 3rd line, 6th line, and 10th line of Table 3 shown in white background. Figure 4 shows that the distributions of the E-field vectors on these four modes on cross section of Model I conform to the TEM mode shown in Fig. 3.

Table 3: Resonant frequencies and quality factors calculated by HFSS

No.	Model I			Model II			Mode
	PEC		Cu & AL	PEC		Cu & AL	
	f_R (MHz)	f_R (MHz)	Q	f_R (MHz)	f_R (MHz)	Q	
1	24.63	23.15	2253	11.59	11.10	5498	TEM
2	39.21	39.56	14993	20.53	20.71	43591	TE01
3	46.72	44.36	3210	22.06	21.28	7846	TEM
4	58.80	59.10	12285	30.01	30.01	164607	TE01
5	61.58	61.57	108379	30.37	30.68	34829	TE10
6	68.66	66.10	4497	32.58	31.61	10974	TEM
7	73.47	73.91	63825	36.01	36.10	121977	TE11
8	79.61	80.13	13688	40.12	40.48	37769	TE01
9	85.24	85.24	135189	40.86	40.85	205474	TE10
10	92.36	89.43	5506	43.98	42.81	13516	TEM

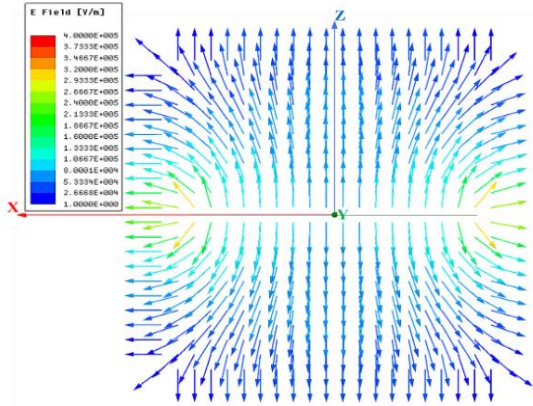


Fig. 4. TEM mode field distribution in Model I.

In the eigenmode of HFSS, to enhance the internal resonance effect of TEM Cells, the input and output ports of the TEM Cells are set as total reflection ports instead of the actual matching impedance. Therefore, the simulation results show that the resonant mode is the TEM mode, like a dedicated coaxial resonant cavity, which will not occur in actual use. The quality factor of this virtual resonant mode is also significantly lower than other real resonant modes. Therefore, these situations are excluded when analyzing high-order modes. The 2nd, 4th, 5th, 7th, 8th, and 9th resonant modes in Table 3 respectively correspond to the TE011, TE012, TE101, TE111, TE013, and TE102 modes. According to the cross section, the m, n of the resonance mode can be known, and the k of the resonance mode can be known from the longitudinal section. For example, Fig. 5 shows the electric field distribution of the 8th mode. It is known by the cross section that it is the TE01 mode. According to the longitudinal section, it has three standing waves, so it is the TE013 mode.

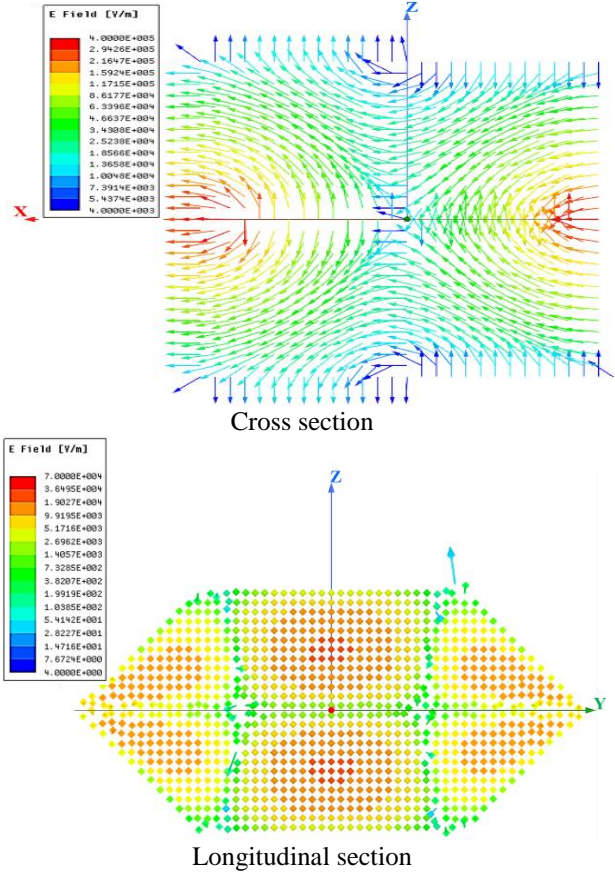


Fig. 5. The 8th resonant mode field distribution in Model I.

The order of the first six higher-order modes obtained by HFSS simulation are inconsistent with Hill and Chen's calculations. The order given by them is TE011, TE101, TE012, TE111, TE102 and TE013 modes. Possibly, X_{mn} estimated value given in Equation 2 may lead to the problem. Hill believes that the same cutoff mode has the same X_{mn} . However, a more reasonable speculation is that there is an inverse relationship between the wavelength and X_{mn} , and the opening angle of the tapered section is proportional to X_{mn} . Table 4 is the X_{mn} values calculated from the HFSS simulation results.

Table 4: X_{mn} calculated by HFSS

p	Model I		Model II	
	X_{01}	X_{10}	X_{01}	X_{10}
1	0.86	0.39	0.66	0.38
2	0.94	0.45	0.8	0.45
3	1	0.88	0.86	0.63

The estimated value of X_{mn} is calculated by Hill based on the frequency of the first high-order mode, so

this error has no effect on the first high-order mode, but only affects the order in which the higher-order modes appear. Because the operating frequency of the TEM Cells is limited to the first resonant frequency, the error caused by it does not affect the upper limit frequency of the TEM Cells.

III. UPPER LIMIT FREQUENCY OF THE SYMMETRICALLY EXTENDED TEM CELLS

When the basic TEM Cells are symmetrically expanded into dual cells and quadruple cells, the test space will be multiplied, and the resonant frequency may be reduced. The Model I and Model II were extended to dual TEM Cells in HFSS, and the resonant frequency is shown in Table 5.

Table 5: Resonant frequencies and quality factors of dual TEM Cells calculated by HFSS

No.	Model I		Model II		Mode
	Cu & AL		Cu & AL		
	f_R (MHz)	Q	f_R (MHz)	Q	
1	23.14	2241.38	11.02	4182.52	TEM/ Even mode
2	23.36	2245.40	11.09	4179.41	TEM/ Odd mode
3	36.10	13948.24	18.72	40885.57	TE01/ Odd mode
4	39.55	15078.79	20.75	43753.47	TE01/ Even mode
5	43.48	3180.38	20.79	5953.72	TEM/ Odd mode
6	44.36	3202.32	21.14	5910.43	TEM/ Even mode
7	58.60	12257.61	30.01	185562.56	TE01/ Odd mode
8	59.10	12265.43	30.48	34103.58	TE01/ Even mode
9	61.57	126363.77	30.49	12448.22	TE10/ Even mode
10	63.37	7052.79	30.73	34104.86	TE10/ Odd mode

Comparing Table 3, Table 5 shows that two resonant frequencies occur near each resonant frequency of the basic TEM Cells. Taking the 3rd and 4th modes of Table 5 as an example, observe the E field vectors on cross section (Fig. 6). The distribution of electric field vectors on cross section of the 3rd mode can be regarded as two TE01 mode fields of the same amplitude and directions, which is equivalent to an even mode (or common mode); The distribution of electric field vectors on cross section of the 4th mode can be regarded as two TE01 mode fields of the same amplitude and opposite directions. The merging of the distribution is equivalent to an odd mode (or differential mode).

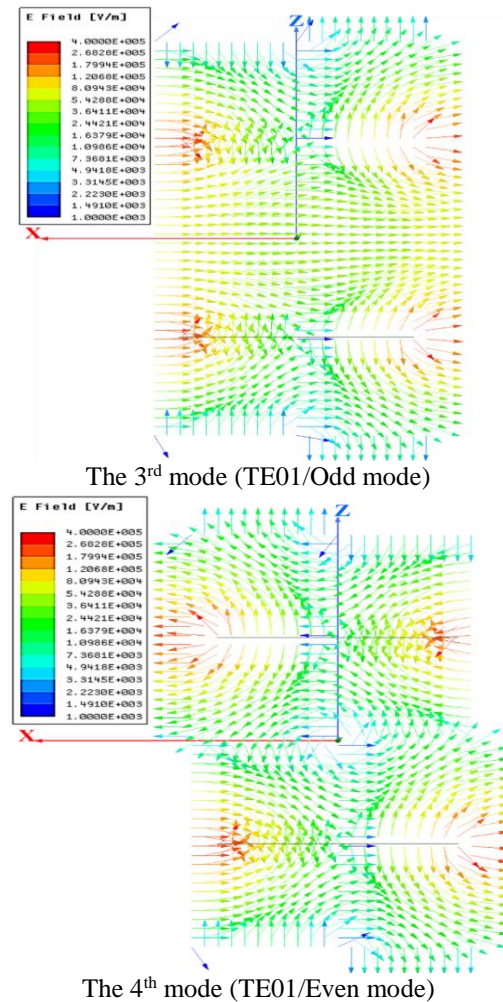


Fig. 6. The distributions of E field vectors on cross section.

Comparing Fig. 7 and Fig. 5, the distributions of E field vectors on longitudinal section of these two modes shows that there is only one standing wave, indicating that they are both TE011 modes.

Compared with the basic TEM Cells and dual TEM Cells, the boundary conditions of the first higher-order modes do not change, so the resonant frequency do not change too. However, the original resonant mode is split into an even mode (or differential mode) and an odd mode (or common mode).

The cutoff frequency of the first higher-order mode $f_{C(m,n)}$ is determined from the cross section of the TEM ell [7]. The dominant mode for a rectangular TEM cell is either the TE01 mode or the TE10 mode; therefore, the first resonant frequency is either $f_{R(011)}$ or $f_{R(101)}$. In dual TEM Cells, the common mode excitation enhances the E-field of the TE01 mode, and the differential mode excitation enhances the E-field of the TE10 mode. Then the interference of the E-field is increased. To avoid the

influence of this interference on the field distribution, the use frequency of dual TEM Cells still should be strictly limited to the resonant frequency of the TE₀₁₁ or TE₁₀₁ mode. The calculation method can continue to use the method for the standard TEM Cells high frequency resonant frequency recommended in IEEE STD 1309-2013.

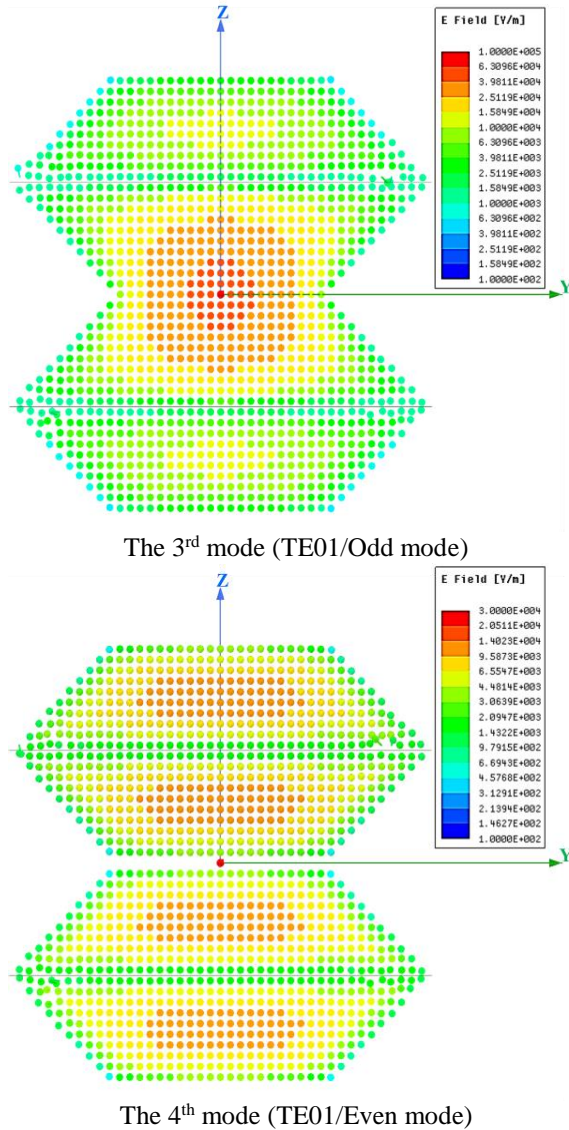


Fig. 7. The distributions of E field vectors on longitudinal section.

IV. CONCLUSION

By comparing and analyzing the resonant frequency data of the high-order mode, it is found that the resonant frequency is not affected by the material, and the quality factor is related to the characteristics of the metal material. However, the order of the resonant modes calculated by TEM Cells will have some errors with the

actual results. This paper believes that there is an error in the estimated value of the X_{mn} parameter used in the traditional standard TEM Cells resonant frequency calculation method, which is the cause of this error. The relationship between the X_{mn} parameter and the TEM cell opening angle will be further studied in the future, and the previous estimation value can be replaced with a more accurate X_{mn} parameter, so that the calculation of the resonance frequency will be more accurate.

Based on the high-order mode resonant frequency law of standard TEM Cells, the resonant frequency characteristics and upper frequency limit of symmetric extended TEM Cells are studied. Compared with the basic TEM Cells and dual TEM Cells, the boundary conditions of the first higher order modes do not change, so the resonant frequency remains unchanged. However, due to the two coupling modes of even mode and odd mode between the two cell units, each of the original resonant frequencies will split two close resonant frequencies, which is to further study the two modes of even mode and odd mode. The law of variation of the coupling mode provides the basis.

For symmetrically extended TEM Cells, the two resonant frequencies split by each resonant frequency are very close to each other. Therefore, the frequency of use of dual TEM Cells should be strictly limited to the resonant frequency of the first higher-order mode. The calculation method can continue to adopt the standard TEM Cells high frequency resonant frequency calculation method recommended in IEEE STD 1309-2013.

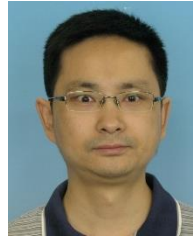
ACKNOWLEDGMENT

This work is supported in part by the National Natural Science Foundation of China. (Grant No. 61571027, 61427803), and supported by the 2011 Collaborative Innovation Center.

REFERENCES

- [1] M. L. Crawford, "Generation of standard EM fields using TEM transmission cells," *IEEE Transactions on Electromagnetic Compatibility*, vol. EMC-16, no. 3, pp. 189-195, Nov. 1974.
- [2] D. A. Hill, "Bandwidth limitation of TEM cells due to resonances," *Journal of Microwave Power*, vol. 18, no. 2, pp. 181-195, 1983.
- [3] P. Wilson and M. Ma, "Simple approximate expressions for higher-order mode cutoff and resonant frequencies in TEM cells," *IEEE Transactions on Electromagnetic Compatibility*, vol. 28, no. 3, pp. 125-130, Aug. 1986.
- [4] M. L. Crawford, J. L. Workman, and C. L. Thomas, "Expanding the bandwidth of TEM cells for EMC measurements," *IEEE Transactions on Electromagnetic Compatibility*, vol. EMC-20, no. 3, pp. 368-375, Aug. 1978.
- [5] IEEE. STD 1309-2005, IEEE Standard for

- Calibration of Electromagnetic Field Sensors and Probes, Excluding Antennas, From 9 kHz to 40 GHz, 2005.
- [6] Z. Chen, "Examinations of higher-order mode cutoff frequencies in symmetrical TEM cells," *IEEE International Symposium on Electromagnetic Compatibility*, Austin, TX, pp. 6-11, Aug. 2009.
- [7] IEEE. STD 1309-2013, IEEE Standard for Calibration of Electromagnetic Field Sensors and Probes, Excluding Antennas, From 9 kHz to 40 GHz, 2013.
- [8] S. W. Deng, D. Pommerenke, T. Hubing, et al., "Mode suppressed TEM cell design for high frequency IC measurements," *IEEE International Symposium on Electromagnetic Compatibility*, 1-6, 2007.
- [9] S. W. Deng, D. Pommerenke, T. Hubing, et al., "An experimental investigation of higher-order mode suppression in TEM cells," *IEEE Transactions on Electromagnetic Compatibility*, vol. 50, pp. 416-419, 2008.
- [10] K. Malathi and D. Annapurna, "Numerical analysis of impedance of asymmetric TEM cell filled with inhomogeneous, isotropic dielectric," *Applied Computational Electromagnetics Society Journal*, vol. 19, pp. 39-45, 2004.
- [11] D. Virginie, "Optimization of three-dimensional TEM cell for electromagnetic compatibility testing," *20th Annual Review of Progress in Applied Computational Electromagnetics*, 2004.
- [12] F. Dai, M. Wang, and D. L. Su, "A design of new twin TEM cells," *IEEE 2005 International Symposium on Microwave, Antenna, Propagation and EMC Technologies for Wireless Communications Proceedings*, vol. 1, pp. 10-13, 2005.
- [13] C. J. Song and X. Y. Feng, "A new design and implementation of expanding testing space of a transverse electromagnetic cell," *The 9th International Conference on Microwave and Millimeter Wave Technology*, vol. 2, pp. 967-969, 2016.



technology.

Chunjiang Song joined the Department of Engineering Physics in Tsinghua University, Beijing, China, in 2012 and he is currently working toward the Ph.D. degree. His research interests include the microwave technology, electronic measurement technology, and EMC



well as Multiphysics simulation.

Xinkai Fu receive the B.Eng. degree in Electronic Engineering from Beihang University, Beijing, China, in 2016, and he is currently working towards the M.S. degree in the same university. His research interests include the microwave technology, EMC technology, as



include the EMC technology, microwave technology, and antennas technology.

Fei Dai receive the Ph.D. degree in Circuits and Systems from Beihang University, Beijing, China, in 2007. He joined the Electromagnetic Compatibility Laboratory at Beihang University, Beijing, in 2007, where he is currently an Associate

Professor. His research interests

On the Correction of the Probe Positioning Errors in a Non-Redundant Bi-Polar Near to Far-Field Transformation

F. D'Agostino, F. Ferrara, C. Gennarelli, R. Guerriero, and M. Migliozi

Department of Industrial Engineering
University of Salerno, via Giovanni Paolo II, 132 - 84084 Fisciano, Italy
fdagostino@unisa.it, flferrara@unisa.it, cgennarelli@unisa.it, rguerriero@unisa.it, mmigliozi@unisa.it

Abstract — An effective procedure allowing one to correct the positioning errors in a bi-polar near to far-field transformation (NTFFT) technique, that requires a minimum number of near-field (NF) data, has been here assessed from the experimental viewpoint. This NTFFT utilizes an optimal sampling interpolation formula, got by considering the antenna under test as contained in an oblate spheroid and applying the non-redundant sampling representation to the probe measured voltage, to precisely determine the NF data needed by the standard NTFFT with plane-rectangular scan from the voltages at the points prescribed by the sampling representation. These voltages are not known and are accurately recovered from the positioning errors affected measured ones by applying an efficient singular value decomposition based technique.

Index Terms — Antenna measurements, bi-polar near to far-field transformation, non-redundant sampling representations, positioning errors correction.

I. INTRODUCTION

As well-known, the far-field (FF) distance requirements cannot be satisfied in an anechoic chamber when the dimensions of the antenna under test (AUT) are large with respect to the wavelength. In this case, only near-field (NF) measurements can be performed and, accordingly, the AUT radiated far field must be reconstructed by applying near to far-field transformation (NTFFT) techniques [1-4]. These techniques generally exploit an expansion of the AUT near field in plane, cylindrical, or spherical waves, whose expansion coefficients are determined from the complex voltages acquired by the probe and rotated probe on a proper lattice of the scanning surface, that will be a plane, a cylinder, or a sphere, respectively. Then, the AUT far field is reconstructed by substituting the so determined coefficients in the corresponding wave expansion valid in the FF region. When the AUT radiates a pencil beam pattern, a NTFFT technique using a planar scan, such as the plane-rectangular (PR) [5, 6], the plane-polar (PP) [7-10], or the bi-polar (BP) scan [11-15], is usually adopted.

The PR NTFFT is surely the most simple of them from the analytical and computational points of view. The PP NTFFT has several advantages compared to the PR one, such as a larger scanning zone for a fixed size of the anechoic chamber, a mechanically simpler scanning system, and etc. [7]. Even more convenient is that adopting the BP scanning. In fact, this scanning retains the benefits of the PP one, but makes use only of rotational motions and, as well-known, turntables provide a greater accuracy with respect to linear positioners. Moreover in the horizontal mounting, it makes easier to preserve the planarity, since the probe is attached to one of the extremities of the arm, whose other end is anchored to the rotator, so that the bending of the arm does not change throughout the acquisition. It is worth noting that the NF data necessary to reconstruct the antenna far field using the standard PR NTFFT were accurately recovered from the collected BP ones in [11, 12] by employing optimal sampling interpolation (OSI) expansions. However, such an approach did not exploit the non-redundant sampling representations of electromagnetic (EM) fields [16, 17] so that an unnecessarily large number of NF data was required. Conversely, by assuming the antenna as contained in an oblate spheroid or in a double bowl (a surface made by two bowls having the same aperture), these representations have been applied in [13-15] to the voltage detected by the scanning probe, thus making available 2-D OSI formulas, which allow one to accurately recover the needed PR NF data from a minimum number of the BP ones.

Unfortunately, as a consequence of a not precise control of the positioners as well as of their finite resolution power, it could not be possible to collect the NF data at the points established by the non-redundant sampling representation. Anyhow, the actual locations of the collected NF data can be accurately determined by means of laser interferometric techniques. For this reason, the availability of an effective and robust technique, enabling the accurate retrieval of the NF data necessary to execute the traditional PR NTFFT from the inaccurately positioned (non-uniform) BP ones, results

to be of primary importance. A procedure based on the conjugate gradient iteration technique and exploiting the fast Fourier transform for non-equispaced data [18] has been adopted for correcting known errors of probe positioning in the classical NTFFTs with planar [19] and spherical [20] scans. Such a procedure is, in any case, not tailored to the non-redundant BP NTFFTs [13-15]. As stressed in [21], wherein a more comprehensive analysis on the non-uniform sampling is reported, the direct recovery of the NF data required to carry out the NTFFT from the not evenly distributed ones is not opportune. A suitable and viable strategy [21] is to first retrieve the evenly distributed (uniform) samples from the non-uniform ones and afterward evaluate the necessary NF data via a precise and robust OSI expansion. Two diverse approaches have been developed for achieving such a purpose. The former makes use of an iterative technique, which turns out to be convergent only if a biunique relation linking each uniform sampling point to the nearest non-uniform one exists, and has been exploited to retrieve the uniform samples in a PR grid [21]. The latter, that does not suffer from the above shortcoming, employs the singular value decomposition (SVD) method and has been adopted to retrieve the uniform samples from the inaccurately positioned ones in the non-redundant NTFFTs with PP [22], cylindrical [23], and BP [24] scannings. Anyhow, to usefully apply this last procedure, it is necessary that the uniform samples recovery can be split into two separate 1-D problems, otherwise a remarkable computational effort is required owing to the large dimensions of the involved matrix. These procedures have been compared via simulations and experimentally validated with reference to a spherical NTFFT using a minimum number of NF data [25], while their experimental assessment in the NTFFTs with the cylindrical and the PP scannings has been provided in [26] and [27, 28], respectively.

Goal of the paper is to give the experimental validation of the SVD based approach [24], which allows one to correct known probe-positioning errors in the non-redundant BP NTFFT adopting an oblate spheroidal surface to model a quasi-planar AUT (see Fig. 1).

II. NON-REDUNDANT VOLTAGE REPRESENTATION ON A PLANE FROM NON-UNIFORM BP SAMPLES

A. Uniform samples representation

An efficient representation of the voltage, measured on a plane d away from the AUT by a probe with a non-directive pattern, using a non-redundant number of its BP samples is summarized in this subsection. In the following, a generic observation point is specified by the spherical coordinates (r, ϑ, φ) , while a point P belonging to the plane can be also identified by the BP ones (α, δ) , where δ is the rotation angle of the BP arm and α that of

the AUT (Fig. 1). As it can be easily shown, the following relations link the polar coordinates (ρ, φ) to the BP ones:

$$\rho = 2L \sin(\delta/2); \quad \varphi = \alpha - \delta/2, \quad (1)$$

where L is the arm length. As shown in [29], the voltage acquired by a non-directive probe is characterized by practically the same spatial bandwidth of the AUT EM field and, hence, the non-redundant sampling representations of EM fields [16] can be conveniently applied to it. Accordingly, the AUT must be modeled by a rotational surface Σ , which bounds a convex domain containing it and fits well its shape, the scanning plane must be represented by means of rings and diameters (as in the PP case), an optimal parameterization η has to be employed to describe each of these curves, and an appropriate phase factor $e^{-j\psi(\eta)}$ must be extracted from the acquired voltage. The so introduced “reduced voltage”:

$$\tilde{V}(\eta) = V(\eta) e^{j\psi(\eta)}, \quad (2)$$

wherein V denotes the voltage V_α or V_δ collected by the probe or by the rotated probe, is spatially almost bandlimited to W_η [16]. The error made when approximating it by a function bandlimited to $\chi' W_\eta$ results to be negligible when an appropriate excess bandwidth factor $\chi' > 1$ is chosen [16]. Since the antennas characterized in a BP NF facility typically have a quasi-planar geometry, an oblate spheroid (with semi-minor and semi-major axes equal to b and a) can be suitably adopted as modeling surface Σ . In this case, the bandwidth W_η , the parameter η , and the function ψ relevant to a diameter are [13, 14]:

$$W_\eta = \frac{2\beta a}{\pi} E\left(\frac{\pi}{2} \mid \varepsilon^2\right); \quad \eta = \frac{\pi E(\sin^{-1}u \mid \varepsilon^2)}{2E(\pi/2 \mid \varepsilon^2)}, \quad (3)$$

$$\psi = \beta a \left[v \sqrt{\frac{v^2-1}{v^2-\varepsilon^2}} - E\left(\cos^{-1} \sqrt{\frac{1-\varepsilon^2}{v^2-\varepsilon^2}} \mid \varepsilon^2\right) \right], \quad (4)$$

wherein β is the free-space wavenumber, $E(\cdot \mid \bullet)$ the second kind elliptic integral, $\varepsilon = f/a$ the eccentricity of the spheroid, $2f$ its focal distance, and $u = (r_1 - r_2)/2f$, $v = (r_1 + r_2)/2a$ the elliptic coordinates, $r_{1,2}$ being the distances between the observation point P and the foci.

When the considered curve is a ring, the angle φ can be properly adopted as optimal parameter, the phase function ψ is constant, and the bandwidth W_φ is [13, 14]:

$$W_\varphi(\eta) = \beta a \sin \vartheta_\infty(\eta), \quad (5)$$

$\vartheta_\infty = \sin^{-1}u$ being the angle between the asymptote to the hyperbola through the point P and the z -axis.

The following OSI expansion,

$$V(\eta(\rho), \varphi) = e^{-j\psi(\eta)} \sum_{n=n_0-q+1}^{n_0+q} \tilde{V}(\eta_n, \varphi) S(\eta, \eta_n, \bar{\eta}, N, N''), \quad (6)$$

allows the fast and accurate evaluation of the voltage V

at any point $P(\rho, \varphi)$ on the plane. In (6), $n_0 = n_0(\eta) = \lfloor \eta/\Delta\eta \rfloor$, $2q$ is the number of the retained nearest intermediate samples $\tilde{V}(\eta_n, \varphi)$, namely, the reduced voltages at the intersections of the sampling rings with the diameter through P :

$$\eta_n = n\Delta\eta = 2\pi n/(2N''+1), \quad (7)$$

$$N'' = \lfloor \chi N' \rfloor + 1; \quad N' = \lfloor \chi' W_\eta \rfloor + 1, \quad (8)$$

$\lfloor x \rfloor$ stays for the greatest integer less than or equal to x , and χ is an oversampling factor necessary for the control of the truncation error [16]. Moreover,

$$S(\eta, \eta_n, \bar{\eta}, N, N'') = \Omega_N(\eta - \eta_n, \bar{\eta}) D_{N''}(\eta - \eta_n), \quad (9)$$

is the interpolation function of the OSI expansion, with

$$\Omega_N(\eta, \bar{\eta}) = \frac{T_N[2\cos^2(\eta/2)/\cos^2(\bar{\eta}/2) - 1]}{T_N[2/\cos^2(\bar{\eta}/2) - 1]}, \quad (10)$$

and

$$D_{N''}(\eta) = \frac{\sin[(2N''+1)\eta/2]}{(2N''+1)\sin(\eta/2)}, \quad (11)$$

being the Tschebyscheff and Dirichlet sampling functions [16]. In (10), $T_N(\eta)$ is the Tschebyscheff polynomial of degree $N = N'' - N'$ and $\bar{\eta} = q\Delta\eta$.

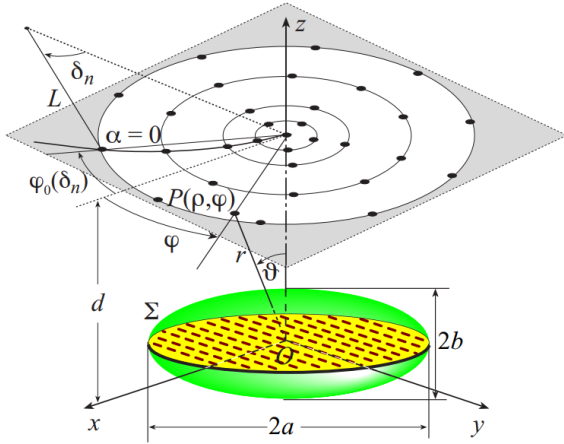


Fig. 1. BP scanning for a quasi-planar AUT.

A quite similar OSI expansion along the rings allows the effective evaluation of the intermediate samples. As shown in [13, 14], it results:

$$\tilde{V}(\eta_n, \varphi) = \sum_{m=m_0-p+1}^{m_0+p} \tilde{V}(\eta_n, \varphi_{m,n}) S(\varphi, \varphi_{m,n}, \bar{\varphi}_n, M_n, M_n'') \quad (12)$$

where $m_0 = m_0(\varphi) = \lfloor (\varphi - \varphi_0(\eta_n))/\Delta\varphi_n \rfloor$, $2p$ is the retained samples number, and,

$$\varphi_{m,n} = \varphi_0(\eta_n) + m\Delta\varphi_n = -\delta_n/2 + 2\pi m/(2M_n''+1), \quad (13)$$

$$M_n'' = \lfloor \chi M_n' \rfloor + 1; \quad M_n' = \lfloor \chi^* W_\varphi(\eta_n) \rfloor + 1; \quad \bar{\varphi}_n = p\Delta\varphi_n, \quad (14)$$

$$\chi^* = 1 + (\chi' - 1)[\sin \varphi_\infty(\eta_n)]^{-2/3}; \quad M_n = M_n'' - M_n'. \quad (15)$$

It must be noticed that the shift $\varphi_0(\eta_n)$ is a

consequence of the different way of the NF data acquisition with respect to that adopted in the PP scanning (Fig. 1).

By properly matching the 1-D OSI expansions (6) and (12), the 2-D OSI one is easily attained. This last allows the accurate reconstruction of the voltages V_α and V_δ at the points needed for the classical PR NTFIT [5, 6] falling in the measurement circle. It is worthy to stress that the probe-compensation formulas in [6] (which in the employed reference system take the form reported in [9, 30]) require that the probe axes are kept parallel to the AUT ones during the scanning, so that the probe must properly co-rotate with it. In any case, such a co-rotation can be avoided by performing a “software co-rotation” when a probe whose far field exhibits a first-order φ -dependence is utilized. If this is the case, it is possible to determine the voltages V_y and V_x , which would be collected when co-rotating the probe and rotated probe, from the knowledge of V_α and V_δ via the relations:

$$V_y = V_\alpha \cos(\varphi - \delta/2) - V_\delta \sin(\varphi - \delta/2), \quad (16)$$

$$V_x = V_\alpha \sin(\varphi - \delta/2) + V_\delta \cos(\varphi - \delta/2). \quad (17)$$

To this end, an open-ended rectangular waveguide can be conveniently employed as scanning probe. In fact, when the fundamental mode TE_{10} is propagating, the corresponding far field radiated in the forward hemisphere has practically such a φ -dependence [31].

B. Uniform samples retrieval

Let us assume that all samples, different from the one at the pole $\rho=0$, are not evenly distributed on rings, which in turn are irregularly spaced on the plane. This is a reasonable assumption when the BP NF data are collected along the rings by exploiting the AUT rotation and the acquisition ring is changed by rotating the arm. This way of operation is mandatory to profit from the reduction in the number of the required samples on the central rings, when applying the described non-redundant representation. In this hypothesis, the 2-D uniform samples retrieval problem is reduced to the solution of two independent 1-D ones, so that the SVD based technique can be conveniently adopted. The former problem concerns the retrieval of the uniform $2M_k''+1$ reduced voltages samples $\tilde{V}(\xi_k, \varphi_{m,k})$ on any non-uniform ring at $\rho(\xi_k)$ from the knowledge of the $J_k \geq 2M_k''+1$ non-uniform ones $\tilde{V}(\xi_k, \phi_j)$. By applying (12), the non-uniform samples $\tilde{V}(\xi_k, \phi_j)$ are expressed as a function of the unknown uniform ones $\tilde{V}(\xi_k, \varphi_{m,k})$, thus attaining the linear system:

$$\underline{B} \underline{X} = \underline{C}, \quad (18)$$

wherein \underline{C} is the vector of the known non-uniform samples, \underline{X} is that of the unknown uniform ones, and \underline{B} is a matrix of dimensions $J_k \times (2M_k''+1)$, whose elements are:

$$b_{jm} = S(\phi_j, \varphi_{m,k}, \bar{\varphi}_k, M_k, M_k''), \quad (19)$$

with $\varphi_{m,k} = m\Delta\varphi_k = 2m\pi/(2M_k'' + 1)$ and $\bar{\varphi}_k = p\Delta\varphi_k$. Since only the samples nearest to the output point are retained in the OSI expansion, the elements b_{jm} of the matrix $\underline{\underline{B}}$ are zero, when the index m is outside the range $[m_0(\phi_j) - p + 1, m_0(\phi_j) + p]$. The best least square approximated solution of (18) is then obtained by applying the SVD method. The latter problem deals with the recovery of the uniform intermediate samples $\tilde{V}(\eta_m, \varphi)$, required by the OSI expansion (6) to evaluate the voltage at $P(\rho, \varphi)$, from the non-uniform ones $\tilde{V}(\xi_k, \varphi)$, obtained using the OSI expansion (12) in correspondence of the intersections between the non-uniform rings and the diameter through P . The non-uniform samples are then expressed using (6) in terms of the unknown uniform ones, thus getting a linear system, which is again solved via the SVD method. To avoid the ill-conditioning of the above linear systems, it has been supposed that both the distances from the non-uniform rings to the corresponding uniform ones and those between the non-uniform sampling points and the associated uniform ones on them are less than one half of the related uniform spacings. Moreover, to reduce the computational effort, the same number N_φ of uniform PP samples, coincident with that needed for the outer uniform ring, have been retrieved on any non-uniform ring. In this way, the number of systems to be solved is minimized being the samples aligned along the diameters.

The so retrieved PP uniform samples are then interpolated via the OSI expansions (6) and (12) (this last suitably adapted to take into account the lack of the shift φ_0 and the redundancy of the samples on the rings) to efficiently recover the voltages V_α and V_δ at the points necessary for the PR NTFFT [5, 6].

III. EXPERIMENTAL TESTING

The experimental validation of the described approach for correcting known positioning errors, which affect the BP NF data, has been carried out through the PP NF measurement facility existing in the anechoic chamber of the Antenna Characterization Laboratory of the University of Salerno. In this facility, the probe is mounted on a vertical linear positioner and the AUT on a turntable having its axis of rotation perpendicular to the vertical positioner. The measurement of the BP NF data is made possible due to the presence of another turntable, located between the probe and the positioner. A vector network analyzer is utilized to measure the complex voltage acquired by the employed probe, an open-ended WR-90 rectangular waveguide. The AUT considered in the following experimental results is a X-band flat-plate slotted array (AUT1), manufactured by Rantec Microwave Systems Inc., having a roughly circular shape with a radius of about 23 cm and working at 9.3 GHz. It is placed on the plane $z = 0$ and is modeled by an oblate spheroid with $b = 8.1$ cm and $a = 23.2$ cm. The uniform

and the non-uniform NF BP samples considered in these results have been acquired on a circle with radius 110 cm on a plane, whose distance from the AUT is 16 cm. In particular, the positions of the uniform sampling points are those required by the previously described non-redundant sampling representation when the BP arm length L is 120 cm and $\chi' = \chi = 1.25$. These chosen values of χ' and χ ensure low aliasing and reconstruction errors. As regards the acquired non-uniform samples, they have been deliberately not regularly spaced along non-uniform rings in such a way that the shifts from the positions of the non-uniform to related uniform rings and those from the non-uniform to associated uniform sampling points are random variables uniformly distributed in $(-\Delta\eta/2, \Delta\eta/2)$ and $(-\Delta\varphi_k/2, \Delta\varphi_k/2)$, respectively, thus avoiding the ill-conditioning of the linear systems involved in the uniform samples retrieval.

The amplitude and phase of the voltage V_α along the diameter at $\varphi = 0^\circ$, recovered through the SVD procedure from the positioning error affected BP samples, are compared in Figs. 2 and 3 with those directly measured (references), whereas the comparison of the retrieved amplitude and phase of V_δ along the diameter at $\varphi = 90^\circ$ with the directly measured ones are shown in Figs. 4 and 5. A further NF reconstruction example relevant to the comparison of retrieved and measured amplitudes of V_α and V_δ along the diameter at $\varphi = 30^\circ$ is reported in Fig. 6. In other words, the solid line patterns refer to the voltage acquired at close spacing on the considered diametral lines, whereas those shown with crosses are relevant to the patterns obtained by interpolating, via the 2-D OSI expansion, the uniform NF samples reconstructed from the positioning errors affected ones through the SVD based approach. As can be noticed, notwithstanding the considerable values of the positioning errors, all the recoveries are very precise save for the zones where the voltage levels are very low. It is worthy to note the smoother behavior of the recovered voltages amplitudes, due to the OSI functions features to filter out the noise sources harmonics greater than the AUT spatial bandwidth. The effectiveness of proposed procedure to correct the positioning errors is further validated by comparing the FF patterns in the principal planes E and H (Figs. 7 and 8) recovered from the non-uniform BP NF data with those obtained from the non-redundant uniform BP NF samples (references). The reconstructed FF patterns attained from the non-uniform BP NF data without applying the positioning errors correction technique are shown, for sake of comparison, in Figs. 9 and 10. As can be clearly seen, they appear severely deteriorated thus confirming the efficacy of the approach. Such an efficacy is even more evident from the comparison between the very low errors in the reconstructed amplitudes reported in Figs. 7 and 8 and the significantly greater ones in Figs. 9 and 10. These errors have been evaluated as differences between the

reconstructed and reference amplitudes, normalized to the maximum of the reference patterns and expressed in dB. Other laboratory results, which validate the

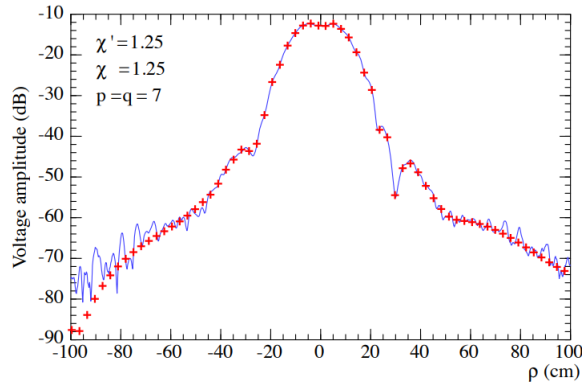


Fig. 2. V_α amplitude along the diameter at $\varphi = 0^\circ$. Line: reference. Crosses: retrieved from the non-uniform BP NF samples.

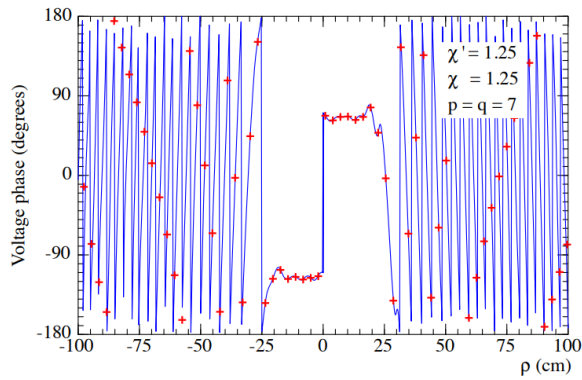


Fig. 3. V_α phase along the diameter at $\varphi = 0^\circ$. Line: reference. Crosses: retrieved from the non-uniform BP NF samples.

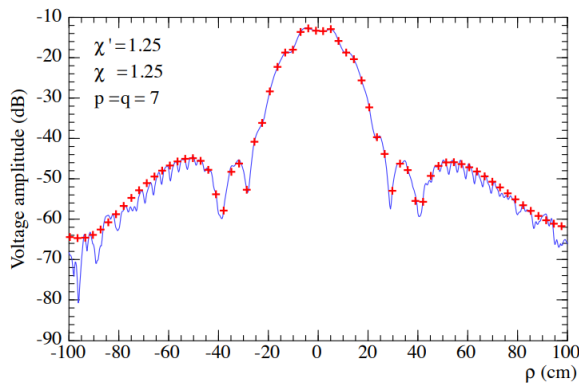


Fig. 4. V_δ amplitude along the diameter at $\varphi = 90^\circ$. Line: reference. Crosses: retrieved from the non-uniform BP NF samples.

effectiveness of the developed technique and relevant to a different antenna, are reported in [32].

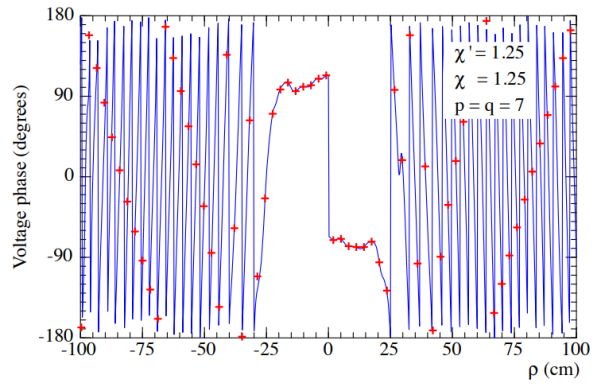


Fig. 5. V_δ phase along the diameter at $\varphi = 90^\circ$. Line: reference. Crosses: retrieved from the non-uniform BP NF samples.

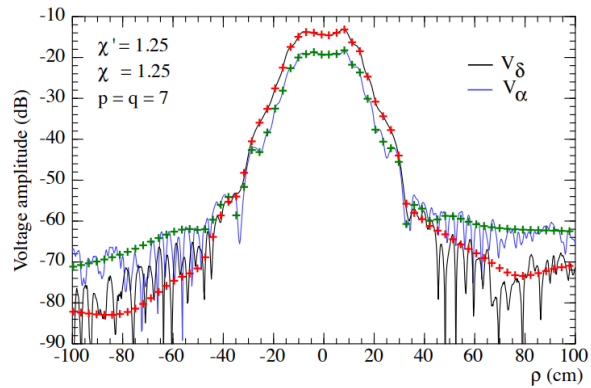


Fig. 6. V_α and V_δ amplitudes along the diameter at $\varphi = 30^\circ$. Lines: reference. Crosses: retrieved from the non-uniform BP NF samples.

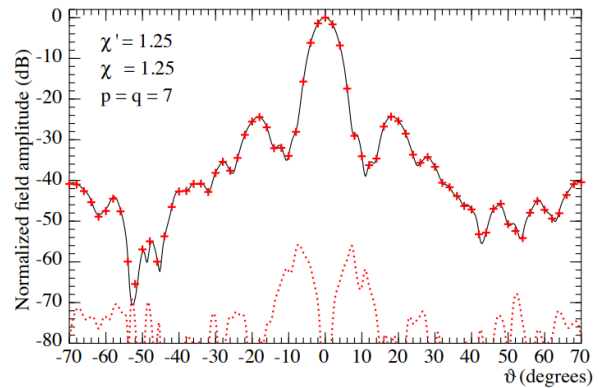


Fig. 7. E-plane pattern. Line: reference. Crosses: obtained from the non-uniform BP NF samples via the SVD procedure. Dashes: reconstruction error.

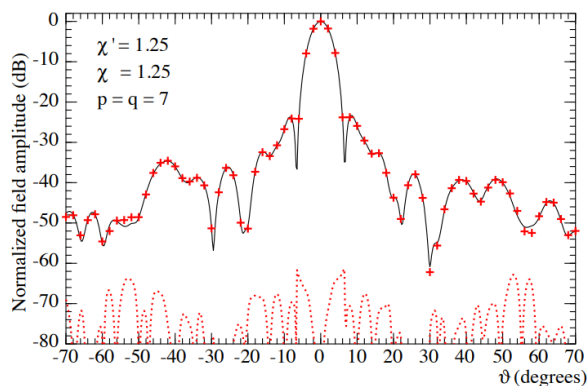


Fig. 8. H-plane pattern. Line: reference. Crosses: obtained from the non-uniform BP NF samples via the SVD procedure. Dashes: reconstruction error.

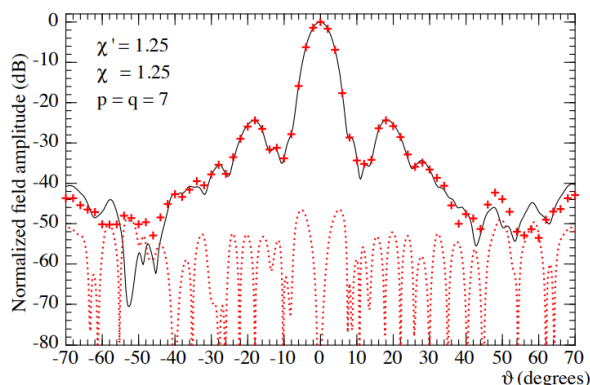


Fig. 9. E-plane pattern. Line: reference. Crosses: obtained from the non-uniform BP NF samples without using the SVD procedure. Dashes: reconstruction error.

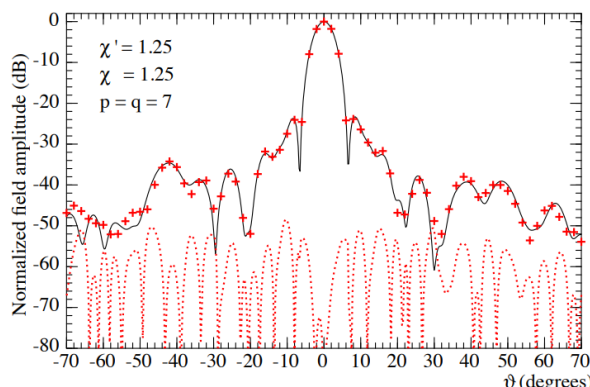


Fig. 10. H-plane pattern. Line: reference. Crosses: obtained from the non-uniform BP NF samples without using the SVD procedure. Dashes: reconstruction error.

A further assessment of the capability of the proposed procedure to compensate also remarkable positioning

errors is provided by the experimental results shown in Figs. 11-14, relevant to the recovery of the far field radiated by a dual pyramidal horn antenna (AUT2), polarized in the vertical plane, operating at 10 GHz, and situated on the plane $z = 0$ of the reference system. The distance between the centers of the horn apertures ($8.9\text{cm} \times 6.8\text{cm}$ sized) is 26.5 cm. This AUT has been modeled by an oblate spheroid with $b = 6.3$ cm and $a = 18.6$ cm. Unlike the previous case, χ' and χ are 1.35 and 1.25, respectively and the scanning plane distance is 16.5 cm. As can be seen, the reconstructions attained by using the SVD procedure result to be much more accurate than those directly obtained from the non-uniform BP NF samples and exhibit a remarkably smaller reconstruction error.

It is interesting a comparison between the number (2098 for the AUT1 and 1836 for the AUT2) of the acquired BP samples and that (23346 for the AUT1 and 19441 for the AUT2) of the NF data needed by the BP NTFIT [11, 12] for covering the same scanning zone.

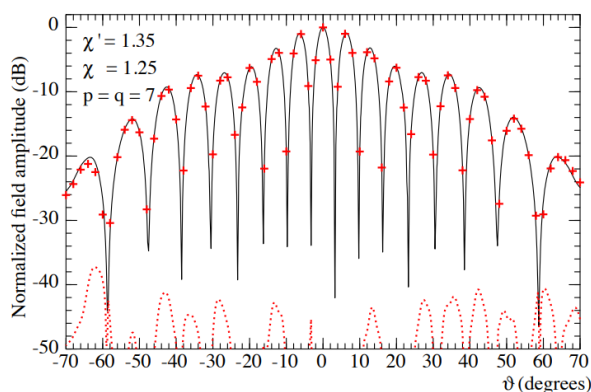


Fig. 11. E-plane pattern (AUT2). Line: reference. Crosses: got from the non-uniform BP NF samples via the SVD procedure. Dashes: reconstruction error.

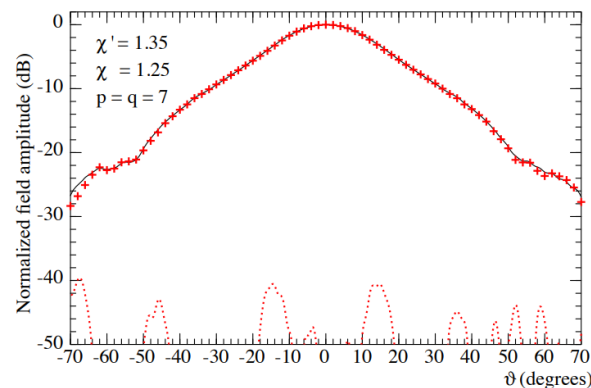


Fig. 12. H-plane pattern (AUT2). Line: reference. Crosses: got from the non-uniform BP NF samples via the SVD procedure. Dashes: reconstruction error.

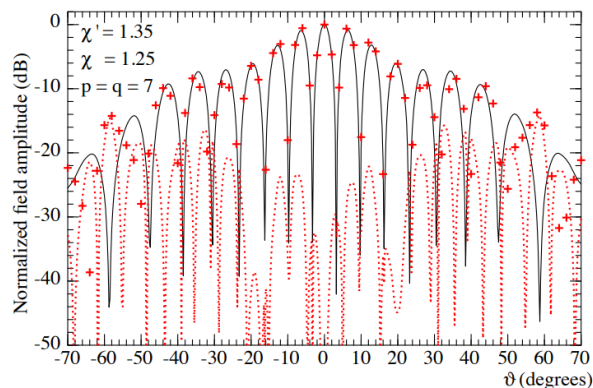


Fig. 13. E-plane pattern (AUT2). Line: reference. Crosses: got from the non-uniform BP NF samples without using the SVD procedure. Dashes: reconstruction error.

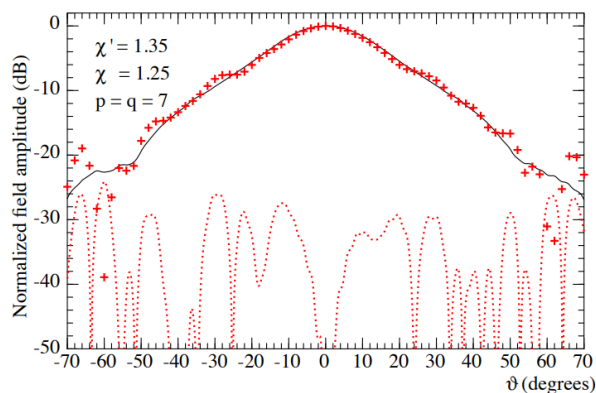


Fig. 14. H-plane pattern (AUT2). Line: reference. Crosses: got from the non-uniform BP NF samples without using the SVD procedure. Dashes: reconstruction error.

IV. CONCLUSION

In this paper, an efficient SVD based procedure, allowing the correction of known positioning errors in the non-redundant NTF with bi-polar scanning adopting an oblate spheroidal AUT modeling, has been further assessed from the experimental viewpoint. Its effectiveness has been confirmed by the accurate NF and FF reconstructions obtained when it is applied even to correct large and pessimistic positioning errors and by the comparison with the severely worsened FF reconstructions directly achieved from the positioning errors affected NF data without exploiting it.

REFERENCES

[1] A. D. Yaghjian, "An overview of near-field antenna measurements," *IEEE Trans. Antennas Prop.*, vol. AP-34, pp. 30-45, Jan. 1986.

[2] M. H. Francis and R. W. Wittmann, *Near-Field Scanning Measurements: Theory and Practice*, in *Modern Antenna Handbook*. C.A. Balanis, Ed.,

chapter 19, John Wiley & Sons, Hoboken, NJ, USA, 2008.

- [3] M. H. Francis, Ed., *IEEE Recommended Practice for Near-Field Antenna Measurements*. IEEE Standard, 1720-2012, 2012.
- [4] F. Ferrara, C. Gennarelli, and R. Guerriero, *Near-Field Antenna Measurement Techniques*, in *Handbook of Antenna Technologies*, Z. N. Chen, D. Liu, H. Nakano, X. Qing, and T. Zwick, Eds., Springer, Singapore, 2016.
- [5] D. T. Paris, W. M. Leach, Jr., and E. B. Joy, "Basic theory of probe-compensated near-field measurements," *IEEE Trans. Antennas Prop.*, vol. AP-26, pp. 373-379, May 1978.
- [6] E. B. Joy, W. M. Leach, Jr., G. P. Rodrigue, and D. T. Paris, "Application of probe-compensated near-field measurements," *IEEE Trans. Antennas Prop.*, vol. AP-26, pp. 379-389, May 1978.
- [7] Y. Rahmat-Samii, V. Galindo Israel, and R. Mittra, "A plane-polar approach for far-field construction from near-field measurements," *IEEE Trans. Antennas Prop.*, vol. AP-28, pp. 216-230, Mar. 1980.
- [8] M. S. Gatti and Y. Rahmat-Samii, "FFT applications to plane-polar near-field antenna measurements," *IEEE Trans. Antennas Prop.*, vol. 36, pp. 781-791, June 1988.
- [9] F. D'Agostino, F. Ferrara, C. Gennarelli, R. Guerriero, and M. Migliozi, "Reconstruction of the antenna far-field pattern through a fast plane-polar scanning," *Appl. Comp. Electromagn. Soc. Jour.*, vol. 31, pp. 1362-1369, Dec. 2016.
- [10] F. D'Agostino, F. Ferrara, C. Gennarelli, R. Guerriero, and M. Migliozi, "Far-field pattern reconstruction from a nonredundant plane-polar near-field sampling arrangement: Experimental testing," *IEEE Antennas Wireless Prop. Lett.*, vol. 15, pp. 1345-1348, 2016.
- [11] L. I. Williams, Y. Rahmat-Samii, and R. G. Yaccarino, "The bi-polar planar near-field measurement technique, Part I: Implementation and measurement comparisons," *IEEE Trans. Antennas Prop.*, vol. 42, pp. 184-195, Feb. 1994.
- [12] R. G. Yaccarino, Y. Rahmat-Samii, and L. I. Williams, "The bi-polar near-field measurement technique, Part II: NF to FF transformation and holographic methods," *IEEE Trans. Antennas Prop.*, vol. 42, pp. 196-204, Feb. 1994.
- [13] F. D'Agostino, C. Gennarelli, G. Riccio, and C. Savarese, "Data reduction in the NF-FF transformation with bi-polar scanning," *Microw. Optic. Technol. Lett.*, vol. 36, pp. 32-36, Jan. 2003.
- [14] F. D'Agostino, F. Ferrara, C. Gennarelli, R. Guerriero, and M. Migliozi, "Fast and accurate far-field prediction by using a reduced number of bipolar measurements," *IEEE Antennas Wireless*

- Prop. Lett.*, vol. 16, pp. 2939-2942, 2017.
- [15] F. D'Agostino, F. Ferrara, C. Gennarelli, R. Guerriero, and M. Migliozi, "Laboratory tests on a near-field to far-field transformation technique from non-redundant bi-polar data," *IET Microw. Antennas Prop.*, vol. 12, pp. 712-717, Apr. 2018.
- [16] O. M. Bucci, C. Gennarelli, and C. Savarese, "Representation of electromagnetic fields over arbitrary surfaces by a finite and non redundant number of samples," *IEEE Trans. Antennas Prop.*, vol. 46, pp. 351-359, Mar. 1998.
- [17] O. M. Bucci and C. Gennarelli, "Application of nonredundant sampling representations of electromagnetic fields to NF-FF transformation techniques," *Int. Jour. Antennas Prop.*, vol. 2012, ID 319856, 14 pages, 2012.
- [18] A. Dutt and V. Rohklin, "Fast Fourier transforms for nonequispaced data," *Proc. SIAM Jour. Scie. Comput.*, vol. 14, pp. 1369-1393, Nov. 1993.
- [19] R. C. Wittmann, B. K. Alpert, and M. H. Francis, "Near-field antenna measurements using nonideal measurement locations," *IEEE Trans. Antennas Prop.*, vol. 46, pp. 716-722, May 1998.
- [20] R. C. Wittmann, B. K. Alpert, and M. H. Francis, "Near-field, spherical-scanning antenna measurements with nonideal probe locations," *IEEE Trans. Antennas Prop.*, vol. 52, pp. 2184-2186, Aug. 2004.
- [21] O. M. Bucci, C. Gennarelli, and C. Savarese, "Interpolation of electromagnetic radiated fields over a plane from nonuniform samples," *IEEE Trans. Antennas Prop.*, vol. 41, pp. 1501-1508, Nov. 1993.
- [22] F. Ferrara, C. Gennarelli, G. Riccio, and C. Savarese, "Far field reconstruction from non-uniform plane-polar data: a SVD based approach," *Electromagnetics*, vol. 23, pp. 417-429, 2003.
- [23] F. Ferrara, C. Gennarelli, G. Riccio, and C. Savarese, "NF-FF transformation with cylindrical scanning from nonuniformly distributed data," *Microw. Optic. Technol. Lett.*, vol. 39, pp. 4-8, Oct. 2003.
- [24] F. Ferrara, C. Gennarelli, M. Iacone, G. Riccio, and C. Savarese, "NF-FF transformation with bi-polar scanning from nonuniformly spaced data," *Appl. Comp. Electromagn. Soc. Jour.*, vol. 20, pp. 35-42, Mar. 2005.
- [25] F. D'Agostino, F. Ferrara, C. Gennarelli, R. Guerriero, and M. Migliozi, "Probe position errors corrected near-field-far-field transformation with spherical scanning," *Appl. Comp. Electromagn. Soc. Jour.*, vol. 31, pp. 106-117, Feb. 2016.
- [26] F. D'Agostino, F. Ferrara, C. Gennarelli, R. Guerriero, and M. Migliozi, "On the compensation of probe positioning errors when using a non-redundant cylindrical NF-FF transformation," *Prog. Electromagn. Res. B*, vol. 20, pp. 321-335, 2010.
- [27] F. D'Agostino, F. Ferrara, C. Gennarelli, R. Guerriero, and M. Migliozi, "Two efficient procedures to correct the positioning errors in the plane-polar scanning," *IET Microw., Antennas Prop.*, vol. 10, no. 13, pp. 1453-1458, 2016.
- [28] F. D'Agostino, F. Ferrara, C. Gennarelli, R. Guerriero, and M. Migliozi, "Near to far-field plane-polar transformation from probe positioning error affected data," *Appl. Comp. Electromagn. Soc. Jour.*, vol. 33, no. 4, pp. 419-429, Apr. 2018.
- [29] O. M. Bucci, G. D'Elia, and M. D. Migliore, "Advanced field interpolation from plane-polar samples: experimental verification," *IEEE Trans. Antennas Prop.*, vol. 46, pp. 204-210, Feb. 1998.
- [30] F. D'Agostino, F. Ferrara, C. Gennarelli, R. Guerriero, S. McBride, and M. Migliozi, "Fast and accurate antenna pattern evaluation from near-field data acquired via planar spiral scanning," *IEEE Trans. Antennas Prop.*, vol. 64, Aug. 2016.
- [31] A. D. Yaghjian, "Approximate formulas for the far field and gain of open-ended rectangular waveguide," *IEEE Trans. Antennas Prop.*, vol. AP-32, pp. 378-384, Apr. 1984.
- [32] F. D'Agostino, F. Ferrara, C. Gennarelli, R. Guerriero, and M. Migliozi, "Nonredundant near-field-far-field transformation from probe positioning errors affected bi-polar data," *Proc. of AMTA 2017*, Atlanta, Georgia, pp. 273-278, Oct. 2017.



Francesco D'Agostino was born near Salerno (Italy) in 1965. He received the Laurea degree in Electronic Engineering from the University of Salerno in 1994, where in 2001 he received the Ph.D. degree in Information Engineering. From 2002 to 2005, he was Assistant

Professor at the Engineering Faculty of the University of Salerno where, in October 2005, he was appointed Associate Professor of Electromagnetics and joined the Department of Industrial Engineering, where he is currently working. His research activity includes application of sampling techniques to electromagnetics and to innovative NF-FF transformations, diffraction problems, radar cross section evaluations, Electromagnetic Compatibility. In this area, D'Agostino has co-authored 4 books and over 220 scientific papers, published in peer-reviewed international journals and conference proceedings. He is a regular Reviewer for several journals and conferences and has chaired some international events and conferences. D'Agostino is a Member of AMTA, EurAAP, and IEEE.



Flaminio Ferrara was born near Salerno, Italy, in 1972. He received the Laurea degree in Electronic Engineering from the University of Salerno in 1999. Since the same year, he has been with the Research Group in Applied Electromagnetics at the University of Salerno. He received the Ph.D. degree in Information Engineering at the same University, where he is presently an Assistant Professor of Electromagnetic Fields. His interests include: application of sampling techniques to the efficient reconstruction of electromagnetic fields and to NF–FF transformation techniques; monostatic radar cross section evaluations of corner reflectors. Ferrara is co-author of more than 220 scientific papers, mainly in international journals and conference proceedings. In particular, he is co-author of 4 books on NF–FF transformation techniques and co-author of the chapter “Near-field Antenna Measurement Rechniques” of the Handbook of Antenna Technologies. He is Reviewer for several international journals and Member of the Editorial board of the International Journal of Antennas and Propagation. He is Member of the IEEE society.



Claudio Gennarelli was born in Avellino, Italy, in 1953. He received the Laurea degree (*summa cum laude*) in Electronic Engineering from the University of Naples, Italy, in 1978. From 1978 to 1983, he worked with the Research Group in Electromagnetics at the Electronic Engineering Department of the University “Federico II” of Naples. In 1983, he became Assistant Professor at the Istituto Universitario Navale (IUN), Naples. In 1987, he was appointed Associate Professor of Antennas, formerly at the Engineering Faculty of Ancona University and subsequently at the Engineering Faculty of Salerno University. In 1999, he has been appointed Full Professor at the same University. The main topics of his scientific activity are: reflector antennas analysis, antenna measurements, diffraction problems, radar cross section evaluations, scattering from surface impedances, application of sampling techniques to electromagnetics and to NF–FF transformations. Gennarelli is co-author of about 400 scientific papers, mainly in international journals and conference proceedings. In particular, he is co-author of 4 books on NF–FF transformation techniques and co-author of the chapter “Near-field Antenna Measurement Techniques” of the Handbook of Antenna Technologies. He is a Senior Member of the IEEE since 2002 and Member of the Editorial board of the Open Electrical and Electronic Engineering Journal and of the International Journal of Antennas and Propagation.



Rocco Guerriero received the Laurea degree in Electronic Engineering and the Ph.D. degree in Information Engineering from the University of Salerno in 2003 and 2007, respectively. Since 2003, he has been with the Research Group in Applied Electromagnetics of University of Salerno, where he is currently an Assistant Professor of Electromagnetic Fields. His interests include: application of sampling techniques to the efficient reconstruction of electromagnetic fields and to near-field-far-field transformation techniques; antenna measurements; inversion of ill-posed electromagnetic problems; analysis of microstrip reflectarrays; diffraction problems. Guerriero is co-author of about 180 scientific papers, mainly in international journals and conference proceedings. In particular, he has co-authored 3 books on NF–FF transformation techniques and is co-author of the chapter “Near-field Antenna Measurement Techniques” of the Handbook of Antenna Technologies. He is Reviewer for several international journals and Member of the Editorial board of the International Journal of Antennas and Propagation. Since 2015, he is Member of IEEE.



Massimo Migliozi received the Laurea degree in Electronic Engineering from the University of Salerno, in 1999. He received the Ph.D. degree in Information Engineering at the same University, where at the present time he is a Research Fellow in Electromagnetic Fields. His scientific interests include: application of sampling techniques to the efficient reconstruction of electromagnetic fields and to NF–FF transformation techniques; antenna measurements; electromagnetic compatibility; antenna design; diffraction problems. Migliozi is co-author of about 140 scientific papers, mainly in international journals and conference proceedings and Reviewer for several international journals.

Far Field Reconstruction based on Compressive Sensing with Prior Knowledge

Baozhu Li¹, Wei Ke^{*1,2}, Huali Lu¹, Shuming Zhang¹, and Wanchun Tang^{1,2}

¹ Jiangsu Province Engineerings Laboratory of Audio Technology
Nanjing Normal University, Nanjing, 210023, China

951408095@qq.com, kewe@njnu.edu.cn, 247588640@qq.com, 1627839409@qq.com, eewctang@njnu.edu.cn

² Jiangsu Center for Collaborative Innovation in Geographical Information Resource Development and Application
Nanjing, 210023, China

Abstract — Far field reconstruction in a large-scale space is time consuming and imprecise. However, if these data are sampled randomly and can be sparse on a specific transform domain, it will become quick and accurate to complete the field reconstruction by using the compressive sensing (CS). By taking the feature of the far field distribution for the half-wave dipole antenna in half space as an important prior knowledge, the sparse transform can be chosen appropriately. Moreover, a piecewise approximation method is presented to reconstruct the far field. The simulated results show that this proposed method has better performance for far field reconstruction than the traditional method.

Index Terms — Field reconstruction, prior knowledge, sparse, compressive sensing.

I. INTRODUCTION

The spatial distribution of electromagnetic (EM) field [1] can provide an intuitive demonstration of radio wave propagation. Accordingly, estimating the totality of electromagnetic field existing at a given location precisely and rapidly offers guidance for wireless network optimization. Simulation softwares such as Wireless Insite [2] and Winprop [3] have been developed for the electromagnetic simulation. In fact, the results of these softwares are not accurate enough due to the complexity of the environment [4]. Therefore, field reconstruction based on measurement by monitoring a station or using a personal dosimeter is still needed. To describe the spatial distribution pattern of the electromagnetic radiation field in the entire region, an efficient method for field reconstruction is necessary [5].

Several interpolation methods can be used to perform EM field reconstruction. The model based parameter estimation (MBPE) [6-8] is used in computational electromagnetics based on polynomial fitting. In [9], a method of weighted minimization of two norms is proposed to interpolate the EM near field when no

information on the radiating source is available. In [10], five spatial interpolation methods for electric field in urban environments are used and compared. However, these methods mentioned above do not perform very well in the large-scale geographic space due to the reflection, transmission and diffraction of EM waves. And in field reconstruction, no prior knowledge about EM field is used. Hence, it is necessary to develop new solutions to reconstruct the EM field.

In [11] the Bayesian compressive sensing algorithm is utilized to fast analyze the EM scattering problem. It is similar to the field reconstruction problem. Compressive sensing enables a signal to be reconstructed completely from a small set of nonadaptive, linear measurements by obtaining a sparse representation in some basis [12-14]. It has been applied to many EM problems [15-18]. Recently, it is used to reconstruct the complex time-harmonic electric field in [19]. The electric field is modeled as a summation of 20 incident homogeneous plane waves with random phase, magnitude, and angle-of-arrival. Actually, incidence, reflection, transmission, and diffraction are not independent of each other. The electric field in a real environment does not have such a sparse representation in the spatial-frequency domain. As an important prior knowledge, feature of EM wave propagation in real environment should be also considered for the field reconstruction.

Therefore, taking the electric field distribution created by a half-wavelength dipole antenna above the ground as an example, far field reconstruction in a large-scale space using compressive sensing is researched. Firstly, the prior knowledge about the electric field distribution feature is introduced. According to the prior knowledge, the selection of transforms for field reconstruction is discussed. Specifically, the method of piecewise approximation reconstruction according to the prior knowledge is proposed. In the end, the electric field in a real environment is reconstructed by the

proposed method.

II. PRIOR KNOWLEDGE FOR FAR FIELD RECONSTRUCTION

Various antennas exist in our lives. One of the most commonly used antenna is the half-wavelength dipole antenna. In this section, the feature of the electric field distribution for the half-wavelength dipole antenna in half space is analyzed. The feature will provide an important prior knowledge for the following field reconstruction.

A. Half-wavelength dipole antenna above the ground

Suppose the geographical space is divided into two half parts, the interface is a smooth plane. The upper half space is air and the lower half is ground. As a result, the total electric and magnetic field in the upper space with a certain height above the ground are the superposition of the incident and reflected components, as shown in Fig. 1.

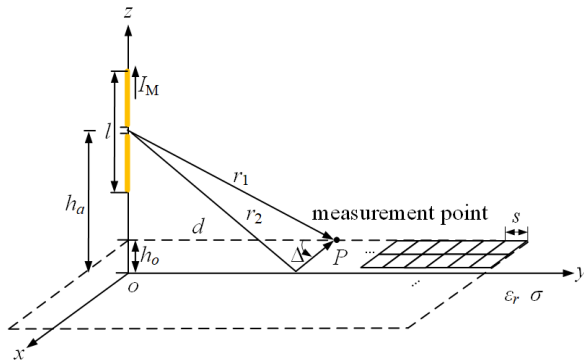


Fig. 1. A half-wavelength dipole antenna above the ground with the observation plane at height of h_o .

In Fig. 1, the observation plane is at a height of h_o above the ground and is divided into uniform grids with grid width of s . Due to the symmetry of the electric and magnetic field distribution on the observation plane, only the field distribution along the path d is studied. Other symbols in Fig. 1 are not described here for brevity.

Significantly, at the Brewster angle [20] of incidence, no TM wave is reflected for this vertical dipole antenna of Fig. 1. The Brewster angle can be calculated by:

$$\Delta_{r0} = \operatorname{arccot} \sqrt{\frac{\varepsilon_c}{\varepsilon_0}}, \quad (1)$$

where ε_c is the complex effective permittivity of ground. Thus, we have:

$$d_{r0} = \frac{h_a + h_o}{\tan \Delta_{r0}}. \quad (2)$$

That means, there is no reflection at $d=d_{r0}$, an important parameter for studying the feature of the electric field

distribution.

B. The feature of the far field distribution as prior knowledge

In order to describe the feature of the far field distribution of the dipole antenna intuitively, one illustrative example of the calculation parameters shown in the Table 1 is given.

Table 1: Calculation parameters

Parameter	Value
s	1m
h_a	20m
h_o	2m
f	3GHz
I_M	1A
ε_r	25
σ	$2 \times 10^{-2} \text{S/m}$

From Eqs. (1) and (2), one can obtain that $d_{r0} = 110\text{m}$. And the electric field distribution along the path d of Fig. 1 can be calculated and is shown in Fig. 2. All the measured points along this path d is in the far field region. The results show that the magnitude of the electric field increases with intense oscillation firstly and then decreases with slow oscillation when the observation point P moves away from the antenna.

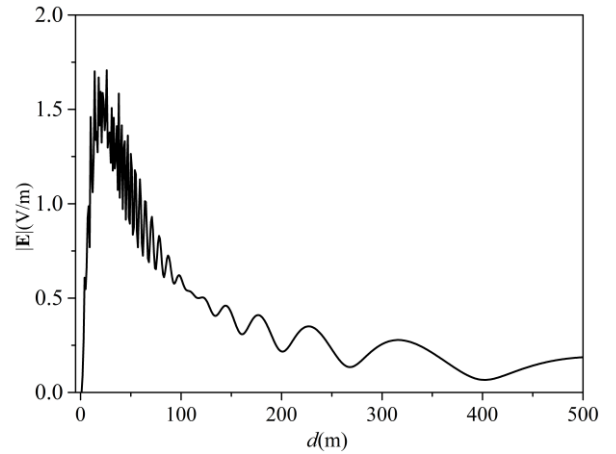


Fig. 2. Electric field distribution of the half-wavelength dipole antenna along the path d .

The feature of the electric field distribution is mainly caused by the phase differences of the incident and reflected waves. This can be explained as follows. When the measured point P is above the ground, there is a propagation path difference ($r_1 < r_2$) between the incident wave and the reflected wave, as shown in Fig. 1. It leads to that the phase changes of the incident wave and the reflected wave are not synchronizable when P moves

away from the antenna. And if d is larger than d_{r0} and continues to increase, the propagation path difference between the incident and reflected waves becomes smaller and smaller, resulting that the phase difference between them oscillates more and more slowly.

Although only the electric field of the vertical dipole antenna above the ground is calculated, other types of antennas also have the above features. That is, when the observation plane is above the ground, the closer the measured point is to the antenna, the more intensely the electric field oscillates, and on the other hand the farther from the antenna, the more slowly the electric field oscillates. Therefore, the distance d_{r0} of Eq. (2) can be taken as an important prior knowledge for the field reconstruction.

III. ELECTRIC FIELD RECONSTRUCTION USING COMPRESSIVE SENSING

Electric field distribution of the antenna in space is not sparse in the measured domain. However it can be sparse on a specific transform domain. In this section the theory of field reconstruction based on compressive sensing with prior knowledge is studied.

A. Compressive sensing

Suppose that \mathbf{x} is the original electric field to be reconstructed, it can be considered as a discrete signal with length of N . The signal \mathbf{x} is compressible if there exists a basis matrix Ψ in that \mathbf{x} becomes nearly sparse:

$$\mathbf{x} = \Psi\theta \Leftrightarrow \theta = \Psi^{-1}\mathbf{x}, \quad (3)$$

where vector θ is the representation of \mathbf{x} in the domain of Ψ^{-1} . If the number of non-zero coefficients in θ is K ($K \ll N$), it is called K -sparse signal.

The basis matrix Ψ is the inverse transform matrix, where the transform may be taken as one of the most popular orthogonal transforms: discrete Fourier transform (DFT), discrete cosine transform (DCT) and discrete wavelet transform (DWT). That is, Ψ transforms the sparse vector θ into the original electric field \mathbf{x} of interest.

On the other hand, the sampled vector \mathbf{y} with $M \times 1$ can be expressed as:

$$\mathbf{y} = \Phi\mathbf{x} = \Phi\Psi\theta = \mathbf{A}^{\text{CS}}\theta, \quad (4)$$

where Φ is the measurement matrix with $M \times N$ ($M < N$) that is incoherent with Ψ and \mathbf{A}^{CS} is the observation matrix. M is the number of measurements.

Here, one should note that the sampled vector \mathbf{y} is actually sampled from the original electric field \mathbf{x} . Then \mathbf{A}^{CS} can be converted to a partial random matrix by randomly selecting the rows of the matrix Ψ .

\mathbf{x} can be exactly reconstructed with overwhelming probability by (3). Under the conditions of $2K < M < N$ the reconstruction is equal to solve the l_0 -norm optimization problem of Eq. (4), namely:

$$\min \|\theta\|_0 \text{ s.t. } \mathbf{A}^{\text{CS}}\theta = \mathbf{y}. \quad (5)$$

However, solving Eq. (5) is a non-deterministic polynomial-time hard problem. In order to reduce complexity, l_1 -norm optimization problem is used as alternative, i.e.,

$$\min \|\theta\|_1 \text{ s.t. } \mathbf{A}^{\text{CS}}\theta = \mathbf{y}. \quad (6)$$

The reconstruction algorithm used in this paper is orthogonal matching pursuit (OMP) [21], which solves (6) by greedy iteration to approach the sampled vector \mathbf{y} .

B. Sparse representation

As described above, three most popular orthogonal transforms can be used. In this subsection, we will study how to select the transform from DFT, DCT and DWT appropriately according to the prior knowledge.

The reconstructed electric field in this paper is taken along the path d within the range of $1\text{m} \leq d \leq 256\text{m}$, with $N=256$ sampled points. According to the prior knowledge of last section, this range can be divided into two parts at $d=128\text{m}$, that is, the region of $1\text{m} \leq d \leq 128\text{m}$ with intense oscillation and the region of $129\text{m} \leq d \leq 256\text{m}$ with slow oscillation.

In order to evaluate the sparsity of DFT, DCT, and DWT, we introduce another vector θ_{normal} as below:

$$\theta_{\text{normal}} = \frac{\theta}{\|\theta\|_2}. \quad (7)$$

By calculating the percentage of element in θ_{normal} less than a threshold ξ (taken as 0.005 in this paper), the sparsity comparison for the three transforms are shown in Table 2.

Table 2: The sparsity comparison of DFT, DCT, and DWT with $\xi=0.005$

Region	DCT	DWT	DFT
$1\text{m} \leq d \leq 256\text{m}$	33.98%	71.48%	23.43%
$1\text{m} \leq d \leq 128\text{m}$	23.19%	50.00%	7.81%
$129\text{m} \leq d \leq 256\text{m}$	89.06%	82.81%	58.59%

From Table 2, one can see that the sparsity percentage in region of $129\text{m} \leq d \leq 256\text{m}$ can be up to 89.06% in DCT domain. In the region of $1\text{m} \leq d \leq 128\text{m}$ and $1\text{m} \leq d \leq 256\text{m}$, the sparsity percentage in DWT domain is the largest.

Furthermore, one can also find that DFT is not the optimal sparse basis transform in any region above. This is because the incident and reflected waves are not independent due to the ground reflection. Moreover, the plane wave angular spectrum varies with the change of propagation path. Therefore, the electric field is not very sparse in DFT domain.

From point view of signal and system, most of the signal energy is concentrated at the lower frequency after DCT, while DWT has more excellent multi-resolution properties than DCT. That means, for the reconstruction of the electric field, DCT is suitable in the region of

electric field with slower oscillation (the region of $129\text{m} \leq d \leq 256\text{m}$ in Table 2), while DWT is suitable in the region of the electric field with intense oscillation (the region of $1\text{m} \leq d \leq 128\text{m}$ in Table 2).

IV. NUMERICAL RESULTS

If the electric field $|\mathbf{E}|$ is inherently 2-D, it can be expressed as the 1-D vector by stacking the matrix columns and is represented by \mathbf{x} with a length of N . The sample \mathbf{y} of the electric field \mathbf{x} is performed by using a random measurement matrix Φ with dimension $M \times N$. Finally, field can be reconstructed by OMP. For each choice of Φ , the quality of the reconstruction is evaluated by computing the relative error between the original and reconstructed field as follows:

$$e = \frac{\|\mathbf{x} - \hat{\mathbf{x}}\|_2}{\|\mathbf{x}\|_2}, \tag{8}$$

where $\hat{\mathbf{x}}$ is the reconstructed field. By choosing, for example 1000, different measurement matrices Φ , the reconstruction error can be obtained by taking the average of the relative errors of Eq. (8).

A. Field reconstruction by traditional approach

The traditional approach to reconstruct the electric field is to sample in the entire interested region and reconstruct it using only one transform matrix. This subsection investigates and compares the reconstruction error versus the number of measurements M for the three different transforms. The reconstructed electric field is in the region of $1\text{m} \leq d \leq 256\text{m}$ of Fig. 2.

Figure 3 illustrates the reconstruction error versus the number of measurements $10 \leq M \leq 250$. It is observed that the quality of the reconstructed electric field is directly related to the sparsity of the three different transforms just as indicated in Table 2. When $M > 115$, the quality of the reconstruction is the best by DWT.

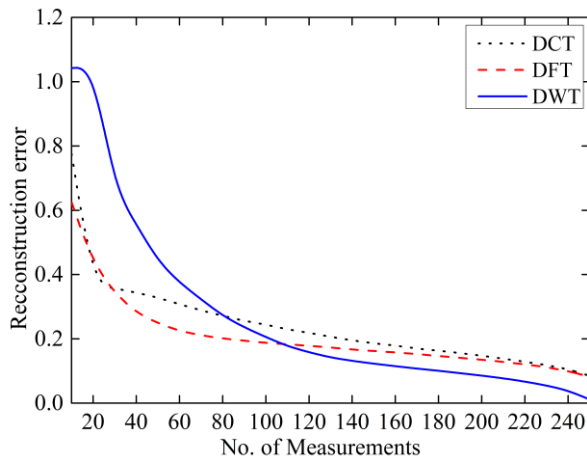


Fig. 3. Reconstruction error comparison in the region of $1\text{m} \leq d \leq 256\text{m}$ for the three different transforms.

Next, we divide the region into two parts, including $1\text{m} \leq d \leq 128\text{m}$ and $129\text{m} \leq d \leq 256\text{m}$, and reconstruct the electric field respectively. The results are shown in Fig. 4 and Fig. 5. As can be seen, in the region of $1\text{m} \leq d \leq 128\text{m}$, the reconstruction error by DWT is lower than DCT and DFT if $M > 55$, while in the region of $129\text{m} \leq d \leq 256\text{m}$, the performance of DCT far exceeds that of the other two transforms.

It is also interesting to observe that the number of measurements M required for a good reconstruction depends on the complexity of the original electric field. As the distance from the source decreases, the oscillation of the field in the space becomes more and more intense, as a result, the more number of measurements are required to improve reconstruction.

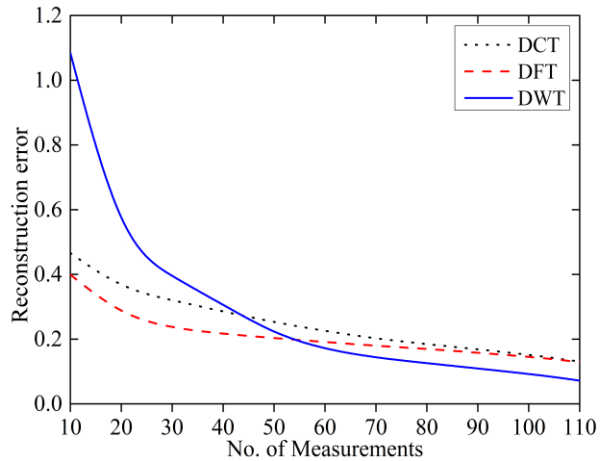


Fig. 4. Reconstruction error comparison in the region of $1\text{m} \leq d \leq 128\text{m}$ for the three different transforms.

B. Field reconstruction by piece-wise approximation with prior knowledge

By dividing the whole region of $1\text{m} \leq d \leq 256\text{m}$ into two parts according to d_{r0} by Eq. (2), a piece-wise approximation with prior knowledge is proposed. That is, DWT is used as the sparse transform with larger M in the region of $1\text{m} \leq d \leq 128\text{m}$, and instead, smaller M is required and DCT is adopted in the region of $129\text{m} \leq d \leq 256\text{m}$.

Figure 6 and Fig. 7 demonstrate the reconstructed electric fields in the region of $1\text{m} \leq d \leq 256\text{m}$ ($N=256$) by traditional approach and the proposed approach, respectively. For the traditional approach, the reconstruction error is 0.201 with $M=100$ and using DWT. For the proposed approach, M is taken as 70 and 30 in the region of $1\text{m} \leq d \leq 128\text{m}$ and $129\text{m} \leq d \leq 256\text{m}$, respectively. And the reconstruction error is 0.067.

Compared with the traditional approach, one can conclude that the piece-wise approximation with prior knowledge proposed in this paper needs less number of

measurements and has smaller reconstruction error.

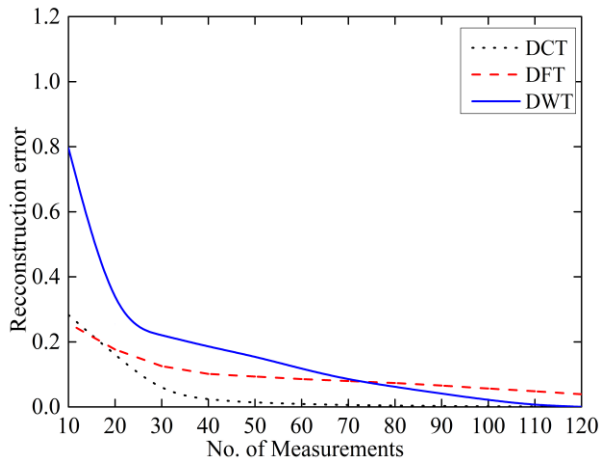


Fig. 5. Reconstruction error comparison in the region of $129\text{m} \leq d \leq 256\text{m}$ for the three different transforms.

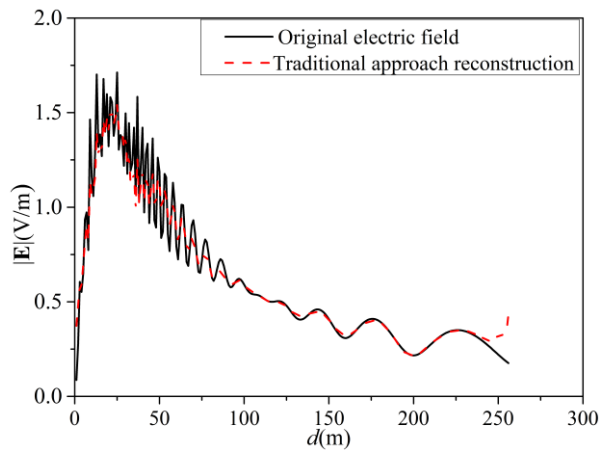


Fig. 6. Reconstructed electric field by the traditional approach and the original electric field.

C. Field reconstruction in real environment

In this subsection, the electric field in a real environment is reconstructed by compressive sensing. The original electric field is simulated in Wireless Insite [2]. There are 168×168 receivers (isotropic antenna) with spacing of 5m in a region of $840\text{m} \times 840\text{m}$ in this environment, as shown in Fig. 8. The transmitter (vertical half-wave dipole antenna) is located at the center of this region and the simulation parameters are listed in the Table 3.

Figure 9 shows the original electric field simulated by Wireless Insite. For field reconstruction, the total region is partitioned into 441 equal-sized cells with the area of $40\text{m} \times 40\text{m}$.

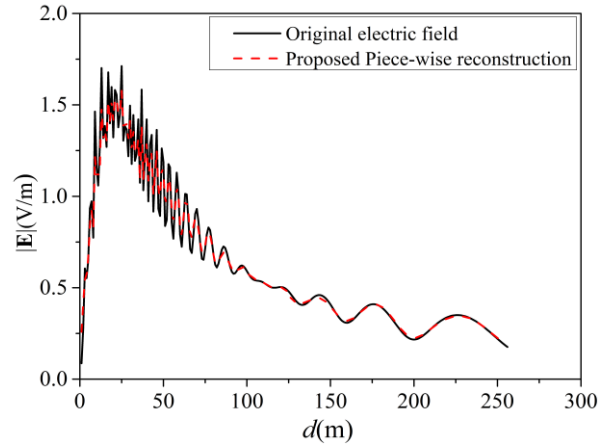


Fig. 7. Reconstructed electric field by the proposed approach and the original electric field.

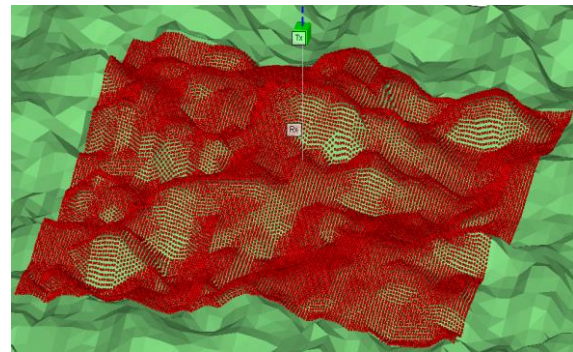


Fig. 8. A real environment modeled in Wireless Insite.

Table 3: Simulation parameters

Parameter	Value
s	5m
h_a	50m
h_o	2m
f	3GHz
I_M	1A
ϵ_r	25
σ	$2 \times 10^{-2} \text{S/m}$

For the traditional approach with DWT, 20% of the number of measurements in each cell are used. The reconstructed electric field is shown in Fig. 10, with the reconstruction error of 0.7308.

For the proposed piece-wise approximation approach, $d_{r,0}$ is 260m by Eq. (2). Hence, a square boundary with the side length of 520m divides the whole region of $840\text{m} \times 840\text{m}$ into two parts, as depicted in Fig. 9. Inside the boundary, DWT is used with 40% measurements, while outside the boundary, DCT is adopted with 20% measurements. The reconstructed

electric field is shown in Fig. 11 with the reconstruction error of 0.1972. Compared with the traditional approach, the proposed piece-wise approximation approach has better performance with not too more measurements increased.

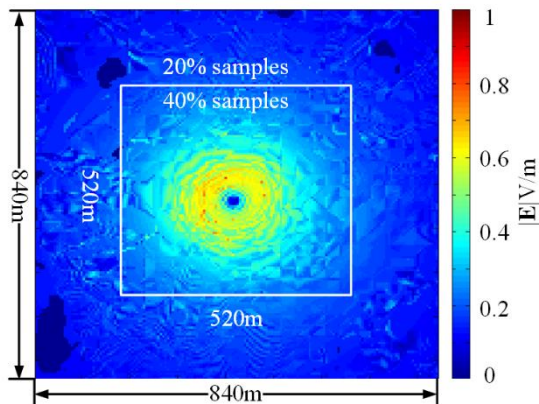


Fig. 9. Original electric field and the number of measurements.

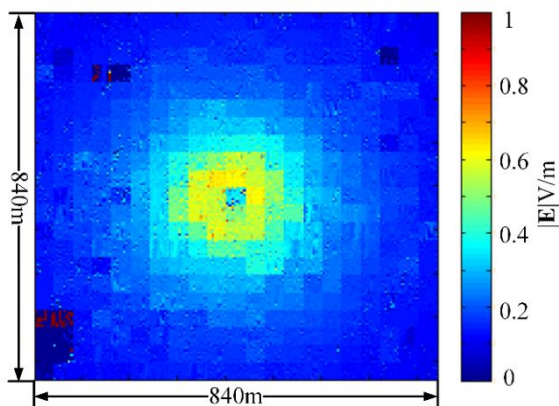


Fig. 10. Reconstructed electric field by the traditional approach.

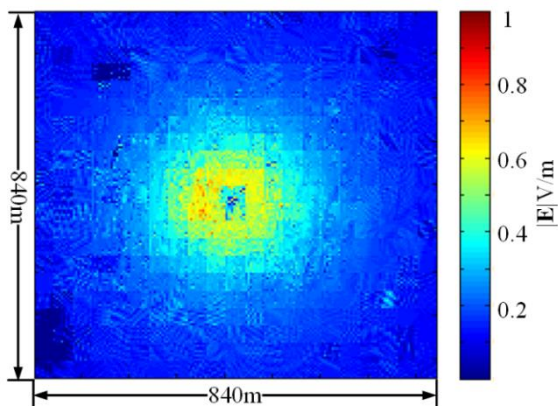


Fig. 11. Reconstructed electric field by the proposed approach.

V. CONCLUSION

The far field feature of half-wave dipole antenna in large-scale half-space is studied and taken as a prior knowledge for the electric field reconstruction by compressive sensing. With this prior knowledge, a new method based on the piece-wise approximation reconstruction is presented. Compared with the traditional approach, the proposed piece-wise approximation method can obtain a higher quality reconstruction field with an appropriate number of measurement points. In the end, the reconstruction in a real environment illustrates the validity and feasibility of the proposed method.

ACKNOWLEDGMENT

This work is supported by the National Key Research and Development Program of China (Grant No. 2017YFB0503500) and the National Natural Science Foundation of China (Grant No. 61571232).

The authors would like to thank Prof. Andrew Massa and Prof. Marco Donald Migliore in the research center of ELEDIA, Italy, for their theoretical guidance on this paper.

REFERENCES

- [1] M. Salovarda and K. Malaric, "Measurements of electromagnetic smog," *IEEE Electrotechnical Conference*, Malaga, Spain, pp. 470-473, July 2006.
- [2] P. Mededovic, M. Veletic, and Z. Blagojevic, "Wireless insite software verification via analysis and comparison of simulation and measurement results," *Mipro, 2012 Proceedings of the, International Convention IEEE*, Opatija, Croatia, pp. 776-781, July 2012.
- [3] R. Hoppe, G. Wölfle, and U. Jakobus, "Wave propagation and radio network planning software WinProp added to the electromagnetic solver package FEKO," *Applied Computational Electromagnetics Society Symposium*, Florence, Italy, pp. 1-2, Mar. 2017.
- [4] Y. O. Isselmou, H. Wackernagel, W. Tabbar, et al., "Geostatistical interpolation for mapping radio-electric exposure levels," *IEEE Conference on Antennas and Propagation*, Nice, France, pp. 1-6, Nov. 2006.
- [5] C. C. Rodríguez, C. A. Forero, and H. O. Boada, "Electromagnetic field measurement method to generate radiation map," *IEEE Communications Conference*, Cali, Colombia, pp. 1-7, July 2012.
- [6] E. K. Miller, "Model-based parameter estimation in electromagnetic Pt. 1," *IEEE Antennas and Propagation Magazine*, vol. 40, no. 1, pp. 40-52, Feb. 1998.
- [7] E. K. Miller, "Model-based parameter estimation in electromagnetic Pt. 2," *IEEE Antennas and Propagation Magazine*, vol. 40, no. 2, pp. 51-65,

- Apr. 1998.
- [8] E. K. Miller, "Model-based parameter estimation in electromagnetic Pt. 3," *IEEE Antennas and Propagation Magazine*, vol. 40, no. 3, pp. 49-66, June 1998.
- [9] B. Fuchs, L. L. Coq, and M. D. Migliore, "On the interpolation of electromagnetic near field without prior knowledge of the radiating source," *IEEE Trans. Antennas Propagat.*, vol. 65, no. 7, pp. 568-3574, May 2017.
- [10] T. A. A. Santana, H. D. D. Andrade, I. S. Q. Júnior, et al., "Comparison of spatial interpolation methods to determine exposure ratio to electric field in urban environments," *Electronics Letters*, vol. 53, no. 18, pp. 1250-1252, Sep. 2017.
- [11] H. H. Zhang, W. E. I. Sha, and L. J. Jiang, "Fast monostatic scattering analysis based on Bayesian compressive sensing," *International Applied Computational Electromagnetics Society Symposium*, Florence, Italy, pp. 1-2, Mar. 2017.
- [12] E. J. Candès, J. Romberg, and T. Tao, "Terence. robust uncertainty principles: Exact signal reconstruction from highly incomplete frequency information," *IEEE Trans. on Infor. Theory*, vol. 52, no. 2, pp. 489-509, Jan. 2006.
- [13] D. L. Donoho, "Compressed sensing," *IEEE Trans. on Infor. Theory*, vol. 52, no. 4, pp. 1289-1306, Apr. 2006.
- [14] E. J. Candès and T. Tao, "Near-optimal signal recovery from random projections: Universal encoding strategies?," *IEEE Trans. on Infor. Theory*, vol. 52, no. 12, pp. 5406-5425, Nov. 2006.
- [15] B. Verdin and P. Debroux, "2D and 3D far-field radiation patterns reconstruction based on compressive sensing," *Progress in Electromagnetic Research M*, vol. 46, pp. 47-56, 2006.
- [16] B. Verdin and P. Debroux, "Reconstruction of missing sections of radiation patterns using compressive sensing," *IEEE International Symposium on Antennas and Propagation & Usnc/ursi National Radio Science Meeting*, Vancouver, Canada, pp. 780-781, Oct. 2015.
- [17] A. Massa, P. Rocca, and G. Oliveri, "Compressive sensing in electromagnetics-A review," *IEEE Trans. Antennas Propagat.*, vol. 57, no. 1, pp. 224-238, Feb. 2015.
- [18] G. Oliveri, M. Salucci, N. Anselmi, and A. Massa, "Compressive sensing as applied to inverse problems for imaging: Theory, applications, current trends, and open challenges," *IEEE Trans. Antennas Propagat.*, vol. 59, no. 5, pp. 34-46, Aug. 2017.
- [19] A. C. M. Austin and M. J. Neve, "Efficient field reconstruction using compressive sensing," *IEEE Trans. Antennas Propagat.*, vol. 66, no. 3, pp. 1624-1627, Jan. 2018.
- [20] J. A. Kong, *Electromagnetic Wave Theory*. John Wiley & Sons, Canada, 1985.
- [21] J. Tropp and A. Gilbert, "Signal recovery from partial information via orthogonal matching pursuit," *IEEE Trans. on Infor. Theory*, vol. 53, no. 12, pp. 4655-4666, Apr. 2005.



Baozhu Li was born in Henan Province, China, in 1990. She received the B.S. degree from Nanjing Normal University Zhongbei College, Nanjing, in Electrical Engineering in 2013. She is working towards the Ph.D. degree with the School of Physics and Technology, NJNU. Her research interests include electromagnetic environment, antennas and signal processing.



Wei Ke received his M.S. degree in Communication Engineering from Nanjing Norm University, China, in 2002, and Ph.D. degree in Signal and Information Processing from Southeast University, China, in 2011. Since 2013, he has been an Associate Professor in Nanjing Norm University, China. His current main research interest is wireless positioning techniques.

A Review of the Modal Decomposition Matrix for Calculating the Far Field of an Infinitely Flanged Rectangular Waveguide

Gregory A. Mitchell¹ and Wasyl Wasykiwskyj²

¹U.S. Army Research Laboratory
Adelphi, MD 20783, USA
gregory.a.mitchell1.civ@mail.mil

²Department of Electrical and Computer Engineering
The George Washington University, Washington, DC 20052, USA
wasykiw@gwu.edu

Abstract — We determine the radiation from an infinitely flanged rectangular waveguide using the modal decomposition matrix (MDM) method. The MDM method computes the electromagnetic field components at the aperture in the Fourier domain by representing the radiated field in terms of a sampling of the free-space transverse wave number. The results of the MDM approach show good agreement with numerical approaches using commercial electromagnetic modeling software.

Index Terms — EM propagation, flanged rectangular waveguide, modal decomposition matrix, spherical value decomposition, stationary phase.

I. INTRODUCTION

In practice, designers use flush mounted aperture antennas widely and approximate their models by an aperture in an infinite conducting surface (infinite flange). The analysis of radiation from an infinitely flanged open rectangular waveguide has been widely studied and presenting using different analytical methods for calculating the electromagnetic (EM) fields at the aperture [1-3]. Furthermore, the solutions determined by these methods reasonably approximate those of a radiating waveguide with a finite flange [4]. After calculating the EM fields at the aperture, the stationary phase equation determines the radiated far field [5]. Although accurate, known methods require the additional calculation of the Fourier transform of the EM fields at the aperture before they can apply them to the stationary phase equation. In high fidelity computer simulations with many millions of mesh cells, algorithms numerically compute the EM fields at the boundaries of every mesh cell across the waveguide aperture. For far field calculations using stationary phase, these methods also require a Fourier transform of every EM field at the boundary of every mesh cell across the aperture leading

to unnecessary additional computational expense.

This paper reviews a less computationally costly approach that analytically computes the components of the EM fields at the aperture of an infinitely flanged open rectangular waveguide in the Fourier domain. Our approach directly solves for these fields without the need of a computationally expensive Fourier transform. The approach uses the modal decomposition matrix (MDM) based on a modal sampling of the transverse free space wave number. This approach results in a matrix equation solving directly for the Fourier field components needed for stationary phase calculations of the radiated far fields. The authors originally published the MDM method as an internal report [6], and mean for this review paper to distribute the results to a wider audience of peer reviewed journals.

We compare the results determined by the MDM method to the far field radiation patterns and return loss calculations achieved by CST Studio Suite 2017 for a 3D model and simulation of the same problem. The comparison shows excellent agreement between the simulations and the numerical techniques using the MDM method.

II. MODAL DECOMPOSITION OF A RECTANGULAR WAVEGUIDE

This section describes the theory of matching the transverse electric (TE) and magnetic (TM) fields that exist inside a uniform rectangular waveguide to those of the radiated far fields in free space. We base the below description of the modal decomposition on known theory [7, 8]. We assume the dominant propagating mode generates the transverse EM fields inside the waveguide. The cutoff frequency (f_c) of the waveguide determines when the dominant mode changes from an attenuating to a propagating mode. For a rectangular waveguide, the dominant mode is TE₁₀ [9].

By matching to the spectral component of the

radiated field at the aperture, we derive a system of equations that yield the transverse aperture EM fields in the Fourier domain. Based on this we use the stationary phase equation to calculate the far field radiation patterns. We now construct the form of the electric and magnetic fields that exist inside the waveguide due to a propagating TE₁₀ mode.

A. Propagating TE₁₀ mode case

We assume the incident TE₁₀ wave in Fig. 1 exists in the waveguide with the following form:

$$\underline{E}_{Tinc}(\underline{r}) = \underline{e}'_N(\underline{\rho})V(z), \quad (1)$$

$$\underline{H}_{Tinc}(\underline{r}) = \underline{h}'_N(\underline{\rho})I(z), \quad (2)$$

where $\underline{r} = x\underline{x}_o + y\underline{y}_o + z\underline{z}_o$, $\underline{\rho} = x\underline{x}_o + y\underline{y}_o$, and $V(z)$ and $I(z)$ are the voltage and current at point z inside the waveguide. N denotes that the incident mode is propagating in the waveguide and $'$ denotes a TE mode while $'$ denotes a transverse magnetic (TM) mode.

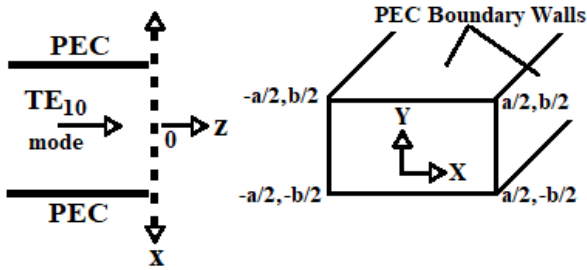


Fig. 1. Illustration of the boundary between the waveguide and free space at $z=0$ and its transverse cross section.

Figure 1 shows two orientations of the same rectangular waveguide. A half space boundary exists at $z=0$, and the waveguide extends to $-\infty$ in the \underline{z}_o -direction. The literature describes this as the semi-infinite waveguide approximation [7].

We define the mode functions $\underline{e}_v(\underline{\rho})$ and $\underline{h}_v(\underline{\rho})$:

$$\begin{aligned} \underline{e}'_v(\underline{\rho}) &= \nabla_T \Phi_v(\underline{\rho}) / (\pi A'_{v'}) \\ &= \left[\underline{x}_o \frac{m}{a} \cos\left(\frac{m\pi}{a}\left(x + \frac{a}{2}\right)\right) \sin\left(\frac{n\pi}{b}\left(y + \frac{b}{2}\right)\right) \right. \\ &\quad \left. + \underline{y}_o \frac{n}{b} \sin\left(\frac{m\pi}{a}\left(x + \frac{a}{2}\right)\right) \cos\left(\frac{n\pi}{b}\left(y + \frac{b}{2}\right)\right) \right] \end{aligned} \quad (3)$$

$$\begin{aligned} \underline{h}'_v(\underline{\rho}) &= \underline{z}_o \times \underline{e}'_v(\underline{\rho}) / (\pi A'_{v'}) \\ &= \left[\underline{x}_o \frac{n}{b} \sin\left(\frac{m\pi}{a}\left(x + \frac{a}{2}\right)\right) \cos\left(\frac{n\pi}{b}\left(y + \frac{b}{2}\right)\right) \right. \\ &\quad \left. - \underline{y}_o \frac{m}{a} \cos\left(\frac{m\pi}{a}\left(x + \frac{a}{2}\right)\right) \sin\left(\frac{n\pi}{b}\left(y + \frac{b}{2}\right)\right) \right] \end{aligned} \quad (4)$$

$$\begin{aligned} \underline{e}''_v(\underline{\rho}) &= \underline{z}_o \times \underline{h}''_v(\underline{\rho}) / (\pi A''_{v'}) \\ &= \left[\underline{x}_o \frac{n}{b} \cos\left(\frac{m\pi}{a}\left(x + \frac{a}{2}\right)\right) \sin\left(\frac{n\pi}{b}\left(y + \frac{b}{2}\right)\right) \right. \\ &\quad \left. - \underline{y}_o \frac{m}{a} \sin\left(\frac{m\pi}{a}\left(x + \frac{a}{2}\right)\right) \cos\left(\frac{n\pi}{b}\left(y + \frac{b}{2}\right)\right) \right] \end{aligned} \quad (5)$$

$$\begin{aligned} \underline{h}''_v(\underline{\rho}) &= -\nabla_T \Psi_v(\underline{\rho}) / (\pi A''_{v'}) \\ &= \left[\underline{x}_o \frac{m}{a} \sin\left(\frac{m\pi}{a}\left(x + \frac{a}{2}\right)\right) \cos\left(\frac{n\pi}{b}\left(y + \frac{b}{2}\right)\right) \right. \\ &\quad \left. + \underline{y}_o \frac{n}{b} \cos\left(\frac{m\pi}{a}\left(x + \frac{a}{2}\right)\right) \sin\left(\frac{n\pi}{b}\left(y + \frac{b}{2}\right)\right) \right] \end{aligned} \quad (6)$$

where v represents the (m, n) pair known as the mode number where $(m, n) \geq 0$. In the remainder of this paper, we use $v=M$ or N to denote non-incident and incident modes in the waveguide, but these also represent (m, n) pairs. For instance, the TE₁₀ mode has mode indices of $m=1$ and $n=0$. We determine $A'_{v'}$ and $A''_{v'}$ by normalizing (3-6) across the transverse plane of the waveguide:

$$A'_{mn}{}^2 \int_{-\frac{b}{2}}^{\frac{b}{2}} \int_{-\frac{a}{2}}^{\frac{a}{2}} \underline{e}'_{mn}(\underline{\rho}) \bullet \underline{e}'_{kl}(\underline{\rho}) dx dy = \delta_{mk} \delta_{nl}, \quad (7)$$

$$A''_{mn}{}^2 \int_{-\frac{b}{2}}^{\frac{b}{2}} \int_{-\frac{a}{2}}^{\frac{a}{2}} \underline{e}''_{mn}(\underline{\rho}) \bullet \underline{e}''_{kl}(\underline{\rho}) dx dy = \delta_{mk} \delta_{nl}, \quad (8)$$

where δ_{mk} is defined as $\delta_{mk}=0$ for $m \neq k$, $\delta_{mn}=1$ and similarly for δ_{nl} . Solving (8, 9) for the normalization constants yield:

$$A'_{mn} = \left(\frac{2}{\pi}\right) \frac{P_{mn}}{\sqrt{m^2 \frac{a}{b} + n^2 \frac{b}{a}}}, \quad (9)$$

$$A''_{mn} = \left(\frac{\sqrt{\xi_m \xi_n}}{\pi}\right) \frac{P_{mn}}{\sqrt{m^2 \frac{b}{a} + n^2 \frac{a}{b}}}, \quad (10)$$

$$\xi_m, \xi_n = \begin{cases} 1; & m, n = 0 \\ 2; & m, n \geq 1 \end{cases}$$

where P_{mn} is the propagating mode's amplitude.

Taking (3-6) and (9, 10) into account we construct the total transverse fields inside the waveguide for $z \leq 0$:

$$\begin{aligned} \underline{E}_T(\underline{r}) &= \underline{e}''_N(\underline{\rho}) \left(e^{-jk''_N z} + \Gamma''_N(z) e^{+jk''_N z} \right) \\ &\quad + \sum_{M \neq N} \left[\Gamma'_M(z) \underline{e}'_M(\underline{\rho}) e^{+jk'_M z} \right. \\ &\quad \left. + \Gamma''_M(z) \underline{e}''_M(\underline{\rho}) e^{+jk''_M z} \right] \end{aligned} \quad (11)$$

$$\begin{aligned} \underline{H}_T(\underline{r}) = & \frac{\underline{h}''_N(\underline{\rho})}{Z''_N} \left(e^{-jk''_N z} - \Gamma''_N(z) e^{+jk''_N z} \right) \\ & - \sum_{M \neq N} \left[\frac{\Gamma'_M \underline{h}'_M(\underline{\rho}) e^{+jk'_M z}}{Z'_M} \right. \\ & \left. + \frac{\Gamma''_M \underline{h}''_M(\underline{\rho}) e^{+jk''_M z}}{Z''_M} \right], \quad (12) \end{aligned}$$

where Γ_v is the reflection coefficient at the aperture. We define Z'_v , Z''_v , and κ_v as:

$$Z'_v = \frac{\kappa_v}{\omega \mathcal{E}}, \quad (13)$$

$$Z''_v = \frac{\omega \mu}{\kappa_v}, \quad (14)$$

$$\kappa_v = \sqrt{k_o^2 - \left(\frac{m\pi}{a}\right)^2 + \left(\frac{n\pi}{b}\right)^2}. \quad (15)$$

Here k_o is the free space wave number, $(m\pi/a)^2 = k_x^2$, and $(n\pi/b)^2 = k_y^2$. We define the equations for the transverse radiated electric and magnetic fields when $z \geq 0$:

$$\underline{E}_T(\underline{r}) = \frac{1}{(2\pi)^2} \int_{-\infty}^{\infty} \int_{-\infty}^{\infty} \tilde{\underline{E}}_{Tv}(k_{Tv}) e^{-jk_r z} dk_x dk_y, \quad (16)$$

$$\underline{H}_T(\underline{r}) = \frac{1}{(2\pi)^2} \int_{-\infty}^{\infty} \int_{-\infty}^{\infty} \tilde{\underline{H}}_{Tv}(k_{Tv}) e^{-jk_r z} dk_x dk_y, \quad (17)$$

where k_{Tv} represents the mode dependent (k_x, k_y) pair and \sim denotes these components are in the Fourier domain.

III. MODAL DECOMPOSITION MATRIX METHOD

We now equate the vector equations of $\underline{E}_T(\underline{r})$ and $\underline{H}_T(\underline{r})$ of (11, 12) to (16, 17). Doing so equates the TE and TM fields at the waveguide free space boundary of $z=0$ in Fig. 1. The expressions obtained populate the MDM allowing us to solve for the Fourier components of the transverse fields at the aperture of the open waveguide.

A. Derivation of MDM equation

To express the fields at the waveguide free space boundary we equate (11) to (16) and (12) to (17). Setting $z=0$ yields:

$$\begin{aligned} (1 + \Gamma''_N) \underline{e}''_N(\underline{\rho}) \\ + \sum_{M \neq N} \left[\Gamma'_M \underline{e}'_M(\underline{\rho}) + \Gamma''_M \underline{e}''_M(\underline{\rho}) \right], \quad (18) \\ = \frac{1}{(2\pi)^2} \int_{-\infty}^{\infty} \int_{-\infty}^{\infty} \tilde{\underline{E}}_{Tv}(k_{Tv}) e^{-jk_r \cdot \underline{\rho}} dk_x dk_y \end{aligned}$$

$$\begin{aligned} (1 - \Gamma''_N) \frac{\underline{h}''_N(\underline{\rho})}{Z''_N} \\ - \sum_{M \neq N} \left[\Gamma'_M \frac{\underline{h}'_M(\underline{\rho})}{Z'_M} + \Gamma''_M \frac{\underline{h}''_M(\underline{\rho})}{Z''_M} \right], \quad (19) \\ = \frac{1}{(2\pi)^2} \int_{-\infty}^{\infty} \int_{-\infty}^{\infty} \tilde{\underline{H}}_{Tv}(k_{Tv}) e^{-jk_r \cdot \underline{\rho}} dk_x dk_y \end{aligned}$$

The following orthogonality equations [6]:

$$\iint_S \underline{e}_k(\underline{\rho}) \bullet \underline{e}_l(\underline{\rho}) dx dy = \delta_{kl}, \quad (20)$$

$$\iint_S \underline{h}_k(\underline{\rho}) \bullet \underline{h}_l(\underline{\rho}) dx dy = \delta_{kl}, \quad (21)$$

allow us to simplify (18, 19) in terms of Γ_v , $\tilde{\underline{E}}(k_x, k_y)$, and $\tilde{\underline{H}}(k_x, k_y)$, where S is the surface dimensions of the rectangular waveguide. By limiting the bounds of integration in (20, 21), we enforce the boundary condition that $\underline{E}_T(\underline{r}) = 0$ on the conducting surface of the waveguide and flange. Using the following substitutions:

$$\hat{\underline{\alpha}}_v(k_{Tv}) = \iint_S \frac{e^{-jk_{Tv} \cdot \underline{\rho}}}{(2\pi)^2} \underline{\alpha}_v(\underline{\rho}) dx dy, \quad (22)$$

$$\begin{aligned} \iint_S \left[\hat{\underline{t}}_v(k_{Tv}) \bullet \tilde{\underline{T}}_{Tv}(k_{Tv}) \right] dk_x dk_y \\ = \left[\hat{\underline{t}}_v(k_{Tv}), \tilde{\underline{T}}_{Tv}(k_{Tv}) \right], \quad (23) \end{aligned}$$

we can rewrite (18, 19) as the following system of equations:

$$(1 + \Gamma''_N) = \left[\hat{\underline{e}}''_N(k_{TN}), \tilde{\underline{E}}_{TN}(k_{TN}) \right], \quad (24)$$

$$(1 - \Gamma''_N) = Z''_N \left[\hat{\underline{h}}''_N(k_{TN}), \tilde{\underline{H}}_{TN}(k_{TN}) \right], \quad (25)$$

$$\Gamma''_M = \left[\hat{\underline{e}}''_M(k_{TM}), \tilde{\underline{E}}_{TM}(k_{TM}) \right], \quad (26)$$

$$\Gamma''_M = -Z''_M \left[\hat{\underline{h}}''_M(k_{TM}), \tilde{\underline{H}}_{TM}(k_{TM}) \right], \quad (27)$$

$$(1 + \Gamma'_N) = \left[\hat{\underline{e}}'_N(k_{TN}), \tilde{\underline{E}}_{TN}(k_{TN}) \right], \quad (28)$$

$$(1 - \Gamma'_N) = Z'_N \left[\hat{\underline{h}}'_N(k_{TN}), \tilde{\underline{H}}_{TN}(k_{TN}) \right], \quad (29)$$

$$\Gamma'_M = \left[\hat{\underline{e}}'_M(k_{TM}), \tilde{\underline{E}}_{TM}(k_{TM}) \right], \quad (30)$$

$$\Gamma'_M = -Z'_M \left[\hat{\underline{h}}'_M(k_{TM}), \tilde{\underline{H}}_{TM}(k_{TM}) \right], \quad (31)$$

We use equations (24-31) to populate the MDM and solve for the Fourier components of the fields at the aperture. By adding like Γ_v terms together from (24-31) we rewrite the system of equations as:

$$\begin{bmatrix} \hat{e}''_v(k_{Tv}), \tilde{\underline{E}}_T(k_{Tv}) \\ \hat{h}''_v(k_{Tv}), \tilde{\underline{H}}_{Tv}(k_{Tv}) \end{bmatrix} + Z''_v \begin{bmatrix} \hat{h}''_v(k_{Tv}), \tilde{\underline{H}}_{Tv}(k_{Tv}) \\ \hat{e}''_v(k_{Tv}), \tilde{\underline{E}}_T(k_{Tv}) \end{bmatrix} = 2\delta_{vN} \quad (32)$$

$$\begin{bmatrix} \hat{e}'_v(k_{Tv}), \tilde{\underline{E}}_T(k_{Tv}) \\ \hat{h}'_v(k_{Tv}), \tilde{\underline{H}}_{Tv}(k_{Tv}) \end{bmatrix} + Z'_v \begin{bmatrix} \hat{h}'_v(k_{Tv}), \tilde{\underline{H}}_{Tv}(k_{Tv}) \\ \hat{e}'_v(k_{Tv}), \tilde{\underline{E}}_T(k_{Tv}) \end{bmatrix} = 2\delta_{vN} \quad (33)$$

By representing the integrals in k space as a Riemann Sum over k_x and k_y , we will formulate the MDM equation. Simplifying (32, 33), we write $\tilde{\underline{H}}_{Tv}(k_{Tv})$ in terms of $\tilde{\underline{E}}_{Tv}(k_{Tv})$ leaving a single unknown. Starting with the expression:

$$\begin{aligned} \tilde{\underline{H}}_{Tv}(k_x, k_y) &= \frac{1}{\omega\mu_o} \left[\left(\underline{z}_o \times \tilde{\underline{E}}_{Tv}(k_{Tv}) \right) k_{zv} \right. \\ &\quad \left. - \left(\frac{k_{Tv} \times \underline{z}_o}{k_{zv}} \right) \left(k_{Tv} \bullet \tilde{\underline{E}}_{Tv}(k_{Tv}) \right) \right] \end{aligned} \quad (34)$$

we form the matrix equation:

$$\begin{aligned} \tilde{\underline{H}}_{Tv}(k_{Tv}) &= \begin{bmatrix} \tilde{\underline{H}}_{xv}(k_{Tv}) \\ \tilde{\underline{H}}_{yv}(k_{Tv}) \end{bmatrix} = \underline{\underline{A}} \bullet \tilde{\underline{E}}_{Tv}(k_{Tv}) \\ &= \begin{bmatrix} \underline{\underline{A}}_{xx} & \underline{\underline{A}}_{xy} \\ \underline{\underline{A}}_{yx} & \underline{\underline{A}}_{yy} \end{bmatrix} \begin{bmatrix} \tilde{\underline{E}}_{xv}(k_{Tv}) \\ \tilde{\underline{E}}_{yv}(k_{Tv}) \end{bmatrix} \end{aligned} \quad (35)$$

We solve for $\underline{\underline{A}}$ by expanding (33) as:

$$\underline{\underline{A}} \bullet \tilde{\underline{E}}_{Tv} = \tilde{\underline{H}}_{Tv} = \frac{K_v}{\omega\mu_o k_v} \bullet \tilde{\underline{E}}_{Tv} \quad (36)$$

$$\underline{\underline{K}}_v = \begin{bmatrix} -k_x k_y & -(k_o^2 - k_x^2) \\ k_o^2 - k_y^2 & k_x k_y \end{bmatrix} \quad (37)$$

where k_x and k_y are mode number dependent.

Equations (36, 37) are a shorthand notation representing the system of equations that construct our MDM equation. However, longhand notation will better demonstrate how (36) maps to a system of equations. We express (36) by a set of two the Riemann sums over k_x and k_y :

$$\sum_{k_y} \sum_{k_x} \left[\left(\hat{e}''_v(k_{Tv}) + Z''_v \underline{\underline{A}} \bullet \hat{h}''_v(k_{Tv}) \right) \bullet \tilde{\underline{E}}_{Tv}(k_{Tv}) \right] \Delta k_x \Delta k_y = \delta_{vN} \quad (38)$$

$$\sum_{k_y} \sum_{k_x} \left[\left(\hat{e}'_v(k_{Tv}) + Z'_v \underline{\underline{A}} \bullet \hat{h}'_v(k_{Tv}) \right) \bullet \tilde{\underline{E}}_{Tv}(k_{Tv}) \right] \Delta k_x \Delta k_y = \delta_{vN} \quad (39)$$

We can now write the MDM from (38, 39) to solve directly for $\tilde{\underline{E}}_{Tv}$ with no need to invoke a Fourier transform. In doing so, each value of v represents a different waveguide mode corresponding to the MDM row index. Each value of v also represents a discrete index of k_x and k_y corresponding to the MDM column index. This creates a square matrix with a total of L samples of k_x and k_y , as well as L modes.

Note from (22) that $\underline{\alpha}_v(\rho)$ still includes an \underline{x}_o and \underline{y}_o vector dependence. If we let,

$$\underline{\underline{M}}''_{vx}(k_{Tv}) = \begin{bmatrix} \hat{e}''_v(k_{Tv}) \\ \hat{h}''_v(k_{Tv}) \end{bmatrix} \bullet \tilde{\underline{E}}_{Tv}(k_{Tv}) \bullet \underline{x}_o + Z''_v \underline{\underline{A}} \bullet \begin{bmatrix} \hat{h}''_v(k_{Tv}) \\ \hat{e}''_v(k_{Tv}) \end{bmatrix} \bullet \tilde{\underline{E}}_{Tv}(k_{Tv}) \bullet \underline{x}_o \quad (40)$$

$$\underline{\underline{M}}''_{vy}(k_{Tv}) = \begin{bmatrix} \hat{e}''_v(k_{Tv}) \\ \hat{h}''_v(k_{Tv}) \end{bmatrix} \bullet \tilde{\underline{E}}_{Tv}(k_{Tv}) \bullet \underline{y}_o + Z''_v \underline{\underline{A}} \bullet \begin{bmatrix} \hat{h}''_v(k_{Tv}) \\ \hat{e}''_v(k_{Tv}) \end{bmatrix} \bullet \tilde{\underline{E}}_{Tv}(k_{Tv}) \bullet \underline{y}_o \quad (41)$$

$$\underline{\underline{M}}'_{vx}(k_{Tv}) = \begin{bmatrix} \hat{e}'_v(k_{Tv}) \\ \hat{h}'_v(k_{Tv}) \end{bmatrix} \bullet \tilde{\underline{E}}_{Tv}(k_{Tv}) \bullet \underline{x}_o + Z'_v \underline{\underline{A}} \bullet \begin{bmatrix} \hat{h}'_v(k_{Tv}) \\ \hat{e}'_v(k_{Tv}) \end{bmatrix} \bullet \tilde{\underline{E}}_{Tv}(k_{Tv}) \bullet \underline{x}_o \quad (42)$$

$$\underline{\underline{M}}'_{vy}(k_{Tv}) = \begin{bmatrix} \hat{e}'_v(k_{Tv}) \\ \hat{h}'_v(k_{Tv}) \end{bmatrix} \bullet \tilde{\underline{E}}_{Tv}(k_{Tv}) \bullet \underline{y}_o + Z'_v \underline{\underline{A}} \bullet \begin{bmatrix} \hat{h}'_v(k_{Tv}) \\ \hat{e}'_v(k_{Tv}) \end{bmatrix} \bullet \tilde{\underline{E}}_{Tv}(k_{Tv}) \bullet \underline{y}_o \quad (43)$$

then we populate the MDM equation using (40-43) and a matrix of four $L \times L$ quadrants:

$$\begin{bmatrix} \underline{\underline{M}}''_{vx} & \underline{\underline{M}}''_{vy} \\ \underline{\underline{M}}'_{vx} & \underline{\underline{M}}'_{vy} \end{bmatrix} \bullet \begin{bmatrix} \tilde{\underline{E}}_x(k_{Tv}) \\ \tilde{\underline{E}}_y(k_{Tv}) \end{bmatrix} = \begin{bmatrix} 2\delta''_{vN} \\ 2\delta'_{vN} \end{bmatrix} \quad (44)$$

$$\underline{\underline{M}}''_{vx} = \begin{bmatrix} M''_{1x}(k_{T1}) & \cdots & M''_{1x}(k_{TL}) \\ \vdots & \ddots & \vdots \\ M''_{Lx}(k_{T1}) & \cdots & M''_{Lx}(k_{TL}) \end{bmatrix} \quad (45)$$

$$\underline{\underline{M}}''_{vy} = \begin{bmatrix} M''_{1y}(k_{T1}) & \cdots & M''_{1y}(k_{TL}) \\ \vdots & \ddots & \vdots \\ M''_{Ly}(k_{T1}) & \cdots & M''_{Ly}(k_{TL}) \end{bmatrix} \quad (46)$$

$$\underline{\underline{M}}'_{vX} = \begin{bmatrix} M'_{1x}(k_{T1}) & \cdots & M'_{1x}(k_{TL}) \\ \vdots & \ddots & \vdots \\ M'_{Lx}(k_{T1}) & \cdots & M'_{Lx}(k_{TL}) \end{bmatrix}, \quad (47)$$

$$\underline{\underline{M}}'_{vY} = \begin{bmatrix} M'_{1y}(k_{T1}) & \cdots & M'_{1y}(k_{TL}) \\ \vdots & \ddots & \vdots \\ M'_{Ly}(k_{T1}) & \cdots & M'_{Ly}(k_{TL}) \end{bmatrix}, \quad (48)$$

$$\tilde{\underline{E}}_{xv}(k_{Tv}) = \begin{bmatrix} \tilde{E}_{x1}(k_{T1}) & \cdots & \tilde{E}_{xL}(k_{TL}) \end{bmatrix}^T, \quad (49)$$

$$\tilde{\underline{E}}_{yv}(k_{Tv}) = \begin{bmatrix} \tilde{E}_{y1}(k_{T1}) & \cdots & \tilde{E}_{yL}(k_{TL}) \end{bmatrix}^T, \quad (50)$$

$$2\tilde{\underline{\delta}}'_{vN} = [2 \ 0 \ \cdots \ 0]^T, \quad (51)$$

$$2\tilde{\underline{\delta}}'_{vN} = [0 \ 0 \ \cdots \ 0]^T. \quad (52)$$

Quadrant $\underline{\underline{M}}'_{vX}$ corresponds to elements that represent TE modes in the \underline{x}_o direction, quadrant $\underline{\underline{M}}'_{vY}$ corresponds to elements that represent TE modes in the \underline{y}_o direction, quadrant $\underline{\underline{M}}'_{vX}$ corresponds to elements representing TM modes in the \underline{x}_o direction, and quadrant $\underline{\underline{M}}'_{vY}$ corresponds to elements representing TM modes in the \underline{y}_o direction. We separate the \underline{x}_o components and \underline{y}_o components to obtain individual solutions to $\tilde{\underline{E}}_{xv}(k_{Tv})$ and $\tilde{\underline{E}}_{yv}(k_{Tv})$ at $z=0$. Each MDM quadrant is $L \times L$ in dimension yielding a $2L \times 2L$ matrix. The solutions to $\tilde{\underline{E}}_{xv}(k_{Tv})$ and $\tilde{\underline{E}}_{yv}(k_{Tv})$ are size L column vectors. The right hand side column vector of equation (44) is zero except for the first element that corresponds to the propagating TE₁₀ mode.

As with any numerical approximation to a continuous function, L must be large enough to ensure an accurate representation of the original function. However, a large L necessitates using many weak attenuating modes in the MDM equation. This leads to a singular matrix, which is not invertible. Therefore, in solving (44) we must use singular value decomposition (SVD) to determine the inverse of the MDM [10].

When using the SVD method the number of singular values used to generate the inverse of the MDM in (44) plays a crucial role. A matrix with dimensions $2L \times 2L$ will have $2L$ singular values. Many of the singular values will have magnitudes approaching zero. The calculation should not use these values or they will skew the accuracy of the numerical results. On the other hand, if you have multiple singular values with large magnitudes then eliminating any of them will also skew the results. Figure 2 shows the singular values in descending order for a 24-mode MDM calculation. The number of singular values used for this particular calculation is 5.

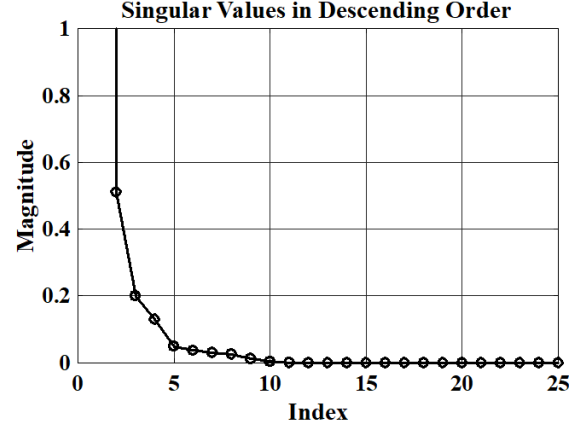


Fig. 2. Plot of singular values of a 24 mode MDM in descending order.

B. Representation of k_x and k_y outside the waveguide

This section describes how to represent the values of k_x and k_y in the MDM equation. Since it is desirable to represent the radiated far field in spherical coordinates (r, θ, ϕ) , we must map k_x and k_y to spherical coordinates to use in the stationary phase calculation.

The far field stationary phase approximation is well known and widely used throughout the literature [6, 11]. We repeat the equation here for convenience:

$$\underline{E}(r, \theta, \phi) \approx j \frac{ke^{-jkr}}{2\pi r} \left[\underline{\theta}_o \left\{ \tilde{E}_x \cos \phi + \tilde{E}_y \sin \phi \right\} - \underline{\phi}_o \cos \theta \left(\tilde{E}_x \sin \phi + \tilde{E}_y \cos \phi \right) \right]. \quad (53)$$

Mapping k_x and k_y to spherical coordinates yields:

$$k_x = k_o \sin(\theta) \cos(\phi), \quad (54)$$

$$k_y = k_o \sin(\theta) \sin(\phi). \quad (55)$$

In order to get a hemisphere mapping of the radiated electric field in the positive propagation direction, we are interested in $-\pi/2 \leq \theta \leq \pi/2$ and $0 \leq \phi \leq \pi/2$. After substituting these values of θ and ϕ into (54, 55), we get a trajectory of k_x and k_y inside a circle of radius k_o as shown in Fig. 3 and Fig. 4.

Figure 3 shows all the k_x and k_y values obtained for $\phi=0$ and $\Delta\theta=1/L$ where L corresponds to the size of each quadrant in (44). The angle of ϕ is represented in Fig. 3 as the angle between the k_x and k_y axes. Since $\phi=0$, all the k_x and k_y values fall on the $k_y=0$ axis. If we use $\phi=\pi/4$ to calculate k_x and k_y , as in Fig. 4, then we see that the values of k_x and k_y fall on a trajectory that makes an angle of $\pi/4$ with the $k_y=0$ axis.

Note that in both Figs. 3 and 4 an equal spacing between values of θ does not result in an equal spacing in k_x and k_y . In addition, any value of k_x and k_y that falls

on the k_o radius yields a value of $|k_T| = k_o$ which corresponds to $\kappa=0$. Any value of k_x and k_y that falls beyond the k_o radius corresponds to an imaginary value of κ . These values represent attenuating modes.

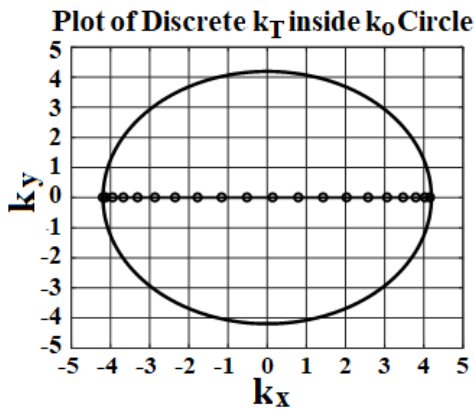


Fig. 3. Plot of k_x and k_y obtained for $\phi=0$.

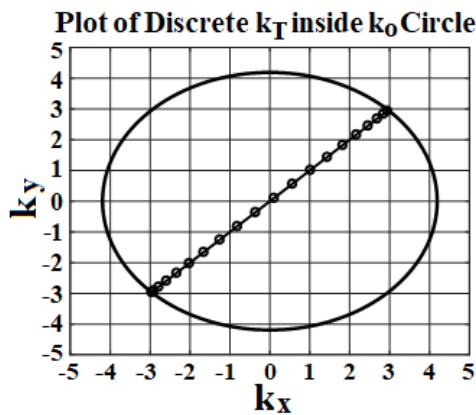


Fig. 4. Plot of k_x and k_y obtained for $\phi= \pi/4$.

IV. ANALYSIS AND COMPARISON TO SIMULATION

We compare the far field patterns and return loss at the air-interface boundary of the waveguide calculated from the MDM method to those generated using 3D EM modeling software. We performed the MDM calculations using Matlab 2017a and simulations with CST Studio Suite 2017 for comparison.

A. Computer model

The transverse dimensions of the waveguide are $\lambda_o/2$ in the x_o direction at 200 megahertz (MHz) and $\lambda_o/4$ in the y_o direction. As long as $a \geq 2b$ in Fig. 1, the dominant mode will be the TE₁₀ mode [9]. The propagation of the dominant mode begins at $f_c=200$ MHz and the propagation of the second mode begins at $2f_c=400$ MHz. For frequencies below 200 MHz no modes will propagate

in the waveguide, and for frequencies above 400 MHz more than one mode will propagate.

The distribution of the propagating TE₁₀ mode generated by a matched waveguide port is a cosine distribution across the waveguide with units of volts per meter (V/m). This is the expected mode distribution for the TE₁₀ mode [9]. The mode distribution peaks and is symmetric about the center of the transverse plane of the waveguide. The mode distribution does not vary in the z_o direction because it is a propagating mode.

B. MDM results and comparison

The calculations and simulations of the far field radiation patterns are determined for a frequency of 300 MHz. We chose this frequency because it stands far away from both f_c and $2f_c$. Figure 5 shows the far field patterns of E_θ and E_ϕ plotted in polar coordinates, and Fig. 6 shows the same patterns plotted in Cartesian coordinates. Figure 7 shows a calculation of the return loss based on the reflection of the TE₁₀ mode at the air interface of the flanged rectangular waveguide.

E_θ and E_ϕ Far Field Radiation Patterns

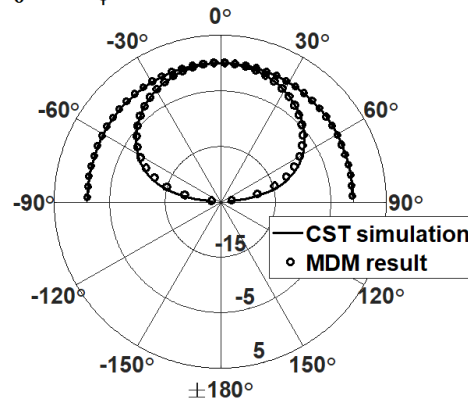


Fig. 5. Polar plot of the normalized E_θ and E_ϕ patterns.

E_ϕ and E_θ Far Field Radiation Patterns

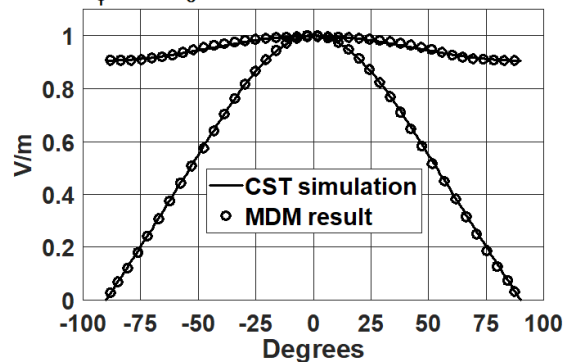


Fig. 6. Cartesian plot of the normalized E_θ and E_ϕ patterns.

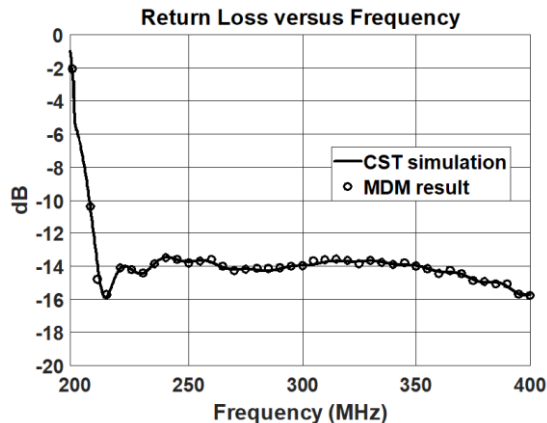


Fig. 7. Plot of return loss versus frequency for the TE_{10} mode at the waveguide air-interface boundary.

These calculations all assume an air-filled waveguide. The results show excellent agreement between the results of the MDM method and those generated by CST. In particular, the return loss at the boundary shown in Fig. 7 demonstrates the accuracy of the mode coefficients calculated using the MDM method to generate these results.

V. CONCLUSION

Traditional methods for analysis of the EM fields at the aperture of an infinitely flanged radiating rectangular waveguide require the computation of the Fourier transform of the EM fields prior to use of stationary phase. These approaches introduce additional computational costs to performing calculations of radiated far fields for this type of problem. We derive a new approach called the MDM method that allows for the direct computation EM fields at the aperture in the Fourier domain, which eliminates the need to make additional computations to obtain the Fourier transform. The result is a matrix equation that directly solves for the Fourier components needed for the far field stationary phase calculations. The results of the MDM method are in agreement with the far field radiation patterns and return loss versus frequency of an infinitely flanged radiating rectangular waveguide generated by CST. The high fidelity of agreement validates the accuracy of the less computationally expensive MDM formulation.

REFERENCES

- [1] R. MacPhie and A. Zaghoul, "Radiation from a rectangular waveguide with infinite flange: Exact solution by correlation matrix," *IEEE Trans. Antennas Propagat.*, vol. AP-28, pp. 497-503, July 1980.
- [2] H. Baudrand, J. Tao, and J. Atechian, "Study of radiation properties of open-ended rectangular waveguides," *IEEE Trans. Antennas Propagat.*, vol. 36, no. 8, pp. 1071-1077, Aug. 1988.
- [3] H. Serizawa and K. Hongo, "Radiation for a

flanged rectangular waveguide," *IEEE Trans. Antennas Propagat.*, vol. 53, no. 12, pp. 3953-3962, Dec. 2005.

- [4] W. Coburn, T. Anthony, and A. Zahgloul, "Open-ended waveguide radiation characteristics – full-wave simulation versus analytical solutions," *APS International Symposium, 2010 IEEE*, 2010.
- [5] C. Balanis, *Antenna Theory: Analysis and Design*. 4th ed., Hoboken, NJ: Wiley and Sons Inc., 2005.
- [6] G. Mitchell and W. Wasykiwskyj, "MDM Method for Directly Calculating the Far Field of an Open Rectangular Waveguide with an Infinite Flange," No. ARL-TR-6536, 2013.
- [7] L. Felsen and N. Maruvitz, *Radiation and Scattering of Waves*. Englewood Cliffs, NJ: Prentice Hall Inc., 1973.
- [8] N. Marcuvitz, *Waveguide Handbook*. New York, NY: McGraw-Hill, 1951.
- [9] David Pozar, *Microwave Engineering*. 3rd ed., John Wiley and Sons, 2005.
- [10] G. Strang, *Introduction to Linear Algebra*. 4th ed. Wellesley, MA: Cambridge Press, 2009.
- [11] A. Ishimaru, *Electromagnetic Wave Propagation, Radiation, and Scattering*. Upper Saddle River, NJ: Prentice Hall, 1991.



Gregory A. Mitchell received his B.S. from the University of Maryland in 2005, his M.S. from The Johns Hopkins University in 2008, and his Ph.D. from The George Washington University in 2015. From 2003 to present, he has been an RF and Antenna Integration Engineer with the U.S. Army Research Laboratory. Research interests include broadband magnetic RF substrates, phased array antennas, and additive manufacturing for antennas. He is a Member of IEEE APS, ACES, and the U.S. National Committee for the International Union of Radio Science Commission A.

Wasył Wasykiwskyj received the B.E.E. degree from the City University of New York in 1957 and the M.S. and Ph.D. degrees in Electrical Engineering from Polytechnic University, Troy, NY, in 1965 and 1968, respectively. His past research and industrial experience covers a broad spectrum of electromagnetics, including microwave components and techniques, phased array antennas, propagation and scattering, radar cross-section modeling as well as modeling of geophysical and oceanographic electromagnetic phenomena. Since 1985, he has held the position of Professor of Engineering and Applied Science at the George Washington University, Washington, DC.

Using Superformula to Miniaturize CPW Rat Race Coupler

Amjad A. Omar¹ and Nihad I. Dib²

¹Department of Electrical, Electronics, and Communications Engineering
American University of Ras Al Khaimah, Ras Al Khaimah, UAE
amjad.omar@aurak.ac.ae

²Department of Electrical Engineering
Jordan University of Science and Technology, Irbid, Jordan
nihad@just.edu.jo

Abstract — This paper proposes a new CPW rat race coupler whose shape has been meandered using the superformula for size reduction. The coupler operates at a center frequency of 1.8 GHz. The size reduction in the proposed design is about 74% as compared to conventional ring rat race coupler. The bandwidth of the proposed coupler defined by $|S_{11}| < -15$ dB is about 31.6%.

Index Terms — Coplanar waveguide, rat-race coupler, superformula.

I. INTRODUCTION

Rat race couplers have been attracting much attention lately for use in several applications such as in mixers, multipliers, amplifiers, beamformers, etc [1-5]. One of the disadvantages with these couplers is that their circumference is large ($3\lambda/2$), where λ is the wavelength at the operating frequency. This makes circuit miniaturization very important.

Several techniques have been used to miniaturize the size of the rat race coupler. This includes the use of phase inverters to reduce the length of the $3\lambda/2$ arm [6]. It also includes the use of Microstrip-to-CPW Broadside-Coupled Structure with Stepped-Impedance Sections [2]. Miniaturization has also been achieved using six synthesized coplanar waveguide (CPW) cells, formed by meander line inductors, parallel-plate capacitors, and interdigital capacitors [7].

This paper attempts to miniaturize the rat race coupler using the superformula that was proposed by John Gielis in the year 2003 [8]. This formula is a generalization of the super ellipse formula. It is used to meander the circumference of the coupler so as to reduce its size. This works as follows; the circumference of the conventional circular coupler ($3\lambda/2$) remains almost the same when the ring CPW is meandered and bent. This has the effect of reducing the radius and hence the surface area of the meandered coupler as compared with the conventional coupler.

The superformula has six different parameters which when properly selected can produce many complex shapes and curves that are found in nature. It has been used by Simeone *et al.* [9] to produce dielectric resonator antennas of different shapes. It has also been used by Bia *et al.* to produce supershaped lens antennas for high frequency applications [10]. Paraforou [11] applied the superformula to get different patch antenna shapes. The same formula has also been used by Naser and Dib [12] to design a compact UWB microstrip-fed patch antenna. More recently, the superformula was used by Omar *et al* [13, 14] to design UWB CPW fed patch antenna that operates in the FCC band (3.1-10.6 GHz) where the proposed patch shape was circular with sawtooth-like circumference.

In this paper, the transmission line element used is coplanar waveguide which enjoys several advantages over microstrip in terms of easier integration with active and passive elements and with shunt and series elements in addition to the more versatility of controlling the characteristic impedance of CPW by controlling the slot-to-strip width ratio.

The basic rat race coupler has 4 ports each of which has 50Ω impedance, while the CPW forming the ring has a 70Ω impedance.

II. COUPLER DESIGN

The superformula proposed by Gielis [8] is a polar formula which has the general form:

$$r = \left[\left| \frac{\cos(\frac{m\theta}{4})}{a} \right|^{n_2} + \left| \frac{\sin(\frac{m\theta}{4})}{b} \right|^{n_3} \right]^{\frac{-1}{n_1}}. \quad (1)$$

The superformula consists of six parameters $n_1, n_2, n_3, m, a,$ and b . Each of the parameters a and b must be chosen to be 1 to insure symmetry of the coupler geometry. The parameters $n_1, n_2,$ and n_3 are positive real numbers. The number m determines the number of points, corners, sectors, or hollows fixed on the shape and their spacing, while n_2 and n_3 determine if the shape is inscribed

or circumscribed in the unit circle. For $n_2=n_3 < 2$, the shape is inscribed, while for $n_2=n_3 > 2$, the shape will sumscribe the circle [8]. In this design, the chosen superformula parameters are $n_1=n_2=n_3=1$, $a=b=1$, $m=24$ (corresponding to 24 bends on the meandered ring). The general shape of the coupler is shown in Fig. 1.

The proposed coupler was designed for operation at 1.8 GHz using CPW on a 1.5 mm thick FR4 substrate ($\epsilon_r=4.4$, loss tangent=0.02). The feeding CPW center conductor is 2.74 mm, and the slot is 0.3 mm resulting in 50 Ω feed line. Bond wires are used to connect the two grounds on either sides of the center conductor, as shown in Fig. 1, for elimination of the undesired coupled slotline mode. The performance of the coupler with and without bond wires is given in Section IV.

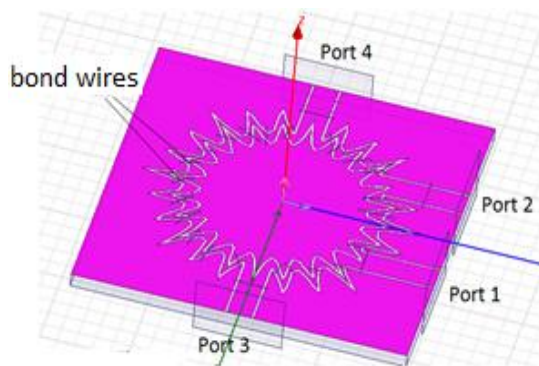


Fig. 1. 3-D view of the simulated rat race coupler.

A. Design procedure

The superformula (Eq. (1)) is programmed in MATLAB to get the data (points) of one of the meandered ring slots shown in Fig. 1, with $n_1=n_2=n_3=1$, $a=b=1$, $m=24$ in Eq. (1). Note that $m=24$ corresponds to the number of bends on the meandered slotted ring. These points are then entered in Excel to generate (x,y) pairs. These pairs are entered in Autocad to draw a polyline shape of the slot ring shown in Fig. 1. The shape generated in Autocad is imported in the simulator HFSS.

The initial dimension of the slot ring is scaled to $3\lambda/2$ at 1.8 GHz (including the meander lengths, with bends). The ring slot is then duplicated and reduced in size to form the other slotted ring and then the 4 ports are added as numbered in Fig. 1, with feeding CPW port center conductor = 2.74 mm, and slot = 0.3 mm resulting in 50 Ω feed lines. Note that the CPW circular ring has an impedance of about 70 Ω (with slot=0.3 mm and center conductor=0.68 mm). The overall dimension of the proposed coupler is 38.4 x 38.4 x 1.5 mm.

The conventional rat race coupler has circular slotted rings (no meander). The circumference of the outermost slotted circle is $3\lambda/2$ at 1.8 GHz (corresponding to a radius of $a=24.5$ mm) and a total surface area of $\pi a^2=1885$ mm². The area of the meandered coupler is obtained using the

“measure surface area” option in HFSS.

III. MEASUREMENTS

The designed coupler was fabricated and built in our lab to measure the S-parameters. A photograph of the measured coupler is shown in Fig. 2 (without bond wires). A second photograph showing the coupler with bond wires and connectors is shown in Fig. 3. Figure 1 shows that ports 1 and 2 are close from each other. This prevented us from measuring the 4 port S-parameters and allowed only measuring 3 port S-parameters with port 2 matched to a 50 Ω load, as shown in Fig. 3.

The design is simulated using high-frequency structure simulation (HFSS). Moreover, the validity of the design is demonstrated by measuring the divider using an E5071C ENA Vector Network Analyzer using standard SMA connectors.

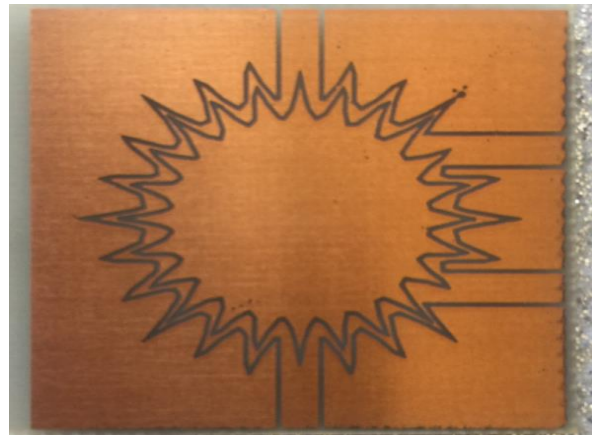


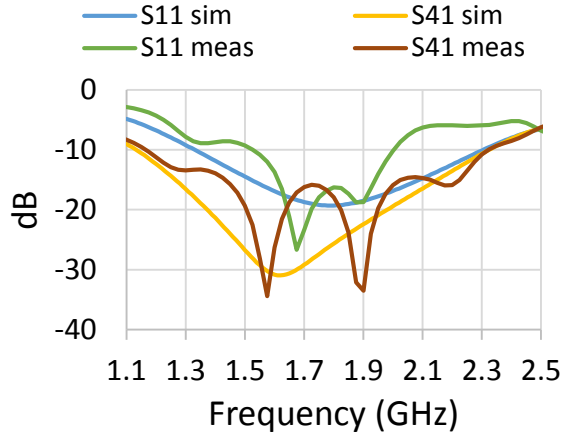
Fig. 2. A photograph of the measured coupler (no bond wires).



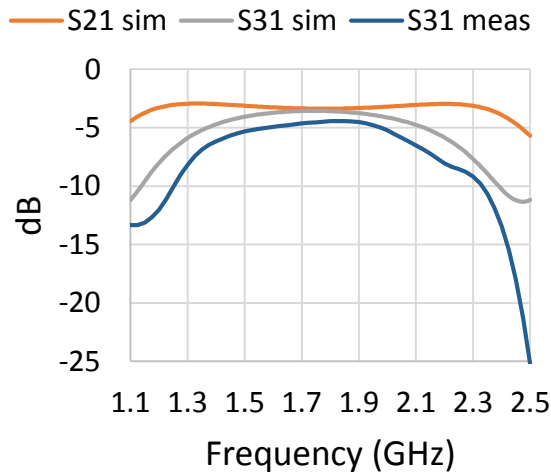
Fig. 3. A photograph of the measured coupler with bond wires and connectors (port 2 is match terminated).

IV. NUMERICAL AND MEASURED RESULTS

Figures 4 (a), (b) show comparison between the numerical results obtained using HFSS and the measured results with port 2 excluded from the measured data. This figure shows good agreement between the two over the operating frequency range. It also shows very good input port matching and very good isolation between ports 1 and 4 at the design frequency. Moreover, S_{21} and S_{31} are close to -3 dB at 1.8 GHz.



(a)



(b)

Fig. 4. (a) Comparison between measured and simulated S_{11} and S_{41} (with bond wires). (b) Comparison between measured and simulated S_{21} and S_{31} (with bond wires). S_{21} was not measured.

Figure 5 below shows the simulated angles of selected S-parameters. The angles of S_{21} and S_{31} are almost the same while the difference between the angles

of S_{34} and S_{24} is about 180° .

The bond wires are important to suppress the undesired coupled slot line (even) mode and allow for the dominant CPW (odd) mode to propagate, hence reducing loss and improving performance. This is shown in Figs. 6 (a), (b) which provide a comparison between the performance of the coupler with and without bond wires. Clearly without bond wires, the return loss reduces to around 10 dB instead of 20 dB with bond wires. Also S_{21} and S_{31} are no longer equal at 1.8 GHz. The bond wire locations are shown in Fig. 1 and Fig. 3.

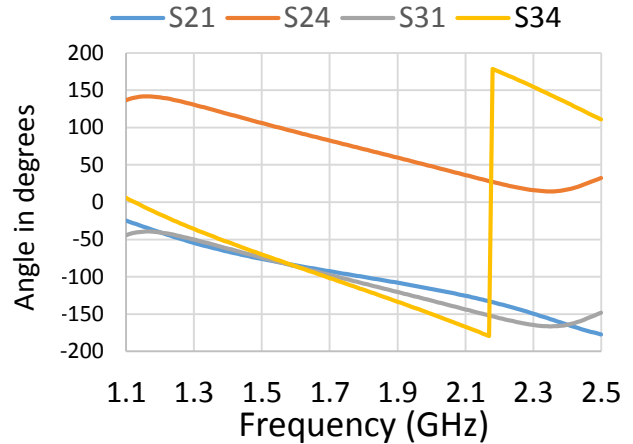
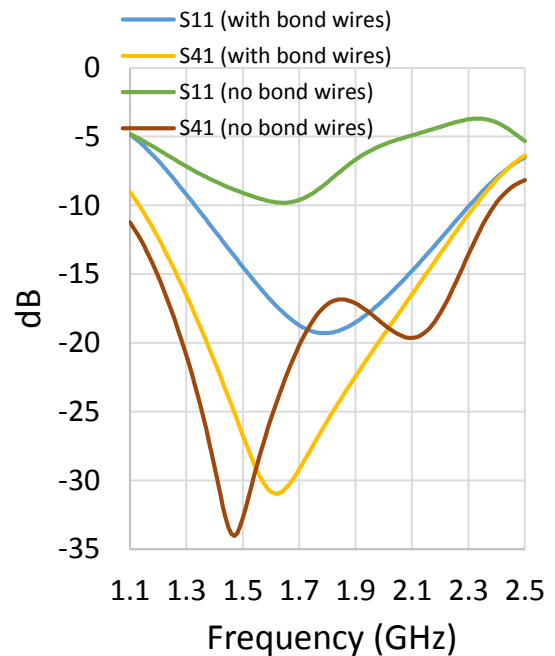
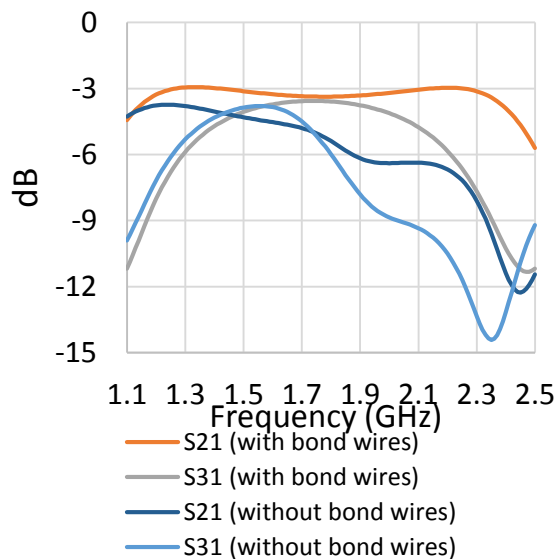


Fig. 5. Simulated angles of S-parameters versus frequency (with bond wires).



(a)



(b)

Fig. 6. (a) Comparison between simulated S_{11} and S_{41} with and without bond wires. (b) Comparison between simulated S_{21} and S_{31} with and without bond wires.

V. SIZE REDUCTION

Table 1 shows a comparison between the size of the proposed rat-race coupler and other sizes presented in the literature.

Table 1: Comparison between the sizes of different couplers

Paper	ϵ_r	Operating Frequency	Proposed Coupler Area/ Conventional Coupler Area
This paper	4.4	1.8 GHz	26%
[1]	2.2	2.5 GHz	41.8%
[16]	2.94	3 GHz	77%
[17]	2.65	5 GHz	45%
[18]	2.5	5 GHz	55.2%

This table shows that the coupler proposed in this paper has more size reduction as compared to the other couplers investigated in Table 1. Note that the conventional coupler area is about 1885 mm².

VI. BANDWIDTH OF COUPLER

Table 2 shows the simulated bandwidth of the proposed coupler using 4 different definitions of bandwidth [1].

VII. CONCLUSION

This paper proposed a new design of coplanar waveguide rat race coupler operating at 1.8 GHz. The size of the coupler has been reduced using the

superformula yielding about 74% size reduction as compared with conventional ring rat race coupler. The proposed coupler has a bandwidth of about 32%.

Table 2: Simulated bandwidth of the proposed coupler

Definition	$ S_{11} < -15$ dB (Input Matching)	$ S_{41} < -20$ dB (Isolation)	$\angle S_{21} - \angle S_{31} = \pm 5^\circ$	$\angle S_{24} - \angle S_{34} = 180 \pm 5^\circ$
Freq. Range (GHz)	1.52-2.09	1.37-1.98	1.17-1.7	1.48-1.72
% Bandwidth	31.6%	33.8%	29.4%	13.3%

REFERENCES

- [1] J.-T. Kuo and C. H. Tsai, "Generalised synthesis of rat race ring coupler and its application to circuit miniaturization," *Progress in Electromagnetics Research*, vol. 108, pp. 51-64, 2010.
- [2] Y.-C. Chiou, J.-S. Wu, and J.-T. Kuo, "Miniaturized $7\lambda/6$ rat race coupler with microstrip-to-CPW broadside-coupled structure and stepped impedance sections," *Asia Pacific Microwave Conference*, Dec. 2008.
- [3] H.-X. Xu, G.-M. Wang, and K. Lu, "Microstrip rat-race couplers," *IEEE Microwave Magazine*, pp. 117-129, 2011.
- [4] M. Shirazi, R. Sarraf Shirazi, G. Moradi, and M. Shirazi, "Three new rat-race couplers with defected microstrip and ground structures," *ACES Journal*, vol. 28, no. 4, pp. 300-306, 2013.
- [5] R. Dehdasht-Heydari, K. Forooraghi, and M. Naser-Moghadasi, "Efficient and accurate analysis of a substrate integrated waveguide (SIW) rat-race coupler excited by four U-shape slot-coupled transitions," *ACES Journal*, vol. 30, no. 1, pp. 42-49, 2015.
- [6] C.-Y. Chang and C.-C. Yang, "A novel broad-band Chebyshev-response rat-race ring coupler," *IEEE Trans. On Microwave Theory Tech.*, vol. 47, pp. 455-462, 1999.
- [7] H.-C. Chiu, C.-H. Lai, and T.-G. Ma, "Miniaturized rat-race coupler with out-of-band suppression using double-layer synthesized coplanar waveguide," *2012 IEEE MTT-S International Microwave Symp. Digest*, June 2012.
- [8] J. Gielis, "A generic geometric transformation that unifies a wide range of natural and abstract shapes," *American Journal of Botany*, vol. 90, pp. 333-338, 2003.
- [9] M. Simeoni, R. Cicchetti, A. Yarovoy, and D. Caratelli, "Circularly polarized supershaped dielectric resonator antennas for indoor ultrawide band applications," *IEEE Int. Symp. Antennas Propag.*, Toronto, July 2010.

- [10] P. Bia, D. Caratelli, L. Mescia, and J. Gielis, "Electromagnetic characterization of supershaped lens antennas for high-frequency applications," *43rd European Microw. Conf. Proc.*, Nuremberg, Oct. 2013.
- [11] V. Paraforou, "Design and Full-wave Analysis of Supershaped Patch Antennas," *Master Thesis*, Delft University of Technology, Delft, Netherlands, 2013.
- [12] S. Naser and N. Dib, "Design and analysis of superformula-based UWB monopole antenna and its MIMO configuration," *Wireless Personal Communications*, vol. 94, pp. 1-13, 2016.
- [13] A. Omar, M. Rashad, M. Al-Mulla, H. Attia, S. Naser, N. Dib, and R. M. Shubair, "Compact design of UWB CPW-fed-patch antenna using the superformula," *5th Int. Conf. on Electronic Devices, Systems, and Applications (ICEDSA-2016)*, UAE, Dec. 2016.
- [14] A. Omar, S. Naser, M. I. Hussein, N. I. Dib, and M. W. Rashad, "Superformula-based compact UWB CPW-fed-patch antenna with and without dual frequency notches," *ACES Journal*, vol. 32, no. 11, pp. 979-986, 2017.
- [15] A. Omar and Y. L. Chow, "A solution of coplanar waveguides with airbridges using complex images," *IEEE Trans. Microwave Theory Tech.*, vol. 40, no. 11, pp. 2070-2077, Nov. 1992.
- [16] K. M. Shum, Q. Xue, and C. H. Chan, "A novel microstrip ring hybrid incorporating a PBG cell," *IEEE Microwave Wireless Compon. Letters*, vol. 11, pp. 258-260, 2001.
- [17] J. Gu and X. Sun, "Miniaturization and harmonic suppression rat-race coupler using C-SCMRC resonators with distributive equivalent circuits," *IEEE Microwave Wireless Compon. Letters*, vol. 15, pp. 880-882, 2005.
- [18] Y. J. Sung, C. S. Ahn, and Y. S. Kim, "Size reduction and harmonic suppression of rat-race hybrid coupler using defected ground structure," *IEEE Microwave Wireless Compon. Letters*, vol. 14, pp. 7-9, 2004.



Amjad A. Omar is a Professor at the Department of Electrical, Electronics, and Communications Engineering at the American University of Ras Al Khaimah (AURAK). He received his Ph.D. in 1993 in Electrical Engineering/Electromagnetics from the University of Waterloo in Canada. He started his career as a Researcher at the Communications Research Center in Ottawa where he worked for 2 years (1993-1994) on the simulation and testing of monolithic microwave integrated circuits. He then worked at several universities in Jordan, UAE, and KSA. He was promoted to Full Professor in Electrical Engineering in January 2014. His research interests are in antennas, numerical electromagnetics, RF circuit design and analysis, NDT for oil and gas, and biological effects of EM radiation on humans.



Nihad I. Dib obtained his B.Sc. and M.Sc. in Electrical Engineering from Kuwait University in 1985 and 1987, respectively. He obtained his Ph.D. in EE (major in Electromagnetics) in 1992 from University of Michigan, Ann Arbor. Then, he worked as an Assistant Research Scientist in the radiation laboratory at the same school. In Sep. 1995, he joined the EE department at Jordan University of Science and Technology (JUST) as an Assistant Professor, and became a Full Professor in Aug. 2006. His research interests are in computational electromagnetics, antennas and modeling of planar microwave circuits.

A Miniaturized Antenna with Optimum Q-Factor and High NFD for UWB Microwave Imaging

M. Tarikul Islam, M. Samsuzzaman, I. Yahya, and M. T. Islam

Center of Advanced Electronic and Communication Engineering
Faculty of Engineering and Built Environment, Universiti Kebangsaan Malaysia, 43600, Bangi, Malaysia
p94299@siswa.ukm.edu.my, samsuzzaman@ukm.edu.my, iskandar.yahya@ukm.edu.my, tariqul@ukm.edu.my

Abstract – This paper presents an ultra-wideband (UWB) micro-strip patch antenna design for microwave breast phantom imaging system. By optimizing the shape of radiating elements, the antenna achieves UWB characteristics with excellent frequency ratio. The antenna was fabricated and tested in both time and frequency domain analysis. Sufficient agreement between the simulated and measured data was observed. The antenna achieves a wider bandwidth of 8.2 GHz (2.5 GHz to 11.2 GHz) with good gain and radiation pattern. The antenna has optimum design comparing to the theoretical Q-factor and the near field directivity (NFD) is also observed. Effective near-field microwave breast phantom measurement systems with an array of 9 UWB antennas is proposed and the performance is tested with and without tumor cells inside the breast phantom. The backward scattered signals analysis shows that the presence of tumor with higher dielectric constant than normal cells. Thus, the proposed antenna can be a good candidate for microwave breast tumor detection.

Index Terms – Antenna array, backscattering, microwave breast imaging, NFD, UWB antenna.

I. INTRODUCTION

In recent years, breast cancer is considered an emerging cause of disease of millions of women across the globe with high mortality rate. Only the early detection of this disease is critical to lessen the mortality rate. Currently, X-ray mammography, magnetic resonance imaging (MRI) and ultrasound imaging are used for breast cancer detection. X-ray is the most widespread techniques for screening but it has some major drawbacks including false negative rate higher than 34%, costly and harmful high frequency radiation. [1]. Furthermore, for getting higher resolution image, mammography causes unpleasant breast compression. As a result, research is being conducted to find an alternate method for early efficient detection of breast tumor cell which will be low cost, easy to implement, high positive rate and comfortable for the patient. Human breast is constructed in the comparatively modest model

rather than other body parts such as thorax, limbs and abdomen. Remarkably, there is an identical difference between the dielectric properties of normal and malignant breast tissue. This difference of electrical properties related to conductivity and permittivity is the fact that normal breast tissue propagates the microwave signal fluently in a lossy and fatty medium rather than lesions which hold more liquid in the response of blood and water. So, any unwanted cell cluster, or cyst, can be identified in this from the scattered signals. Microwave imaging can be the suitable alternative to the conventional breast tumor detection system with respect to harmless, low cost and high-resolution imaging.

The main aim of the microwave imaging technique is to develop a reliable low-cost imaging system which will be adaptable to clinical applications. After the declaration of the unsilenced band of 3.1–10.6 GHz as ultra-wideband (UWB) frequency by FCC, researchers from academia and industry focus on the various application of this band including several wireless communications, microwave imaging, positioning and tracking etc. UWB antennas can be a good candidate for microwave imaging for its wider bandwidth, good gain and large data transmission rate. So, to get high-resolution images the use of UWB antennas are desirable. Several antennas have been reported in detection for breast tumor cells such as monopole antenna, slot antenna, array antenna, bow-tie antenna, line-fed printed wide-slot antenna, disk shape antenna and planar patch antenna [2-12]. Every antenna has their own characteristics and benefits. The antenna proposed in [2] has narrow bandwidth of 4-8GHz where lower frequency can penetrate the human tissue compared to higher frequencies. The antenna operates in 6 and 12.5 GHz [4] and has a larger dimension compared with the proposed antenna. Similarly the proposed prototype has larger bandwidth comparing to [7, 13]. The proposed design is compact in size compared to [4, 7] and has omnidirectional radiation pattern and higher gain. Most of the reported antennas put emphasis on frequency domain characteristics except [7], where time domain characteristics of the proposed antenna is also

analyzed which is essential for microwave imaging. Again, several array structures of breast imaging systems were also proposed [2, 4, 13]. However, it is still a challenge to develop compact low profile low-frequency antennas which cover a wider bandwidth.

In this paper, a compact UWB antenna is proposed which has excellent frequency ratio and wider bandwidth. The antenna covers the entire UWB band with the operating bandwidth of 3-11.5 GHz. The antenna performance is experimentally verified after fabrication and the main aim was to make this antenna suitable for microwave imaging application. The novel structure of the antenna then used to construct an array setup of 9 antennas surrounding a breast phantom. A near-field imaging system is implemented, and the scattered signals are analyzed to observe the difference between the behavior of the received signals with and without the tumor cells inside the phantom.

II. IMAGING SYSTEM SETUP

A. Miniaturized UWB antenna design and parametric study

For efficient radar imaging system, a compact UWB antenna is desirable that will be efficient in transmitting and receiving signal with minimal frequency dispersion. For this purpose, a compact, low profile, wider bandwidth and high efficient antenna is suitable. The prototype presented in this work has modified shaped radiating element with a dimension of $44 \times 42 \times 1.5 \text{ mm}^3$. For this dimension, the resonance frequency, in general, can be calculated using the below equation:

$$f_r = \frac{c}{\left[x \sqrt{2(\epsilon_r + 1)} \right]} \quad (1)$$

Where f_r is the center frequency, the speed of light is c , ϵ_r denotes relative permittivity and overall length of the main resonator is x . The dimension is optimized such a way that it can radiate efficiently with large bandwidth spectrum. A modified slotted antenna is generated from a rectangular microstrip patch antenna. The simplest model is the transmission line model that delivers a good physical perception. So this method is mostly accepted for designing the proposed antenna. The antenna covers two radiating element connected with the transmission line W_1 . The nonhomogenous line consists of two dielectric, one is substrate and another one is surrounding air. The patch radiator dimension is calculated by the simplified formulation of the transmission line model. The width is calculated by:

$$W = \frac{c}{2f_r} \left(\frac{\epsilon_r + 1}{2} \right)^{\frac{1}{2}} \quad (2)$$

Here, c is the speed of light in free space and f_r is the resonant frequency. To find the effective permittivity of the substrate the equation can be derived as:

$$\epsilon_{re} = \frac{\epsilon_r + 1}{2} + \frac{\epsilon_r - 1}{2} \left(1 + \frac{12h}{W} \right)^{-\frac{1}{2}} \quad (3)$$

Here, h is the substrate thickness. The path length (L) can be calculated as:

$$L = \frac{c}{2f_r \sqrt{\epsilon_{re}}} - 2\Delta L \quad (4)$$

The design structure of the proposed antenna prototype is shown in Fig. 1. For ensuring a good penetration inside the breast phantom the antenna is optimized for achieving a wider bandwidth including low and high frequency. A modified slotted patch and the partial ground are acting as a main radiating element and the prototype is fed with a transmission line of 50Ω using SMA connector. Several parametric studies during the design of the proposed antenna were done using HFSS simulation solver. Figure 2 illustrates the different tested patch shape. Figure 3 shows the effect of patch shape of the proposed prototype on reflection coefficient (S_{11}). A narrow vertical slot with inside the left arm perturbs the distinctive current flow and density. This modification helps to move the resonant frequency to the lower frequency than the elliptical patch shape. The repetition of the same type of arm structure on the right side helps the upper resonant frequency to shift towards a higher frequency that enhances the bandwidth. Different tested ground shape is shown in Figs. 4 (a-c). The effect of ground shape over the reflection coefficient (S_{11}) is shown in Fig. 4 (d). For investigation, different types and lengths of ground has been preferred to find the best-suited ground shape of the proposed antenna. There is the noticeable effect of bandwidth along with reflection coefficient with respect to the change of ground plane. It seems that the partial ground case has better impedance matching in parametric study but from Fig. 4 (e) it is clear that due to modified proposed ground shape the gain performance is better than the partial ground. According to the electromagnetic wave propagation basic theory of patch antenna, the surface current in the radiating component creates an equal and opposite phase surface current on the ground plane [14]. The compact ground plane creates low cross-coupling effect and aids substantially larger bandwidth. After the numerical analysis, it is observed the proposed partially slotted ground plane covering the non-radiating portion of the feed line offers the widest bandwidth comparing to the other tested shapes.

The simulated current distribution of the proposed antenna on two different frequencies is presented in Fig. 5. At a lower frequency of 4.5 GHz, it is observed that majority of the current concentration is along with feed line and slot of the left portion of the patch and ground slot on the other arm upper portion of the patch conduct a poor amount of current. This indicates that the slot in patch and ground has a significant effect on lower

frequency. So, for lower frequency, the impedance matching is much dependent on modified left slot of the patch and partial slot on ground. For the higher frequency, most of the current concentrate on feedline, knitting of the feedline and upper radiator and upper right slot of the radiator, hence the ground has weak current flow near feed line. Consequently, the ground is weaker than the lower frequency. Also, feed gap has a great impact on impedance matching. Different modified parameters of the proposed antenna are presented in Table 1.

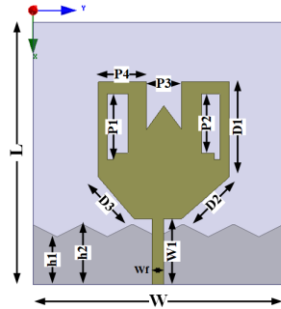


Fig. 1. Antenna geometry.

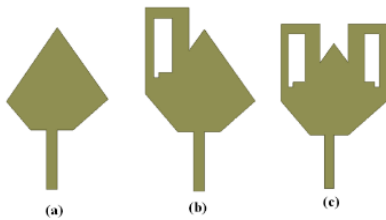


Fig. 2. Different tested patch shapes: (a) without arm, (b) with one arm, and (c) the proposed one.

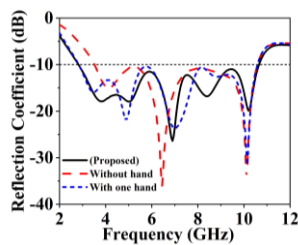


Fig. 3. Reflection coefficient (S_{11}) characteristics of the designed antenna for different patch shape.

The simulated current distribution of the proposed antenna on two different frequencies is presented in Fig. 5. At a lower frequency of 4.5 GHz, it is observed that majority of the current concentration is along with feed line and slot of the left portion of the patch and ground slot on the other arm upper portion of the patch conduct a poor amount of current. This indicates that the slot

in patch and ground has a significant effect on lower frequency. So, for lower frequency, the impedance matching is much dependent on modified left slot of the patch and partial slot on ground. For the higher frequency, most of the current concentrate on feedline, knitting of the feedline and upper radiator and upper right slot of the radiator, hence the ground has weak current flow near feed line. Consequently, the ground is weaker than the lower frequency. Also, feed gap has a great impact on impedance matching. Different modified parameters of the proposed antenna are presented in Table 1.

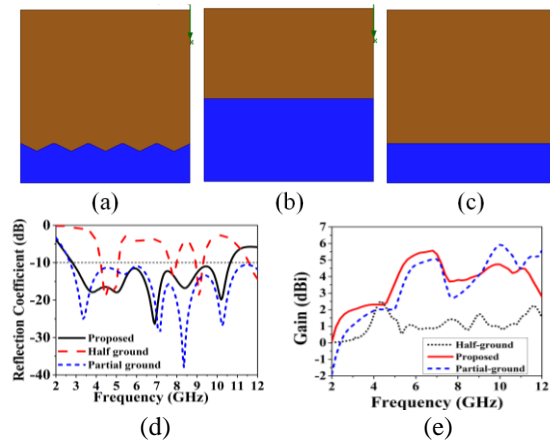


Fig. 4. Different tested ground shapes: (a) proposed, (b) half ground, (c) the partial ground, (d) effect of ground shape on reflection coefficient (S_{11}), and (e) effect of ground shape on peak realized gain.

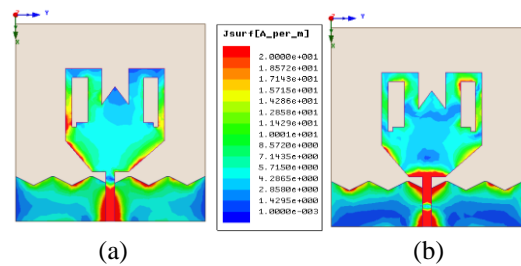


Fig. 5. Surface current distribution at a lower frequency: (a) 4.5 GHz and higher frequency of (b) 8.5 GHz.

Table 1: Modified parameters

Parameters	mm	Parameters	mm
W	42	$P3$	8.1
L	42	$P4$	4.94
$D1$	16	$h1$	8
$D2$	10.63	$h2$	10
$D3$	9.21	$W1$	11
$P1$	11	h	1.6
$P2$	10		

B. Synthetic and experimental results

The performance of the proposed design is analyzed by EM simulator ANSYS HFSS. HFSS is based on a Finite Element Method (FEM). After the optimization, a prototype is fabricated for experimental verification, as depicted in Figs. 6 (a), (b). A vector network analyzer from Keysight Technologies is used to measure the VSWR responses. The VSWR curves of the optimized design are displayed in Fig. 7. It is evident from the figure that the fabricated design achieved a band from 2.50 GHz to 11 GHz for $VSW \leq 2$ which makes it suitable for WiMAX, WLAN, UWB, C-band and X-band communication applications. The slight deviation of the measured VSWR observed at around 6 - 7 GHz band may be due to the mismatch at that band resulted from imperfect prototyping, the effect of feeding cable during measurement and high losses of FR4 dielectric material. StarLab near-field antenna measurement system as shown in Fig. 6 (d) is used to measure the radiation pattern, efficiency and gain of the prototype. Figure 7 (a) represents the measured and simulated voltage standing wave ratio (VSWR) of the proposed prototype from 2GHz - 11GHz. It is observed that a wide bandwidth from 2.5 GHz to 11.2 GHz is below which covers the overall band of UWB (3.1-10.6 GHz). The measured and simulated gain of the antenna along the Z-axis ($\phi=0^\circ$ and $\theta=0^\circ$) are exhibited in Fig. 7 (b). With an average gain of 4.5dBi, the antenna has a maximum gain of 5.5 dBi over the UWB band. The slight deviation from the simulated curve is because of extended coaxial cable for feeding the antenna while measurement. Figure 8 shows the measured and simulated 2D and 3D normalized radiation pattern at 3.5, 6.5 and 9.5 GHz. Broadside radiation patterns are investigated for both the xz and yz plane. Here xz plane is acting as an Electric plane (E-plane) and yz plane is acting as a Magnetic plane (H-plane). In the E-plane, the patterns show the eight-shape-figure with some asymmetry for higher frequency. For H-plane cross-polarization radiation is higher than that of E-plane but still maintain the donut-shape with little distortion. It verifies that the antenna shows stable omnidirectional radiation pattern over the operating frequency. Due to fabrication and measurement tolerances, a little variation is observed in both E- and H-plane form simulated to the measured pattern.

Figure 9 (a) shows the antenna group delay. The group delay of face-to-face direction is more steady and lower than other two setup. It is because of the face to face direction most of the radiated power is received with minimum distortion. So, the prototype antenna will radiate efficiently towards the Region of Interest (ROI) while not coupling significantly with adjacent array elements. Furthermore, the group delay is linearly distributed over the frequency band.

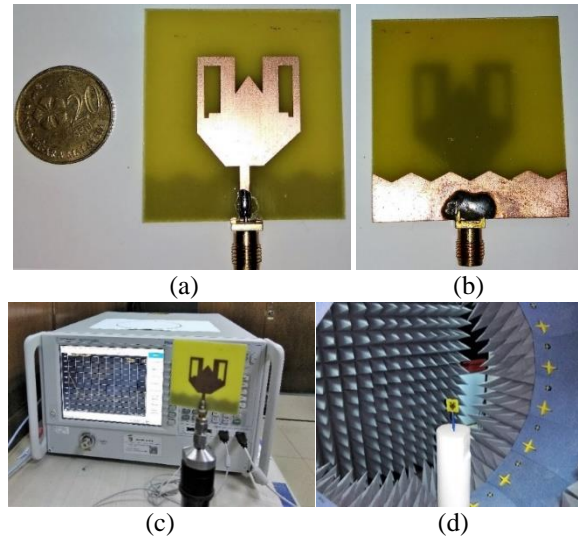


Fig. 6. Fabricated photograph of the prototype: (a) top view, (b) bottom view and measurement setup, (c) PNA network analyzer, and (d) Satimo Star Lab UKM.

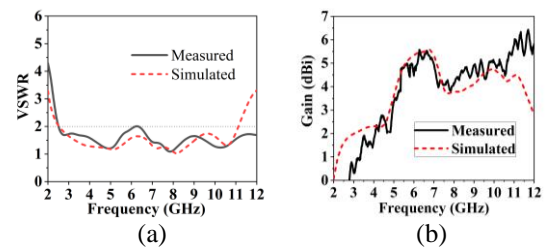
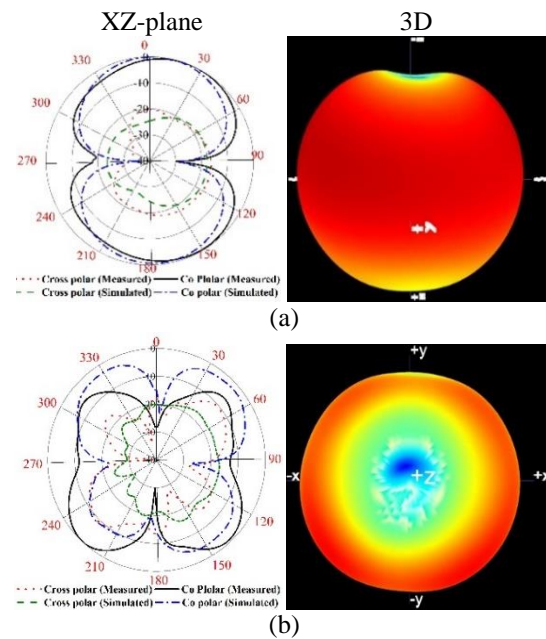


Fig. 7. Measured and simulated: (a) VSWR and (b) gain.



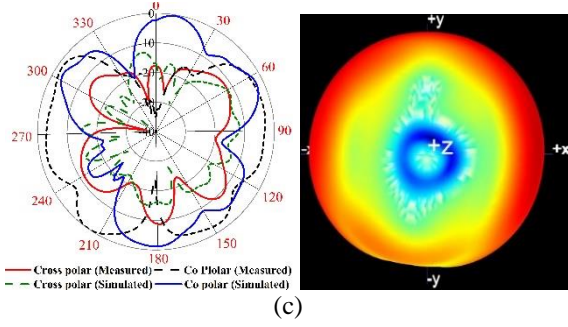


Fig. 8. 2D and 3D radiation pattern at: (a) 3.5 GHz, (b) 6.5 GHz, and (c) 9 GHz.

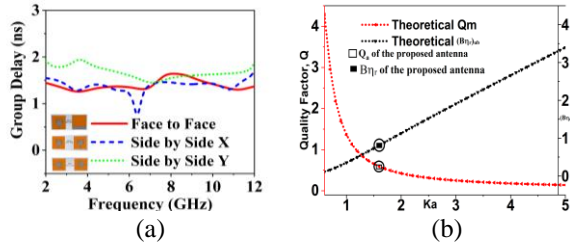


Fig. 9. (a) Group delay for antenna positioned in face to face, side by side x and side by side y direction, and (b) theoretical limits and calculated Q_a and $(B\eta_r)_{ub}$.

Quality Factor:

With respect to the physical dimension of the antenna, minimum quality factor can be achieved by using the following equation [15]:

$$Q_{lb} = \eta Q. \quad (5)$$

Where $Q = \frac{1}{k^3 a^3} + \frac{1}{ka}$, $k = \frac{2\pi}{\lambda}$ and a denotes minimum sphere radius enclosed to the antenna. The higher bound of the radiation efficiency is:

$$(B\eta_r)_{ub} = \frac{1}{\sqrt{2}} \left[\frac{1}{ka} + \frac{1}{k^3 a^3} \right]^{-1}. \quad (6)$$

The Q_m and $(B\eta_r)_{ub}$ for different theoretical values of ka is shown in Fig. 9 (b). The antenna calculated value of $ka=1.59$ for the 1st resonant frequency. From the ideal curve it is noticed that the minimum limit of Q_m is 0.59 and $(B\eta_r)_{ub} = 0.81$. The quality factor of the prototype is estimated through:

$$Q_a = \frac{2\sqrt{\beta}}{B}, \quad (7)$$

where, $\sqrt{\beta} = \frac{s-1}{2\sqrt{s}} \leq 1$.

Here $s=2$ is considered as the maximum accepted VSWR. The achieved Q_a of the anticipated antenna is 0.56 and $(B\eta_r)_{ub} = 0.80$ which indicates that the theoretical and

calculated value is very close. This verifies that the antenna design is optimal.

C. Near field performance analysis

Since the dielectric properties can vary significantly between different patients, it is not reasonable to optimize the antenna in presence of a specific dielectric breast phantom. After optimization in free space, the authors checked the fidelity factor and near field directivity (NFD) to ensure that the near field radiation properties, like phase linearity, are maintained. The fidelity factors were investigated with the antennas in close proximity similar to the final imaging setup. The pattern of the output signal at receiving antenna depends on the input signal and transfer function. By performing the inverse Fourier transform, the transfer function can be turned to the time domain. Figures 10 (a-c) shows the time domain performance of the prototype for three different scenarios of face-to-face, side-by-side X and side-by-side Y at 300 mm distance. It is observed that the wave pattern is almost similar to the input and received signal for three cases which ensures that the antenna is able to transmit short pulses in minimum time and different directions with minimal distortion. Fidelity factor (FF) is critical [16, 17] to validate the correspondence between the transmitter (Tx) and received (Rx) signals. The highest value of cross-correlation between transmitting and receiving pulse is known as fidelity factor. Naturally, the pulse becomes almost distorted if an adjustment is higher than 50% ($FF < 0.5$) [16]:

$$F = \max \left(\frac{\int_{-\infty}^{+\infty} x(t) y(t-\tau) dt}{\sqrt{\int_{-\infty}^{+\infty} |x(t)|^2 dt \int_{-\infty}^{+\infty} |y(t)|^2 dt}} \right). \quad (8)$$

Where, $x(t)$ and $y(t)$ represents the T_x and R_x signals, respectively. For different scenario, the fidelity factor is 84%, 78% and 72% for face to face, side by side X and side by side Y respectively which indicates that the antennas transmitting and receiving capability are quite decent. The higher fidelity factor indicates the lower distortion and also suggests that this can be used for target detection. The phase distortion of the signal of an antenna is represented by group delay.

The NFD can be computed by using the formula presented in [18]. The NFD factor is the proportion of the power radiated inside the front side (Pf) and through the surface of the phantom (PT):

$$NFD = \frac{Pf}{PT}. \quad (9)$$

Figure 10 (d) illustrates the NFD of the proposed antenna with breast phantom. It is observed that about 67% of the total power is emitted through the ROI.

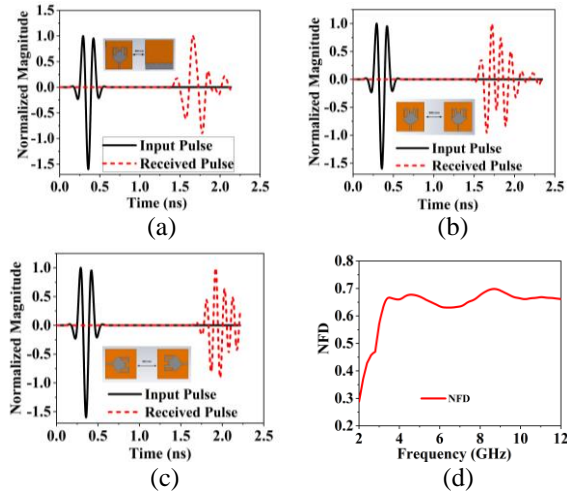


Fig. 10. The normalized magnitude of the proposed prototype for three different scenarios: (a) face to face, (b) side by side X, (c) side by side Y, and (d) NFD of the proposed antenna.

D. Imaging setup and results

The dielectric properties of the human breast are introduced in this section. A breast phantom is used to test the antenna array performance in detection of breast tumor. The phantom is constructed with four layers of skin, breast tissue, fat and regular air layer. The skin layer width is 2.5mm and dielectric constant is 38 with a conductivity of 1.49 S/m. The width of the breast tissue is 8.75 cm with a dielectric constant of 5.14 and 0.141 S/m of conductivity. The dielectric property of breast phantom is summarized in Table 2 [19]. An imaging setup is proposed in this paper and shown in Fig. 11 (a). A heterogeneous breast phantom is used for characterization. The setup consists of 9 antenna unit placed vertically surrounding the breast phantom in every 40-degree interval from each other. The distance between the phantom and antenna array is 15mm. Frequency domain setup is applied to analyze the backscattering signal placing the antenna 1 as transmitter and rest of the antennas are acting as transmitter. By feeding the 1st antenna the effect of breast tissues is observed. Figure 11 (b) shows the Skin, Fat and Tumor dielectric constant vs frequency.

Table 2: The dielectric property of breast phantom

Tissue	ϵ'
Normal Tissue	38
Fat	5.14
Tumor (Malignant)	67

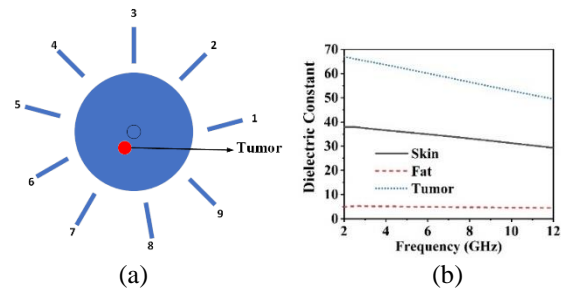


Fig. 11. Proposed model of breast phantom screening using: (a) 9-antenna unit; No. 1 is transmitting and another 8 are receiving the signal, and (b) skin, fat and tumor dielectric constant vs frequency.

Figure 12 represents the s-parameters of the proposed antenna array setup for two different scenarios. Figure 12 (a) represents the s parameters without the presence of tumor inside the phantom while antenna 1 is transmitting and another 8 antennas are receiving the scattered signals. Figure 12 (b) represents the backscattered signal of the system setup with the presence of tumor inside the breast phantom. There is a significant distortion of the backscattering signal of the two graphs. For the absence of tumor, the maximum of the reflection coefficient at the peak resonance frequency is recorded as -65dB while with tumor the peak is around -80dB. The scattered waveform is different because of the higher dielectric properties of the tumor comparing to the normal breast tissue. This indicates that our system can be a good candidate for microwave imaging to detect the unwanted cell like tumor through analyzing backscattering signal efficiently. A comparative study of reported antennas with proposed one is listed in Table 3. The considered parameters are bandwidth (BW), dimension, antenna gain, no of array elements and application. It is observed that the proposed antenna has compact dimension, good gain and wider bandwidth than the reports antennas.

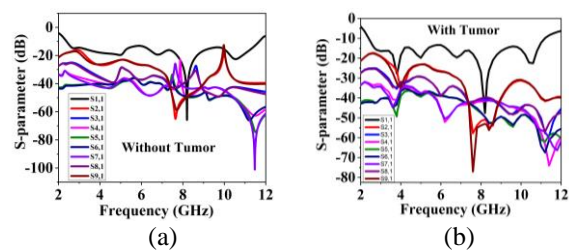


Fig. 12. S-parameter of the antenna array setup: (a) without the presence of tumor inside the phantom, and (b) with the presence of tumor inside the phantom.

Table 3: Comparison between the reported antenna and proposed antenna

Antennas	BW GHz (−10 dB)	Dimension Area (Single Element) (mm ²)	Gain (dBi)	Array Element	Applications
[4]	3.5–15	44 × 52.4	Not reported	4×4	Microwave Imaging
[7]	2.7–7	45 × 53	7.7	Single antenna	Microwave Imaging
[9]	3.5-18	38 × 40	4.5	Single antenna	Microwave Imaging
[13]	1.2–7	30 × 15	Not reported	16	Microwave Sensing
Proposed	2.5 – 11.2	44 × 42	5.5	9	Microwave Imaging

III. CONCLUSION

The design of a novel compact UWB antenna with excellent frequency ratio for microwave breast imaging for tumor detection with the electrical dimension of $0.367\lambda \times 0.350\lambda \times 0.013\lambda$ has been measured and categorized. The results show that the antenna has the fractional bandwidth of 127% (2.5 GHz to 11.2 GHz) with $VSWR < 2$. The antenna has optimum design with good Q-factor value. The antenna has stable omnidirectional radiation pattern with peak gain of 5.5 dBi. The antenna also shows excellent time domain performance to be selected as suitable for microwave imaging. The NFD performance is also satisfactory. This compact and low-cost antenna is further used to design an array setup with a breast phantom to observe the behavior of the normal breast tissue and tumor cell by analyzing the received backscattering signals. The analysis of the signal shows that the tumor behaves different than normal breast tissue and this is the key point to identify the presence of tumor cell inside breast tissue. The antenna is a good candidate for early breast tumor detection through microwave imaging as it covers the UWB bandwidth with good performance in both time and frequency domain characteristics.

ACKNOWLEDGMENTS

This work was supported by the University Kebangsaan Malaysia, under GUP-2017-095 and MI-2017-001.

REFERENCES

- [1] P. T. Huynh, A. M. Jarolimek, and S. Daye, "The false-negative mammogram," *Radiographics*, vol. 18, pp. 1137-1154, 1998.
- [2] T. Henriksson, M. Klemm, D. Gibbins, J. Leendertz, T. Horseman, A. Preece, *et al.*, "Clinical trials of a multistatic UWB radar for breast imaging," in *Antennas and Propagation Conference (LAPC), 2011 Loughborough*, pp. 1-4, 2011.
- [3] M. Bassi, M. Caruso, M. S. Khan, A. Bevilacqua, A.-D. Capobianco, and A. Neviani, "An integrated microwave imaging radar with planar antennas for breast cancer detection," *IEEE Transactions on Microwave Theory and Techniques*, vol. 61, pp. 2108-2118, 2013.
- [4] T. Sugitani, S. Kubota, A. Toya, X. Xiao, and T. Kikkawa, "A compact 4x4 planar UWB antenna array for 3-D breast cancer detection," *IEEE Antennas and Wireless Propagation Letters*, vol. 12, pp. 733-736, 2013.
- [5] M. Rokunuzzaman, M. Samsuzzaman, and M. T. Islam, "Unidirectional wideband 3-D antenna for human head-imaging application," *IEEE Antennas and Wireless Propagation Letters*, vol. 16, pp. 169-172, 2017.
- [6] A. Afifi, A. Abdel-Rahman, A. Allam, and A. A. El-Hameed, "A compact ultra-wideband monopole antenna for breast cancer detection," in *Circuits and Systems (MWSCAS), 2016 IEEE 59th International Midwest Symposium on*, pp. 1-4, 2016.
- [7] M. Z. Mahmud, M. T. Islam, M. N. Rahman, T. Alam, and M. Samsuzzaman, "A miniaturized directional antenna for microwave breast imaging applications," *International Journal of Microwave and Wireless Technologies*, vol. 9, pp. 2013-2018, 2017.
- [8] W. Shao, A. Edalati, T. R. McCollough, and W. J. McCollough, "A time-domain measurement system for UWB microwave imaging," *IEEE Transactions on Microwave Theory and Techniques*, 2018.
- [9] M. Kahar, A. Ray, D. Sarkar, and P. Sarkar, "An UWB microstrip monopole antenna for breast tumor detection," *Microwave and Optical Technology Letters*, vol. 57, pp. 49-54, 2015.
- [10] T. Gholipur and M. Nakhkash, "Optimized matching liquid with wide-slot antenna for microwave breast imaging," *AEU-International Journal of Electronics and Communications*, 2018.
- [11] M. Islam, M. T. Islam, M. R. I. Faruque, N. Misran, M. Samsuzzaman, M. Hossain, *et al.*, "A compact disc-shaped super wideband patch antenna with a structure of parasitic element," *International Journal of Applied Electromagnetics and Mechanics*, vol. 50, pp. 11-28, 2016.
- [12] M. Mahmud, S. Kibria, M. Samsuzzaman, N. Misran, and M. Islam, "A new high performance hibiscus petal Pattern monopole antenna for UWB Applications," *Applied Computational Electromagnetics Society Journal*, vol. 31, 2016.
- [13] M. Jalilvand, X. Li, L. Zwirello, and T. Zwick, "Ultra wideband compact near-field imaging system for breast cancer detection," *IET Microwaves*,

Antennas & Propagation, vol. 9, pp. 1009-1014, 2015.

- [14] W. L. Stutzman and G. A. Thiele, *Antenna Theory and Design*. John Wiley & Sons, 2012.
- [15] G. A. Mavridis, D. E. Anagnostou, and M. T. Chryssomallis, "Evaluation of the quality factor, q , of electrically small microstrip-patch antennas [wireless corner]," *IEEE Antennas and Propagation Magazine*, vol. 53, pp. 216-224, 2011.
- [16] G. Quintero, J.-F. Zurcher, and A. K. Skrivervik, "System fidelity factor: A new method for comparing UWB antennas," *IEEE Transactions on Antennas and Propagation*, vol. 59, pp. 2502-2512, 2011.
- [17] M. T. Islam, M. Samsuzzaman, M. Rahman, and M. Islam, "A compact slotted patch antenna for breast tumor detection," *Microwave Opt. Technol. Lett.*, vol. 60, pp. 1600-1608, 2018.
- [18] R. K. Amineh, A. Trehan, and N. K. Nikolova, "TEM horn antenna for ultra-wide band microwave breast imaging," *Progress In Electromagnetics Research*, vol. 13, pp. 59-74, 2009.
- [19] S. Gabriel, R. Lau, and C. Gabriel, "The dielectric properties of biological tissues: II. Measurements in the frequency range 10 Hz to 20 GHz," *Physics in Medicine and Biology*, vol. 41, p. 2251, 1996.



Md. Tarikul Islam was born in Patuakhali, Bangladesh in 1994. He received his B.Sc. in Computer Science and Engineering from Patuakhali Science and Technology University (PSTU) in 2016. Currently he is working as a master's student in the Universiti Kebangsaan Malaysia (UKM), Malaysia. He has authored or co-authored a number referred journals and conference papers. He is currently a Graduate Research Assistant at the Department of Electrical, Electronic and Systems Engineering, UKM, Malaysia. His research interests include the communication antenna design, Wireless Communication, RF Engineering and Microwave Imaging.



Md. Samsuzzaman was born in Jhenaidah, Bangladesh in 1982. He received his B.Sc. and M.Sc. degrees in Computer Science and Engineering from the Islamic University Kushtia, Bangladesh in 2005 and 2007, respectively, and the Ph.D. degree from the Universiti Kebangsaan Malaysia, Malaysia 2015. From February 2008 to

February 2011, he worked as a Lecturer at the Patuakhali Science and Technology University (PSTU), Bangladesh. From February 2011 to 2015, he worked as an Assistant Professor at the same university. He is now working as a Post-doctoral Fellow at the Universiti Kebangsaan Malaysia. He has authored or co-authored approximately 100 referred journals and conference papers. His research interests include the communication antenna design, satellite antennas, and satellite communication.



Iskandar Yahya is a Senior Lecturer at the Centre of Advanced Electronic and Communication Engineering (PAKET), Faculty of Engineering and Built Environment, Universiti Kebangsaan Malaysia (UKM). He is also an Associate Research Fellow at the Institute of Microengineering and Nanoelectronics (IMEN) in UKM. He obtained his Master of Engineering (M.Eng.) in Electrical & Electronic Engineering (Communications) from The University of Sheffield in 2006. He later joined the Advanced Technology Institute, University of Surrey as a post-graduate and in 2013 obtained his Ph.D. in Electronics Engineering. His research interests include semiconductor devices, nanoelectronics devices, carbon-based electronics and advanced materials for electromagnetic propagation devices. He is currently teaching undergraduate electrical and electronic engineering courses for the electrical and electronic engineering program in UKM.



Mohammad Tariqul Islam is a Professor at the Department of Electrical, Electronic and Systems Engineering of the Universiti Kebangsaan Malaysia (UKM) and visiting Professor of Kyushu Institute of Technology, Japan. He is the author and co-author of about 350 research journal articles, nearly 165 conference articles, and a few book chapters on various topics related to antennas, microwaves and electromagnetic radiation analysis with 16 inventory patents filed. Thus far, his publications have been cited 3709 times and his H-index is 33 (Source: Scopus). His Google scholar citation is 5200 and H-index is 36. He is the recipient of more than 40 research grants from the Malaysian Ministry of Science, Technology and Innovation, Ministry of Education, UKM research grant, international research grants from Japan and Saudi Arabia. His research interests include communication antenna design, radio astronomy antennas, satellite antennas, and electromagnetic radiation analysis. Islam currently serves as the Editor-in-Chief for the International Journal of Electronics and Informatics and Associate Editor for Electronics Letter. He received several International Gold

Medal Awards, a Best Invention in Telecommunication Award, a Special Award from Vietnam for his research and innovation, and Best Researcher Awards in 2010 and 2011 at UKM. He also won the Best Innovation Award in 2011 and the Best Research Group in ICT Niche in 2014 by UKM. He was the recipient of Publication Award from Malaysian Space Agency in 2014, 2013, 2010, 2009

and the Best Paper Presentation Award in 2012 International Symposium on Antennas and Propagation, (ISAP 2012) at Nagoya, Japan and in 2015 in IconSpace. He is a Senior Member of IEEE, Chartered Professional Engineer-CEng, Member of IET (UK) and member of IEICE (Japan).

Powering Sensors in IoT System by Using Compact Seven Band PIFA Rectenna

Nermeen A. Eltresy^{1,2}, Dalia M. Elsheakh^{2,3}, Esmat A. Abdallah²,
and Hadia M. Elhennawy¹

¹Electronics and Communication Engineering Department
Ain Shams University, Cairo, Egypt

²Microstrip Department
Electronics Research Institute, Giza, 12622, Egypt
nermeen@eri.sci.eg

³Hawaii University at Manoa
Hawaii Center for Advanced Communication, Honolulu, 96922, Honolulu, Hawaii, USA

Abstract — A compact seven band coplanar waveguide fed planar inverted F antenna (PIFA) is presented. The proposed antenna is designed to harvest the ambient radio frequency energy at GSM 900, GSM 1800, LTE band 11 and 7, UMTS 2100, Wi-Fi 2.4, LTE and WIMAX 5.2. The antenna is simulated using 3D electromagnetic simulators CST and HFSS. Moreover, the antenna is fabricated and it is used to measure the indoor RF spectrum in Egypt. A simple AC to DC converter unit is designed by using HSMS 2850 Schottky diode to convert the collected RF energy to DC energy. The antenna and the AC to DC converter are integrated to form the RF energy harvesting system. The maximum measured efficiency obtained at 2.4 GHz is about 63.7%.

Index Terms— Ambient RF waves, Energy Harvesting (EH), Internet of things (IoT), Printed F Antenna (PIFA), rectifier, rectenna, Radio Frequency (RF).

I. INTRODUCTION

Internet of things (IoT) is a system that connects anything at any time through the internet to enable exchanging and collecting data [1]. The IoT system consists of six main items which are identification, sensing, communication, computation, services, and semantics. The identification stage is to mark each object by a unique identifier. Then sensors are used to collect data from the objects after that the collected data is sent to the database or cloud to be analyzed for performing the required user actions. Gas, light, and motion are examples of IoT system sensors. The computation services for IoT are processed using microcontrollers. Microcontrollers are devices that use limited power to perform a simple and specific function. The semantics is the final process and it refers to the ability of extracting

the knowledge in a smart manner. Semantics also include properly analyzing data collected in order to make sense of the right decision to provide the required service. So, semantic is considered the brain of the IoT by sending the correct request to the right resource [2]. The IoT sensors nodes and controllers need to be powered by an electrical source. Usually the IoT sensors can be replaced anywhere also they may be buried or fixed in a specific location according to the required IoT application. So that batteries are used to power sensors because it will be extremely complex to power the IoT sensors by wire cables. However, the batteries are not the ideal solution for powering these sensors because after a certain time the batteries need to be replaced. As a result of that using energy harvesting for powering IoT sensors is the solution [3].

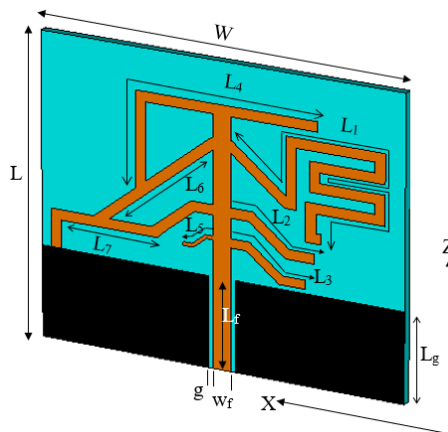


Fig. 1. The structure geometry of optimized antenna.

There are different energy harvesting sources. These

different sources can be classified into three main categories which are thermal, radiant, and mechanical energy harvesting. The thermal energy can be collected from a body heat or from an external source of heat [4, 5, 6]. The mechanical energy has a lot of shapes like the body motion, vibrations, air flow, and blood flow [7]. The radiant energy can be found in the form of visible light, infrared waves, or radio waves [8].

Nowadays the electromagnetic energy exists in all places (faculties, companies, trading centers, streets). That is because of the spectacular growing of wireless devices and as a result of that the sources of the radiated RF energy have been enlarged. The RF energy is located at the air all the day even at the night but it has distinct levels of power according to the distance from the electromagnetic source. RF energy harvesting system consists of receiving antenna, rectifier, matching circuit in between the antenna and rectifier. So, the overall system is called (rectenna) which means the rectifier integrated to the antenna. There are a lot of antennas which were designed for the ambient RF energy harvesting. In [9] microstrip antenna was used to harvest the ambient power from the downlink GSM-900 system. A novel of dual linear polarization antenna was introduced in [10]. Where the antenna has two ports, the horizontal port was used for the data communication and the vertical port was used for the energy harvesting with a good isolation between the two ports. A CPW broadband fractal antenna was designed for RF energy harvesting in [11] where a simple rectifier circuit was designed at frequency of 2.4 GHz.

The rapid progress of wireless communication makes multiband antennas important. A tri-band microstrip-fed slot antenna was designed for WLAN/WiMAX applications in [12]. Multi-band (UWB) Multiple Input Multiple Output (MIMO) antenna was designed in [13] to meet the requirement of multi-band/UWB communication applications. In [14] a small-size CPW-feed multi-band planar monopole antenna was introduced. A novel of compact triband coplanar waveguide fed metamaterial antenna was proposed in [15].

In this paper a CPW fed PIFA antenna operates at seven different frequency bands is introduced, Fig. 1. The proposed antenna is designed to harvest RF energy at mobile application frequency bands of GSM 900, LTE band 11 (1.4 GHz), GSM 1800, UMTS 2100, LTE band 7 (2.6 GHz), Wi-Fi 2.4 and WIMAX 5.2 applications. The fundamental operating frequency of proposed antenna is at 0.9 GHz. Its size is reduced by about 36.4% compared to traditional PIFA antenna operating at this frequency. Moreover, the designed antenna has more compact size than the CPW fed PIFA antennas which were designed before at the same frequency 0.9 GHz and at higher frequency 2.4 GHz. The antenna in [16] was designed to operate at 2.5 GHz however it has a large

area. While the antennas in [17-19] have compact areas but they have large thickness of 8 mm and they are not compatible with RF energy harvesting.

The paper is organized as the following: Section II presents the proposed antenna design procedure in details. Section III presents the measured results of fabricated antenna and ambient RF spectrum in Egypt. The rectifier design, simulation results, and the measurement results are presented in Section IV. Section V introduces the overall RF system integrated and measured. The conclusion is given in Section VI.

II. ANTENNA DESIGN PROCEDURE

The antenna is designed on the low-cost FR-4 substrate with a dielectric constant $\epsilon_r=4.5$, $\tan \delta = 0.02$ and substrate thickness equal to 1.6 mm. The antenna has area of $W \times L$. A 50Ω feeding line with width of W_f and length of L_f is used to feed the antenna. Particle Swarm Optimization (PSO) in the CST program package [20] is used to optimize the antenna reflection coefficient. The separation gap between the feeding line and the ground plane is g . The ground plane length is L_g . By comparing the area between the compact PIFA with dimensions $70 \times 60 \times 1.6 \text{ mm}^3$ and the traditional CPW PIFA with dimensions $110 \times 60 \times 1.6 \text{ mm}^3$ which resonates at the same resonant frequency 900 MHz in Fig. 2 (a), we found that the reduction between the two antennas size is 36.4%. This is indicated in Figs. 2 (a) and 2 (b). In addition to that, the proposed antenna has seven resonant bands. The start point is optimization for (W_f, g) and design of a traditional PIFA fed by CPW in order to operate at 0.9 GHz. The open-ended arm (arm_1) length is shown in Fig. 2 (a) of traditional PIFA antenna is calculated using equation 1 [18]. Where f is the resonant frequency, ϵ_{eff} is the effective dielectric constant of the substrate:

$$arm_1 = \frac{c}{4f\sqrt{\epsilon_{eff}}}. \quad (1)$$

A. Antenna design steps

The proposed antenna design steps are as the following: first the short-ended arm of the traditional CPW fed PIFA antenna is sloped by 40° in order to reduce the antenna size as shown in Fig. 2 (a). Second step is performed by meandering the open-ended arm. Meandering of arm_1 reduces the total length from L_a to L_b , as $L_a=91$ mm and $L_b=63$ mm. Then another arm (arm_2) is added as shown in Fig. 2 (b). By adding arm_2 two frequency bands are achieved. After that other three arms of (arm_3, arm_4, arm_5) are added to the antenna, each arm improves the antenna matching and increasing extra band according to the arm length and position. This can be seen in Fig. 3 which indicates the reflection coefficient variation versus frequency for each step in the antenna design. We can notice that by adding extra arm a new resonant frequency appears. Table 1 lists each arm length and the corresponding resonant frequency.

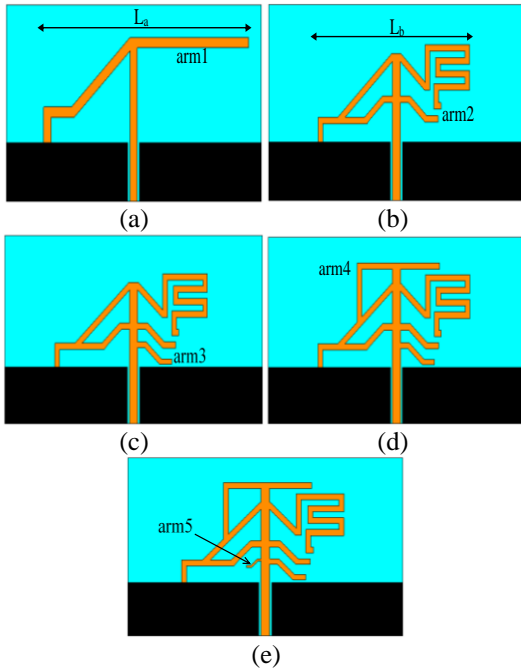


Fig. 2. (a) to (e) Design steps of the proposed antenna.

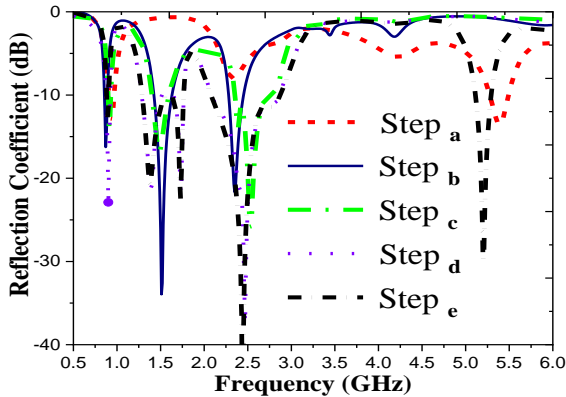


Fig. 3. Reflection coefficient variation versus frequency for design steps of proposed antenna.

Table 1: Antenna arm with corresponding length and frequency

Arm	Length (mm)	Frequency (GHz)
arm ₁	47.6	0.9
arm ₂	18.3	1.4 and 2.4
arm ₃	15	2.6
arm ₄	54.2	1.7 and 2.1
arm ₅	6.5	5.2

B. Antenna parametric study and optimization

Figures 4 (a), (b) and (c) present reflection coefficient results for the performed study on arm₁, arm₂, and arm₃ lengths, respectively. After each design step, the PSO optimization technique in CST is applied for adjusting

PIFA arm’s length, width, and position in order to get optimum result at all operating frequency bands. The final optimized antenna is shown in Fig. 1 and the dimensions of the antenna are listed in Table 2. The HFSS is used to verify the final optimized results of CST [20,21]. Figure 6 shows very good agreement between the CST and HFSS results.

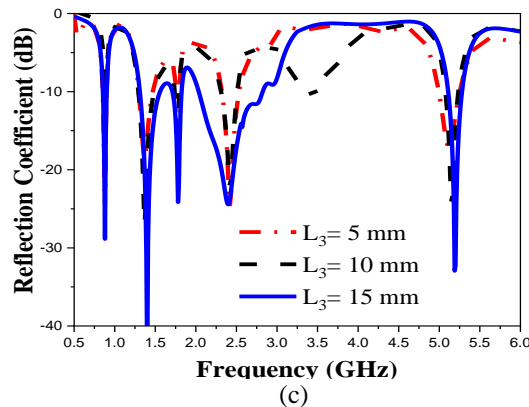
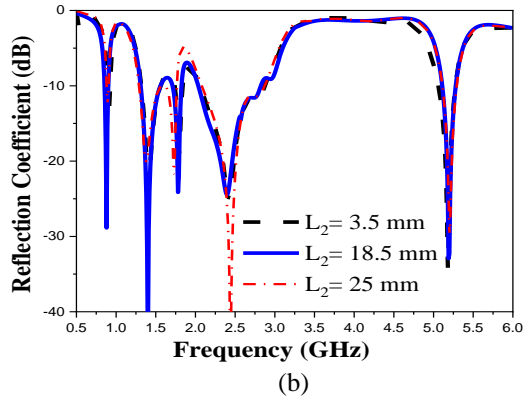
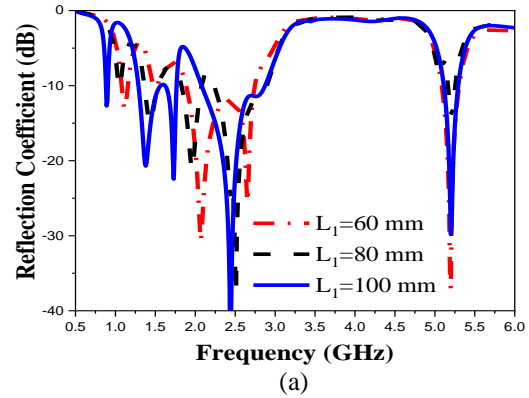


Fig. 4. Reflection coefficient variation versus frequency for different values of: (a) L_1 , (b) L_2 , and (c) L_3 .

The current density distribution on the antenna at different frequencies of 0.9, 1.4, 1.71, 2.1, 2.4, 2.6, and 5.2 GHz is indicated in Fig. 5. The current distribution illustrates that each arm generates a resonant frequency and each arm has a slight effect on the other resonant

frequencies. The simulation values of the antenna gain and radiation efficiency are listed in Table 3.

Table 2: Optimized antenna dimensions (units: mm)

L	W	h
70	60	1.6
L_g	L_f	W_f
18	18	3.5
g	L_1	L_2
0.35	100	18.5
L_3	L_4	L_5
15	54.2	6.656
L_6	L_7	
26.4	19	

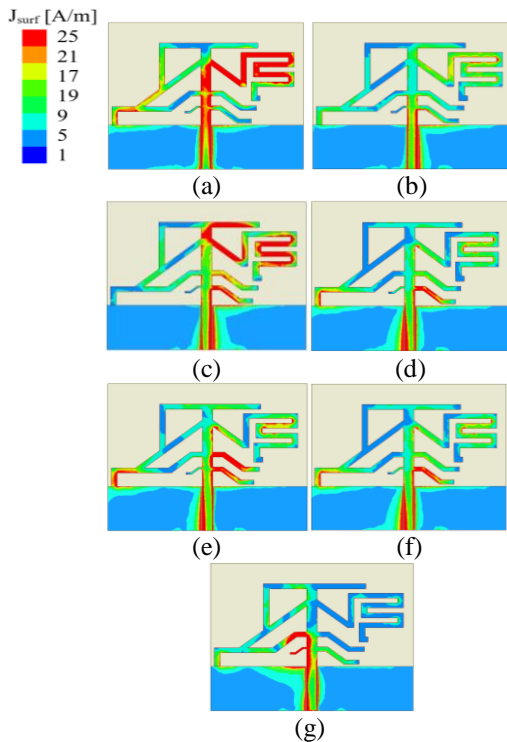


Fig. 5. (a) to (g) Current density distribution of antenna at all antenna frequency resonances at 0.9, 1.4, 1.7, 2.1, 2.4, 2.6, and 5.2GHz, respectively.

Table 3: The simulated radiation characteristics for the proposed antenna

Freq. (GHz)	Gain (dBi)	Rad. Efficiency %
0.9	1.5	90.9
1.4	3	90
1.7	3.4	90.1
2.1	1.1	84.6
2.4	2.12	76.1
2.6	1.1	73
5.2	2.2	60

III. ANTENNA FABRICATION AND RF SPECTRUM MEASUREMENT

The proposed antenna is fabricated. Figure 6 shows the photo of the fabricated antenna and a comparison between the measured and simulated reflection coefficient. There is a good agreement between the simulated and the experimental measured results. The antenna radiation pattern is measured in anechoic chamber with near field system Inc. (NSI) 7005-30 spherical near field system. Comparison between the simulation and the measured radiation patterns of the antenna in E-plane (XZ), and H-plane (XY) at different frequencies are shown in Table 4. Generally, the radiation pattern of the antenna at 0.9, 1.4, 2.6 GHz is omnidirectional in the XZ and XY planes, where at 1.7, 2.4, 5.2 GHz the radiation pattern is directive only in XY plane.

The most difficult thing in the ambient RF energy harvesting system is that ambient power is very low. Unfortunately, the low value of the received power effects on the overall system efficiency. The Friis transmission equation gives the relation between the received power P_r and the transmitted power P_t through a distance R as [9]:

$$p_r = p_t G_t G_r \left(\frac{\lambda}{4\pi R}\right)^2, \quad (2)$$

where G_t is the transmitting antenna gain, G_r is the receiving antenna gain, and λ is the wavelength of the transmitted signal. The ambient power is measured using the proposed antenna to see the levels of the power at different frequencies. The spectrum measurement was performed using the Agilent Technology N9918A which works as a spectrum analyzer. It can be seen in Fig. 7 the received ambient power variation versus frequency which indicates that there are seven peaks of power. That is because the proposed antenna is a multiband antenna. The maximum values of these peaks and each peak frequency are listed in Table 5.

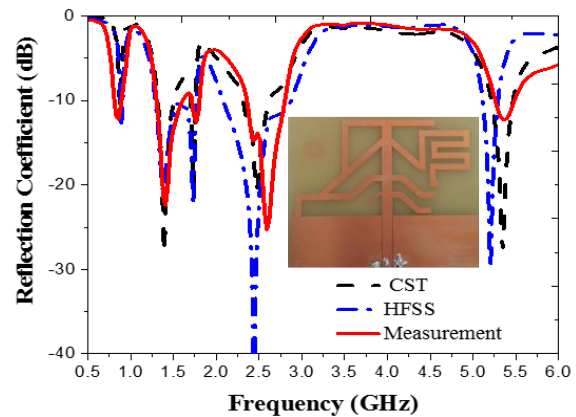


Fig. 6. Photo of the fabricated antenna and comparison between simulated and measured reflection coefficient.

Table 4: The simulated and measured radiation pattern of the CPIFA antenna in the XZ, XY planes at the different operating frequencies. 0.9 GHz, 1.4 GHz, 1.7 GHz, 2.1 GHz, 2.4 GHz, 2.6 GHz, and 5.2 GHz.

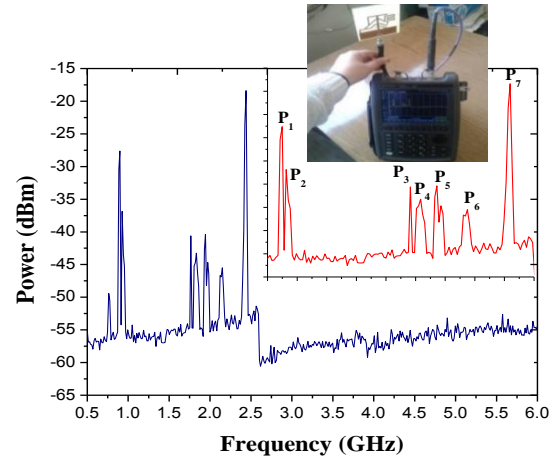
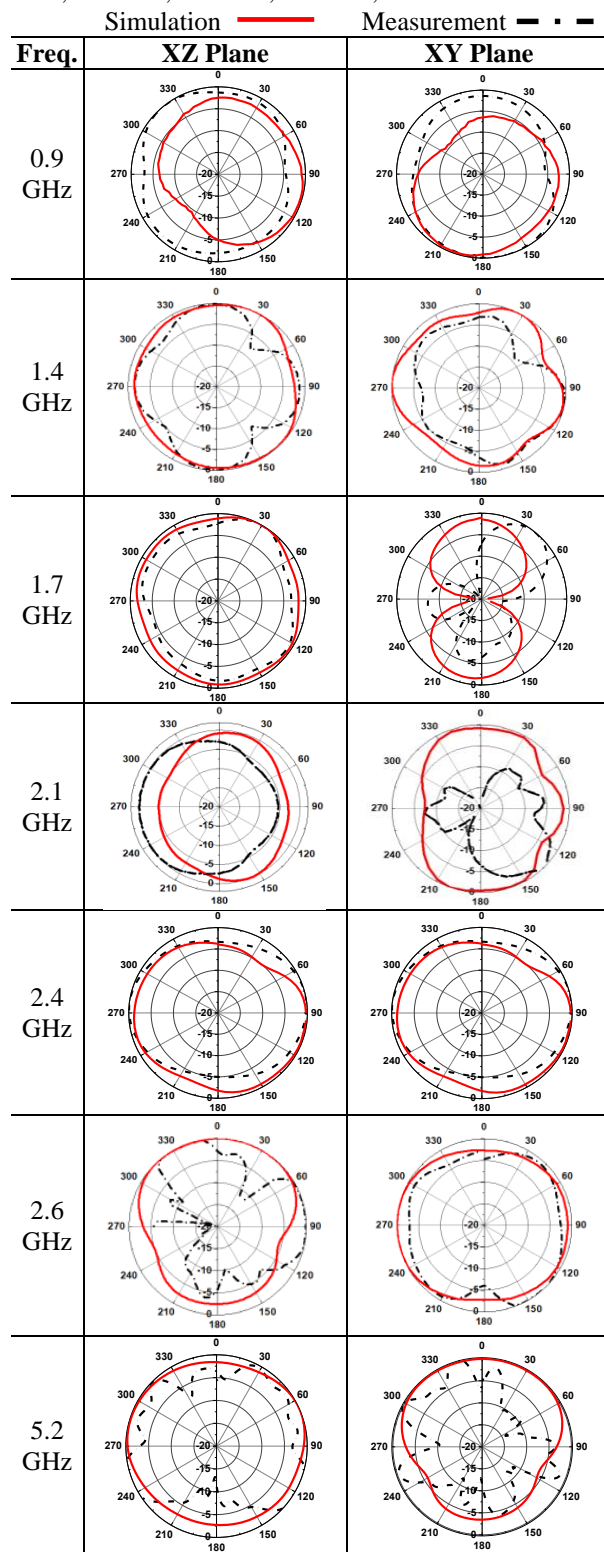


Fig. 7. The received ambient power variation versus frequency using the CPIFA antenna, indoor measurement at 12 pm with photo taken during the spectrum measurement.

Table 5: Values of peaks for received ambient power using CPIFA antenna

Peak	Frequency	Power (dBm)	Power (μ w)
P ₁	0.89 GHz	-27.6 dBm	1.7378
P ₂	0.92 GHz	-36.8 dBm	0.2089
P ₃	1.71 GHz	-40.6 dBm	0.0870
P ₄	1.83 GHz	-43.2 dBm	0.0478
P ₅	1.94 GHz	-40.3 dBm	0.0933
P ₆	2.1 GHz	-45.5 dBm	0.0281
P ₇	2.4 GHz	-18.38 dBm	14.5211

IV. RECTIFIER AND MATCHING CIRCUIT

The voltage doubler circuit is designed for converting the received RF power into DC volt and doubling the received voltage. The circuit is designed using HSMS 2850 Schottky diode which has high sensitivity reaches to 150 mV [22] and the output DC volt is taken through output resistance R_L . The equivalent circuit of the diodes is given in Fig. 8 (a). The turn-on voltage of the diode is 150 mV, the breakdown voltage is 3.8V. The resistance R_j is variable with the operating conditions. Using the ADS (Advanced Design System) program, the input impedance of the voltage doubler circuit is found to be $7.9-j105.4$, the reflection coefficient is -0.5 dB at 0 dBm input power and 700 Ohm load resistance at 2.4 GHz operating frequency. The impedance of the input source is 50 Ohm. These parameters are used to design the matching circuit with short ended stub between the antenna. Figure 8 (b) shows the rectifier schematic circuit integrated with matching circuit. Different matching circuits are designed at different frequencies. The reflection coefficient variation versus frequency for the three different AC to DC converter unit, where each

one is designed to operate at a specific frequency which are $F_1=1.71$ GHz, $F_2=1.94$ GHz, and $F_3=2.4$ GHz is shown in Fig. 9 (a), Fig. 9 (b) shows comparison between the ADS simulated and measured results of the reflection coefficient when the rectifier attached to the short-ended matching stub of 2.4 GHz.

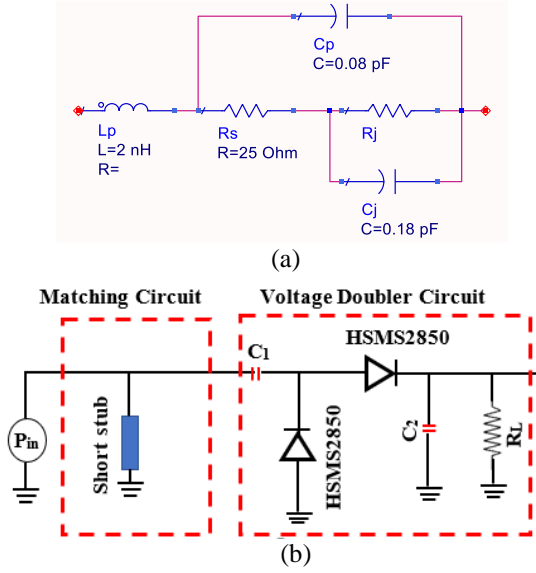


Fig. 8. (a) HSMS2850 equivalent circuit, and (b) single stage voltage doubler.

V. SYSTEM INTEGRATION AND RESULTS

The antenna is integrated with the matching circuit and the voltage doubler circuit. Figure 10 (a) shows photo of proposed antenna connected to rectifier circuit. The measurement setup shown in Fig. 10 (b) is used for testing the rectenna system. The Anritsu MG3697C RF is used as a signal generator to feed a wide band horn antenna. Two antennas are used because one of them is connected to spectrum analyzer for recording received value of RF power and the other antenna is integrated with matching circuit and voltage doubler in order to get harvested DC voltage through a parallel connected Tektronix MD04104C oscilloscope for checking DC output wave form versus time variation. Different levels of power are used to feed the horn antenna. Each time the received RF power by proposed antenna is recorded and each corresponding output DC volt is recorded in order to calculate the measurement overall rectenna efficiency.

The rectenna efficiency η is calculated using equations (3) and (4) [10]. The DC output power is $p_{out(DC)}$, the RF input power is $p_{in(RF)}$, $V_{o(DC)}$ is the DC output volt, and the R_L is the load resistance:

$$\eta = \frac{p_{out(DC)}}{p_{in(RF)}}, \quad (3)$$

$$\eta = \frac{V_{o(DC)}^2}{p_{in(RF)} \times R_L}. \quad (4)$$

Comparison between simulated, measured output volt and conversion efficiency variation versus RF input power for rectifier at different frequencies of $F_1=1.71$ GHz, $F_2=1.94$ GHz, $F_3=2.4$ GHz and $R_L=700 \Omega$ is shown in Fig. 11 (a) and Fig. 11 (b), respectively.

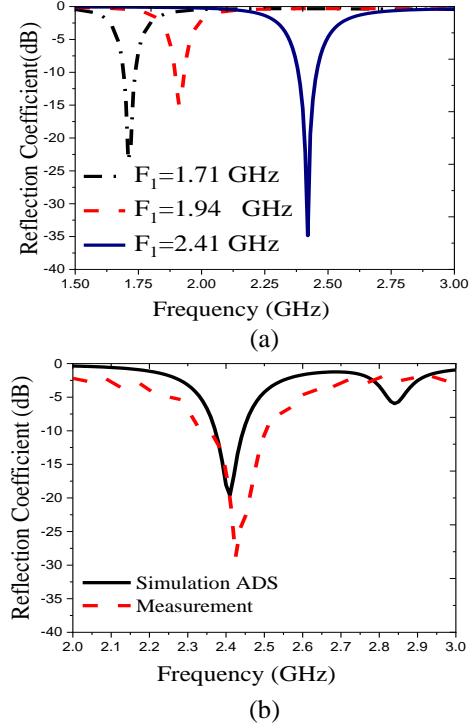


Fig. 9. (a) Reflection coefficient variation versus frequency for three different AC to DC converter unit, and (b) ADS simulated and measured results for rectifier.

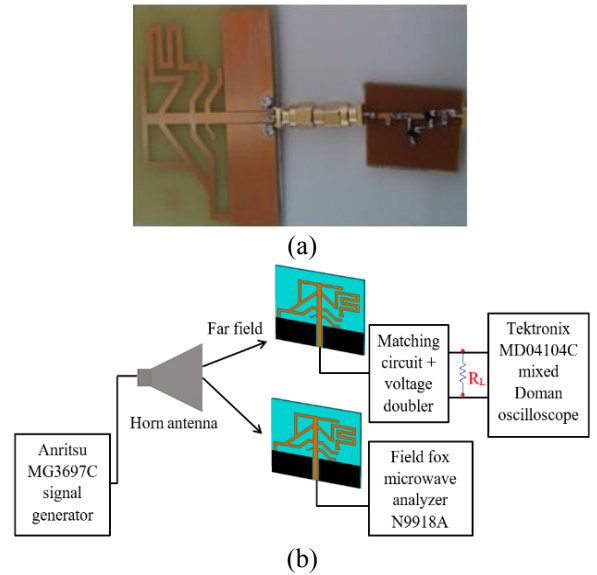


Fig. 10. (a) Photo of rectenna system, and (b) experimental setup for measuring rectenna.

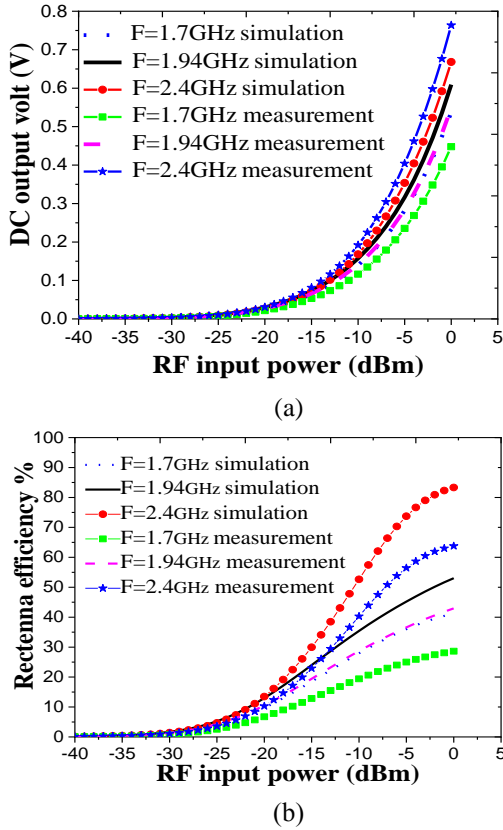


Fig. 11. Comparison between simulation, measured at $R_L=700\Omega$: (a) DC output volt, and (b) rectenna conversion efficiency versus p_{in} .

Photos for the measured output volt of proposed rectenna using digital multimeter are shown in Figs.

12 (a) and (b), where the output DC volt is 61.4 mV, 129.6 mV at RF received power of -15 dBm, -10 dBm, respectively at 1.94 GHz, and $R_L=700\Omega$. Table 6 lists the values of measured V_o (mV) and $\eta\%$ at different RF input power. The comparison between other rectennas reported previously and our proposed rectenna is listed in Table 7. It can be seen that our design has advantage of high conversion efficiency in low input power level.

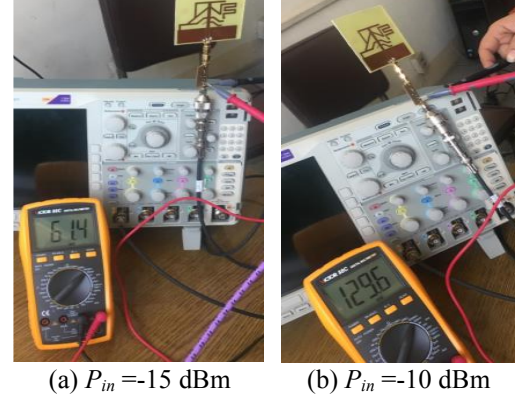


Fig. 12. The measured output volt of the proposed rectenna using digital multimeter at $F_2=1.94$ GHz and $R_L=700\Omega$.

Table 6: Values of measured V_o (mV) and $\eta\%$

Freq	$P_{in}=-15dBm$		$P_{in}=-10dBm$		$P_{in}=-5dBm$	
	V_o	$\eta\%$	V_o	$\eta\%$	V_o	$\eta\%$
F_1	53	12.6	116	19.2	235	24.9
F_2	61	16.8	130	24.1	284	36.4
F_3	80	28.9	190	51.5	353.5	56.3

Table 7: Comparison between rectennas reported previously and the proposed rectenna

Ref.	Frequency (GHz)	Antenna Size (mm^3)	Maximum Gain (dBi)	Input Power Level (dBm)	Conversion Efficiency %
[11]	0.88-8.45	100×100×1.6	8.7	0	51.8
[23]	0.9	62×62×0.254	9	3	48
[24]	0.915 and 2.45	60×60×60	1.87 and 4.18	-9	37 and 30
Proposed rectenna	2.4	79×60×1.6	3.4	-5	56.3

VI. CONCLUSION

Compact CPW fed PIFA antenna with seven different resonant bands namely GSM 900, LTE 11 (1.4 GHz), GSM 1800, UMTS 2100, WIFI 2.4, LTE 7 (2.6 GHz), and WIMAX 5.2 with 36.4% size reduction was designed and measured. The proposed antenna was used to harvest RF energy for IoT system. The antenna dimensions were optimized. The antenna was fabricated and measured with a good agreement between the simulation results and measurement results. A simple AC to DC converter was designed to convert the RF received power into DC power.

ACKNOWLEDGMENT

This work was funded by the National Telecommunication Regularity Authority (NTRA), Ministry of Communication and Information Technology, Egypt. We would like to express our sincere gratitude to Professor Ahmed Attiya because of his help and support for the measurement results.

REFERENCES

- [1] L. Atzoria, A. Ierab, and G. Morabito, "The internet of things: A survey," *Computer Networks*, vol. 54, no. 15, pp. 2787-2805, Oct. 2010.

- [2] R. Arpita, K. Saxena, and A. A. Bhadra, "Internet of things," *International Journal of Engineering Studies and Technical Approach*, vol. 1, no. 4, pp. 36-42, Apr. 2015.
- [3] C. Knight, J. Davidson, and S. Behrens, "Energy options for wireless sensor nodes," *Wireless Sensor Technologies and Applications*, vol. 8, no. 12, pp. 8037-8066, Dec. 2008.
- [4] H. Wong and Z. Dahari, "Human body parts heat energy harvesting using thermoelectric module," *Conference on Energy Conversion (CENCON)*, Malaysia, 19-20 Oct. 2015.
- [5] M. Ashraf and N. Masoumi, "Thermal energy harvesting power supply with an internal startup circuit for pacemakers," *IEEE Transactions on Very Large Scale Integration (VLSI) Systems*, vol. 24, no. 1, pp. 26-37, Jan. 2016.
- [6] S. E. Jo, M. K. Kim, M. S. Kim, and Y. J. Kim, "Flexible thermoelectric generator for human body heat energy harvesting," *Electronics Letters*, vol. 48, no. 16, pp. 1013-1015, Aug. 2012.
- [7] S. T. Yusuf, A. M. Yatim, A. S. Samosir, and M. Abdulkadir, "Mechanical energy harvesting devices for low frequency applications: revisited," *ARPJ Journal of Engineering and Applied Sciences*, vol. 8, no. 7, pp. 504-512, July 2013.
- [8] Available:https://www.researchgate.net/profile/Sanjib_Panda2/publication/264889802/figure/fig6/AS:392161456607247@1470509985797/Fig-8-Types-of-ambient-energy-sources-suitable-for-energy-harvesting-Some-energy.jpg
- [9] N. M. Din, C. K. Chakrabarty, A. B. Ismail, K. K. A. Devi, and W.-Y. Chen, "Design of RF energy harvesting system for energizing low power devices," *Progress In Electromagnetics Research (PIER)*, vol. 132, pp. 49-69, 2012.
- [10] X. Yang, C. Jiang, A. Z. Elsherbeni, F. Yang, and Y.-Q. Wang, "A novel compact printed rectenna for data communication systems," *IEEE Transactions on Antennas and Propagation*, vol. 61, no. 5, pp. 2532-2539, May 2013.
- [11] X. Bai, J. Zhang, L. J. Xu, and B. Zhao, "A broadband CPW fractal antenna for RF energy harvesting," *ACES Journal*, vol. 33, no. 5, pp. 482-487, May 2018.
- [12] D.-L. Jin, T.-T. Bu, J.-S. Hong, J.-F. Wang, and H. Xiong, "A tri-band antenna for wireless applications using slot-type SRR," *ACES Journal*, vol. 29, no. 1, pp. 47-53, Jan. 2014.
- [13] Y. Li, W. Li, and W. Yu, "A multi-band/UWB MIMO/diversity antenna with an enhanced isolation using radial stub loaded resonator," *ACES Journal*, vol. 28, no. 1, pp. 8-20, Jan. 2013.
- [14] B. Yan, D. Jiang, and J. Chen, "Triple notch UWB antenna controlled by novel common direction pentagon complementary split ring resonators," *ACES Journal*, vol. 29, no. 5, pp. 422-427, May 2014.
- [15] K. L. Sheeja, P. K. Sahu, S. K. Behera, and N. Dakhli, "Compact tri-band metamaterial antenna for wireless applications," *ACES Journal*, vol. 27, no. 115, pp. 947-955, Nov. 2012.
- [16] A. M. Soliman, D. M. Elsheakh, and E. A. Abdallah, "Quad band CPW-planar IFA with independent frequency control for wireless applications," *Proceedings of the 2012 IEEE International Symposium on Antennas and Propagation*, Chicago, USA, pp. 1-2, July 2012.
- [17] D. M. Elsheakh, A. M. Soliman, and E. A. Abdallah, "Low specific absorption rate hexa-band coplanar waveguide-fed planar inverted-F antenna with independent resonant frequency control for wireless communication applications," in *IET Microwaves, Antennas & Propagation*, vol. 8, no. 4, pp. 207-216, Mar. 2014.
- [18] C. L. Tsai, S. M. Deng, C.-K. Yeh, and S.-S. Bor, "CPW-fed PIFA with finite ground plane for WLAN dual-band applications," *2006 IEEE Antennas and Propagation Society International Symposium*, Albuquerque, USA, pp. 4269-4272, 14 July 2006.
- [19] A. Soliman, D. Elsheakh, E. Abdallah, and H. El-Henawy, "CPW fed planar IFA with applied electromagnetic band-gap ground plane," *2013 IEEE Antennas and Propagation Society International Symposium (APSURSI)*, Orlando, USA, pp. 282-283, July 2013.
- [20] CST Microwave Studio, ver. 2012, Computer Simulation Technology, Framingham, MA, 2012.
- [21] Ansoft High Frequency Structure Simulator (HFSS) ver. 14, Ansoft Corp., 2014.
- [22] Surface Mount Microwave Schottky Detector Diodes, HSMS-2850/2860 Series Agilent (Hewlett-Packard), 1998.
- [23] S. Ladan, N. Ghassemi, A. Ghiotto, and K. Wu, "Highly efficient compact rectenna for wireless energy harvesting application," *IEEE Microwave Magazine*, vol. 14, no. 1, pp. 117-122, Feb. 2013.
- [24] K. Niotaki, S. Kim, S. Jeong, A. Collado, A. Georgiadis, and M. M. Tentzeris, "A compact dual-band rectenna using slot-loaded dual band folded dipole antenna," *IEEE Antennas and Wireless Propagation Letters*, vol. 12, pp. 1634-1637, Dec. 2013.



Nermeen A. Eltresy received the B.S., and M.S. from Menoufia University, Menoufia, Egypt, in May 2012 and January 2016, respectively. Her Master's thesis was about study and design of nanoantennas element and arrays for different applications. She is currently working toward the Ph.D. degree at Ain Shams University. She is a Assistant Researcher from 2016 until now in the Microstrip Department, Electronics Research Institute. She has published 5 papers in periodical Journals and 6 papers in conferences and a book in the area of nanoantennas design and applications.



Dalia M. Elsheakh received the B.Sc., M.Sc. and Ph.D. degrees from Ain Shams University in 1998, 2005 and 2010, respectively. M.S. thesis was on the design of Microstrip PIFA for mobile handsets. Ph.D. Thesis was in Electromagnetic Band-Gap Structure. From 2010 to 2015, she was Assistant Professor and from 2016 until now she is Associate Prof. in Microstrip Dept., Electronics Research Institute. She was Assistant Researcher at the HCAC, College of Engineering, Hawaii University, USA in 2008 and Assistant Prof. in 2014 and 2018. She has published 50 papers in peer-refereed journals and 45 papers in International Conferences.



Esmat A. Abdallah graduated from the Faculty of Engineering and received the M.Sc. and Ph.D. degrees from Cairo University, Giza, Egypt, in 1968, 1972, and 1975, respectively. She was nominated as Assistant Professor, Associate Professor and Professor in 1975, 1980, and 1985, respectively. She has focused her research on microwave circuit designs, planar antenna systems, and recently on

EBG structures, UWB components, and antenna and RFID systems. She has authored and coauthored more than 250 research papers in highly cited international journals and in proceedings of international conferences in her field, such as IEEE Transactions on Antenna and Propagation and IEEE Transactions on Microwave Theory Techniques., etc. She supervised more than 70 Ph.D. and M.Sc. thesis. She has been the President of the Electronics Research Institute in Egypt for more than ten years.



Hadia M. El Hennawy received the B.Sc. and the M.Sc. degrees from Ain Shams University, Cairo, Egypt, in 1972 and 1976, respectively, and the Ph.D. degree from the Technische Universität Braunschweig, Germany, in 1982. In 1982, she returned to Egypt and joined the Electronics and Communications Engineering Department, Ain Shams University, as an Assistant Professor. She was nominated an Associate Professor in 1987 and then a Professor in 1992. In 2004, she was appointed as the Vice-Dean for Graduate Study and Research. In 2005, she was appointed as the Dean of the Faculty of Engineering, Ain Shams University. She has focused her research on microwave circuit design, antennas, microwave communication and recently wireless communication. She has been the Head of the Microwave Research Lab since 1982. She has published more than 100 journal and conference papers and supervised more than 50 Ph.D. and M.Sc. students. She was the Editor-in-Chief of the Faculty of Engineering, Ain Shams University, Scientific Bulletin from August 2004 to August 2005 and is a Member of the Industrial Communication Committee in the National Telecommunication Regulatory Authority (NTRA), Educational Engineering Committee in the Ministry of Higher Education, and Space Technology Committee in the Academy of Scientific Research. She is deeply involved in the Egyptian branch activities.

Linearization of S-Parameter Cascading for Analysis of Multiple Reflections

Richard J. Allred^{1,2} and Cynthia M. Furse²

¹ Signal Integrity Software, Inc. (SiSoft)
Maynard, MA 01754
richard.allred@gmail.com

² Department of Electrical and Computer Engineering
University of Utah, Salt Lake City, Utah, 84112, USA
cfurse@ece.utah.edu

Abstract — This paper develops a method to derive intuitive understanding of the root causes of reflective interference created by the many impedance discontinuities between the packages, PCBs and connectors. Scattering parameters are cascaded to describe the system response and linearized to analyze the multiple reflections. An upper error bound of the linearization is derived and is validated with Monte Carlo studies.

Index Terms — Inter-symbol interference (ISI), networks and circuits, scattering parameters, signal integrity, signal processing, transmission line matrix.

I. INTRODUCTION

Computer interconnect design has become a critical aspect of integrated circuit (IC) signal integrity, which has become more complex due to the exponential increase in on-chip computing bandwidth [1]. The simplest model of a computer interconnect includes only the wires that connect two ICs. More realistically, an interconnect includes packages that hold each IC, printed circuit board (PCB) transmission lines and vias (which transition between PCB layers) and connectors, as seen in Fig. 1. When the signal stream of 0's and 1's traverses the interconnect at very low data rate frequencies (kHz to low MHz), the interconnect features are much smaller than the wavelength, and the wires are typically modeled as simple delays. As the data rate increases, the interconnect model requires more fidelity that includes impedance mismatch, dielectric loss, skin effect and copper surface roughness. At today's data rates which can exceed 28 Giga-bits-per-second, it is typical to model transmission lines with 2D solvers [2]. Also, fine geometric features that were neglected at lower speeds, such as the PCB vias, must be accurately modeled, typically with 3D full wave FEM or FDTD solvers [3].

The transfer function for detailed high frequency interconnect models is found by cascading (combining

in series) the individual transmission line and 3D model segments. This cascading process [5, 6] is excellent for quantifying the total behavior of the system but obscures the source of multiple reflections, in part because the cascading process is non-linear, as will be shown in this paper. Linearization will enable the separation of the transfer function into physically meaningful pieces that allow us to determine which system features contribute most to the multiple reflections. This then enables redesign to reduce those reflections and improve signal integrity.

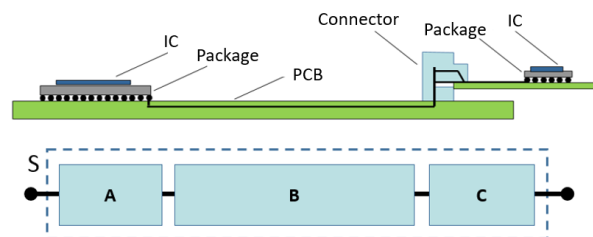


Fig. 1. Diagram of the 28G VSR computer interface [4] and an example of how the link can be modeled with three S-parameter segments: package (A), PCB (B), line card PCB (C). This interface is used in back-end servers for switching of internet traffic.

While others have addressed the need to identify and resolve reflective interference [7-9] the method described in this paper is, to our knowledge, the first rigorous process to do so. In lieu of a direct comparison of the proposed method with a traditional method, we will validate our method against Monte Carlo studies.

Section II discusses system level analysis and existing procedures for identifying sources of multiple reflections in a wired communication link such as the CEI 28G-VSR (very short reach) interface [4] shown in Fig. 1. Section III will describe an alternative to the standard ABCD matrix cascading approach, using

the analytic Mason's rule. Section IV derives the linearization of the cascading process. In Section V we derive an upper bound on the error introduced by the linearization and validate the bound with analytic and empirical Monte Carlo (MC) studies. Finally, we conclude with a discussion of the limitations of the proposed linearization, next steps and applications.

II. SYSTEM LEVEL ANALYSIS

Segments of an interconnect model such as those shown in Fig. 1 are usually represented by frequency domain scattering parameters (S-parameters):

$$\mathbf{S}(f) = \begin{bmatrix} S_{11}(f) & S_{12}(f) \\ S_{21}(f) & S_{22}(f) \end{bmatrix},$$

where $S_{ij}(f)$ is the complex voltage transfer function versus frequency between port j and port i [5]. $S_{11}(f)$ represents the reflective behavior looking into the input port 1, while $S_{21}(f)$ represents the through transfer function between the input port 1 and the output port 2. As it is understood that \mathbf{S} is a frequency domain response, our notation will drop the explicit frequency reference. Also note that for passive and lossy interconnects considered here that $|S_{21}| = |S_{12}| \leq 1$, $|S_{11}| \ll 1$ and $|S_{22}| \ll 1$. This means that products of \mathbf{S} matrix components will have magnitudes much less than 1.

The design of today's high speed interconnects for computer communication interfaces (e.g., PCIe4, 100G Ethernet) requires a careful budgeting of losses for long channels, as these can severely disperse and attenuate the signal [10]. Additionally, short channels can suffer from reflective interference caused by impedance discontinuities. These require an altogether different approach to resolve. While channel loss budgets are helpful for long channels, there is no similar reflection budget for short channels and their complicated multipath behavior. This paper proposes an approach to linearize the \mathbf{S} matrix cascading process (the combining of \mathbf{S} matrices together) which opens the door to innovative approaches for analyzing key features of reflective wired channels.

Consider the CEI 28G-VSR interface [4] shown in Fig. 1. This short channel can display highly reflective behavior from the impedance discontinuities at the package, PCB and connector junctions. To ensure that the transmitter and receiver circuit equalization schemes can overcome these channel and noise impairments, the design process uses a simulation of this environment. (Measuring multiple designs of the system would be too expensive and time consuming.) Figure 1 also shows an example of dividing the system into three segments which model the package (A), PCB (B) and connector with line card PCB (C). Each of these 2-port differential \mathbf{S} matrices describes the frequency domain behavior of the segment and is obtained from either measurement, simulation (for example FEM or FDTD methods) [11],

or empirical equations [12]. The segmentation of the system requires that the signal conductors at the boundary support TEM propagation and that any higher order modes have sufficiently attenuated [13].

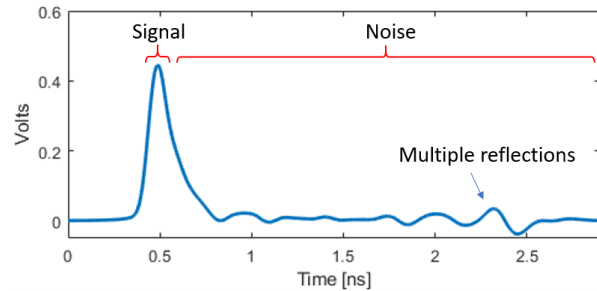


Fig. 2. Reflective noise can cause trouble for communication systems as can be seen by the pulse response of the system shown in Fig. 1. The energy from a single positive bit bounces around inside the system, and these multiple reflections show up much later than the desired signal. These stray voltages can interfere with later signals and could potentially corrupt the recovery of sent information.

System level analysis involves a simulator cascading the segments together into a total end-to-end \mathbf{S} matrix for the system [6, 14], before converting to the time domain pulse response as shown in Fig. 2. This channel pulse response can then be used to combine with the transmitter and receiver equalization to determine the link's performance [15]. This analysis assumes that the \mathbf{S} matrices are of good quality in that they are passive, causal and accurate [3, 16]. If they are not, numerical noise can propagate through the cascading process and corrupt the total end-to-end response.

This process of cascading segment models is excellent for quantifying the system performance but obscures the source of the multiple reflections, which makes redesigning to minimize them very difficult. To find the source of the multiple reflections in a system, the literature suggests a guess-and-check approach. The most common procedure is to consult the simulated time domain reflectometry (TDR) waveform to estimate where the largest impedance discontinuity is located [8]. Alternatively, the frequency domain insertion loss can be examined for problematic resonances whose frequencies are inversely proportional to the electrical length of the segment creating the reflective interference [17]. This section of the interconnect is then modified by removal or redesign to see if the system performance improves [7, 17]. When applied iteratively, this approach usually identifies the primary source of reflective interference. However, the process is not systematic or wholly repeatable due to the many subjective choices involved. Additionally, removing or modifying a segment of the system fundamentally changes the system. This makes

the true impact of a single discontinuity difficult to quantify. It is challenging to determine what to modify and how to modify it [7].

We would like to find a way to quantify how each \mathbf{S} matrix segment contributes to the reflections in the total system response. Others have hinted at this goal [9], but we will demonstrate how to actually achieve this. Because the process of cascading \mathbf{S} matrices is non-linear, a linearization or decomposition will be required to separate the transfer function into physically meaningful pieces. In this paper, we will apply the analytic Mason's rule to the \mathbf{S} matrix cascading process and linearize this result. This will allow us to resolve the effects of reflections from individual segments of the system, thus enabling redesign to remove these effects.

III. MASON'S RULE

The usual approach to cascading a series of \mathbf{S} matrices involves converting each \mathbf{S} matrix to an ABCD matrix [5] or transmission matrix [6], multiplying the matrices together, and then converting back to \mathbf{S} matrix form. The cascading process can determine the total system behavior, but it obscures how each segment contributes to the overall response. We propose an alternative approach, expressing the series of \mathbf{S} matrices (for example three \mathbf{S} matrices named \mathbf{A} , \mathbf{B} and \mathbf{C}) as a signal flow graph, as shown in Fig. 3 (a), and then combining them with Mason's rule [18]. The signal flow graph is created by placing each \mathbf{S} matrix's through responses (e.g., A_{21} and A_{12}) and reflection responses (e.g., A_{11} and A_{22}) as shown in Fig. 3 (a). Mason's rule provides an analytic solution (though non-linear) of the total system response. It also provides intuition into how reflective multipath behavior occurs in the system. A major insight is that pairs of impedance discontinuities form resonant loops (Fig. 3 (b)) which trap energy before returning it to the system. This delayed energy can eventually arrive at the receiver and may create an error in the bit decision.

The Mason's rule procedure to solve for the total S_{21} of the signal flow graph in Fig. 3 (a) is to first identify all forward paths. For our application, a forward path is one that starts on the left, ends on the right and does not circle back on itself; the only forward path in Fig. 3 (b) is $G_1 = A_{21}B_{21}C_{21}$. Second, identify the loops (paths that start and end at the same location) as shown in Fig. 3 (b) which are $L_1 = A_{22}B_{11}$, $L_2 = B_{22}C_{11}$, and $L_3 = A_{22}B_{21}C_{11}B_{12}$.

The next step is to identify the determinant (Δ) of the graph and the co-factor (Δ_i) of each path. The determinant, Eqn. 1, is found by collecting products of loop terms which do not touch. These products are taken one-at-a-time, two-at-a-time, three-at-a-time, etc. until all possible non-touching loop combinations are included. This calculation accounts for the interactions

that occur between loops which do touch, and as will be seen below, a modification of this calculation opens the opportunity for linearization:

$$\Delta = 1 - \sum L_i + \sum_{\substack{\text{non-touching} \\ \text{non-touching}}} L_i L_j - \sum_{\substack{\text{non-touching} \\ \text{non-touching}}} L_i L_j L_k + \dots \quad (1)$$

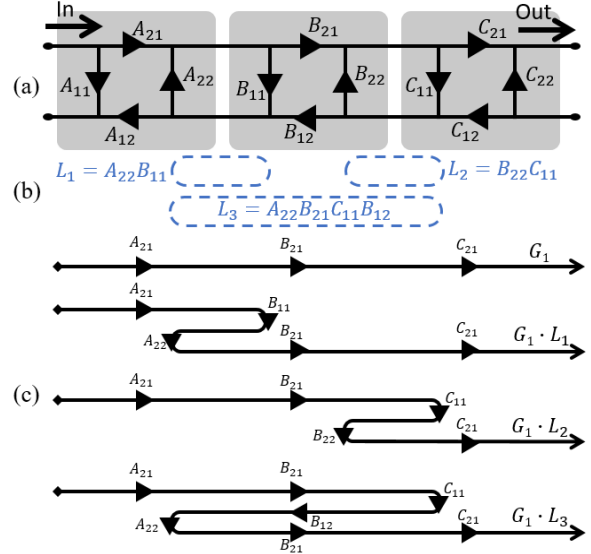


Fig. 3. (a) There are an infinite number of ways that energy can travel through a series of \mathbf{S} matrix segments \mathbf{A} , \mathbf{B} , \mathbf{C} in this signal flow graph. (b) Energy can resonate (get trapped) in the loops, L_1 , L_2 , and L_3 . (c) Energy Transfer Diagram. A 1st order linearization of S_{21} is found by summing the possible paths through the signal flow graph. This includes the forward path $G_1 = A_{21}B_{21}C_{21}$ and all the paths going once through each of the loops in the system (or two bounces).

For our three-segment example, there are three one-at-a-time loops terms (L_1 , L_2 , L_3), one non-touching two-at-a-time loop term (L_1L_2) and no non-touching three-at-a-time loop terms. This results in the determinant of:

$$\Delta = 1 - L_1 - L_2 - L_3 + L_1L_2. \quad (2)$$

The cofactor of a forward path is defined as the determinant calculation over the set of loops which do not touch the forward path. Since the forward path G_1 touches all the loops, $\Delta_1 = 1$.

Once the paths, loops, determinant and cofactors are identified, Mason's rule provides a way to directly write down the transfer function equation:

$$G = \frac{\sum_k G_k \Delta_k}{\Delta}. \quad (3)$$

The Mason's rule process is summarized in Table 1. Finally, the total S_{21} of the signal flow graph in Fig. 3 (a) is:

$$S_{21} = \frac{A_{21}B_{21}C_{21}}{1 - L_1 - L_2 - L_3 + L_1L_2}. \quad (4)$$

Observe that the denominator collects the resonant behavior of the network and can significantly change with the inclusion of additional \mathbf{S} matrix segments. This shows that the cascading of \mathbf{S} matrices is a non-linear process, and the addition of more segments can significantly change the response.

While S_{21} could also be obtained through the ABCD or transmission matrix approach, the intuitive Mason's rule result provides insight into the physical behavior of the system. The linearization of this equation will decompose the response into a sum of physically meaningful terms which can then be analyzed individually to provide more insight into the causes of the reflective behavior of the system. This insight can be very useful in redesigning the system. The downside to the signal flow graph approach is that graphs which have many paths and many interacting loops can be very challenging to apply Mason's rule to by hand, and either simplifications to the structure or application of a matrix approach are required.

Table 1: Mason's rule analysis process summary

Step	Action
0	From a signal flow graph,
1	Identify desired input port and output port of network.
2	Identify all possible forward paths G_i between the input and output ports.
3	Identify all loops L_i in network.
4	Calculate the graph determinant: From the set of all loops, identify the combinations of loops which do not touch for groupings of two-at-a-time terms, three-at-a-time terms, etc. until all possible combinations are considered.
5	For each forward path G_i , calculate the cofactor Δ_i by identifying those loops which do not touch path G_i and then performing the determinant calculation over this set of loops.
6	Combine the forward paths G_i , cofactors Δ_i , and determinant Δ according to Eqn. 3 to obtain the transfer function between the input and output ports.

IV. LINEARIZATION DERIVATION

Our goal is to separate the expression for the total through response (S_{21}) of the system into a series of terms (visualized in Figs. 3 and 4) that can be analyzed individually so that we can identify which features are the most significant cause of multiple reflections. This decomposition or linearization is accomplished by

simplifying Mason's rule to assume that all the loops are independent and do not touch each other. This leads to a denominator (i.e., the determinant, Δ , from Eqn. 1) that can be factored as shown in Eqn. 5 below:

$$S_{21} \approx \frac{A_{21}B_{21}C_{21}}{1 - L_1 - L_2 - L_3 + L_1L_2 + L_1L_3 + L_2L_3 - L_1L_2L_3}$$

$$S_{21} \approx \frac{A_{21}B_{21}C_{21}}{(1 - L_1)(1 - L_2)(1 - L_3)}. \quad (5)$$

Next, by applying the geometric series, $\frac{1}{1-x} = \sum_{n=0}^{\infty} x^n$ if $|x| < 1$, we can move the loop terms from the denominator to the numerator:

$$S_{21} \approx A_{21}B_{21}C_{21} \left(\sum_{n=0}^{\infty} L_1^n \right) \left(\sum_{n=0}^{\infty} L_2^n \right) \left(\sum_{n=0}^{\infty} L_3^n \right). \quad (6)$$

This expression can be further simplified by truncating the infinite series at $n = 1$ and discarding cross-terms which come from expanding the parentheses:

$$S_{21} \approx A_{21}B_{21}C_{21}(1 + L_1)(1 + L_2)(1 + L_3) \quad (7)$$

$$S_{21}^* = A_{21}B_{21}C_{21}(1 + L_1 + L_2 + L_3).$$

We call S_{21}^* the 1st order linearization of the through response S_{21} , and it shows how each resonant loop contributes to the total response. In the three-segment scenario, expanding the parentheses gives one forward path term and three loop terms which can be analyzed to determine which one is dominant. It is also the same expression that could be found by analyzing an energy transfer diagram and collecting all terms that have one loop (or two bounces), as shown in Fig. 3 (c). The utility of such a decomposition is that for signal integrity systems which suffer from high reflective interference, the impact of each loop response on the total system performance can be quantified [19].

The first order linearization for systems with more than three \mathbf{S} matrix segments is generalized as:

$$S_{21}^* \approx (A_{21}B_{21}C_{21} \dots) \left(1 + \sum L_i \right). \quad (8)$$

If the system has many large impedance discontinuities, significant energy can travel through more than one loop, and the 1st order linearization of S_{21} can be poor. To account for these additional multiple reflections, we return to the exact result of Eqn. 4 and bring the whole denominator to the numerator using the geometric power series relation:

$$S_{21} = \frac{A_{21}B_{21}C_{21}}{1 - L_1 - L_2 - L_3 + L_1L_2}$$

$$= A_{21}B_{21}C_{21} \left(\sum_{n=0}^{\infty} (L_1 + L_2 + L_3 - L_1L_2)^n \right). \quad (9)$$

Expanding the infinite series to $n = 2$ yields Eqn. 10 and discarding the terms with more than two loops (e.g., $L_1L_2^2$ and $L_1L_2L_3$) yields S_{21}^\ddagger , the 2nd order linearization shown in Eqn. 11. This is generalized for systems with more than three \mathbf{S} matrix segments in Eqn. 12.

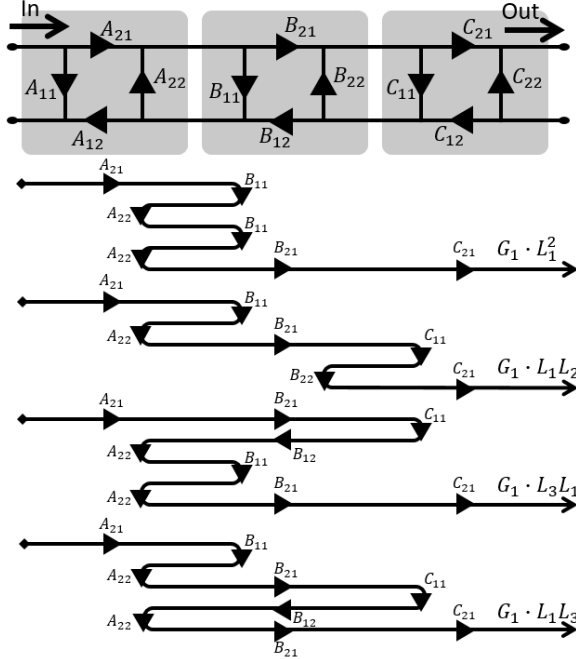


Fig. 4. Energy transfer diagram. The 1st order linearization of S_{21} can be improved (which we call the 2nd order linearization) by including all paths which travel through two loops (four bounces). Shown above are all such two loop paths which include the loop L_1 . Additional two loop paths not shown are $G_1 L_2^2$, $G_1 L_3^2$, $G_1 L_2 L_3$ and $G_1 L_3 L_2$.

The energy transfer diagram in Fig. 4 provides an intuitive understanding of Eqn. 12 and shows that the 2nd order linearization can be found by augmenting the 1st order linearization with the energy transfer terms that contain two loops (or four bounces). It is interesting to note that the energy transfer terms $G_1 L_3 L_1$ and $G_1 L_1 L_3$ represent two separate ways to traverse the signal flow graph and therefore both must be included, thus the ‘2’ coefficient in Eqn. 12 for touching loop terms.

For signal integrity systems of cascaded 2-port \mathbf{S} matrices, the truncation of the infinite series at $n = 2$ is quite accurate as will be shown in the next section. For highly resonant systems, more terms may be needed. The linearization can be applied to differential, common, mode-conversion and single ended 2-port \mathbf{S} matrices, depending on the desired application. The linearization is straightforward to calculate, as it only requires the determination of the primary loops and loops taken two-at-a-time. The Mason’s rule response of these systems

may be difficult to directly apply due to the many n -at-a-time loop combinations that must be considered. The numerical solution procedure of the linearization is summarized in Table 2 below.

Table 2: Linearization process summary

Step	Action
0	Diagram the signal flow graph for the network of 2-port S-parameters.
1	Calculate the forward path $G_1 = A_{21} B_{21} C_{21} \dots$
2	Identify and determine the expression for each loop in the system, $L_1 = A_{22} B_{11}$, $L_2 = B_{22} C_{11}$, $L_3 = A_{22} B_{21} C_{11} B_{12}$, etc. For N segments, there will be $\frac{N(N-1)}{2}$ loops.
3	For 1 st order linearization, calculate the loop responses by multiplying the forward path G_1 with each of the loops.
4a	For 2 nd order linearization, determine the list of all two-at-a-time combinations of loops.
4b	For each combination determine if the two loops are touching in the signal flow graph.
5	Calculate the loop responses by multiplying the forward path response G_1 by each loop term.
	Single loop terms: $G_1 \sum L_i$.
	Single loop squared terms: $G_1 \sum L_i^2$.
	Non-touching terms: $G_1 \sum_{non-touching} L_i L_j$.
	Touching loop terms $2 \cdot G_1 \sum_{touching} L_i L_j$.
6	Calculate the linearization error.
6a	Find the true S_{21} by numerically cascading the S parameter segments [6].
6b	Calculate S_{21}^* or S_{21}^\ddagger by summing the forward path with the loop responses.
6c	Calculate the error as the difference between S_{21} and S_{21}^* or S_{21}^\ddagger .

The linearization is useful as an insight into the reflective behavior of the system, but it can be computationally intense depending on the size of the system. For a system with N segments, the number of multiplication operations per frequency to cascade \mathbf{S} matrices with the ABCD matrix approach is $O(26N)$, while to calculate the loop responses for the 1st order linearization is $O(N^3/3)$ and for the 2nd order linearization is $O(N^4/4)$ due to the exponential number of loops and combinations of loops to consider.

$$S_{21} = A_{21} B_{21} C_{21} \left(\begin{array}{c} 1 + \\ L_1 + L_2 + L_3 - L_1 L_2 + \\ L_1^2 + 2L_1 L_2 + L_2^2 + 2L_1 L_3 + 2L_2 L_3 + L_3^2 - L_1^2 L_2 - L_1 L_2^2 - L_1 L_2 L_3 + L_1^2 L_2^2 \\ + \dots \end{array} \right), \quad (10)$$

$$S_{21} \approx S_{21}^\ddagger = A_{21} B_{21} C_{21} (1 + L_1 + L_2 + L_3 + L_1^2 + L_2^2 + L_3^2 + L_1 L_2 + 2L_1 L_3 + 2L_2 L_3), \quad (11)$$

$$S_{21}^\ddagger = (A_{21}B_{21}C_{21} \dots) \left(1 + \sum (L_i + L_i^2) + \sum_{non-touching} L_i L_j + 2 \cdot \sum_{touching} L_i L_j \right). \quad (12)$$

V. ERROR ANALYSIS

As will be shown, the linearization error is proportional to the magnitude of the largest impedance discontinuity and the number of \mathbf{S} matrix segments in the system. The relative error ratio, found by normalizing the error by the actual value, is evaluated, as it allows for extensive simplification. When applied to a three-segment system with 1st order linearization, the relative error ratio is:

$$\begin{aligned} & \left| \frac{(S_{21} - S_{21}^\ddagger)}{S_{21}} \right| \\ &= \left| \frac{\frac{A_{21}B_{21}C_{21}}{1-L_1-L_2-L_3+L_1L_2} - A_{21}B_{21}C_{21}(1+L_1+L_2+L_3)}{\frac{A_{21}B_{21}C_{21}}{1-L_1-L_2-L_3+L_1L_2}} \right| \quad (13) \\ &= |1 - (1-L_1-L_2-L_3+L_1L_2)(1+L_1+L_2+L_3)| \\ &= |L_1^2 + L_2^2 + L_3^2 + 2L_1L_2 + 2L_1L_3 + L_2L_3 - L_1L_2L_3 \\ &\quad - L_1^2L_2 - L_1L_2^2|. \end{aligned}$$

Observe that all the single loop terms (i.e., L_1, L_2, L_3) of the simplified relative error ratio for the 1st order linearization cancel out, leaving only terms with products of two or more loops. Similarly, the simplified relative error ratio for the 2nd order linearization (not shown due to space considerations) includes only error terms composed of the products of three or more loops. To derive an upper bound on the error, we define $\nu = \max(|L_i|)$ and substitute ν for each loop in the relative error ratio. For $N=3$ segment and $N=6$ segment systems the 1st and 2nd order maximum error bounds are given in Table 3.

Table 3: Maximum error bound for linearization of order O for systems with N segments

N	O	Maximum Error Bound
3	1	$8\nu^2 - 3\nu^3$
3	2	$21\nu^3 - 8\nu^4$
6	1	$190\nu^2 - 497\nu^3 + 411\nu^4 - 134\nu^5 + 15\nu^6$
6	2	$2353\nu^3 - 6239\nu^4 + 5186\nu^5 - 1695\nu^6 + 190\nu^7$

Figure 5 shows the 1st and 2nd order upper error bounds for a three-segment system as well as the 2nd order error bounds for the four-, five- and six-segment systems. This illustrates that the larger the loop terms (i.e., ν), the larger the error. Further, the more segments in the system, the more variability and thus the higher the

upper error bound.

We will use an analytic MC study to validate this upper error bound. The exact S_{21} (Eqn. 4) and the 2nd order linearization (Eqn. 11), are calculated with $A_{21} = B_{21} = C_{21} = 1$ (representing a lossless system) and with random values of A_{22} , B_{11} , B_{22} and C_{11} which are calculated as follows. By noting that the diagonal S_{ii} terms of \mathbf{S} are reflection coefficients, and by utilizing the reflection coefficient equation $\Gamma = \frac{Z_L - Z_1}{Z_L + Z_1}$ between a load impedance of Z_L and a line impedance Z_1 , we relate the line impedance to the load impedance with the ratio r , $Z_1 = rZ_L$. This leads to $\Gamma = \frac{1-r}{1+r}$, which gives the reflection coefficient in terms of the ratio of impedance discontinuity, r . For the application of high speed interconnects, the manufactured characteristic impedance variation of mid-priced PCB transmission lines is typically +/- 15%. A conservative range for r is 0.5 to 1.5 which relates to an impedance variation of 50% to 150%. Therefore, each of the S_{ii} terms are calculated with the random variable r , drawn from the normal distribution $\mathcal{N}(1, 0.15^2)$ which has approximately the range of 0.5 to 1.5. The results of the MC study are shown in Fig. 6. The upper error bound (given in Table 3) is not exceeded by 10^8 MC evaluations of the relative error ratio. Although not an absolute proof, this lends credibility to the upper bound calculation. The analytic MC study procedure is summarized in Table 4.

Table 4: Analytic MC validation of Error Bound for $N=3$ segments

Step	Action
0	Let $A_{21} = B_{21} = C_{21} = 1$.
1	Calculate A_{22} , B_{11} , B_{22} and C_{11} .
1a	Select the ratio of impedance discontinuity, r , from $\mathcal{N}(1, 0.15^2)$.
1b	Transform r to a reflection coefficient with $\Gamma = \frac{1-r}{1+r}$ and assign to return loss term.
2	Calculate the exact S_{21} from Eqn. 4.
3	Calculate the 2 nd order linearization S_{21}^\ddagger from Eqn. 11.
4	Calculate the relative error ratio.
5	Determine the max loop value, $\nu = \max(L_i)$.
6	Plot ν vs relative error ratio.

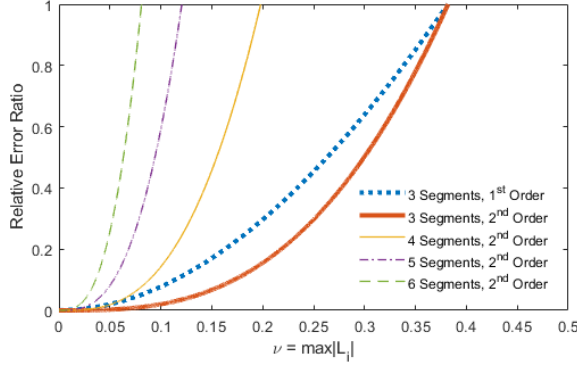


Fig. 5. The larger the impedance discontinuities in the system the larger the linearization error. The upper error bound is reduced by using the 2nd order linearization. The upper error bound is also dependent on the number of \mathbf{S} matrix segments in the system, since each additional segment increases the number of loops or pairs of impedance discontinuities in the system.

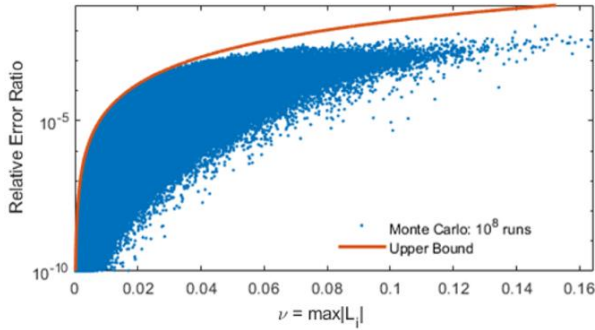


Fig. 6. 100 million MC runs validate the upper error bound for three \mathbf{S} matrix segments with the 2nd order linearization of S_{21} . The solid line is the bound from Table 3 and the dots are Monte Carlo (MC) experiments.

An empirical MC study of the linearization error bound is accomplished by cascading transmission line \mathbf{S} matrix models. These models were created using the IEEE 802.3bj 2-port differential transmission line model (TLM) equations [20] with parameter values from Table 5. These models are attractive to use, because they are readily available and are guaranteed to be causal by construction. The DC loss term is γ_0 , a_1 is the attenuation and phase constant proportional to the square root of frequency, a_2 is the attenuation and phase constant proportional to frequency, and τ is the primary delay constant. Z_c is the differential characteristic impedance, and d is the transmission line length. The values of the behavioral attenuation and phase constants were obtained by the standards task force by fitting the equations to measured transmission line PCB data [21].

Table 5: IEEE 802.3bj 2-port differential Transmission Line Model (TLM) parameters

Parameter	Value	Units
γ_0	0	1/mm
a_1	1.734×10^{-3}	ns ^{1/2} /mm
a_2	1.455×10^{-4}	ns/mm
τ	6.141×10^{-3}	ns/mm
Z_c	$U(60, 140)$	Ω
d	$U(6, 177)$	mm

The MC study entailed cascading $N=3$ and $N=6$ \mathbf{S} matrix segments to evaluate the linearization error. In each case, each \mathbf{S} matrix segment was obtained by using the parameter values in Table 5 and randomly selecting the characteristic impedance Z_c from a uniform distribution between 60 and 140 Ω and randomly selecting the length d from a uniform distribution between 6 and 177 mm. Care must be taken when selecting the frequency vector over which the TLM is created. Too coarse frequency sampling may lead to an incorrect phase delay of the TLM, while too fine frequency sampling will add unnecessary computation time with minimal improvement in accuracy.

For each experiment, the maximum error (over frequency) was determined, and ν was found as the maximum loop response, $\max(|L_1|, |L_2|, \dots)$, at the frequency of the maximum error. The empirical MC study is summarized in Table 6.

Table 6: Empirical MC validation of error bound with transmission line for $N=3$ and $N=6$ segments

Step	Action
0	For each MC experiment,
1	Create transmission line \mathbf{S} matrices from 1 to N .
1a	Randomly select $Z_c \in U(60, 140)$ and $d \in U(6, 177)$ and use parameter values from Table 5.
1b	Calculate \mathbf{S} matrix through and reflection terms.
2	Calculate total S_{21} by cascading [6].
3	Calculate 2 nd order linearization S_{21}^\ddagger by following the procedure in Table 2.
4	Calculate the relative error ratio. Find the max error and the frequency it occurs at. Find $\nu = \max(L_i)$ at the max error frequency.
5	Plot max error vs. ν .

The results for the $N=3$ and $N=6$ \mathbf{S} matrix segments MC study are shown in Fig. 7. We observe that for 1000 experiments the error bound is not exceeded. These studies further validate the upper error bound and show

some of the limitations of the linearization. Systems which have many large impedance discontinuities (greater than +/- 20% impedance mismatch) have large linearization error. Yet even in these situations, the linearization may still provide insight into the system and could still be the basis of useful analysis techniques.

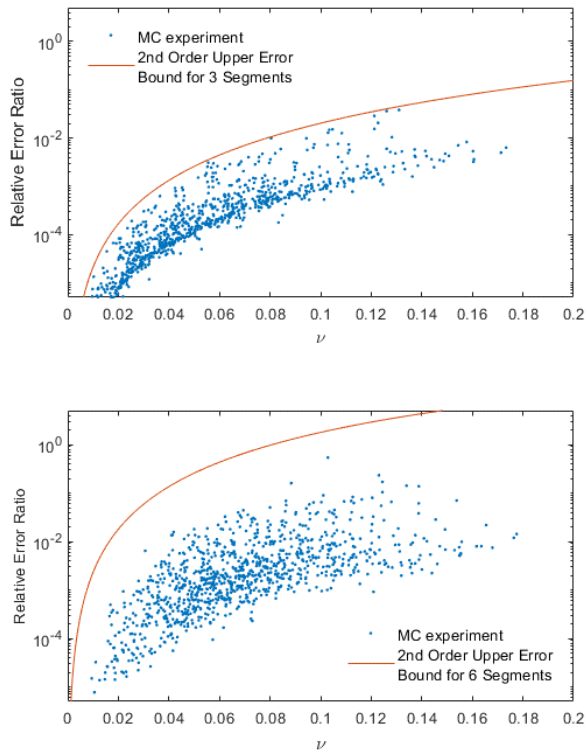


Fig. 7. The upper error bound holds for a realistic MC experiment from systems with three and six transmission line \mathbf{S} matrix segments.

VI. CONCLUSION

To better analyze reflective multi-path behavior, this paper advocates the use of Mason's rule, as compared to the ABCD matrix approach, for the cascading of \mathbf{S} matrix segments. This analytic formulation shows how resonant loops in the system give rise to reflective noise. A linearization or decomposition of this analytic formula allows for the independent analysis of physically meaningful terms to quantify how each resonant loop contributes to the overall multi-path behavior. An error bound is derived and shown to be dependent on the number of segments and the magnitude of the largest impedance discontinuities in the system. The error bound is validated with analytic and empirical MC studies. Overall, this linearization can yield more insight into the reflective behavior of complex systems and provide avenues to unique analysis techniques that will improve the design process of signal integrity interfaces or provide the capability to enable a reflective interference

budgeting methodology.

The \mathbf{S} matrix linearization method has been applied to optimizing a CEI 28G-VSR signal integrity interface [19, 22]. Here the first order linearization could successfully quantify the impact on receiver performance of each pair of impedance discontinuities.

Future work will explore applications of reflective interference budgeting for high-speed communication computer interfaces, sensitivity analysis of systems to catastrophic resonant behavior and interconnect optimization.

REFERENCES

- [1] B. Casper, "Electrical interconnect potential and limits," in *Optical Interconnects Conference, 2014 IEEE*, 2014.
- [2] T. Liang, S. Hall, H. Heck, and G. Brist, "A practical method for modeling PCB transmission lines with conductor surface roughness and wide-band dielectric properties," in *Microwave Symposium Digest, 2006. IEEE MTT-S International*, pp. 1780-1783, 2006.
- [3] I. Bardi, E. Bracken, M. Commens, and R. Petersson, "Finite Element Method Practices to Result in Accurate and Causal Broad Band Frequency Sweeps in Simulating PCBs and Interconnects," *28th Annual Review of Progress in Applied Computational Electromagnetics*, 2012.
- [4] "OIF2010.404.04: CEI-28G-VSR draft IA," 2010.
- [5] D. M. Pozar, *Microwave Engineering*. John Wiley & Sons, 2009.
- [6] J. Frei, X.-D. Cai, and S. Muller, "Multiport S-parameter and T-parameter conversion with symmetry extension," *IEEE Transactions on Microwave Theory and Techniques*, vol. 56, no. 11, pp. 2493-2504, 2008.
- [7] D. Telian, S. Camerlo, K. Matta, M. Steinberger, B. Katz, and W. Katz, "Moving Higher Data Rate Serial Links into Production - Issues & Solutions," *Presented at the DesignCon 2014 Conference*, Santa Clara CA, 2014.
- [8] D. Telian, S. Camerlo, M. Steinberger, B. Katz, and W. Katz, "Simulating Large Systems with Thousands of Serial Links," *Presented at the DesignCon 2012 Conference*, Santa Clara CA, 2012.
- [9] C.-W. Huang, C. E. Smith, A. Z. Elsherbeni, and B. Hammond, "A novel simplified four-port scattering parameter model for design of four-pair twisted-pair cabling systems for local area networks," *IEEE Transactions on Microwave Theory and Techniques*, vol. 48, no. 5, pp. 815-821, 2000.
- [10] W. T. Beyene, N. Cheng, and C. Yuan, "Design and analysis of multi-gigahertz parallel bus interfaces of low-cost and band-limited channels," in

Electrical Performance of Electronic Packaging, 2003.

- [11] J. Lu and D. Thiel, "EMC Computer Modeling and Simulation Techniques," *22nd Annual Review of Progress in Applied Computational Electromagnetics*, 2006.
- [12] H. Yordanov, M. T. Ivrlac, A. Mezghani, J. A. Nossek, and P. Russer, "Computation of the Impulse Response and Coding Gain of a Digital Interconnection Bus," *24th Annual Review of Progress in Applied Computational Electromagnetics*, 2008.
- [13] M. Schneider, "Computation of impedance and attenuation of TEM-lines by finite difference methods," *IEEE Transactions on Microwave Theory and Techniques*, vol. 13, no. 6, pp. 793-800, 1965.
- [14] "Quantum Channel Designer User Manual," *Signal Integrity Software, Inc.*, 2018.
- [15] "I/O Buffer Information Specification (IBIS) Version 6.1.," 2015.
- [16] P. Triverio, S. Grivet-Talocia, M. S. Nakhla, F. G. Canavero, and R. Achar, "Stability, causality, and passivity in electrical interconnect models," *IEEE Transactions on Advanced Packaging*, vol. 30, no. 4, pp. 795-808, 2007.
- [17] Z. N. Yong, *et al.*, "Main cause of resonance appeared around 7.5 GHz on the frequency response of S-parameters of PWB," in *Electronic Packaging Technology and High Density Packaging (ICEPT-HDP), 2011 12th International Conference on*, 2011.
- [18] S. J. Mason, "Feedback theory: Further properties of signal flow graphs," *Proceedings of the IRE*, vol. 44, no. 7, pp. 920-926, 1956.
- [19] R. J. Allred, B. Katz, and C. Furse, "Ripple analysis: Identify and quantify reflective interference through ISI decomposition," in *Signal and Power Integrity (SPI), 2016 IEEE 20th Workshop on*, 2016.
- [20] *IEEE Standard for Ethernet, Amendment 2: Physical Layer Specifications and Management Parameters for 100 Gb/s Operation Over Backplanes and Copper Cables*, IEEE Std 802.3bj-2014, 2014.
- [21] "Proposal for a causal transmission line model," IEEE P802.3bj Task Force, http://www.ieee802.org/3/bj/public/mar14/healey_3bj_01_0314.pdf, March 2014.
- [22] R. J. Allred, "System and method for signal integrity waveform decomposition analysis," U.S. Patent 9,633,164, issued April 25, 2017.



Richard J. Allred is a Principle Engineer at Signal Integrity Software, Inc. (SiSoft). He received his BS/MS in Electrical Engineering in 2006 from the University of Utah and is currently pursuing a Ph.D. in Electrical Engineering from the University of Utah.

He technically led Signal Integrity teams to design high speed graphics memory interfaces at Intel, contributed to the first 100 Gigabit Ethernet CMOS PHY at Inphi and provided software tool development and Tx/Rx IBIS-AMI models for SiSoft. He is a Member of IEEE and is currently researching how non-linear effects impact interconnect performance and performance estimation.



Cynthia M. Furse is the Associate Vice President for Research at the University of Utah and a Professor of Electrical and Computer Engineering. Furse received her B.S. in Electrical Engineering with a Mathematics minor in 1985, M.S. degree in Electrical Engineering in 1988, and her Ph.D. in Electrical Engineering from the University of Utah in 1994.

She has applied her expertise in electromagnetics to sensing and communication in complex lossy scattering media such as the human body, geophysical prospecting, ionospheric plasma, and aircraft wiring networks. She has taught electromagnetics, wireless communication, computational electromagnetics, microwave engineering, antenna design, and introductory electrical engineering and has been a leader in the development of the flipped classroom.

Furse is a Fellow of the IEEE and the National Academy of Inventors. She is a past AdCom Member for the IEEE AP Society and past chair of the IEEE AP Education Committee. She has received numerous teaching and research awards including the 2009 IEEE Harriett B. Rigas Medal for Excellence in Teaching. She is a Founder of LiveWire Innovation, Inc., a spin-off company commercializing devices to locate intermittent faults on live wires.

Biomimetic Radar Target Recognition Based on Hypersausage Chains

Huan-Huan Zhang and Pei-Yu Chen

The School of Electronic Engineering
Xidian University, Xi'an, 710071, China
hhzhang@xidian.edu.cn

Abstract — A biomimetic radar target recognition method is proposed in this paper. From a geometrical perspective, the high resolution range profiles of radar targets are considered as points in high-dimensional feature space. Hypersausage chains are used to cognize the low-dimensional manifold embedding in the high-dimensional space. The topological framework construction algorithm for a hypersausage chain is improved and described in detail. A procedure for a reasonable selection of the hypersphere radius is also involved, which guarantees both acceptable generalization capability and excellent rejection capability of the classifier. The performance of proposed method is compared with the commonly used support vector machine (SVM) method with a radial basis function kernel or a polynomial kernel. Simulation results show that our proposed method outperforms the SVM methods in anti-noise capability, generalization capability and especially rejection capability.

Index Terms — Biomimetic radar target recognition, high resolution range profiles, hypersausage chains, manifold.

I. INTRODUCTION

With the widespread application of high resolution radars, high resolution range profile (HRRP) of radar targets becomes more and more accessible. HRRP carries information of target scattering centers distribution along the radar pointing direction, which reflects details of target structure such as scatterer centers strength, scatterer centers position, target size and so on. Therefore, HRRP plays an increasingly important role in the field of radar automatic target recognition (RATR) [1]–[5].

There is a common process flow in a typical radar HRRP target recognition system. Provided that the wide band electromagnetic scattering field and the raw HRRP of the target is obtained, a preprocessing procedure, which contains alignment, localization, averaging and normalization, will be carried out firstly to improve the quality of raw HRRP. Then a feature extraction procedure is used to select proper feature vectors for the classifier. Four kinds of feature vectors are frequently

used in existing literature: 1) HRRP after preprocessing procedure, this means classification procedure is conducted directly after preprocessing. 2) Transformation of HRRP, such as differential power spectrum [6], bispectrum [7], [8], higher order spectra [9] and so on. All of these features can eliminate the sensitivity of the HRRP to the translation of target in the range window. 3) Target structure information extracted from HRRP, such as the amplitude of scatterer centers, scatterer centers position, target length and so on. 4) Dimensionality reduction of HRRP using principal component analysis (PCA), linear discriminant analysis (LDA), neighborhood preserving projections (NPP) [10] and so on. These dimensionality reduction methods can also be used after 2) or 3). The application of these methods can avoid the curse of dimensionality and facilitate the classifiers. It can be conclude that the sensitivity of HRRP to translation can be eliminated or the dimensionality of HRRP vectors can be reduced based on the feature vectors in 2) to 4). But some transformation methods and dimensionality reduction methods will cause loss of information and influence the recognition accuracy. So provided that the preprocessing procedure is done well enough to eliminate the sensitivity of HRRP to translation and the classifier is efficient to handle high dimensional data (It can be seen that the proposed method is very convenient to deal with high dimensional data), we directly use the HRRP after preprocessing procedure as feature vectors in this paper. Finally the classifier will give the recognition result by using the feature vectors.

Many traditional statistical learning methods have been used as classifier in radar target recognition, such as neural networks (NN) [11]–[13], genetic programming [14], support vector machine (SVM) [15]–[18] and so on. These methods always aim at best distinguishing the samples of different classes based on their differences in feature space. Taking the SVM method as an example, it maps the training samples to a higher dimensional space and finds a linear separating hyperplane with the maximal margin for them. However, people cognize things in a very different manner. When you see a new thing, your first response is that you are not familiar with

it rather than to compare it with things you know. The latter is the manner in which traditional statistical learning methods do. This reflects that people focus on cognizing things whereas traditional statistical learning methods are concerned with distinction of things. It is not difficult to foresee that the latter will suffer from two drawbacks in radar target recognition. First, if encountering a new target without learning, it cannot realize that the target is not trained. It can only assign it to one of the trained target constrainedly, which makes the rejection capability of traditional statistical learning methods very poor. Second, if a new target needs to be learned, we must add its samples to the database and retrain samples of all classes. This makes the efficiency of traditional statistical learning methods very low when training new samples. Imitating the cognitive nature of human, a biomimetic pattern recognition method based on hypersausage chain was proposed [19]–[21]. In this paper, we improve this method and apply it to radar target recognition. The experiment results show that the proposed method has better anti-noise capability, generalization capability and especially rejection capability compared with the SVM method. It is worth mentioning that the proposed method works in optical scattering region. For the radar target recognition method in resonance region, there also exist some works which focus on discriminating unknown targets from known targets [22], [23].

The remainder of this paper is organized as follows. Section II describes the raw HRRP database prepared for radar target recognition. In Section III, we introduce the biomimetic radar target recognition algorithm based on hypersausage chains. Section IV shows the experiments and results. Finally, section V gives some conclusions.

II. DATA PREPARATION

A raw HRRP database is built for five scaled models (F15, F117, VFY218, plane model and missile model). Physical optical (PO) method [24]–[26] is employed to simulate the VV polarization backscattering field of them at an elevation angle of 10° . For the computation of F15, F117 and VFY218 models, the azimuth angle is changed continuously from 0° (nose-on direction) to 90° with an interval of 0.4° . For the simulation of the plane and missile models, 75 azimuth angles are selected randomly from 0° to 90° . In each angle, 201 frequencies from 8GHz to 12GHz with a frequency step of 20 MHz are calculated, yielding 4GHz bandwidth. Then the raw range profiles are obtained by inverse fast Fourier transform (FFT). At last, each raw range profile is normalized by their maximum and minimum so that values of each range profile are scaled to between 0 and 1.

It can be found through above description the database has 226 range profiles for F15, F117, VFY218 models separately and 75 range profiles for plane, missile models separately. In the experiment stage, we

will only use some range profiles of F15, F117, VFY218 models to train the classifier and the other range profiles will be used to test the performance of the classifier.

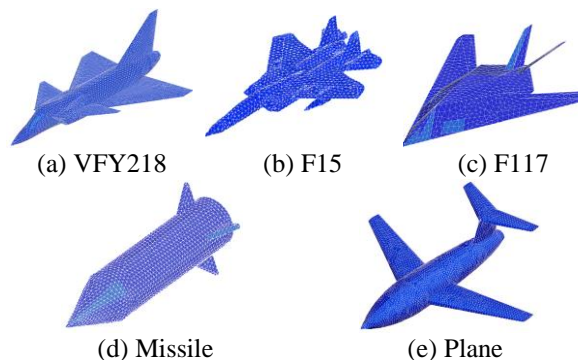


Fig. 1. Five meshed models.

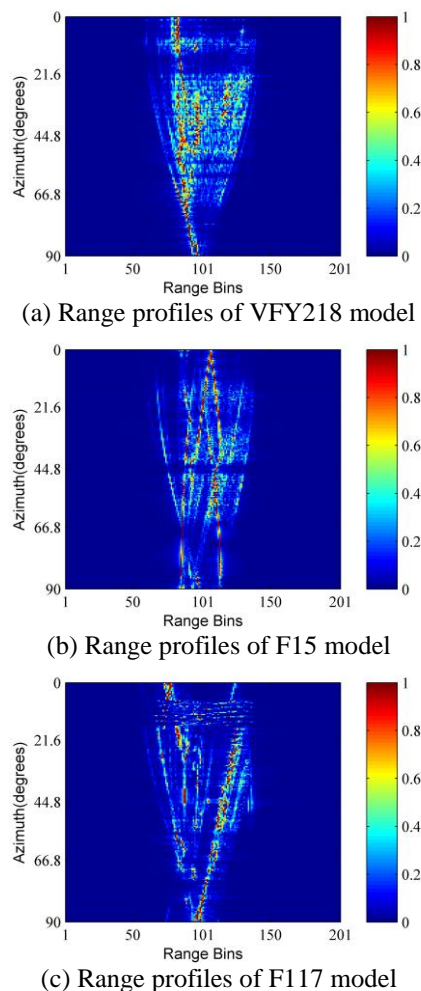


Fig. 2. Range profiles of three models.

The five scaled models are shown in Fig. 1. The sizes of them are shown in Table 1. By considering the

frequency range and the dimensions of the targets, we can find that they fall into optical scattering region. The normalized range profiles of F15, F117, VFY218 models are illustrated in Fig. 2. As evidenced by Fig. 2, the range profiles of targets are very sensitive to the azimuth angle, which implies that radar HRRP target recognition requires plenty of range profiles from various azimuth angles to guarantee reliable recognition accuracy. As mentioned in the introduction, the above normalized range profiles will be used directly as feature vectors for the classification experiment in Section IV.

Table 1: The dimensions of five targets

Targets	Length (m)	Width (m)	Height (m)	Scaling Ratio
VFY218	3.09	1.78	0.82	4.85
F15	3.00	2.10	0.66	6.48
F117	3.00	2.03	0.37	6.69
Missile	2.99	1.17	1.17	1.00
Plane	3.00	2.97	0.87	9.53

III. BIOMIMETIC RADAR TARGET RECOGNITION BASED ON HYPERSAUSAGE CHAINS

A. Theory and principle

The theoretical basis of biomimetic pattern recognition is the principle of homology-continuity (PHC), which points out that samples from the same class change gradually and continuous variation sequences exist between any two samples of same class. This principle implies that biomimetic pattern recognition takes advantage of some prior knowledge of samples. It is obvious that the radar HRRP feature also obeys this principle. So the biomimetic pattern recognition method can be applied to radar target recognition problems. In the following of this paper, we will use biomimetic radar target recognition (BRTR) to call the proposed method.

For the realization of BRTR, a range profile from some class is considered to be a point in high-dimensional space. All the range profiles of the same class can be represented as a point set. Base on the PHC, neighboring points of the point set have strong correlations. This can produce observation which lies on low-dimensional manifold. So we can use some geometry to cover the low-dimensional manifold of a target if we want to cognize the target. In the context of radar target recognition, we believe that one-dimensional (1D) connectivity takes a major role among possible types of connectivity. So we consider a manifold resulted from a product of a hyper-sphere and a 1D continuous curve, where the 1D continuous curve represents the trend of the manifold and the hyper-sphere indicates the perturbation in other directions. For the sake of efficient implementation, a hypersausage chain (shortly HSN chain) formed by moving the center of a hypersphere

along a chain of line segments is used as an approximation model to this kind of manifold. It can be observed that such a hypersausage chain is composed of many sausage-like units, each of which stems from the product of a hypersphere with a line segment. This kind of sausage-like unit is termed as hyper sausage neuron (HSN). The 2D models of HSN chain and HSN are illustrated in Fig. 3, where \mathbf{x}_a and \mathbf{x}_b are the two nodes of the line segment, r is the radius of the hypersphere.

According to the above theory, the main task in the training stage of biomimetic radar target recognition is to find proper hypersausage chains to cover the low-dimensional manifold of different classes. This can be done in two steps. First, the chain of line segments, which is the topological framework of the HSN chain, must be constructed. Second, the radius of the hypersphere must be determined. III-B and III-C will introduce these two steps, respectively.

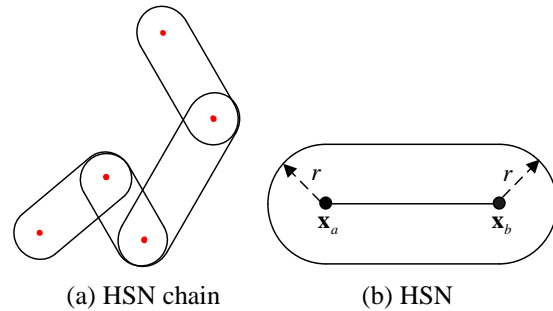


Fig. 3. 2D model of HSN chain and HSN.

B. Topological framework construction algorithm

First of all, we choose the HRRP vector of the first angle as the starting node of the first hyper sausage neuron. Then HRRPs of other angles can be sorted based on this reference point according to the sorting criterion that the mid HRRP vector is more close to the former HRRP vector than the latter one among three adjacent HRRP vectors. This guarantees that HRRP vectors in the high dimensional space change continuously. Using X to represent the set of ordered range profiles from some target, the aforementioned criterion can be described as:

$$X = \{ \mathbf{x}_i, \rho(\mathbf{x}_{i-1}, \mathbf{x}_i) \leq d < \rho(\mathbf{x}_{i-1}, \mathbf{x}_{i+1}) \} \quad (1)$$

$$i = 1, 2, \dots, Na,$$

where \mathbf{x}_i represents the i th range profiles. $\rho(\mathbf{x}, \mathbf{y})$ refers to the Euclidean distance between vectors \mathbf{x} and \mathbf{y} . Na denotes the number of range profiles used as training data set. The topological framework of the HSN is formed by a subset of X whose elements are elaborately selected as the nodes of the hypersausage neurons and can reflect the trend of all the HRRP vectors in high-dimensional space. We use S to represent this subset, where $S = \{ \mathbf{s}_i \}, i = 1, 2, \dots, n_1, n_1 < Na$. Because the two

nodes of each hypersausage neuron is determined in the same manner and the start node of the latter neuron is the end node of the former neuron (the start node of the first neuron is the first HRRP vector in X , namely \mathbf{x}_1), we will only take one hypersausage neuron as an example to introduce the method for its end node selection in the following of this section. The whole topological framework of the HSN will be constructed after the nodes of all hypersausage neurons are determined. The entire algorithm will be described at the end of this section.

Assuming that $\mathbf{x}_j \in X$ refers to the start node of a neuron, ε_1 represents the filter interval, ε_2 denotes the disturbance tolerance, d is the Euclidean distance between current filtered HRRP vector and the start node, $\mathbf{x}_{j+1}, \mathbf{x}_{j+2}, \dots, \mathbf{x}_{N_a}$ will be filtered sequentially to determine its end node. There are three typical cases in the process of filtering:

- 1) As illustrated in Fig. 4 (a), if the distance d increases continually and exceeds ε_1 , the current filtered HRRP vector will be selected as the end node of the neuron.
- 2) Figure 4 (b) shows that the distance d decreases in the process of increasing and the decreased value is smaller than ε_2 . This kind of decrease is a slight disturbance and does not influence the trends of topological framework of the HSN. So it can be tolerated and continue to filter the following HRRP vectors until d exceeds ε_1 .
- 3) In Figs. 4 (c) and (d), the distance d increases to a value smaller than ε_1 then decreases continually. If the decreasing value is greater than ε_2 , the turning point will be considered as the end node of the neuron, and it is also the start node of next neuron. As in [19], the end node of the next neuron will be filtered from current HRRP vector for the purpose of accelerating computation. But this ignores the distribution of HRRP vectors between the turning point and current point. If the distribution of these points is very complicated, the topological framework obtained by original method may not describe the trends very well. Taking the case in Fig. 4 (d) as an example, the first point is the start node of current neuron and the second to tenth points will be filtered to find the end node of current neuron. From the second to fifth point, the distance d is increasing all the time but does not exceed ε_1 . Then it decreases but the decreased value does not exceed ε_2 from the sixth to ninth point until the tenth point. According to [19], the fifth point will be selected as the end node of current neuron. Then the filtering process will continue from the tenth point to find the end node of next neuron and the sixth to ninth points

are ignored. But it is obvious that the distance between the fifth and ninth point exceeds ε_1 and the ninth point should be selected as the end node of the next neuron. So in order to acquire a more accurate topological framework, in this paper we choose the turning point as the end node of current neuron and the start point of the next neuron, meanwhile the end node of the next neuron will also be filtered from the turning point.

Based on the above analysis, the entire algorithm for the topological framework construction can be summarized in Table 2. It is necessary to point out that the selection of the filter interval ε_1 and disturbance tolerance ε_2 will affect the recognition effect of proposed method. If the nearest distance of all the samples is d_1 and the farthest distance of them is d_2 , we recommend choosing ε_1 in the range of (d_1, d_2) by using cross-validation. ε_2 is selected between a third and half of ε_1 .

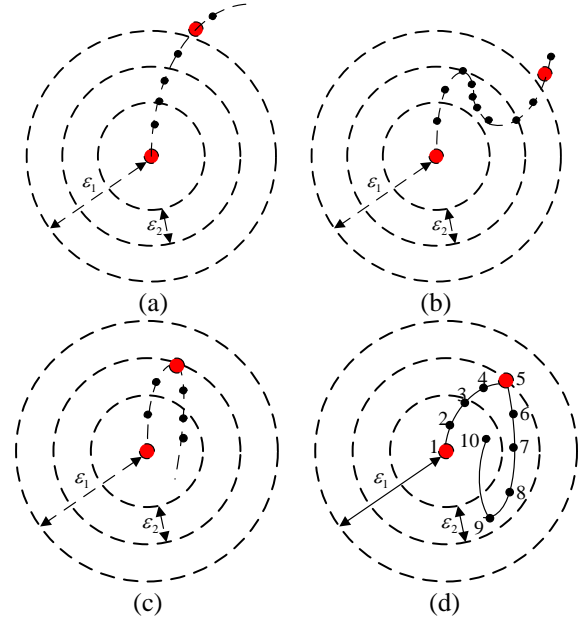


Fig. 4. Three typical cases in the construction of topological framework. The red points represent the nodes of current neuron. The black points denote the feature vectors not selected as nodes of current neuron.

C. The radius of hypersphere

The topological framework describes the main trend of the HSN chain while the radius of the hypersphere decides its coverage area. A larger coverage area means better generalization capability of the classifier while a smaller one implies better rejection capability. So one can strengthen generalization or rejection capability by adjust the radius of the hypersphere. An instructive procedure for the selection of a proper radius will be given in the following of this section.

Table 2: The topological framework construction algorithm of HSN chain

Input: The set of ordered HRRP vectors corresponding to the HRRP of all angles:

$$X = \{\mathbf{x}_i, i = 1, 2, \dots, Na\}.$$

Output: The set of ordered HRRP vectors forming the topological framework of HSN:

$$S = \{\mathbf{s}_i | i = 1, 2, \dots, n_1, n_1 < Na\}.$$

Initialization:

1. Initialize the first feature vector \mathbf{x}_1 as reference point \mathbf{s}_b , set $\mathbf{s}_b = \mathbf{x}_1$.
2. Save the first HRRP vector to the aforementioned set S , set $S = \{\mathbf{x}_1\}$.
3. Initialize $\mathbf{s}_{\max} = \mathbf{0}$, where \mathbf{s}_{\max} represents the farthest HRRP vector from the reference point.
4. Initialize $d_{\max} = 0$, where d_{\max} denotes the distance between \mathbf{s}_{\max} and the reference point.
5. Initialize $i=2$, where i refers to the number of next HRRP vector to be filtered in set X .

Find the end node of a neuron and reinitialize:

1. Filter the i th to N th HRRP vectors. The i th HRRP vector is recorded as \mathbf{s} , the Euclidean distance between \mathbf{s} and the reference point \mathbf{s}_b is $d = \|\mathbf{s} - \mathbf{s}_b\|$.
- 2.1 If $d_{\max} < d < \varepsilon_1$, set $\mathbf{s}_{\max} = \mathbf{s}$, $d_{\max} = d$, $num=i$, $i=i+1$, go to step 1;
- 2.2 If $d > d_{\max}$ and $d > \varepsilon_1$, save \mathbf{s} to set S , namely $S = S \cup \{\mathbf{s}\}$, reinitialize $\mathbf{s}_b = \mathbf{s}$, $\mathbf{s}_{\max} = \mathbf{0}$, $d_{\max} = 0$, $i=i+1$, go to step 1;
- 2.3 If $d \leq d_{\max}$ and $d_{\max} - d < \varepsilon_2$, $i=i+1$, go to step 1;
- 2.4 If $d \leq d_{\max}$ and $d_{\max} - d > \varepsilon_2$, save \mathbf{s}_{\max} to set S , $S = S \cup \{\mathbf{s}_{\max}\}$, reinitialize $\mathbf{s}_b = \mathbf{s}_{\max}$, $d_{\max} = 0$, $\mathbf{s}_{\max} = \mathbf{0}$, $i=num$, go to step 1.

First of all, the distance between a HRRP vector and a HSN is defined as follows:

$$d(\mathbf{x}, \overline{\mathbf{x}_a \mathbf{x}_b}) = \begin{cases} \|\mathbf{x} - \mathbf{x}_a\| & p(\mathbf{x}, \mathbf{x}_a, \mathbf{x}_b) < 0 \\ \|\mathbf{x} - \mathbf{x}_b\| & p(\mathbf{x}, \mathbf{x}_a, \mathbf{x}_b) > \|\mathbf{x}_b - \mathbf{x}_a\| \\ \sqrt{\|\mathbf{x} - \mathbf{x}_a\|^2 - p^2(\mathbf{x}, \mathbf{x}_a, \mathbf{x}_b)} & \text{otherwise} \end{cases} \quad (2)$$

As illustrated in Fig. 3 (b), \mathbf{x}_a and \mathbf{x}_b are the start node and end node of the HSN, respectively, $p(\mathbf{x}, \mathbf{x}_a, \mathbf{x}_b)$ represents the projection of $\mathbf{x}_a \mathbf{x}_b$ on the unit vector in the direction of $\overline{\mathbf{x}_a \mathbf{x}_b}$ and $p(\mathbf{x}, \mathbf{x}_a, \mathbf{x}_b) = \left\langle \mathbf{x} - \mathbf{x}_a, \frac{\mathbf{x}_b - \mathbf{x}_a}{\|\mathbf{x}_b - \mathbf{x}_a\|} \right\rangle$.

Then the distance between a HRRP vector and the HSN chain is defined as the nearest distance between the HRRP vector and all the neurons of the HSN chain. Finally, Radius can be computed by using different methods according to the number of training HRRP vectors:

- 1) A small number of training HRRP vectors

Find the farthest three samples from the topological framework of HSN chain. Average the distance between the framework and them and record it as r_1 . The purpose of averaging operation is to relieve the influence of outlier. The radius is given as $r_1 + \Delta r_1$, where Δr_1 is a small positive number.

- 2) A large number of training HRRP vectors

According to Section III-B, S refers to the subset whose elements construct the topological framework of HSN chain. We can use a set $T=X-S$ to represent the remainder of X . The distances between every HRRP vector of T and the HSN chain can be computed and they constitute a set $D_T = \{d_1, d_2, \dots, d_{n_2}\}$. n_2 is the number of HRRP vectors in set D_T . When n_2 is large, the elements in D_T are considered to obey Gaussian distribution, namely:

$$P(d) = \frac{1}{\sqrt{2\pi}\sigma} e^{-d^2/2\sigma^2}. \quad (3)$$

The maximum likelihood estimation of μ and σ are:

$$\hat{\mu} = \frac{1}{n_2} \sum_{j=1}^{n_2} d_j, \quad (4)$$

$$\hat{\sigma}^2 = \frac{1}{n_2} \sum_{j=1}^{n_2} (d_j - \hat{\mu})^2. \quad (5)$$

The radius r_2 can be calculated by:

$$\int_0^{r_2} P(x) dx = 1 - \Delta r_2, \quad (6)$$

where Δr_2 is a very small positive number.

D. Testing method

By constructing the topological framework and selecting proper radius, we can train a HSN chain for each target. Then the testing procedure is to judge whether a testing HRRP is in the coverage of some trained HSN chain. Firstly, we introduce a decision function $f_{HSNC}(\mathbf{x})$ to indicate how close a testing HRRP \mathbf{x} is to a HSN chain:

$$f_{HSNC}(\mathbf{x}) = 2^{-d^2(\mathbf{x}, HSNC)/r^2} - 0.5. \quad (7)$$

Where $d(\mathbf{x}, HSNC)$ denotes the distance between the testing HRRP and a HSN chain. If a testing HRRP \mathbf{x} is covered by a HSN chain of a target, the distance $d(\mathbf{x}, HSNC)$ is smaller than r , this will result that

$f_{HSNC}(\mathbf{x}) > 0$. Moreover, the smaller $d(\mathbf{x}, HSNC)$ is, the closer $f_{HSNC}(\mathbf{x})$ is to 0.5. On the contrary, if \mathbf{x} is outside the HSN chain, $f_{HSNC}(\mathbf{x})$ will be less than zero. Now the testing method can be concluded as below:

Assuming that there are N kinds of targets, the HSN chain of them are noted as $HSNC_1, HSNC_2, \dots, HSNC_N$. The decision function $f_{HSNC_i}(\mathbf{x})$ associated with a testing HRRP and the i th HSN chain is computed, where $i = 1, 2, \dots, N$. If all these decision functions are less than zero, this means that the testing HRRP belongs to none of the above HSN chain. Its corresponding target will be considered as unknown and rejected. If there is only one decision function greater than zero, the testing HRRP is exclusively covered by the corresponding HSN chain. The classifier will judge that the testing HRRP comes from the corresponding target. There is a troublesome case that the testing HRRP is covered by more than one HSN chain simultaneously. In this case, there will be more than one decision functions greater than zero. Based on the idea that the testing HRRP is generally more closed to the HSN chain of its corresponding target, the classifier will judge that the testing HRRP belongs to the target corresponding to the largest decision function value.

IV. EXPERIMENTS AND RESULTS

Several experiments are conducted to examine the performance of the proposed BRTR method. The results are compared with that of support vector machine method [27]. The SVM program is provided by LibSVM [28]. The training sets and testing sets of SVM are always the same as that of the proposed method. Both the polynomial kernel and the radial basis function (RBF) kernel are used as the kernel functions of SVM in each of the following experiments. The parameters of RBF kernel are selected according to the procedure recommended in [29] and reasonable results can always be obtained. Because the polynomial kernel has more parameters than the RBF kernel, it is difficult to select optimal parameters for it, which results that the RBF kernel usually has a better performance than polynomial kernel in our experiments. So we will only show the results of SVM with RBF kernel.

In the following experiment, we use P_c to represent correct recognition rate, P_r to denote correct rejection rate. The correct recognition rate is the probability of correctly classifying a known target. The correct rejection rate refers to the percentage of an unknown target rejected correctly. Here we use the terms “known” and “unknown” to indicate targets in the training database and those that are not.

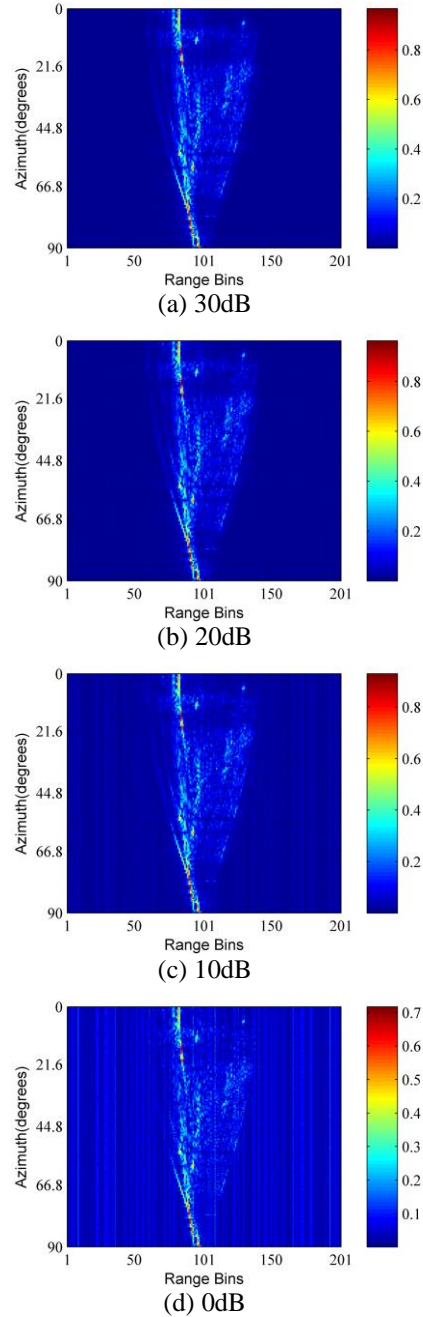


Fig. 5. Range profiles of VFY218 model with different noise level.

A. Anti-noise capability

The first experiment is designed to examine the anti-noise capability of the classifier. The scattered fields of VFY218, F15 and F117 models in frequency domain are contaminated by independent additive White Gaussian noise (AWGN) to achieve the signal to noise ratios (SNR) from 0 to 30dB with a 5dB increment. Then the

contaminated range profiles are obtained by inverse fast Fourier transform and normalized between 0 and 1. Figure 5 shows the contaminated range profiles of VFY218 at the noise levels of 0dB, 10dB, 20dB and 30dB. It is clear that the small values of range profiles are buried in noise when the SNR is low. In this experiment, the odd contaminated range profiles of each target are chosen as training set while the even ones are chosen as testing set, providing 113 different training vectors for each target and totally 339 different testing vectors at each SNR level.

The correct recognition rates against various SNR are demonstrated in Fig. 6. To obtain a correct recognition rate at some SNR, the training and testing processes are repeated 100 times with 100 independent AWGN realizations. Then the resultant 100 correct recognition rates are averaged as the final correct recognition rate P_c .

As it can be seen in Fig. 6, the correct recognition rate of BRTR method is very similar to that of SVM method when the SNR is above 15db. However, for the cases of SNR below 15db, the BRTR method slightly outperforms the SVM method. So we can conclude that the BRTR method is robust to noise and has a better performance than SVM method at a low SNR level.

B. Generalization capability

Generally speaking, the more samples used in training stage, the better performance can be achieved in testing stage. However, it is impractical to build a huge training database for radar target recognition because of cost concerns. So a desired classifier should provide robust and acceptable accuracy when only limited training samples can be obtained.

In the second experiment, different amounts of range profiles from original data set of each model are used as training set to examine the generalization capability of the classifier. The training set of each target is selected from original data set of VFY218, F15 and F117 models with the interval varying from 2 to 6. And the increment is 1. The rest of range profiles from original data set are used as the test set. In other words, there are 113, 76, 57, 46, 38 range profiles for the training of each target and correspondingly 113×3, 150×3, 169×3, 180×3, 188×3 range profiles for testing. Here the decreasing of the training range profiles means increasing the azimuth interval of two neighboring training range profiles, which will reduce the correlations between training sets and testing sets.

The experiment results in Fig. 7 show that the correct recognition rates of BPTR and SVM method are above 96% when the number of training range profiles is more than half of the testing range profiles. But when the number of training range profiles decreases less than half of the testing range profiles, the correct recognition rate of SVM method decreases sharply while that of BPTR drops relatively slow. So the BPTR method is superior

to SVM method for small size of training set. In other words, the BPTR method has better generalization capability than SVM method.

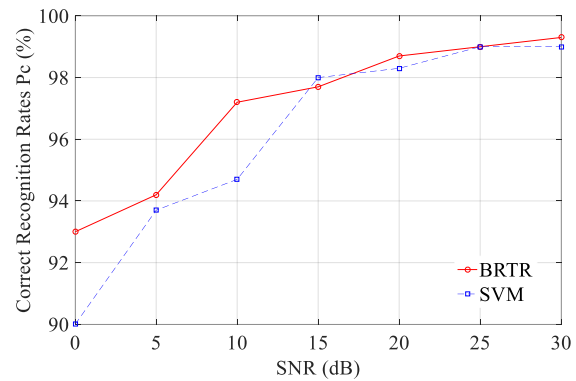


Fig. 6. Performance of biomimetic radar target recognition method and support vector machine method at different levels of SNR.

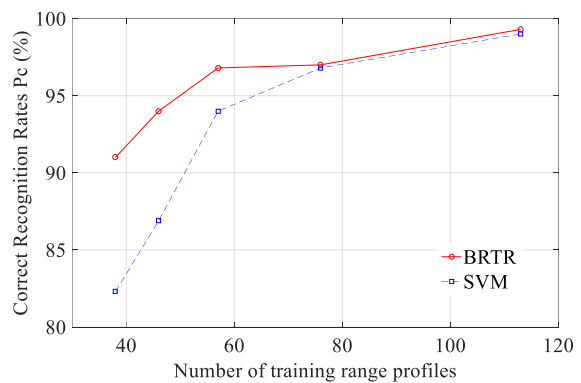


Fig. 7. Performance of biomimetic radar target recognition method and support vector machine method when the number of training and testing range profiles varies.

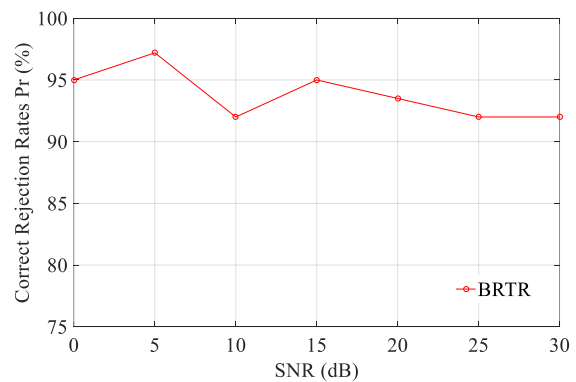


Fig. 8. Rejection capability of biomimetic radar target recognition method at different levels of SNR using the same training range profiles in the anti-noise capability experiment.

C. Rejection capability

Most of the classifiers used for radar target recognition are trained and tested with known targets, but there exist targets which are not included in the training database in reality. Rejection of unknown targets is a very challenging problem not only in the field of radar HRRP recognition but also in the entire automatic target recognition community. Though rejection capability of radar automatic target recognition is of great importance, it does not attract enough attention. One of the most fascinating abilities of our proposed method is its rejection capability.

The third experiment is designed to examine this capability of the classifier. The training range profiles in the anti-noise experiment at different SNR levels are also chosen as the training set in this experiment. The 150 range profiles of two additional unknown targets (plane and missile model) constitute the testing set. It is necessary to point out that the parameters ε_1 and ε_2 are also the same as that in anti-noise experiment, which guarantees that the proposed method can have good rejection capability without sacrificing the anti-noise capability. The experiment results in Fig. 8 show that our proposed method can achieve over ninety percent correct rejection rate, which overcomes the weakness of the traditional statistical learning methods. Moreover, it can be observed that the rejection performance becomes slightly better with lower SNR levels. The reason is that when the SNR is high, a HRRP of the two unknown targets at some azimuth angle may be similar to some HRRP of the known targets since the size of all the targets are similar and they share some common features. However, when the SNR is very low, the HRRPs will be contaminated by noise severely. The similarity of HRRPs between the known targets and unknown targets will also be weakened.

All the above experiments are carried out on a PC with 2.83 GHz CPU and 8 GHz RAM. The parameters $\varepsilon_1=0.6$ and $\varepsilon_2=0.25$ for VFY218, F15 and F117 models. A large number of training HRRP vectors is assumed and $\Delta r_2=0.001$, resulting in that r_2 equals to 0.66, 0.64 and 0.54 for VFY218, F15 and F117 models, respectively. The average training time of the proposed method and the SVM method are 658 ms and 260 ms respectively for different SNR levels. The average testing time of them are 46 ms and 42 ms, respectively.

V. CONCLUSION

A biomimetic radar target recognition method based on hypersausage chains has been proposed and its performance was investigated. Distinct from the distinguishing scheme of traditional statistical learning methods, the proposed method aims at cognizing targets, which is inspired by the cognition nature of human. From a geometrical point of view, the HRRP vectors are

considered to be points in high dimensional space. A hypersausage chain is utilized to optimally cover the points of each target. Three experiments have been conducted and the results show that the proposed method is more robust to noise and the size of training sets compared with the SVM method. Moreover, it is worth mentioning that the proposed method has an excellent rejection capability which is a basic capability of human. This capability is extremely important for a real radar target recognition system. An additional advantage of the proposed method is that it does not need to retrain all the samples in the database when the samples of a new target are added to the database, while the traditional statistical learning methods must retrain all the samples when any new target is included into the database.

ACKNOWLEDGMENT

The authors would like to thank the support of National Natural Science Foundation of China under Grant 61701376, China Postdoctoral Science Foundation under Grant 2017M613071, 2018T111016, Open Project Foundation of the State Key Laboratory of Millimeter Waves under Grant K201808, Open Project Foundation of Key Laboratory of High-Speed Circuit Design and EMC, Ministry of Education. The authors would also like to thank the earnest work of the editors and anonymous reviewers.

REFERENCES

- [1] H. J. Li, Y. D. Wang, and L. H. Wang, "Matching score properties between range profiles of high-resolution radar targets," *IEEE Trans. Antennas Propag.*, vol. 44, no. 4, pp. 444-452, Apr. 1996.
- [2] R. A. Mitchell and J. J. Westerkamp, "Robust statistical feature based aircraft identification," *IEEE Trans. Aerosp. Electron. Syst.*, vol. 35, no. 3, pp. 1077-1094, July 1999.
- [3] Z. H. Guo and S. H. Li, "One-dimensional frequency-domain features for aircraft recognition from radar range profiles," *IEEE Trans. Aerosp. Electron. Syst.*, vol. 46, no. 4, pp. 1880-1892, Oct. 2010.
- [4] H. H. Zhang, D. Z. Ding, Z. H. Fan, and R. S. Chen, "Adaptive neighborhood preserving discriminant projection method for HRRP based radar target recognition," *IEEE Antennas Wirel. Propag. Lett.*, vol. 14, pp. 650-653, 2015.
- [5] L. Du, H. He, L. Zhao, and P. Wang, "Noise robust radar HRRP target recognition based on scatterer matching algorithm," *IEEE Sensors Journal*, vol. 16, no. 6, pp. 1743-1753, Mar. 2016.
- [6] Z. H. Guo and S. H. Li, "Radar target recognition using the differential power spectrum," in *Conf. Rec. 2005 IEEE Int. Conf. Communications and Signal Processing*, pp. 385-387, 2005.
- [7] I. Jouny, E. D. Garber, and R. L. Moses, "Radar

- target identification using the bispectrum: A comparative study," *IEEE Trans. Aerosp. Electron. Syst.*, vol. 31, no. 1, pp. 69-77, Jan. 1995.
- [8] B. Pei, Z. Bao, and M. D. Xing, "Logarithm bispectrum-based approach to radar range profile for automatic target recognition," *Pattern Recognition*, vol. 35, no. 11, pp. 2643-2651, Nov. 2002.
- [9] L. Du, H. W. Liu, Z. Bao, and M. D. Xing, "Radar HRRP target recognition based on higher order spectra," *IEEE Trans. Signal Process.*, vol. 53, no. 7, pp. 2359-2368, July 2005.
- [10] X. Yu, X. Wang, and B. Liu, "Supervised kernel neighborhood preserving projections for radar target recognition," *Signal Processing*, vol. 88, no. 9, pp. 2335-2339, Sept. 2008.
- [11] I. Jouny, F. D. Garber, and S. C. Ahalt, "Classification of radar targets using synthetic neural networks," *IEEE Trans. Aerosp. Electron. Syst.*, vol. 29, no. 2, pp. 336-344, Apr. 1993.
- [12] E. C. Botha, E. Barnard, and C. J. Barnard, "Feature-based classification of aerospace radar targets using neural networks," *Neural Netw.*, vol. 9, no. 1, pp. 129-142, Jan. 1996.
- [13] G. Sun, J. Wang, S. Qin, and J. Na, "Radar target recognition based on the multi-resolution analysis theory and neural network," *Pattern Recogn. Lett.*, vol. 29, no. 16, pp. 2109-2115, Dec. 2008.
- [14] J. S. Kobashigawa, H.-S. Youn, M. F. Iskander, and Z. Q. Yun, "Classification of buried targets using ground penetrating radar: Comparison between genetic programming and neural networks," *IEEE Antennas Wirel. Propag. Lett.*, vol. 10, pp. 971-974, 2011.
- [15] F. A. Sadjadi, "Polarimetric radar target classification using support vector machines," *Opt. Eng.*, vol. 47, no. 4, 046201, Apr. 2008.
- [16] Q. Zhao and J. C. Principe, "Support vector machines for SAR automatic target recognition," *IEEE Trans. Aerosp. Electron. Syst.*, vol. 37, no. 2, pp. 643-654, Apr. 2001.
- [17] M. A. Selver, M. M. Taygur, M. Secmen, and E. Y. Zoral, "Hierarchical reconstruction and structural waveform analysis for target classification," *IEEE Trans. Antennas and Propagation*, vol. 64, no. 7, pp. 3120-3129, July 2016.
- [18] M. A. Selver, M. Secmen, and E. Y. Zoral, "Comparison of scattered signal waveform recovery techniques under low SNR for target identification," *European Conference on Antennas and Propagation (EUCAP) 2017*, pp. 1091-1095, Paris, France, Mar. 2017.
- [19] S. J. Wang and J. L. Lai, "Geometrical learning, descriptive geometry, and biomimetic pattern recognition," *Neurocomputing*, vol. 67, pp. 9-28, Aug. 2005.
- [20] S. J. Wang, "Computational information geometry and its applications," in *Conf. Rec. 2005 IEEE Int. Conf. Neural Networks and Brain*, pp. PL-63-9, Oct. 2005.
- [21] L. Wang, L. D. Xu, R. J. Liu, and H. H. Wang, "An approach for moving object recognition based on BPR and CI," *Inf. Syst. Front.*, vol. 12, no. 2, pp. 141-148, Apr. 2010.
- [22] M. Secmen and G. Turhan-Sayan, "An electromagnetic target classification method for the target sets with alien target: Application to small-scale aircraft targets," *PIERS Online*, vol. 6, no. 5, pp. 425-429, 2010.
- [23] M. Secmen, "Novel Music Algorithm based Electromagnetic Target Recognition Method in Resonance Region for the Classification of Single and Multiple Targets," *Ph.D. dissertation*, Dept. Elect. Electron. Eng., Middle East Tech. Univ., Ankara, Turkey, 2008.
- [24] R. G. Kouyoumjian, "Asymptotic high-frequency methods," *Proc. IEEE*, vol. 53, no. 8, pp. 864-876, Aug. 1965.
- [25] A. B. Gorji, B. Zakeri, and R. C. Janalizadeh, "Physical optics analysis for RCS computation of a relatively small complex structure," *Applied Computational Electromagnetics Society Journal*, vol. 29, no. 7, pp. 530-540, Dec. 2014.
- [26] F. Weinmann, "UTD shooting-and-bouncing extension to a PO/PTD ray tracing algorithm," *Applied Computational Electromagnetics Society Journal*, vol. 24, no. 3, pp. 281-293, June 2009.
- [27] C. Cortes and V. Vapnik, "Support-vector network," *Mach. Learn.*, vol. 20, no. 3, pp. 273-297, Sept. 1995.
- [28] C. C. Chang and C. J. Lin, "LIBSVM: A library for support vector machines," *ACM Trans. Intell. Syst. Technol.*, vol. 2, no. 3, Article 27, Apr. 2011. Software Available: <http://www.csie.ntu.edu.tw/~cjlin/libsvm>
- [29] C. W. Hsu, C. C. Chang, and C. J. Lin, "A practical guide to support vector classification," Apr. 2010. Available : <http://www.csie.ntu.edu.tw/~cjlin/libsvm>



Huan Huan Zhang received the Ph.D. degree in Electromagnetic Fields and Microwave Technology from Nanjing University of Science and Technology in 2015. He was a Postdoctoral Research Fellow with the Center of Electromagnetics and Optics, the University of Hong Kong, Hong Kong, from 2015 to 2016. He is currently a

Lecturer with the School of Electronic Engineering, Xidian University, Xi'an, China.

Zhang serves as the Reviewer of the IEEE Transactions on Antenna and Propagation, Communications in Computational Physics, IEEE Microwave and Wireless Components Letters, IEEE ACCESS, IET Radar, Sonar & Navigation, Applied Computational Electromagnetic Society Journal, etc. His current research interests include multiphysics simulation, computational electromagnetics, and radar signal processing.



signal processing.

Pei Yu Chen received the bachelor's degree from Luoyang Normal University in 2016. Now she is working towards the master's degree in Electromagnetic Fields and Microwave Technology at Xidian University. Her current research interests include multiphysics simulation and radar

SAR Electromagnetic Image Conditioning Using a New Adaptive Particle Swarm Optimization

B. Malakonda Reddy and Md. Zia Ur Rahman

Department of Electronics and Communication Engineering, Koneru Lakshmaiah Education Foundation
Green Fields, Vaddeswaram, Guntur-522502, A.P., India
mdzr@kluniversity.in

Abstract — In Synthetic Aperture Radar (SAR) image Objects or region detection is a difficult task because of improper variation of boundary due to speckle noise. So, it creates the problems of human being for the analysis. In fact, this process leads to inaccurate in the detection and measurement of object parameters. In this paper proposes a new automatic detection of objects from SAR images. For detection of objects an effective method is introduced using the variance of Particle Swarm Optimization (PSO) called Adaptive PSO (APSO). In this paper develops the dynamically varying the inertia weight for PSO and tuning the social components, cognitive components. This APSO find the optimal threshold value for making the better segmentation by preprocessing SAR image with effective Filter. The proposed APSO method has also compared with existing methods in terms of detection of object regions and parameter calculations.

Index Terms — Preprocessing, SAR Image, segmentation, sensing system, swarm optimization, threshold.

I. INTRODUCTION

Synthetic Aperture Radar (SAR) image analysis makes the difficult for analysis for region extraction or identification because of in cleared visualization due to speckle noise. In general, the lakes at anywhere on the ground surface varies their dimensional nature from season to season. In order to analyze the boundary information and the size of the lakes in SAR image. It requires the proper segmentation methodology for extraction of the lake regions by preprocessing with an isotropic diffusion filter SRAD [1] instead of normal filters [2] which smooth's the image by reducing the speckle noise. The automatic detection and processing system are required to detect the objects and regions. This results basic pointer for diagnosis the object. From the literature study it is observed that only few authors are working on regions or objects in SAR image. Deng et al. invented watershed algorithm and region growing methods for segmentation [3]. Further, the contrast of the de-speckling image can be improved by histogram

equalization and to enhance the segmentation process to work on high intensity objects. Objects can be extracted from active contour without edge method. In most cases it is verified that Otsu method is the best technique for image segmentation [4]. Another hybrid technique based on k-means particle swarm optimization introduce by Sepas-Moghaddam [5]. PSO has been used in many other applications which include image de-noising [6], [7], [8], Image analysis and wireless sensor networks. Ali Mohammad Nick Farjam et al. segmented the conical image using Otsu method by which the threshold was optimized by using PSO method. In multilevel thresholding the PSO technique reduces the complexity [9]. To grasp the color objects PSO has been applied to the color image. To remove the speckle various de-speckling filtering techniques are introduced [10], [11]. A novel FO-DPSO is introduced for the remote sensing image segmentation. Image registration, denoising and measuring features is done by various PSO techniques [12]. ShuoLiu, Ali Qusay Al-Faris et al. introduces the MRI image segmentation with Otsu combination with PSO. Effective automatic segmentation methods are suggested in SAR images.

This paper puts the order as follows. Section II describes the proposed modified Otsu method. Section III gives the overview of particle swarm optimization. Section IV gives the detail about the proposed APSO to obtain optimum threshold. The performance evaluation described in Section V and Section VI gives the conclusion of this paper.

II. BACK GROUND OF OTSU METHOD

The challenging task is to find the optimum threshold value for automatic detection of objects in an image sensing and recording system. Otsu method is one of the basic techniques to find the optimum threshold for an image [13]-[15]. In modified Otsu technique iterative method is the basis for finding the initial threshold value. The average threshold value for image histogram is taken at τ . δ_1 and δ_2 represents the mean of the intensity values which is greater than and less than the current threshold respectively.

The calculated threshold is,

$$\tau[i] = \frac{\delta_1^{(i)} + \delta_2^{(i)}}{2}. \quad (1)$$

This threshold value is forwarded to the next iteration. This iteration continuous up to the value where the threshold value converges to $\tau[i] - \tau[i - 1]$. At the end of the iteration the new threshold value is calculated as:

$$\tau^{opt} = \frac{\delta_1^{(i)} + \delta_2^{(i)}}{2}. \quad (2)$$

This calculated threshold value τ^{opt} is used as an initial threshold value for the conventional Otsu method. Based on this τ^{opt} value image divided in to two groups. The mean of the two groups is represented as:

$$m_{t1}(i) = \sum_{k=1}^{\tau^{opt}} \frac{dP(k)}{\rho_1(i)}, m_{t2}(i) = \sum_{k=\tau^{opt}+1}^s \frac{dP(k)}{\rho_2(i)}. \quad (3)$$

For whole image the mean is calculated as:

$$m_t = \sum_{k=1}^s dP(k). \quad (4)$$

Here, s represents the number of gray levels. The optimum threshold value is calculated as:

$$t^* = \operatorname{argmax}[\rho_1(m_{t1} - m_t)^2 + \rho_2(m_{t2} - m_t)^2], \quad (5)$$

where ρ_1 and ρ_2 are the estimated group probabilities. These values are calculated using:

$$\rho_1 = \sum_{k=1}^{\tau^{opt}} p(k), \rho_2 = \sum_{k=\tau^{opt}+1}^s \frac{dP(k)}{\rho_2(i)}. \quad (6)$$

The results of Otsu method and proposed Modified Otsu method are shown in Fig. 1 (c) and Fig. 3 (d). This segmentation is done on the image of preprocessing SAR input image by the SRAD filter shown in Fig. 1 (b). The segmented results of Conventional Otsu and Modified Otsu overlaid on the input SAR image are shown in Fig. 1 (e) and Fig. 1 (f).

The proposed Modified Otsu method is tested under 52 SAR images. From the experimental results it is observed that the proposed Modified Otsu method detects the better lake positions compared to Otsu method and it matches almost matches the segmented regions of human experts. In this paper introduced an idea to optimize the objective function that described by a modified Otsu method using PSO and the proposed APSO. The main problem is to find the optimum threshold for making the proper segmentation. The proposed approach is able to find the optimum set of thresholds with larger between class variance than the other techniques.

III. PARTICLE SWAM OPTIMIZATION FOR SAR IMAGE PROCESSING

It is based on the population based evolutionary technique proposed by Kennedy and Eberhart based on swarm intelligence [18] and other contributions [16], [17], [19] and [20]. For discrete solutions PSO is one of the solutions at the initial stage after it replicates the social behavior of fish and birds in a group for search food. The population of particles flies through the search

space looking for an optimal value. Every particle in the search space having its own fitness value accessed by the object function. The population of random particles is initiated by PSO that is looking for a global optimum solution. All through the generations every particle is updated by particle best and global best values [23]-[25]. After getting these two values based on the distance from the best particle of the population and the distance from the own best position, the position and velocity of the particle are updated. By iteratively, it estimates the fitness value, the particle velocities and positions are deliberated by the following standard equations:

$$M_{k,n}^{i+1} = W_0 M_{k,n}^i + \theta_1 \operatorname{rand}_1 (PBest_{k,n} - P_{k,n}^i) + \theta_2 \operatorname{rand}_2 (GBest_{k,n} - P_{k,n}^i), \quad (7)$$

$$P_{k,n}^{i+1} = P_{k,n}^i + M_{k,n}^{i+1}. \quad (8)$$

Here in the Eq. (7) $M_{k,n}^i$ is the momentum component, n represents the search space, i represents the iteration, $P_{k,n}^i$ represents the position of a particle, θ_1 and θ_2 are cognitive and social components taken as constant in standard PSO and W_0 is the initial weight. The rand_1 and rand_2 are the random values, not the same for all the iterations, but in the range of 0 and 1 only. $GBest$ and $PBest$ are the globally best and particle best values. The effects of social, Inertia weight and cognitive components are obtained by PSO algorithm. The insertion of this inertia weight impacts the history of the velocities on the current history. This inertia weight can be a constant or time varying, where the large and small values have a capability to assist the global and local explorations. In this paper, the inertia weight with constant and dynamically varying values are applied to the SAR image. Initially the constant inertia weight (CIW) is taken as 0.8. In order to get the optimal solution better tuning is significant. For this Eberhart have proposed a new improved PSO concept by means of Dynamically Varying Inertia Weight (DVIW) which is given by:

$$W_0 = W_{max} - (W_{max} - W_{min}) \cdot \operatorname{Iter} / \operatorname{Iter}_{max}, \quad (9)$$

where W_{min} and W_{max} values are set at 0.2 and 0.1 respectively. $\operatorname{Iter}_{max}$ and Iter represents the maximum number of iterations and current iteration. The DVIW provides better weight in order to get the optimum solution.

IV. THE PROPOSED ADAPTIVE PARTICAL SWARM OPTIMIZATION

The main problem with this in this PSO process is the most suitable tuning of the social and cognitive components. In order to meet the global optimal solution here proposed a dynamically varying acceleration coefficient in PSO method [21], [22].

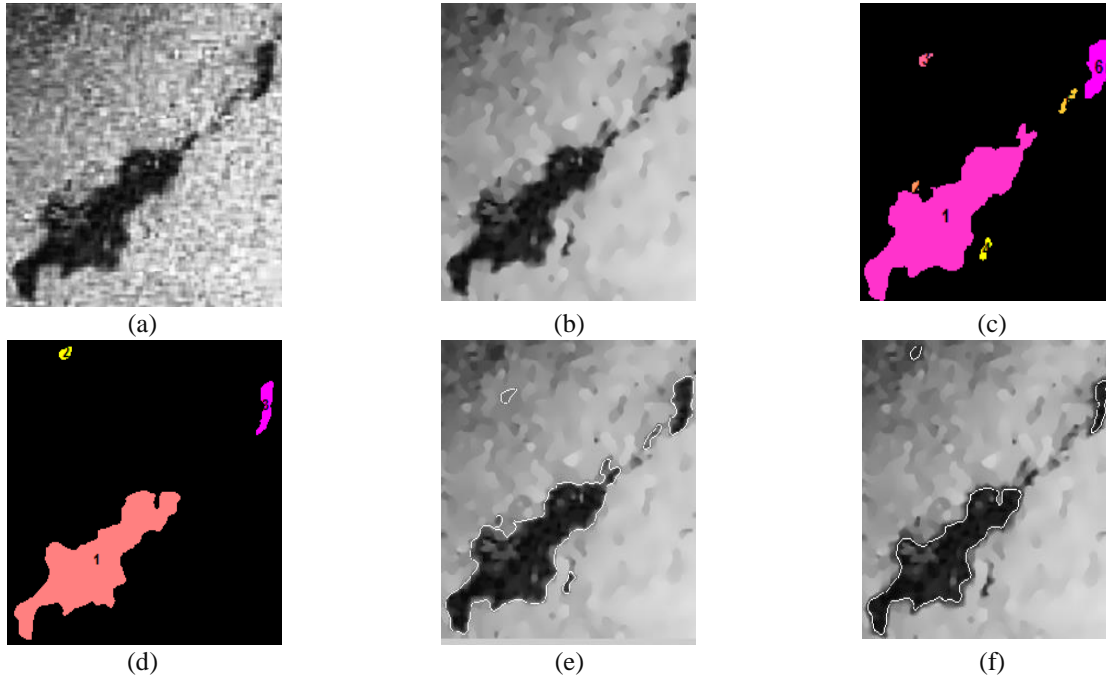


Fig. 1. Segmentation results of Lake Objects in SAR image. (a) Original SAR image, (b) SARD filtered image, (c) Segmented results by Otsu, (d) Segmented results by Modified Otsu, (e) Otsu results overlaid on the original image, and (f) Modified results overlaid on the original image.

To flock the optimum global solution social practical with large value and cognitive with small values is allowed. Tuning of these parameters is done as describing the following equation,

$$M_{k,n}^{i+1} = W_0 M_{k,n}^i + \theta_1 \text{rand}_1 (P_{\text{Best}_{k,n}} - P_{k,n}^i) + \theta_2 \text{rand}_2 (G_{\text{Best}_{k,n}} - P_{k,n}^i)$$

$$\text{Where } \theta_1 = (\theta_{1S} - \theta_{1i}) * \frac{1}{\text{Iter}_{\text{max}}} + \theta_{1i}$$

$$\theta_2 = (\theta_{2S} - \theta_{2i}) * \frac{1}{\text{Iter}_{\text{max}}} + \theta_{2i}. \quad (10)$$

Here the θ_{1S} , θ_{1i} , θ_{2S} and θ_{2i} are constants, Iter_{max} is the maximum number of iterations. In this paper θ_{1S} and θ_{2S} are taken as 0.5, θ_{1i} and θ_{2i} are taken as 2.65.

A. Methodology of proposed APSO for SAR image analysis

The automatic object detection system in this paper proposed APSO method to maximize the between class variance. The frame work is developed based on several contributions presented in [26]-[32]. From the Fig. 2 initial velocity and position are allocated to each particle randomly. The fitness of all the particles is computed using Eq. (5) and particle positions and velocities are updated according to Eqs. (7) and (8). In each iteration particle identifies the better position and those locations are stored.

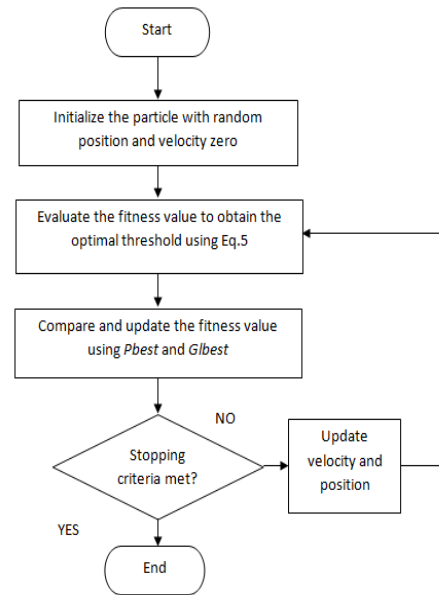


Fig. 2. Proposed APSO method operating flow chart.

The optimal threshold value can be calculated using proposed APSO algorithm described as below:

Step 1. Initialization: At initial the population size is arranged between the ranges of 0 to 255. The correct threshold value is identified by modifying Otsu method

to detect the objects views of the lakes in the SAR images.

Step 2. Evaluation of Objective Function: The object function is specified in Eq. (5). Every particle in the SAR image gives the optimal value based on this function. The obtained optimal threshold value maximizes the between class variance of the foreground and background pixels.

Step 3. Updating the swarm: In this step the updated

object values and positions are calculated using object function. The determined new value is assigned to $Pbest$. Like wise best of $Pbest$ is assigned to $GBest$. Based on this $Pbest$ and $GBest$ the position of the new particle is updated for every iteration.

Step 4. Stopping Criteria: This Iteration process continues up to the maximum number of iterations. $GBest$ is the position of particle optimum threshold value.

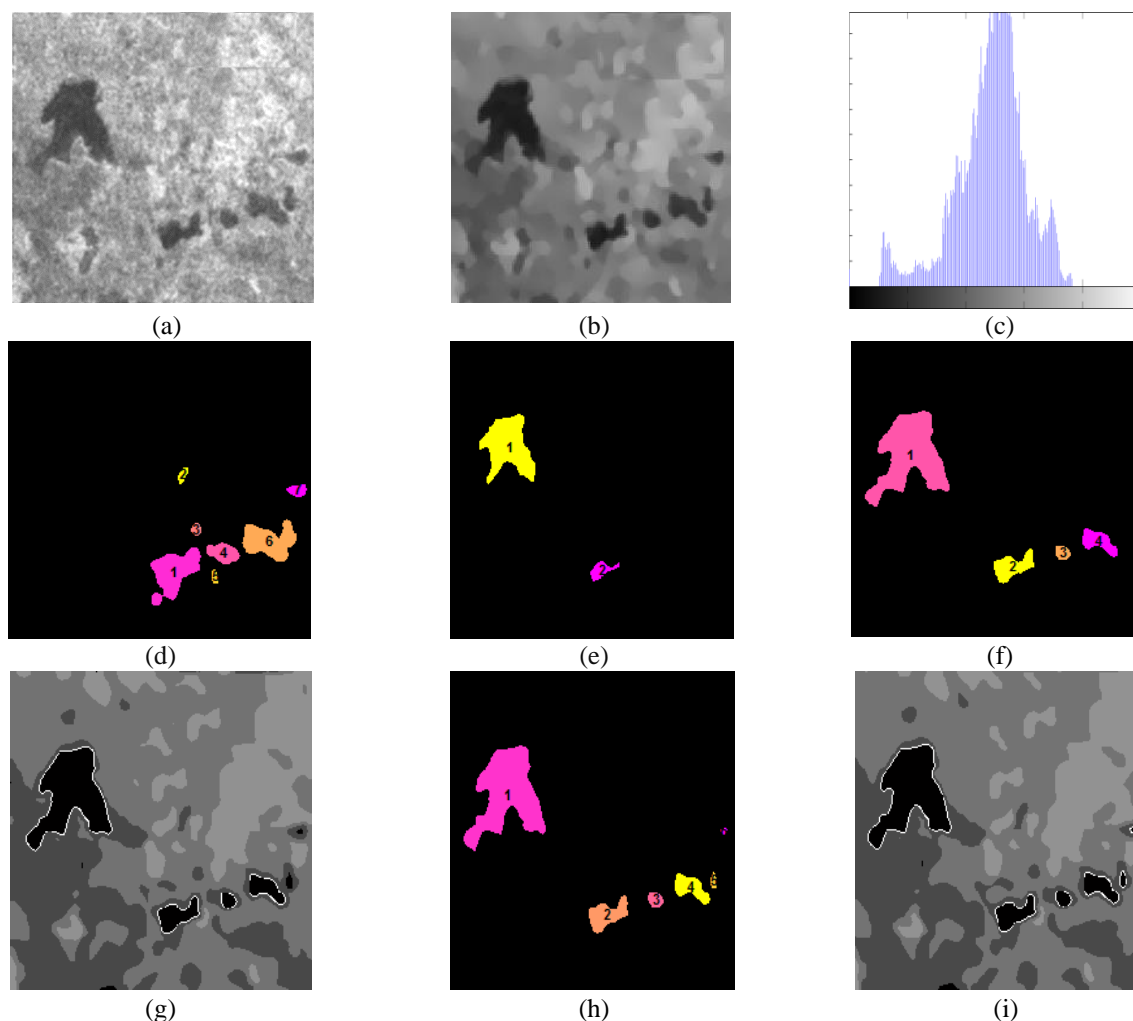


Fig. 3. Comparative results of proposed APSO + Modified Otsu with existing methods. (a) Original image, (b) SRAD filtered image, (c) Histogram of SAR image, (d) Segmented results by the Otsu method, (e) Segmented results by Modified Otsu, (f) Segmented results of PSO with Modified Otsu, (g) Segmented results of PSO with Modified Otsu overlaid on the original image, (h) Segmented results of proposed APSO with Modified Otsu, and (i) Segmented results of proposed APSO with Modified Otsu overlaid on the original image.

V. EXPERIMENTAL RESULTS

This work describes the automatic detection of the lakes in SAR image using proposed APSO method. The SAR image strips obtained from NASA/JPL during Titan-flyby. The experiments have been executed on the

HP with Intel Core 2 Duo CPU@2GHz with 4 GB RAM running on a windows 7 operating system. The proposed APSO method implemented in MATLAB 2012a software. The performance measures of PSO and proposed APSO methods are shown in Tables 1, 2, 3 and 4.

Table 1: Optimized parameter values for constant inertia weight

Parameter Description	Parameter Value
Population	50
Iteration	150
W_0	1.2
θ_1	0.8
θ_2	0.8

Table 2: Optimized parameter values for particle swarm optimization

Parameter Description	Parameter Value
Population	50
Iteration	150
W_{MIN}	0.1
W_{MAX}	1.5
θ_1	0.8
θ_2	0.8

Table 3: Optimized parameter values for proposed adaptive particle swarm optimization

Parameter Description	Parameter Value
Population	50
Iteration	150
W_0	1.2
θ_{1S}, θ_{2S}	0.5
θ_{1i}, θ_{2i}	2.65

Table 4: Feature information of the identified objects by proposed APSO with modified Otsu method

Method	Extent	Circularity	Tortuosity
APSO + Modified Otsu	0.485609	0.341809	0.250798
	0.494286	0.494776	0.352329
	0.733728	0.955424	0.351079
	0.525333	0.569329	0.389926
	0.692308	0.75906	0.411692
	0.760000	1.280154	0.390931
No. of Objects:6			

Here is the optimal threshold value is getting from the proposed APSO method. For analysis, SAR input image Fig. 3 (a) is taken. It is preprocessed by the SRAD filter for smooth image shown in Fig. 3 (b). Figure 3 (c) represents the corresponding histogram for input image. Figures 3 (d), (e) show the segmented results for Otsu and Modified Otsu. Figures 3 (f)-(i) show the segmented results for PSO and proposed APSO with modified Otsu, which extracts the lake objects from the SAR input image. From this, the size and shape of the objects are extracted to identify the proper objects. Extracts the boundary of the lake objects and overlaid on the input SAR image for analysis. This gives the better identification and accurate detection of the unclear objects.

The Object shape and features like Perimeter, Area, Eccentricity, Minor axis, Major axis, Circularity, Extent and Tortuosity are extracted from segmented image. From the Circularity, Extent and Tortuosity range, it is possible accurately identifying the object appearance. Figures 4, 5 and 6 compares the Object features information about the proposed APSO method with existing methods. From these figures the conventional Otsu method detects the 10 objects among them, 5 are matched with the real objects. The proposed modified Otsu detects the 2 objects are detected without any false objects, but it does not cover all the lakes in the image. PSO is intrigued to optimize the class variance for improving the performance of Modified Otsu. Modified Otsu with PSO method detects the 4 out of 6 objects that reduce the false detection rate compared to Conventional Otsu. Further, using proposed APSO with Modified Otsu produces the segmented results that detect the all the objects combatively verified with the lake areas identified by human experts. The feature extraction information due to various methods is given in Tables 5, 6 and 7; the comparison of various techniques is presented in Table 8.

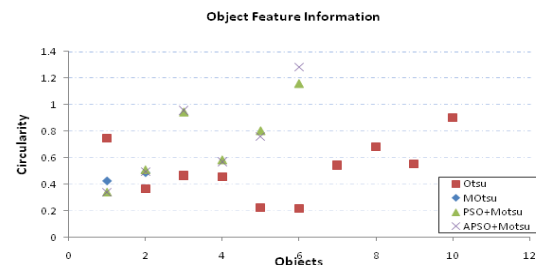


Fig. 4. Comparison of Circularity of identified objects.

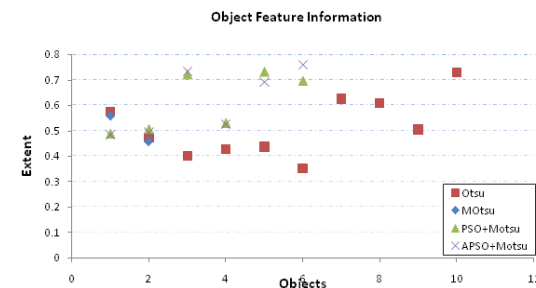


Fig. 5. Comparison of Extent of identifying objects.

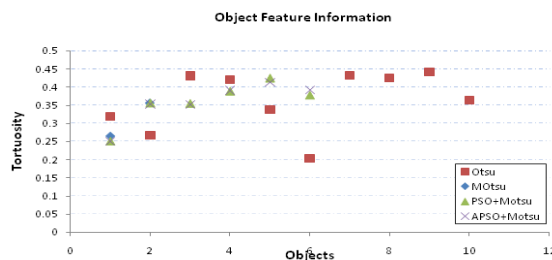


Fig. 6. Comparison of Tortuosity of identifying objects.

Table 5: Feature information of the identified objects by proposed PSO with modified Otsu method

Method	Extent	Circularity	Tortuosity
PSO + Modified Otsu	0.486607	0.339503	0.250904
	0.504762	0.507405	0.35651
	0.71978	0.942214	0.35533
	0.529032	0.582062	0.389345
	0.730769	0.80123	0.425641
	0.694444	1.155998	0.378359
No. of Objects: 6			

Table 6: Feature information of the identified objects by proposed modified Otsu method

Method	Extent	Circularity	Tortuosity
Modified Otsu	0.560333	0.425186	0.264153
	0.459276	0.486309	0.355806
No. of Objects: 2			

Table 7: Feature information of the identified objects by Otsu method

Method	Extent	Circularity	Tortuosity
PSO + Modified Otsu	0.573427	0.744097	0.318594
	0.470588	0.364074	0.265996
	0.400000	0.463283	0.431508
	0.425926	0.455406	0.420552
	0.435537	0.2229	0.337682
	0.350538	0.216019	0.202886
	0.624339	0.542438	0.433129
	0.607143	0.678756	0.425554
	0.503497	0.552815	0.441658
	0.727273	0.899488	0.363988
No. of Objects: 10			

Table 8: Comparison of proposed method with various methods based on experimental results

Methods		Number of Objects Identified from SAR Image		
		I-Identified, O-Objects, NO-Not Objects		
		Image 1	Image 2	Image 3
APSO + Modified Otsu	I	1	6	3
	O	1	6	3
	NO	-	-	-
PSO + Modified Otsu	I	4	6	6
	O	1	4	3
	NO	3	2	3
Modified Otsu	I	4	2	3
	O	1	2	2
	NO	3	-	1
Otsu	I	4	10	6
	O	1	5	2
	NO	3	5	4
Manual Expert		1	6	3

This method has been tested on 78 images, it necessitates the modification of the PSO for good performance. The proposed APSO with Modified Otsu offers maximize fitness function. This method detects all the objects. A visual assessment is made with the segment's results of the Conventional Otsu, Modified Otsu, PSO + Modified Otsu and APSO + Modified Otsu are presented on the Fig. 3. All the algorithms give the best results by preprocessing the image with SRAD filter. In this paper evaluate the threshold value of the proposed APSO method and the performance of the successive rate should be analyzed using Table 8. Among all these algorithms the only proposed APSO with Modified Otsu segmented object matches with the objects identified by human experts. Moreover, it is the more proficient automatic detection and precise algorithm for identifying the objects from the SAR image.

VI. CONCLUSION

In this paper automatic object detection system is proposed to detect the regions of SAR image. The proposed method applies the PSO technique to avoid the problem in the manual detection in SAR images. Due to the simplicity and effectiveness of PSO technique, it is used in many applications to optimize the complex problems. The proposed APSO method detects the optimized threshold. This method is implemented by the combination of Modified Otsu method which gives the effective segmentation results. Here are the results which show the better comparative results of the proposed method with all existed methods by making the calculation of effective fitness value. But these segmentation methods gave the better segmentation by preprocesses the original SAR image with SRAD filter instead of all other de-speckled filter techniques Lee, Frost, Adaptive Frost etc. This APSO out performs the measurement parameters in terms of accuracy.

REFERENCES

- [1] Y. Yu and S. T. Acton, "Speckle reducing anisotropic diffusion," *IEEE Transactions on Image Processing*, vol. 11, no. 11, Nov. 2002.
- [2] J. Zhu, J. Wen, and Y. Zhang, "A New Algorithm for SAR Image Despeckling using an Enhanced Lee Filter and Median Filter," *IEEE Conference Publications Image and Signal Processing*, vol. 1, pp. 224-228, 2013.
- [3] Y. Deng, Y. Wang, and Y. Shen, "An automatic diagnostic system of polycystic ovary syndrom based on objects growing," *Journal of Artificial Intelligence I Medicine*, Elsevier Science Publishers Ltd. Essex, UK, vol. 51, no. 3, pp. 199-209, Mar. 2011.
- [4] N. Otsu, "A threshold selection method from gray-

- level histograms," *IEEE Transactions on Systems, Man, Cybernet, SMC*, vol. 9, pp. 62-66, 1979.
- [5] A. S. Moghaddam, D. Yazdani, and J. Shahabi, "A novel hybrid segmentation method," *Progress in Artificial Intelligence*, vol. 3, no. 1, pp. 39-49, Aug. 2014.
- [6] T. Chan and L. Vese, "Active contours without edges," *IEEE Transactions Image Processing*, vol. 10, no. 2, pp. 266-277, 2001.
- [7] T. Pun, "A new method for grey-level picture thresholding using the entropy of the histogram," *Signal Processing*, vol. 2, pp. 223-237, 1980.
- [8] J. Kennedy and R. Eberhart, "Particle Swarm Optimization," in the *Proceedings of IEEE International Conference on Neural Networks*, Perth, Australia, vol. 4, pp. 1942-1948, 1995.
- [9] P. Yin, "Multilevel minimum cross entropy threshold selection based on particle swarm optimization," *Applied Mathematics and Computation*, vol. 184, pp. 503-513, 2007.
- [10] A. Akl, K. Tabbara, and C. Yaacoub, "An enhanced Kuan filter for suboptimal speckle reduction," *Advances in Computational Tools for Engineering Applications (ACTEA)*, pp. 91-95, 2012.
- [11] T. C. Aysal and K. E. Barner, "Rayleigh maximum like hood filtering for speckle reduction of ultrasound images," *IEEE Transactions on Medical Imaging*, vol. 26, no. 5, pp. 712-727, 2007.
- [12] W. Doyle, "Operation useful for similarity-invariant pattern recognition," *J. Assoc. Comput. Mach* 9, vol. 9, pp. 259-267, Apr. 1962.
- [13] Z. Qu and L. Zhang, "Research on Image Segmentation Based on the Improved Otsu Algorithm," 2010.
- [14] Z. Ningbo, W. Gang, Y. Gaobo, and D. Weiming, "A Fast 2D Otsu Thresholding Algorithm based on Improved Histogram," in *Pattern Recognition, 2009, CCPR 2009, Chinese Conference on*, pp. 1-5, 2009.
- [15] J. Liu, W. Li, and Y. Tian, "Automatic Thresholding of Gray-level Pictures using Two Dimension Otsu Method," *China 1991 International Conference on Circuits and Systems*, pp. 325-328, 1991.
- [16] P. Ghamisi, M. S. Couceiro, F. M. L. Martins, and J. Atli Benediktsson, "Multi level image segmentation based on fractional-order Darwiinian PSO," *IEEE Transaction on Geoscience and Remote Sensing*, vol. 52, no. 5, pp. 2382-2394, June 2013.
- [17] H. Cai, Z. Yang, X. Cao, W. Xia, and X. Xu, "A new iterative tri class thresholding technique in image segmentation," *IEEE Transactions on Image Processing*, vol. 23, no. 3, pp. 1038-1045, Mar. 2014.
- [18] J. Kennedy and R. Eberhart, *Swarm Intelligence*, San Francisco: Morgan Kaufmann Publishers, 2001.
- [19] M. Sezgin and B. Sankur, "Survey over image thresholding techniques and quantitative performance evaluation," *J. Electron. Imaging*, vol. 13, no. 1, pp. 146-165, 2004.
- [20] J. Marcello, F. Marques, and F. Eugenio, "Evaluation of thresholding techniques applied to oceanographic remote sensing imagery," *SPIE*, 5573, pp. 96-103, 2004.
- [21] E. Zahara, S. S. Fan, and D. Tsai, "Optimal multi-thresholding using a hybrid optimization approach," *Pattern Recognition Letters*, Elsevier, vol. 26, pp. 1082-1095, 2005.
- [22] Y. Zhiwei, C. Hongwei, L. Wei, and Z. Jinping, "Automatic Threshold Selection based on Particle Swarm Optimization Algorithm," in the *Proceedings International Conference on Intelligent Computation Technology and Automation*, pp. 36-39, 2008.
- [23] T. Hongmei, W. Cuixia, H. Liying, and W. Xia, "Image Segmentation Based on Improved PSO," the *Proceedings of the International Conference on Computer and Communication Technologies in Agriculture Engineering (CCTAE2010)*, pp. 191-194, 2010.
- [24] Y. Shi and R. Eberhart, "A Modified Particle Swarm Optimizer," in the *Proceedings of the IEEE International Conference on Evolutionary Computation*, Piscataway, NJ, pp. 69-73, 1998.
- [25] A. Ratnaveera, S. K. Halgamuge, and H. C. Watson, "Self-organizing hierarchical particle swarm optimizer with accelerating coefficients," *IEEE Transactions and Evolutionary Computations*, vol. 8, no. 3, pp. 240-255, 2004.
- [26] Y. J. Zhang, "A survey on evaluation methods for image segmentation," *Pattern Recognition*, Elsevier, vol. 29, no. 8, pp. 1335-1346, 1996.
- [27] H. Zhang, J. E. Fritts, and S. A. Goldman, "Image segmentation evaluation: A survey of unsupervised methods," *Computer Vision and Image Understanding*, vol. 110, no. 2, pp. 260-280, 2008.
- [28] J. Kennedy and R. Eberhart, "Particle Swarm Optimization," *Proceedings of IEEE International Conference on Neural Networks*, IEEE Press, Piscataway, NJ, pp. 1942-1948, 1995.
- [29] R. Eberhart and Y. Shi, "Comparing Inertia Weights and Constriction Factors in Particle Swarm Optimization," *Proceedings of 2000 IEEE Congress on Evolutionary Computation*, IEEE Press, Piscataway, NJ, pp. 84-88, 2000.
- [30] B. Al-Kazemi and C. K. Mohan, "Training Feed Forward Neural Networks using Multi-phase Particle Swarm Optimization," *Proceedings of the 9th International Conference on Neural Information Processing*, Singapore, pp. 2615-

- 2619, 2002.
- [31] Y. Shi and R. A. Krohling, "Co-evolutionary Particle Swarm Optimization to Solve Min-max Problems," *IEEE Congress on Evolutionary Computation*, Honolulu, Hawaii, USA, 2002.
- [32] R. Eberhart and J. Kennedy, "A New Optimizer Using Particle Swarm Theory," *Proc. 6th International Symposium on Micro Machine and Human Science*, IEEE Service Center, Piscataway, NJ, pp. 39-43, 1995.

A Study on the Distribution and Uniformity of Symmetric Extended TEM Cells

Chunjiang Song¹, Yuntao Jin², and Fei Dai^{2,*}

¹Department of Engineering Physics
Tsinghua University, Beijing, 100084, China

²School of Electronic and Information Engineering
Beihang University, Beijing, 100191, China
*daphige@buaa.edu.cn

Abstract — TEM Cells can generate computable standard fields, which are often used in electromagnetic measurement systems. Their electromagnetic field uncertainty has a great influence on the evaluation of system measurement results. In this paper, a method and index for rigorous evaluation of the uniformity of electromagnetic field distribution in the test area are presented. The relationship between different measurement accuracies and the size limits of the test object is analyzed by HFSS. According to this relationship, the limit condition of the sample size is established when the E field measurement accuracy is 1dB. Among them, the height requirements are consistent with the traditional experience requirements, and the width requirements are more stringent. On this basis, the electric field distribution law of the symmetric extended TEM chamber is studied and analyzed. It shows that the field uniformity of the symmetric extended TEM room is basically unchanged when the test space is multiplied.

Index Terms — Electric field, field uniformity, TEM Cells, uncertainty.

I. INTRODUCTION

TEM Cells consist of a rectangular outer conductor and a core between the top and bottom layers. As the name suggests, the standard TEM Cell is essentially a two-conductor transmission line that operates in TEM mode. In the case of additional excitation and matching loads, a computable standard field [1] can be constructed. In IEEE 1309-2013 [2], it is recommended to use TEM cells below 200 MHz as a common generation device for probe calibration systems.

To ensure the validity of the measurement results, the TEM Cells are used in the electromagnetic measurement system. The main problems are the accurate calculation of the standard field and the

uncertainty evaluation of the system measurement results. For the standard field calculation, it is mainly related to the measurement of the net power P_{net} , the characteristic impedance real part Z_0 and the TEM cell half height d of the TEM Cells [3]. The uncertainty assessment of the system measurement results is mainly determined by the uncertainty of the standard field generated by the TEM Cells. When Crawford [1] proposed the design of TEM Cells in 1974, it made a preliminary assessment of its calibration uncertainty and proposed a method to correct the field disturbance of the electric field [4]. Lu's [5] research suggests that field distortion is not easy to predict, so it is necessary to limit the size of the test object. However, the effect of position on the field in the original TEM Cells is not given.

Most of the current research focuses on the uncertainty of the standard field generated by standard TEM cells, but there are few studies on the uncertainty of TEM cells after expanding the test space. Wilson and Ma proposed asymmetric TEM cells [6]. K. Malathi studied the extended characteristic impedance of asymmetric TEM cells [7]. Virginie proposed a three-dimensional TEM cell [11]. Dai and Song et al. proposed TEM cells with dual and quadruple symmetric extensions [9,10]. Based on the standard TEM Cell field uniformity analysis, the field distribution and uniformity of symmetrically extended TEM cells are further studied in this paper.

II. FIELD UNIFORMITY ANALYSIS OF STANDARD TEM CELLS

According to IEEE STD 1309-2013 [2], the characteristic impedance of TEM Cells is calculated by the following formula:

$$Z_0 = \frac{94.2}{\frac{w}{b} + \frac{2}{\pi} \ln[1 + \coth(\frac{\pi g}{2b})]}, \quad (1)$$

where the b , g , w is given in the Fig. 1.

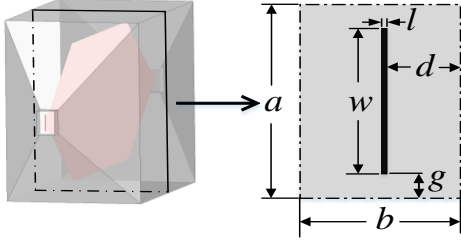


Fig. 1. Cross section of a basic TEM Cell.

In general, the characteristic impedance is designed to be 50 ohms to match the impedance of the measurement system. The field strength in the TEM Cells is calculated according to the formula (2) where P_{net} is the input net power of the TEM cells:

$$E = \frac{\sqrt{P_{net}Z_0}}{d} \quad (2)$$

For Model I proposed by Hill [11], $Z_0 = 51.7\Omega$ can be obtained from formula (1); substituting $P_{net} = 1W$, $d=1.5m$ into formula (2) can get $E=4.8V/m$. In fact, the electric field distribution in the TEM Cells is not completely uniform, and there will be obvious distortion on both sides of the core board. To this end, it is generally required that the width of EUT does not exceed $a/2$, and the height does not exceed $d/3$ (or $b/6$); for more accurate tests, the height does not even exceed $d/5$ [2]. This empirical requirement does not fully explain the degree of field uniformity. Therefore, in this paper, the mean (E_{mean}), standard deviation (E_{SD}), coefficient of variation (CV_E), dynamic range (DR_E), etc. of the E field in the test area are used to indicate the field uniformity.

The mean of the E field can be used to describe the level of the built-in E field of the TEM Cells for a given input net power. To compare the performance difference between different TEM cells, this paper uses the mean of the field strength, when the input field power is 1W, E_{mean}^{1W} as a parameter.

Both the standard deviation and the coefficient of variation can describe the dispersion of the electric field values in the test area. The smaller they are, the more concentrated the electric field value distribution is in the mean:

$$CV_E = \frac{E_{SD}}{E_{mean}} \quad (3)$$

Formula (3) shows that CV_E is the result of normalization of E_{SD} relative to E_{mean} , which is more general.

E_{mean}^{1W} and CV_E illustrate the statistical properties of the built-in E field of TEM Cells, and the dynamic range shows the maximum differences in the distribution of E field values:

$$DR_E = 20 \times \log\left(\frac{E_{max}}{E_{min}}\right) \quad (4)$$

Model I was simulated by HFSS in Driven Modal to study the field uniformity of the test area. Based on

the requirements of traditional experience, the original test area is divided into three areas according to the height. The height of these areas is about $d/3$, and the test area at each height is further divided into three according to the width. There are 9 test areas for $a/6$, $d/3$, and $a/2$, as shown in Fig. 2 and Table 1. These test areas are on the cross section of the middle section of the TEM Cells along the direction of the signal propagation, and the cross section is parallel to the XZ plane. On each test area, the height (Z axis) is divided into 15-line segments, and 16 test points are evenly arranged for each line segment, for a total of 240 test points. From the E field simulation results of 240 points, the mean (E_{mean}^{1W}), coefficient of variation (CV_E) and dynamic range (DR_E) of each test area are calculated, as shown in the Figs. 3-5.

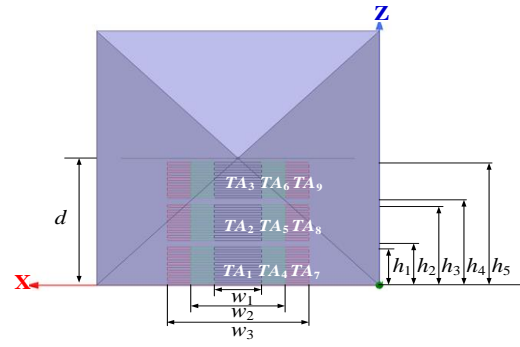


Fig. 2. Test areas divided in Model I.

Table 1: 9 test areas in the Model I

Test Area	Width (m)	Lower Limit (m)	Upper Limit (m)	Height (m)
No. 1	$w_1 = 0.5$	0.03	$h_1 = 0.45$	0.42
No. 2	$w_1 = 0.5$	$h_2 = 0.53$	$h_3 = 0.95$	0.42
No. 3	$w_1 = 0.5$	$h_4 = 1.03$	$h_5 = 1.45$	0.42
No. 4	$w_2 = 1$	0.03	$h_1 = 0.45$	0.42
No. 5	$w_2 = 1$	$h_2 = 0.53$	$h_3 = 0.95$	0.42
No. 6	$w_2 = 1$	$h_4 = 1.03$	$h_5 = 1.45$	0.42
No. 7	$w_3 = 1.5$	0.03	$h_1 = 0.45$	0.42
No. 8	$w_3 = 1.5$	$h_2 = 0.53$	$h_3 = 0.95$	0.42
No. 9	$w_3 = 1.5$	$h_4 = 1.03$	$h_5 = 1.45$	0.42

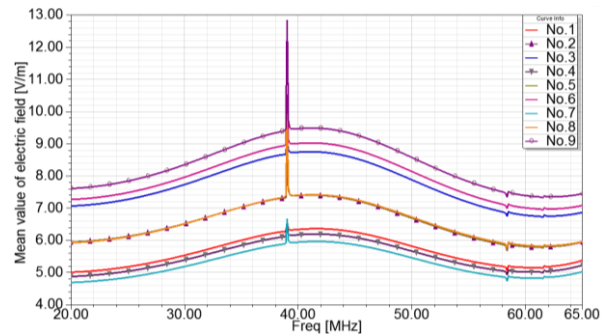


Fig. 3. Mean value of E field.

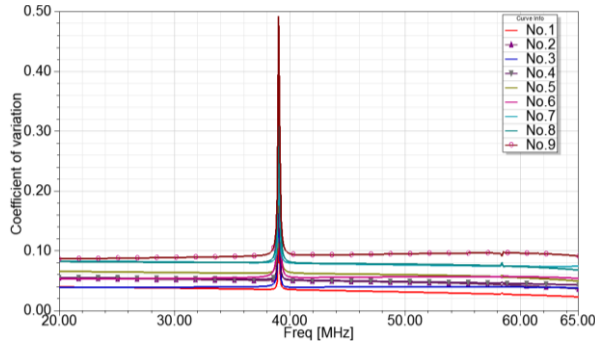


Fig. 4. Coefficient of variation of E field.

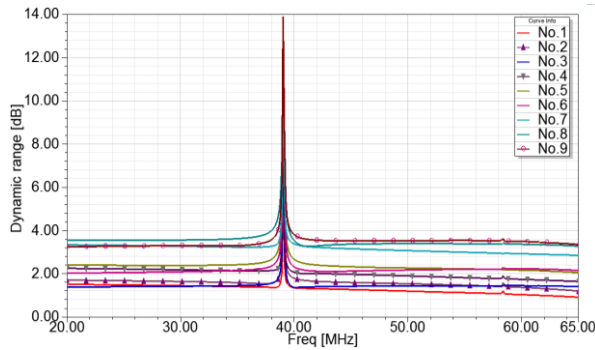


Fig. 5. Dynamic range of E field.

Figures 3-5 show three extreme points with frequencies of 39.01MHz, 58.36MHz, and 61.62MHz, which are consistent with the resonant frequencies calculated in the Eigen Mode of Table 1, corresponding to the TE011, TE012, and TE101 modes, respectively. In the TEM Cells of the Model I, since the propagation mode is the TEM mode, the frequency band lower than 39.01 MHz can be used. In the TEM mode, the average E field strength in the bottom region of the TEM cells is about 5 V/m, which is equivalent to the calculation result of the formula (2). What's more, analysis of Figs. 3-5 can lead to the following conclusions:

- 1) The magnitude of the field strength is related to the position of the test area. The closer the E field is to the bottom, the smaller the E field is. The closer it is to the septum which is no more than 2 times the bottom field strength, the bigger the E field is.
- 2) The change in the coefficient of variation indicates that the smaller the width of the test area, the more uniform the electric field distribution. Although the electric field distribution in the bottom test area is relatively more uniform, the effect of the position is not significant. The coefficient of variation for all regions is less than 0.1, indicating that the electric field distribution in TEM Cells is generally uniform.
- 3) The dynamic range presents a similar law to the coefficient of variation. When the test area height

is $d/3$, the maximum difference of the electric field value is less than 2dB when the width is only $a/6$, which indicates that for the precision test such as E field probe calibration, the conventional upper limit of $a/2$ is too loose.

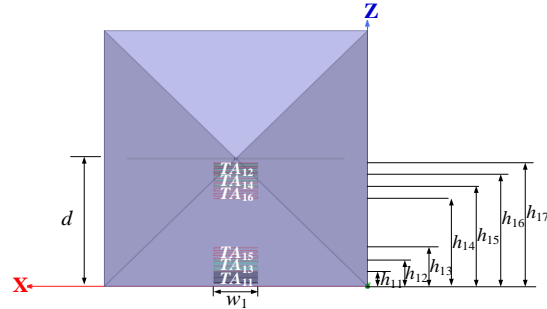


Fig. 6. Test areas divided in Model I.

Table 2: 9 test areas in the Model I

Test Area	Width (m)	Lower Limit (m)	Upper Limit (m)	Height (m)
No. 11	$w_1 = 0.5$	0.03	$h_{11} = 0.17$	0.14
No. 12	$w_1 = 0.5$	$h_{16} = 1.31$	$h_{17} = 1.45$	0.14
No. 13	$w_1 = 0.5$	0.03	$h_{12} = 0.31$	0.28
No. 14	$w_1 = 0.5$	$h_{15} = 1.17$	$h_{17} = 1.45$	0.28
No. 15	$w_1 = 0.5$	0.03	$h_{13} = 0.45$	0.42
No. 16	$w_1 = 0.5$	$h_{14} = 1.03$	$h_{17} = 1.45$	0.42

Further, the influence of the height and position of the test area on the uniformity of the field was analyzed. According to the above conclusion (1), two regions with a height of $d/3$ and a width of $a/6$ close to the core plate and the bottom are selected, and the two regions are divided into three test regions by the height of the region. The height of each test area is $d/9$, $2d/9$, $d/3$, as shown in Fig. 6 and Table 2. On each test area, the height (Z axis) is divided into 15-line segments, and 16 test points are evenly arranged for each line segment, for a total of 240 test points. From the E field simulation results of 240 points, the mean (E_{mean}^{1W}), coefficient of variation (CV_E) and dynamic range (DR_E) of each test area are calculated, as shown in Figs. 7-9.

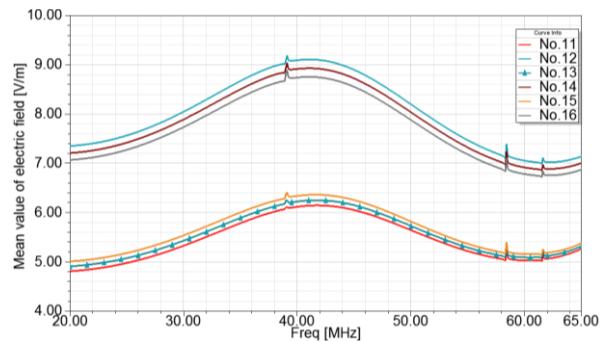


Fig. 7. Mean value of E field.

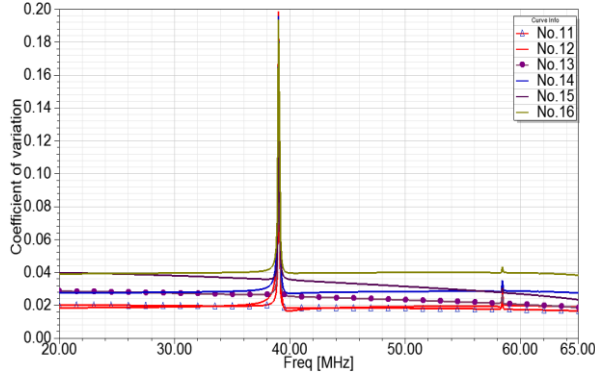


Fig. 8. Coefficient of variation of E field.

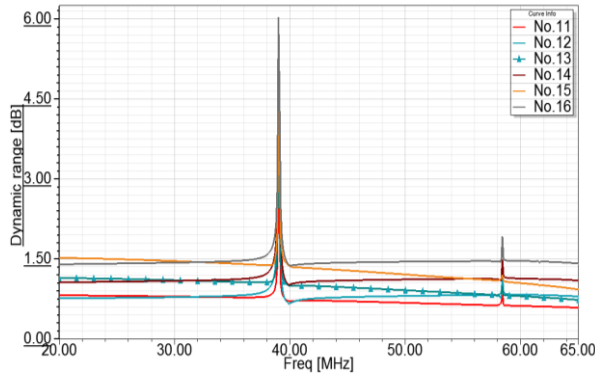


Fig. 9. Dynamic range of E field.

Figure 7 and Fig. 3 show the same law: the magnitude of the field strength is related to the position of the test area. The closer to the bottom, the E field is smaller. The closer to the septum which is no more than the bottom field strength, the E field is bigger. Figure 8 shows that the smaller the height of the test area, the smaller the coefficient of variation, and the coefficient of variation is not significantly affected by the position. Although the height of the test area has an influence on the coefficient of variation, the coefficient of variation in the six cases of Fig. 8 are all less than 0.05. Further, in combination with Fig. 4, it can be found that the coefficient of variation is approximated by the law of the width and height of the test area. The dynamic range of Fig. 9 shows a similarity to the coefficient of variation. When the height of the test area does not exceed $d/3$, the maximum difference of the E field value is 1.5 dB. When the height of the test area does not exceed $2d/9$, the maximum difference of the E field value is 1 dB.

From this we can conclude that when the amplitude measurement accuracy within the TEM Cells is required to be better than 1 dB, the width of the test area cannot exceed $a/6$ and the height cannot exceed $d/5$. This result is stricter than the provisions of the existing standards.

III. ELECTRIC FIELD DISTRIBUTION LAW IN DUAL CELLS

In Fig. 10, the bottom walls/plates of two identical TEM Cells are bonded together first and removed then. When the cells of the symmetric TEM cells are differentially excited and the same power P_{net} is input, the voltage difference between the internal spacers becomes twice that of the ordinary TEM cells, but the distance between the spacers becomes $2d$, so the internal field strength can still be calculated by formula (2).

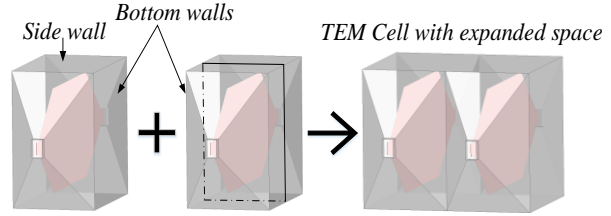


Fig. 10. A symmetric Extended TEM Cells.

Taking symmetric binary TEM cells as an example, let the input signal of one of the ports be:

$$V_1 = Vj^\varphi. \tag{5}$$

Then the ideal signal for the other port (differential port) input should be:

$$V_2 = Vj(\varphi+\pi). \tag{6}$$

If the phase of V_2 is not ideal, it can be expressed as:

$$V_2 = Vj(\varphi+\theta+\pi). \tag{7}$$

If the magnitude of V_2 is not ideal, it can be expressed as:

$$V_2 = Vj(\varphi+\theta+\pi). \tag{8}$$

The paper using HFSS analyzes the effect of the phase θ within $\pm 5^\circ$ and the amplitude error does not exceed $\pm 10\%$ on the electric field in the TEM Cells. The simulation model is shown in Fig. 11, where $w_1 = 0.5m$, $h_{21} = 0.28m$ and test areas TA_{21} and TA_{22} are TA_{13} and TA_{14} doubled in height, respectively.

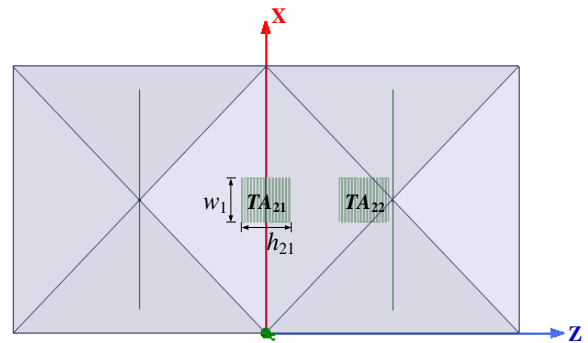


Fig. 11. Symmetric extended TEM Cells.

The simulation frequency is set at 25MHz, and the internal electric field of the TEM Cells is the TEM mode. The reference port in the differential input port has an input power of 1W and a phase of 0°. According to the range of amplitude and phase accuracy of the general signal source, the input power range of the other input port is 0.9~1.1W, and the phase is 175~185°. The simulation results are shown in Figs. 12-17.

Figures 12-17 show that after the TEM cells are symmetrically expanded into dual chambers, the bottom can be multiplied by the test area, and the ability to generate electric fields and field uniformity is consistent with a single TEM Cell. When the phase error of the input differential signal does not exceed $\pm 5^\circ$ and the amplitude error does not exceed $\pm 10\%$, the disturbance to the electric field can be neglected.

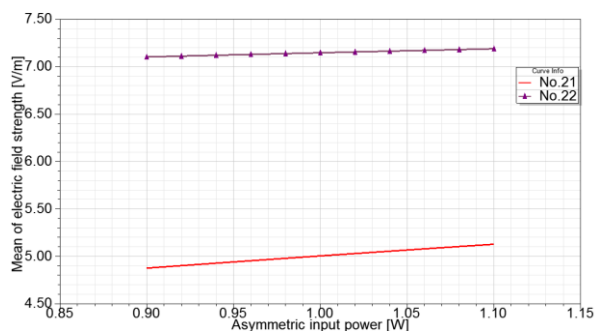


Fig. 12. E field strength vs. Asymmetric input power.

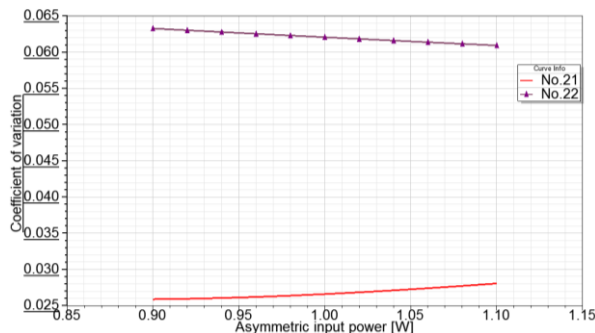


Fig. 13. Coefficient of variation vs. Asymmetric input power.

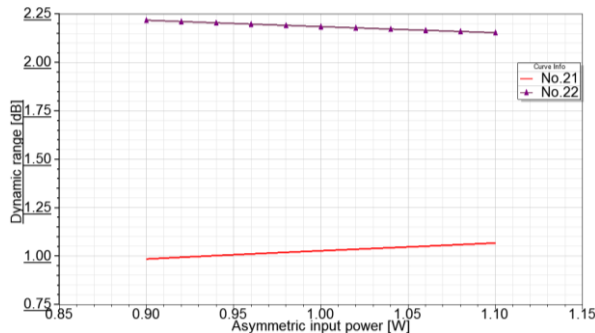


Fig. 14. Dynamic range vs. Asymmetric input power.

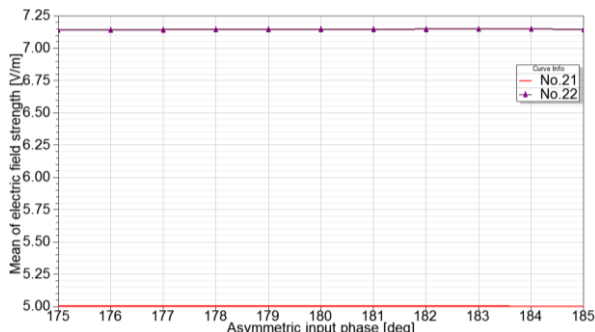


Fig. 15. E field strength vs. Asymmetric input phase.

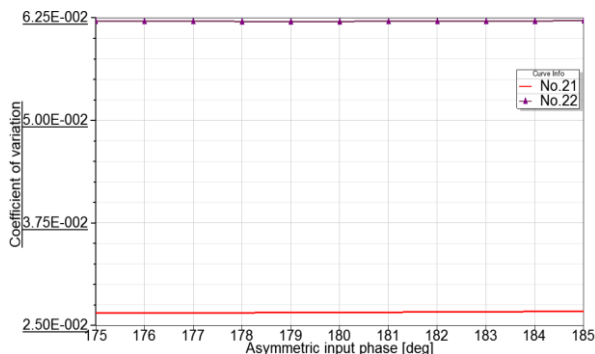


Fig. 16. Coefficient of variation vs. Asymmetric input phase.

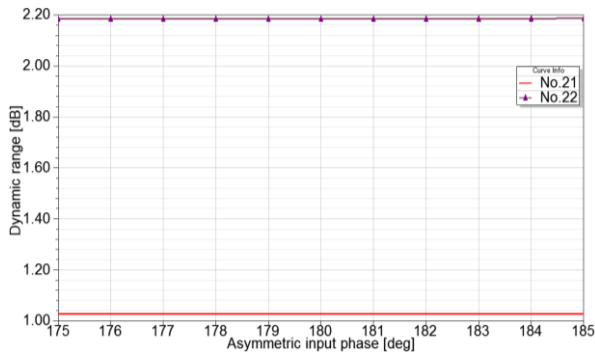


Fig. 17. Dynamic range vs. Asymmetric input phase.

IV. CONCLUSION

Based on the field-average value, this paper further proposes the method of describing the field uniformity in standard TEM cells by parameters such as standard deviation (E_{SD}), coefficient of variation (CV_E), dynamic range (DR_E) etc. Based on these indicators, the relationship between different measurement accuracy requirements and the size of the test object was determined, and a method for rigorously assessing the uniformity of electromagnetic field distribution in the test area was given. In the traditional experience requirements, when the electric field measurement accuracy requirement is 1dB, the width of the test

object cannot exceed $a/6$, and the height cannot exceed $d/5$.

In this paper, the electric field distribution of symmetrically extended TEM cells is further studied. Studies have shown that after the TEM cells are multiplied into double chambers with test areas, their ability to generate electric fields and field uniformity are consistent with standard TEM cells. Based on the accuracy range of the existing signal source, it is found that when the input differential signal phase error does not exceed $\pm 5^\circ$ and the amplitude error does not exceed $\pm 10\%$, the influence of the input signal error on the electric field generated in the TEM cells can be ignored.

Based on the research content of this paper, the law of electric field distribution and uniformity after loading the test object in symmetric extended TEM cells will be studied, and the factors affecting the uncertainty of symmetric extended TEM cells will be further analyzed.

ACKNOWLEDGMENT

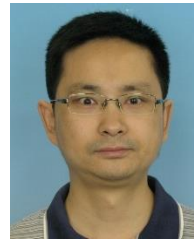
This work is supported in part by the National Natural Science Foundation of China. (Grant No. 61571027, 61427803), and supported by the 2011 Collaborative Innovation Center.

REFERENCES

- [1] M. L. Crawford, "Generation of standard EM fields using TEM transmission cells," *IEEE Transactions on Electromagnetic Compatibility*, vol. EMC-16, no. 3, pp. 189-195, Nov. 1974.
- [2] IEEE. STD 1309-2013, IEEE Standard for Calibration of Electromagnetic Field Sensors and Probes, Excluding Antennas, From 9 kHz to 40 GHz, 2013.
- [3] M. T. Ma, M. Kanda, M. L. Crawford, and E. B. Larsen, "A review of electromagnetic compatibility/interference measurement methodologies," *Proceedings of the IEEE*, vol. 73, no. 3, pp. 388-411, Mar. 1985.
- [4] M. L. Crawford and J. L. Workman, "Using a TEM Cell for EMC Measurement of Electronic Equipment," *U. S. National Bureau of Standards Technical Note 1013*, Apr. 1979.
- [5] X. Lu, "Characteristic impedance variation of the TEM cell caused by the introduction of the equipment under test," *IEICE/IEEE International Symposium on Electromagnetic Compatibility*, Tokyo, Japan, pp. 596-599, May 1999.
- [6] P. Wilson and M. Ma, "Simple approximate expressions for higher order mode cutoff and resonant frequencies in TEM cells," *IEEE Transactions on Electromagnetic Compatibility*, vol. 28, no. 3, pp. 125-130, Aug. 1986
- [7] K. Malathi and D. Annapurna, "Numerical analysis

of impedance of asymmetric TEM cell filled with inhomogeneous, isotropic dielectric," *Applied Computational Electromagnetics Society Journal*, vol. 19, pp. 39-45, 2004.

- [8] D. Virginie, "Optimization of three-dimensional TEM cell for electromagnetic compatibility testing," *20th Annual Review of Progress in Applied Computational Electromagnetics*, 2004.
- [9] F. Dai, M. Wang, and D. L. Su, "A design of new twin TEM cells," *IEEE 2005 International Symposium on Microwave, Antenna, Propagation and EMC Technologies for Wireless Communications Proceedings*, vol. 1, pp. 10-13, 2005.
- [10] C. J. Song and X. Y. Feng, "A new design and implementation of expanding testing space of a transverse electromagnetic cell," *The 9th International Conference on Microwave and Millimeter Wave Technology*, vol. 2, pp. 967-969, 2016.
- [11] D. A. Hill, "Bandwidth limitation of TEM cells due to resonances," *Journal of Microwave Power*, vol. 18, no. 2, pp. 181-195, 1983.



technology.

Chunjiang Song joined the Department of Engineering Physics in Tsinghua University, Beijing, China, in 2012 and he is currently working toward the Ph.D. degree. His research interests include the microwave technology, electronic measurement technology, and EMC



include the microwave technology and EMC technology.

Yuntao Jin receive the B.Eng. degree in Electronic Engineering from Soochow University, Jiangsu, China, in 2017, and he is currently working towards the M.S. degree in the School of Electronic and Information Engineering at Beihang University. His research interests



include the EMC technology, microwave technology, and antennas technology.

Fei Dai receive the Ph.D. degree in Circuits and Systems from Beihang University, Beijing, China, in 2007. He joined the Electromagnetic Compatibility Laboratory at Beihang University, Beijing, in 2007, where he is currently an Associate Professor. His research interests

Air Plasma Key Parameters for Electromagnetic Wave Propagation at and Out of Thermal Equilibrium: Applications to Electromagnetic Compatibility

P. Andre¹, G. Faure¹, A. Mahfouf¹, and S. Lall  ch  re²

¹LPC, UMR CNRS 6533

Universit   Clermont Auvergne, F-63000 CLERMONT-FERRAND, France
{pascal.andre}/{geraldine.faure}@uca.fr, mahfoufphysique@gmail.com

²Institut Pascal, UMR CNRS 6602

Universit   Clermont Auvergne, CNRS, BP 10448, F-63000 Clermont-Ferrand, France
sebastien.lallechere@uca.fr

Abstract — This article addresses the importance of accurate characterization of plasma parameters for electromagnetic compatibility (EMC) purposes. Most of EMC issues involving plasma materials are obviously multi-physics problems (linking chemical, mechanical, thermal and electromagnetic wondering) with deep interactions. One of the main objectives of this paper is to establish the theoretical effect of thermal non-equilibrium of the plasma on electromagnetic wave propagation. This will be characterized throughout plasma key parameters (including complex permittivity). Numerical simulations based upon Finite Integral Technique (FIT) will demonstrate the EMC interest of this methodology for shielding purposes and general air plasma.

Index Terms — Dielectric parameters, electromagnetic compatibility, electromagnetic propagation, plasmas, plasma modelling, thermal equilibrium.

I. INTRODUCTION

The interaction of an electromagnetic wave with an air plasma can be found in many applications as the Inductively Coupled Plasmas (ICPs) used for spectrochemical analyses [1], in plasmas analyses (the electromagnetic wave can be used to measure the electronic concentration) [2], in the dielectric barrier discharge that have promised applications as the regeneration of Diesel particle or the Gas Insulated System (GIS) [3, 4], in telecommunication applications [5] for instance.

Intentional or non-intentional plasma generations imply highly multi-physics studies involving chemistry, thermic, physics and of course electromagnetics to properly characterize electromagnetic (EM) fields. Previous studies [6-7] have demonstrated that a better understanding is needed to avoid microwave breakdowns and so improve shielding effectiveness (SE) of enclosures

embedded with slots and equipment under test. Some current electromagnetic compatibility (EMC) issues require an accurate assessment of materials EM properties in various configurations: for instance damaging of aeronautical systems (wires, antennas) due to lightning, spacecraft re-entry (radio frequency, RF, plasma generation).

The electromagnetic wave can produce useful plasma as in ICPs, can go through existing plasma as in plasma analyses or in telecommunication applications, or can produce an electrical breakdown.

Due to their higher mobility the electrons can reach a temperature (T_e) higher than the one of the other chemical species (T_h). The temperatures have been measured in several applications as discharges with liquid non-metallic electrodes [8], have been evaluated from the applied electrical field [9], or have been taken into account in modelling [10], circuit breakers, arc tracking, RADAR applications.

Modelling of electromagnetic waves in interaction with a material requires available physical properties of the material as dielectric permittivity [11]. The dielectric permittivity depends greatly on thermodynamic state and in the case of plasma on temperatures (T_e , T_h). It is also to be noticed that the dual interaction electromagnetic (EM) field/dielectric permittivity and dielectric permittivity/EM field has been recently explored in [5] regarding electrostatic fields and low permittivity barriers. The latter parametric study highlighted the importance of dielectric slab properties (e.g., permittivity, width, EM field's magnitude). It provided optimized characteristics (e.g., barrier width) with regards to the value needed for breakdown voltage.

In a previous work [12], we have shown that thermal non-equilibrium plays a major influence on argon plasma properties as London and Kelvin lengths. Consequently magnetic field is absorbed by the material in a direct way depending on the thermal state of the plasma.

The effect of thermal disequilibrium on the plasma properties (London and Kelvin lengths, dielectric permittivity) depends on chemical composition. To determine the concentrations of the chemical species concentration versus heavy species temperatures, we use the Gibbs free energy method [13]. We need to know for each chemical species the chemical potential as describe in [14]. We assume a dry air initial composition that is to say 80% of nitrogen N_2 and 20% of oxygen O_2 in molar percentage. We take 9 monatomic chemical species (N , N^+ , N^{++} , N^{+++} , O , O^+ , O^{++} , O^{+++}), 9 diatomic chemical species (N_2 , N_2^- , N_2^+ , NO , NO^- , NO^+ , O_2 , O_2^- , O_2^+) and 11 polyatomic species (N_2O , N_2O_3 , N_2O_4 , N_2O_5 , N_2O^+ , N_3 , NO_2 , NO_2^- , NO_3 , O_3 , NO_3^-) and electrons into account.

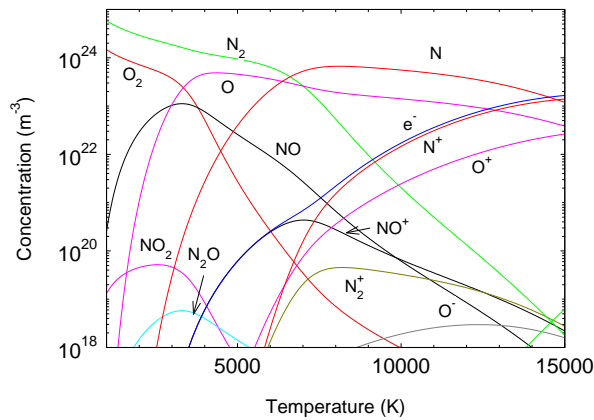


Fig. 1. Air composition at atmospheric pressure at thermal equilibrium.

In Figs. 1 and 2, we show the concentration evolution of the considered chemical species versus heavy species temperature (T_h) at thermal equilibrium and out of thermal equilibrium ($\theta = T_e/T_h$) for air plasma at atmospheric pressure. These figures clearly depict the high differences existing between concentrations of heavy species and electrons at and out of thermal equilibrium for air plasma at atmospheric pressure. In the latter figures, we can observe that ionisation appears at lower heavy species temperature when the thermal non equilibrium ratio θ increases for a given heavy species temperature T_h . So the electrons appear at lower temperature and have certainly an influence on physical parameters. Consequently, one of the main purposes of the paper is to study the influence of the thermal disequilibrium on the key physical parameters needed to EM simulation.

This article is organized as follows: in Section II we describe the theoretical methodology and the key parameters (plasma frequency, electron collision frequency, permittivity) for EM simulations are evaluated in an air plasma at atmospheric pressure at thermal equilibrium and out of thermal equilibrium. In Section

III we study the EM field propagation through the plasma, and an EMC illustrative example is proposed. The contribution ends with Section IV constituting a conclusion with some prospects.

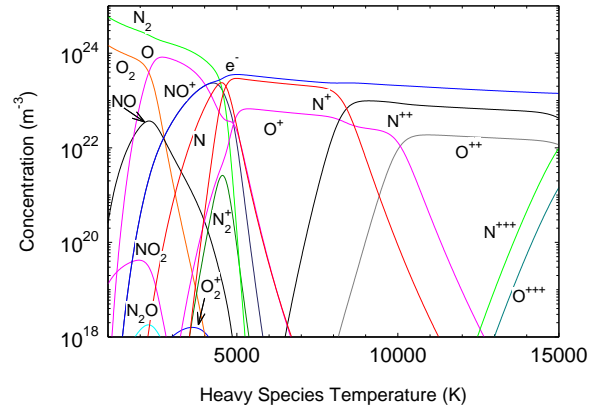


Fig. 2. Air composition at atmospheric pressure out of thermal equilibrium $\theta = T_e/T_h = 3$.

II. PLASMA KEY PARAMETERS AT AND OUT OF THERMAL EQUILIBRIUM

A. Theoretical model

By considering one electron inside a given electromagnetic environment (depicted by electric field E), one can obtain from the Newton's second law:

$$m_e \frac{dv}{dt} = -eE - k m_e v, \quad (1)$$

where $-k m_e v$ is a restoring force, v is the velocity of electron, and m_e and e are respectively mass and elementary charge of electron. Assuming the electric field as $\underline{E} = E_0 e^{i\omega t}$ and neglecting dipole creation inside plasma resolving (1), the celerity of electrons is obtained:

$$v = \frac{eE_0}{k + i\omega m_e} e^{i\omega t}. \quad (2)$$

Introducing the drift velocity one can obtain when $\omega = 0$ the parameter equal to the collision frequency ν_{ep} of electrons with the other particles inside the plasma. So the real current density can be written as:

$$\vec{J}_e = -\frac{n_e e}{m_e} \left(\frac{-e\vec{E}_0}{\nu_{ep} + i\omega} \right) e^{i\omega t}. \quad (3)$$

Introducing effective current inside Ampere's law we obtain:

$$\vec{\nabla} \times \vec{H} = \varepsilon_0 \frac{\partial \vec{E}}{\partial t} + \vec{J}_e = \varepsilon \frac{\partial \vec{E}}{\partial t}. \quad (4)$$

Then the real permittivity is written as:

$$\varepsilon = \varepsilon_0 \left(1 - \frac{\omega_p^2}{\omega(\omega - i\nu_{ep})} \right). \quad (5)$$

This permittivity is available for isotropic and non-magnetized plasma. We can feature key parameters: plasma pulsation $\omega_p = 2\pi f_p$ and collision frequency ν_{ep} of electrons, and the thermal velocity of electrons. This last parameter will be given in the following, jointly

with plasma characteristic parameters (i.e., f_p and ν_{ep}) taking into account in an original way the physical properties of plasma material.

B. Plasma characteristics and equivalent complex permittivity

Figure 3 shows frequency collisions of electrons and plasma frequency extracted from air composition and thermal assumptions (see Figs. 1-2). From equation (5), we can deduce that the formulation depends greatly on plasma state and wave frequency.

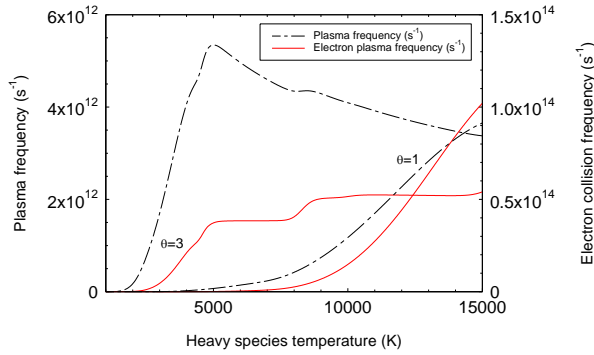


Fig. 3. Plasma frequency and electrons collisions frequency in air plasma at atmospheric pressure.

As a matter of fact, as we can see in Fig. 3, the electron plasma frequency is restricted for weaker temperatures. As a first approximation, plasma can be considered as a dielectric material. In Figs. 4-5, we have plotted the real and imaginary part of the relative permittivity for the air plasma at and out of thermal equilibrium. It is to be noted (data not shown here) that, for the lower temperature the real relative permittivity is close to 1 and the imaginary part is close to zero. Figures 4 and 5 show real components of dielectric constant are lower than unit ($T_h = 10,000$ K).

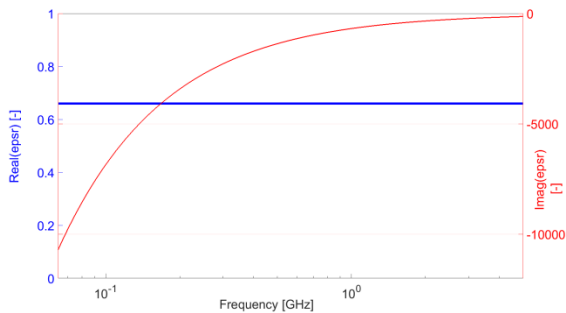


Fig. 4. Complex permittivity of the air plasma at thermal equilibrium ($\theta = 1$): real (blue) and imaginary (red) parts at $T_h = 10,000$ K from 64 MHz to 5 GHz.

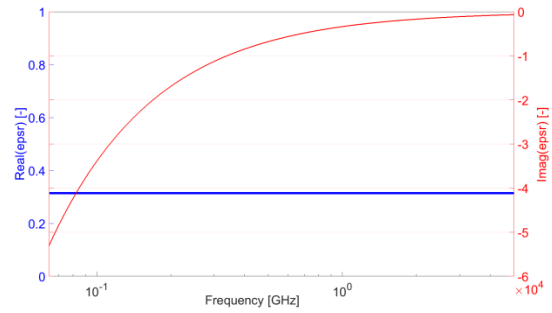


Fig. 5. Complex permittivity of the air plasma out of thermal equilibrium ($\theta = 3$): real (blue) and imaginary (red) parts at $T_h = 10,000$ K from 64 MHz to 5 GHz.

III. NUMERICAL RESULTS: PLASMA CHARACTERIZATION FOR SHIELDING EFFECTIVENESS (SE) APPLICATIONS

Some EM simulations were achieved using CST© MWS to assess EM field penetration inside air plasma at and out of thermal equilibrium. Time solver and dispersive model based upon data from Fig. 3 were used to quantify plasma shielding strength (i.e., E-field magnitude decreasing while penetrating plasma material) up to 5 GHz. For the sake of exhaustiveness, the next sections will detail numerical simulations.

A. Test case #1: Assessment of canonical shielding effectiveness (SE)

The first test case is inspired from Zheng et al. works [5]. Indeed, we would like to characterize the influence of plasma physical key parameters (plasma frequency, electron collision frequency, permittivity) on electromagnetic wave (EMW) propagation in to a slab. The physical key parameters depends grandly on the chemical concentrations has can be seen by comparing the Fig. 3 with Figs. 1 and 2. The crucial part of the work relies on the characterization of material throughout models and plasma key parameters (i.e., plasma frequency f_p , and collision frequency ν_{ep}) as depicted in Fig. 3. Those characteristics are highly dependent to the thermal equilibrium through the chemical composition.

The aims of this section are to demonstrate the difference that may be expected from taking into account (or not) potential thermal non-equilibrium jointly with the relevance of using computational electromagnetics tool (e.g., CST© with time domain solver). First of all, we put the focus on a canonical case, and in order to prepare numerical experiments in Section III.2 (test case #2), we propose to model two kinds of plasmas (data given in Fig. 3) for $T_h = 10,000$ K and $T_h = 15,000$ K with CST© MWS at thermal and non-thermal equilibrium.

Figure 6 depicts the numerical setup proposed for

straightforward characterization of the EM attenuation of waves throughout plasma illuminated by a normal-incidence plane wave. The plasma slab is a $2 \times 2 \times 1 \text{ cm}^3$ volume (Fig. 6). The time simulation (CST© MWS, time solver) is maintained up to ensure at least that more than 40 dB of the maximum energy has vanished from the computational domain. The plasma dielectric dispersion relies on purely dispersive modelling according to data in Figs. 4-5.

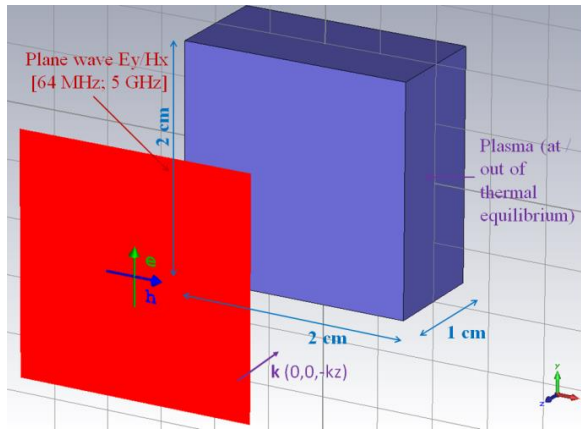


Fig. 6. Numerical setup for plane wave impinging on plasma slab ($2 \times 2 \times 1 \text{ cm}^3$, infinitely extended in x- and y-directions) using CST© MWS time solver and plasma material modelling (dispersive one).

A huge number of potential EM applications of plasma layers exist in literature as expressed in the introduction. Canonical characterization of plasma attenuation at atmospheric pressure is carried out, for example, in [15] whereas spacecraft flight re-entry is studied in [5]. In each of the two previous cases, attenuation is defined in a different manner. We will next consider the shielding effectiveness (SE) of the plasma (Fig. 9) as follows:

$$SE = \frac{\text{incident EMW}}{\text{transmitted EMW}}, \quad (6)$$

$$SE_{dB} = -20 \log \frac{E_{in}}{E_{out}}, \quad (7)$$

where E_{in} is the electric field located behind the infinite plasma slab (transmitted electromagnetic wave, EMW), and E_{out} is the incident EMW.

In the following and based upon relations (6-7), the transmitted electric field (E_{in}) is computed from CST© time domain solver and dispersive medium given by original theoretical models from Section II. The numerical results are compared to the analytical approach from [5] where the transmission coefficient t ($t = E_{in}/E_{out}$ in relation (7)) is obtained as follows:

$$t = \frac{2\sqrt{\varepsilon_r} e^{ik_0 d}}{2\sqrt{\varepsilon_r} \cosh(ik_p d) + (\varepsilon_r + 1) \sinh(ik_p d)}, \quad (8)$$

where ε_r is the complex permittivity of plasma, k_0 is the wave number in bulk medium (air), k_p is the wave

number in plasma (here with different characteristics in terms of temperature, thermal equilibrium...), and d is the width of considered plasma slab.

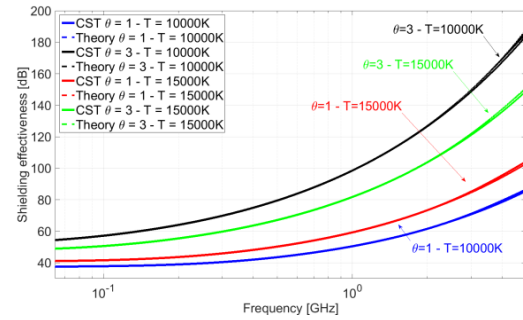


Fig. 7. Shielding effectiveness (attenuation in dB from 64 MHz to 5 GHz) at thermal equilibrium $\theta=1$ (blue, $T_h = 10,000 \text{ K}$; red, $T_h = 15,000 \text{ K}$) and out of thermal equilibrium $\theta=3$ (black, $T_h = 10,000 \text{ K}$; green $T_h = 15,000 \text{ K}$) relying on analytical formulation (dotted lines: reference [5]; dielectric permittivity from Figs. 4 and 5) and CST© (plain lines).

Figure 7 illustrates the impact of non-thermal equilibrium of air plasma at atmospheric pressure and at $T_h = 10,000 \text{ K} / T_h = 15,000 \text{ K}$ on material SE in function of frequency; similarly to Figs. 4-5, the dielectric properties of plasma are obtained at $T_h = 15,000 \text{ K}$ (data not shown here) with original works based upon assessment of plasma characteristics from air plasma composition (Figs. 1-2). The obtained results are in accordance with the results of other authors [5, 15]. Indeed, assuming similar characteristics of plasma (e.g., pressure, heavy species distribution, width of plasma slab), tens dB of attenuation are expected in [5, 15]. We remark that electron collision frequency play major roles, their increase leading to a proportional decrease of transmitted electric fields. Consequently, the physical parameters need for EM modelling depend on plasma composition (Figs. 1 and 2.) The maximum gap existing between SE at and out of thermal equilibrium is higher for $T_h = 10,000 \text{ K}$ than for $T_h = 15,000 \text{ K}$. Indeed, the gap is comprised between 3 dB and 45 dB considering heavy species temperature $T_h = 15,000 \text{ K}$, whereas SE is between 5 dB and 100 dB higher out of thermal equilibrium than at thermal equilibrium at temperature $T_h = 10,000 \text{ K}$. Finally, it is noted that the SE differences between $\theta=3$ and $\theta=1$ increases with frequency for each plasma temperature. By comparing our results with analytical formulation (8), Fig. 7 validates the use of fully dispersive plasma model obtained from the theoretical model proposed in this work (Section II). The next section will illustrate the importance of a careful definition of plasma characteristics (via complex permittivity and plasma characteristic frequencies) in

EMC framework.

B. Test case #2: Cabinet shielding at and out of thermal equilibrium

Relying on previous results for canonical case (test case #1), we illustrate the influence of thermal or non-thermal equilibrium assumption throughout an EMC shielding example. The numerical configuration is illustrated in Fig. 8: a perfectly conducting (PEC) enclosure ($6 \times 6 \times 3.96 \text{ cm}^3$) is considered jointly with a square aperture (length=4 cm) and 4 mm-walls (and 4mm-width of plasma). Figure 8 shows the direction of the impinging plane wave (incident electric field $E_y = 260 \text{ kV/m}$). Plasma characteristics are based upon results given in Figs. 4-5 ($T_h = 10,000 \text{ K}$). Unlike the work of [16], we have to precise that the plasma is produced independently of the impinging plane. Furthermore, here we do not want to study the breaking electrical field produced by an impinging plane wave since the presence of plasma is assumed. We will discuss the non-linear nature of plasma characteristics latter in this section.

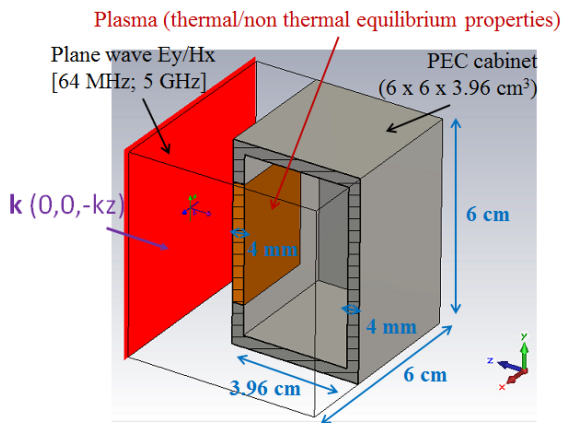


Fig. 8. Characterization of the influence of thermal ($\theta=1$) or non-thermal ($\theta=3$) equilibrium (numerical setup) on the SE of PEC cabinet (sectional view) subject to plane wave illumination.

Figure 9 represents the evolution of the SE of the cabinet in relation with frequency [0.064 MHz; 5 GHz]. The averaged gap existing between plasma at thermal (red) and non-thermal (green) equilibrium is between 9 dB and 45 dB. It is to be noticed that, due to the proposed configuration (worst case regarding size of the aperture and plane wave source), the shielding effectiveness without plasma material quickly decrease within negative levels (i.e., field enhancement instead of shielding) from 2.8 GHz. Contrary to previous case, the plasma slab improves SE of the system (enclosure +

plasma) up to 45 dB ($\theta=1$) and 85 dB ($\theta=3$). It should also be noticed that the system is subject to cavity resonances, decreasing SE for instance at $f=4.859 \text{ GHz}$ (resonance frequency in accordance with inner sizes of the enclosure). Finally, due to dispersive effect, plasma slab closes the cabinet and involve enhancement of 4.859 GHz-resonance frequency as depicted in Fig. 9.

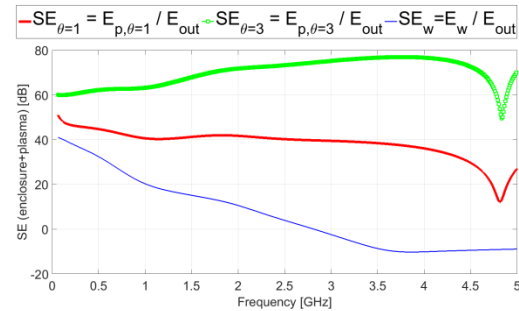


Fig. 9. SE of the cabinet (electric field measured at the center of the enclosure, Fig. 8) with plasma at (red)/out of (green) thermal equilibrium, and without plasma (blue, E_w) including only the enclosure. Results are given by normalizing data following relation (7) with E_{out} .

In order to illustrate the importance of taking into account inner thermal characteristics of plasma (differences between electrons and heavy species temperatures), it is proposed to focus on the influence of plasma by normalizing SE (Fig. 9) obtained in the two cases ($\theta=1$) and ($\theta=3$) by results computed without plasma material. Figure 10 shows the plasma attenuation (based upon electric field E_y -component computing) following the respective dB-differences $20 \log_{10}(E_{\theta=1}/E_{out})$ and $20 \log_{10}(E_{\theta=3}/E_{out})$ (see Fig. 9). As expected the cabinet is involved for a noticeable part in shielding characteristics. Figure 10 gives an overview of the dedicated effect of plasma material in the proposed EMC configuration (Fig. 8) by normalizing with test case involving only the enclosure. This lays emphasis on the importance of considering thermal equilibrium or not from theoretical model to EMC application since high gaps exist (from 10 dB to 40 dB) over the whole frequency bandwidth. As aforementioned in Fig. 9 and due to the characteristics of starting resonance frequency (i.e., the presence of the air aperture, see Fig. 8, involving both the resonance mode vanishing and a huge reflection of impinging plane wave), the shielding effectiveness is considerably spoiled in 'empty' case (without plasma, see blue line in Fig. 9). Contrary to previous case, plasma plays dual role since it affects the levels of fields penetrating in the cabinet but also closes it, enhancing first resonance mode influence around 4.859 GHz as illustrated in Fig. 9.

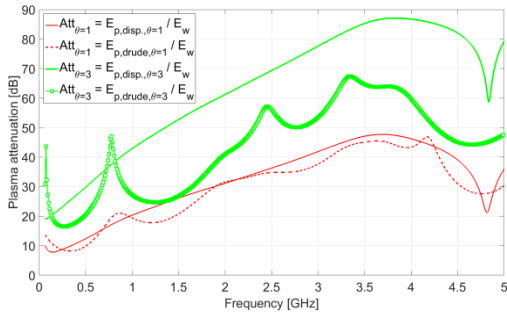


Fig. 10. Plasma attenuation including the effect of the enclosure (normalization with E-field given without plasma, E_w) at (red) and out of (green) thermal equilibrium; results are proposed including dispersive plasma medium (plain lines, see relation (5) and Figs. 4 and 5) and Drude’s model (dotted lines and markers) based upon plasma characteristics (Fig. 3).

A sufficient radiation level of impinging wave in air at low temperature can enhanced an electrical breakdown. The value of breakdown electrical field depends on the air pressure, hygrometry, the cavity shape. Furthermore the nature of plasma, that vary with time, strongly depends on the shape and the power of impinging wave. Similarly to Fig. 9, Fig. 10 illustrates previous point and enriches the discussion by providing data obtained with time simulations taking into account the non-linear nature of plasma characteristics via Drude’s modelling [11]. Indeed, in that case, the definition of plasma dielectric properties relies on intrinsic plasma characteristics (Fig. 3) jointly with a non-linear E-field threshold breakdown modelling as explained in the following. By varying the plasma density within a given field level, plasma attenuation is decreased relatively to purely dispersive medium (see Figs. 7 and 9). It is to be noted in Fig. 10 that weak gaps exist regarding thermal equilibrium ($\theta=1$, red curves); huger differences are obtained out of thermal equilibrium ($\theta=3$, green curves). The same trends between dispersive and Drude’s material are observed in Fig. 10 for $\theta=1$ (red) whereas up to 35 dB-gaps are computed for $\theta=3$ (green). These variations mostly depend on Drude’s model including: plasma characteristics (e.g., plasma frequency f_p and collision frequency ν_{ep} from developments in Section II, here see Fig. 3 and temperature $T_h = 10,000$ K), and electric field breakdown level (we approximate breakdown electrical field by a constant value $E_{break} = 100$ kV/m). As aforementioned in [6], plasma induced by microwave may efficiently offer EMC advantages by providing interesting EM shielding properties. Indeed, when overcoming E_{break} -threshold, the plasma barrier appears as a highly conductive dielectric material. In this case, we demonstrate the capability of time domain simulations (including Drude’s

modelling and breakdown level) to enrich purely dispersive approach. This also lays emphasis on the huge importance of properly defining plasma characteristics (plasma frequencies and/or complex permittivity) in EMC context, especially when thermal equilibrium assumption is not satisfied. It should be noticed that, for air plasma at atmospheric pressure, purely dispersive plasma modelling is sufficient to accurately assess the EM shielding properties of the material. In this framework, plasma characterization may be useful to improve the assessment of EMC shielding.

IV. CONCLUSION AND PROSPECTS

This contribution aims at demonstrating the importance of modelling plasma behaviour in EMC framework. In this context, a particular care needs to be taken in order to properly define the impact of the physical conditions assumed for the definition of plasma. Of course, it is well-known that the composition, temperature, pressure of the material (plasma) is of great importance. The thermal equilibrium respectively between the temperatures of electrons and heavy species plays also a key role as illustrated by the different characteristics of plasma (i.e., plasma and collision frequencies) given at and out of thermal equilibrium. Obviously, this involves major changes regarding the dielectric properties of the material (complex permittivity; non-thermal equilibrium may lead to increase dielectric losses up to a scaling factor of 6 in comparison with thermal equilibrium assumption).

In this paper, we have shown the influence of the plasma thermodynamic state on the shielding properties in EMC context. At thermal equilibrium, we have observed comparable levels of electromagnetic attenuation than results found in literature. On the contrary, non-thermal equilibrium may involve noticeable increase in attenuation (here 40 dB at maximum). Using “Full-Wave” simulation tool such as CST© jointly with the proposed theoretical plasma models upgrade the physical understanding of wave propagation in complex media. Moreover, the assessment of EMC criteria (e.g., shielding effectiveness) is improved.

Further works are nowadays under consideration to enhance this study. Parametric and multi-physics works based upon these models may be useful for EMC applications and/or various electromagnetic issues (e.g., material characterization, plasma, lightning, transport, space re-entry, and communications). It should also be useful to assess the effect of non-linear field behaviour due to plasma inclusion. Based upon proposed work, it should be noticed that plasma material may be modelled throughout use of proposed plasma frequency and collision frequency (parallel to complex permittivity). This may lead to enrich time domain model and illustrates threshold effects in EMC context (involving shielding or field enhancement) and offers an extension

to multi-physics issues (e.g., electromagnetic and thermal ones).

REFERENCES

- [1] S. Alavi, T. Khayamian, and J. Mostaghimi, "Conical torch: The next-generation inductively coupled plasma source for spectrochemical analysis," *Analytical Chemistry*, vol. 90, p. 3036, December 2017.
- [2] N. Derkaoui, C. Rond, T. Gries, G. Henrion, and A. Gicquel, "Determining electron temperature and electron density in moderate pressure H₂/CH₄ microwave plasma," *J. Phys. D: Appl. Phys.*, vol. 47, p. 205201, May 2014.
- [3] X. Pu, Y. Cai, Y. Shi, J. Wang, L. Gu, J. Tian, and W. Li, "Diesel particulate filter (DPF) regeneration using non-thermal plasma induced by dielectric barrier discharge," *Journal of the Energy Institute*, vol. 91, pp. 655-667, June 2018.
- [4] R. Brandenburg, "Dielectric barrier discharges: progress on plasma sources and on the understanding of regimes and single filaments," *Plasma Sources Sci. Technol.*, vol. 26, p. 053001, July 2017.
- [5] L. Zheng, Q. Zhao, and X. J. Xing, "Effect of plasma on electromagnetic wave propagation and THz communications for reentry flight," *ACES Journal*, vol. 30, no. 11, November 2015.
- [6] M. Backstrom, U. Jordan, D. Andersson, A. V. Kim, M. Lisak, and O. Lunden, "Can intentional electrical discharges be used for HPM protection?," *IEEE Int. Symp. on EMC*, pp. 14-19, August 2011.
- [7] A. Hamiaz, R. Klein, X. Ferrieres, O. Pascal, and J. P. Boeuf, "Modelization of plasma breakdown by using finite volume time domain method," in *Proc. 27th Annual Review in Applied Computational Electromagnetics*, Williamsburg, VA, USA, March 2011.
- [8] P. André, Y. A. Barinov, G. Faure, and S. M. Shkol'nik, "Characteristics of discharge with liquid non-metallic cathode burning in air flow," *J. Phys. D: Appl. Phys.*, vol. 51, 445202, September 2018.
- [9] P. André and M. Abbaoui, "Déséquilibre thermique dans un plasma d'air ensemencé d'aluminium (in French)," *JITIPEE*, vol. 3, no. 2, 3, 2017.
- [10] H. Li, Y. Liu, Y.-R. Zhang, F. Gao, and Y.-N. Wang, "Nonlocal electron kinetics and spatial transport in radio-frequency two-chamber inductively coupled plasmas with argon discharges," *Journal of Applied Physics*, vol. 121, p. 233302, June 2017.
- [11] C. Durochat, S. Lanteri, R. Léger, C. Scheid, and J. Viquerat, "Modélisation numérique de la propagation des ondes EM en nanophotonique: une approche de GD en domaine temporel (in French)," in *Proc. Int. Symp. on EMC, CEM 2014*, Clermont-Ferrand, France, July 2014.
- [12] P. André, G. Faure, S. Lalléchère, and A. Mahfouf, "Influence of the electric field and magnetic field on Debye length, London length and Kelvin length," in *Proc. Int. Symp. On EMC, CEM 2014*, Clermont-Ferrand, France, July 2014.
- [13] P. André, M. Abbaoui, R. Bessege, and A. Lefort, "Comparison between Gibbs energy minimization and the mass action law for a low multitemperature plasma with application to nitrogen," *Plasma Chem. and Plasma Process.*, vol. 17, no. 2, pp. 207-217, 1997.
- [14] P. André, "Partition functions and concentrations in plasmas out of thermal equilibrium," *IEEE Transactions on Plasma Science*, vol. 23, no. 3, pp. 453-458, 1995.
- [15] M. Laroussi and W. T. Anderson, "Attenuation of electromagnetic waves by a plasma layer at atmospheric pressure," *Int. Jour. of Infrared and Millimeter Waves*, vol. 19, no. 3, 1998.
- [16] M. Talaat, M. A. Farahat, and T. Said, "Numerical investigation of the optimal characteristics of a transverse layer of dielectric barrier in a non-uniform electric field," *Journal of Physics and Chemistry of Solids*, vol. 121, pp. 27-35, October 2018.



Pascal André received a Ph.D. degree in Plasma Physics from the Blaise Pascal University in 1995. He is the author or co-author of more than 70 papers in the domain of thermal plasma physics. At the present time, he is a Full Professor at the Clermont-Auvergne University and Editor of the French journal *JITIPEE* (Journal International de Technologie, de l'Innovation, de la Physique, de l'Energie et de l'Environnement). His interests involve plasma out of thermodynamic equilibrium included in industrial purposes such as fuses, circuit breakers, lighting strikes at the physical laboratory of Clermont.



Géraldine Faure received a Ph.D. degree in Plasma Physics from University Blaise Pascal, Clermont-Ferrand in 1997. She is working at the physical laboratory of Clermont. Her research interests cover the fields of thermal plasmas, air and air-water plasma, atomic and molecular emission.



Ali Mahfouf received Ph.D. degree in the Domain of Thermal Plasma Physic working at the Clermont-Ferrand University in 2016. His research is focused on new approach to calculate numerically the classical transport collision integrals.

computational methods for electromagnetics. He is currently an Associate Professor at Université Clermont Auvergne and Institut Pascal, Clermont-Ferrand, France. His research interests cover the fields of EMC including antennas and propagation, complex media, computational electromagnetics, stochastic modeling and sensitivity analysis in electrical engineering.



Sébastien Lalléchère received the M.Sc. and Ph.D. degrees in Computational Modeling and Electronics/Electromagnetics from Polytech Clermont and Université Blaise Pascal (UBP), Clermont-Ferrand, France, in 2002 and 2006. He served as a Research Engineer in LASMEA, Clermont-Ferrand, France, in 2007 focusing on intensive

Fast Calculation of the Filamentary Coil Impedance Using the Truncated Region Eigenfunction Expansion Method

Grzegorz Tytko and Leszek Dziczkowski

Institute of Electronics
Silesian University of Technology, Gliwice, 44-100, Poland
grzegorz.tytko@wp.pl, leszek.dziczkowski@polsl.pl

Abstract — The paper presents a mathematical model of an ideal filamentary coil with a finite number of turns, derived by means of the method called truncated region eigenfunction expansion (TREE). The proposed solution allows quick computation of the filamentary coil impedance as well as of the impedance changes caused by the presence of a two-layered conductive material. The final formulas were presented in the closed form and implemented in Matlab. The results were verified using the finite element method in the COMSOL Multiphysics package as well as by means of other mathematical models. In all cases they show a very good agreement. The obtained values of coil impedance changes were compared in terms of the time of reaching the final results. In the case of the most significant calculations, which consisted of many iterations, the proposed solution turned out to be by far the fastest one.

Index Terms — Eddy current testing, impedance calculation, single turn coil, truncated region eigenfunction expansion.

I. INTRODUCTION

Mathematical models of probes are applied in eddy current testing, both in the process of interpreting the results and in calculating the values of the measuring system parameters. The derivation of expressions describing a change in coil impedance makes it possible to obtain information about electrical and geometrical properties of the workpiece. Such an opportunity can be used to detect flaws in materials being examined, derive the thickness of coating or for electrical conductivity measurements.

What is highly useful for the optimum choice of the probe's geometrical dimensions or creating a scale of the measuring device are mathematical models of the ideal filamentary coil. Such a coil, shown in Fig. 1, is made of N infinitely thin turns concentrated in a circle of radius r_0 and situated at a distance h_0 from the surface of the investigated material. According to the method described in [1], any cylindrically symmetric

coil used for eddy current tests can be experimentally associated with a filamentary coil with the same number of turns and with the corresponding parameters r_0 and h_0 . The authors successfully apply this method to device calibration and in eliminating the influence of undesired factors on the test result. Probes of very different structures are compared using an ideal coil that has only three parameters: equivalent radius r_0 , equivalent distance h_0 and the number of turns N . On the basis of the proposed mathematical model of such a coil, it is possible, for any real coil, to apply the same mechanism of calculating the measured values and eliminating the influence of factors that disturb the measurement. Complex and time-consuming calculations are replaced with much faster ones performed for the ideal filamentary coil.

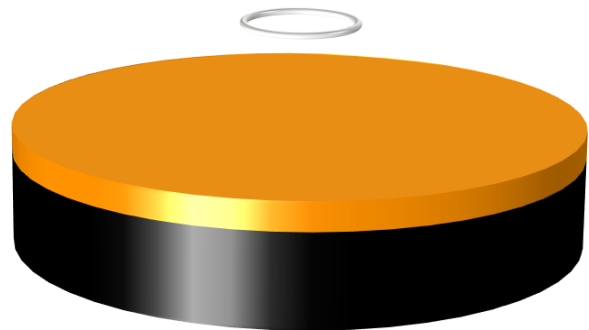


Fig. 1. Filamentary coil located above a two-layered conductive half-space.

A single turn coil situated above a conductive half-space was analyzed by Cheng [2] and then by Dodd and Deeds [3] using a computer program. In subsequent papers, the Legendre functions Q , elliptic integrals E and K [4] and the perturbation method [5] were applied. The problem of the ideal filamentary coil with N turns was presented in [6]. The final formulas describing the change in coil impedance due to the presence of a conductive half-space were derived using the Hankel transform. These expressions were verified many times,

they were thoroughly examined and used, inter alia, in [7].

In the present paper a mathematical model, created by the aid of the Truncated Region Eigenfunction Expansion (TREE) method, of the filamentary coil with N turns situated above a two-layered conductive material, was proposed. The domain of the problem was truncated to a cylinder of radius b . The final formulas for coil impedance were presented using matrix notation not containing integrals and were implemented in Matlab. The results were verified by the finite element method (FEM) in the COMSOL Multiphysics package and by means of other mathematical models. The obtained values showed a very good agreement in all cases and the time of making calculations based on the proposed method turned out to be the shortest.

II. SOLUTION

The problem illustrated in Fig. 2 was solved by the TREE method described in detail in [8] and applied in [9-13]. The filamentary coil composed of N turns concentrated in a circle of radius r_0 was situated at a distance h_0 from the surface of a two-layered conductive material with relative permeability μ_3, μ_4 and electrical conductivity σ_3, σ_4 . The conductive material has the shape of a cylinder whose radius has been truncated to the b parameter value. The problem was split into 4 regions for which the magnetic vector potential A_ϕ was written using a series:

$$A_1(r, z) = \sum_{i=1}^{N_s} J_1(q_i r) e^{-q_i z} C_{1i}, \quad (1)$$

$$A_2(r, z) = \sum_{i=1}^{N_s} J_1(q_i r) (e^{-q_i z} C_{2i} + e^{q_i z} B_{2i}), \quad (2)$$

$$A_3(r, z) = \sum_{i=1}^{N_s} J_1(q_i r) (e^{-s_{3i} z} C_{3i} + e^{s_{3i} z} B_{3i}), \quad (3)$$

$$A_4(r, z) = \sum_{i=1}^{N_s} J_1(q_i r) e^{s_{4i} z} B_{4i}. \quad (4)$$

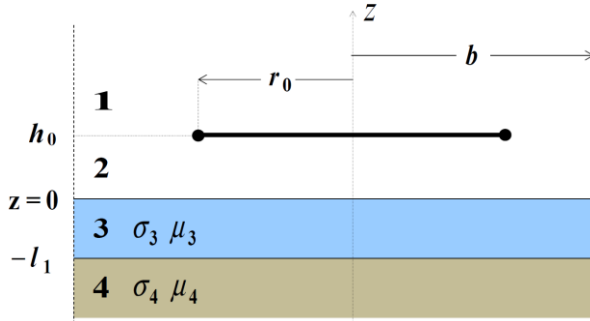


Fig. 2. Rectangular cross-sectional filamentary coil located above a two-layered conductive half-space.

Discrete eigenvalues q_i and coefficients s_{3i}, s_{4i} were computed from equations (5)-(7):

$$J_1(q_i b) = 0, \quad i = 0, 1, 2, \dots, N_s. \quad (5)$$

$$s_{3i} = \sqrt{q_i^2 + j\omega\mu_3\mu_0\sigma_3}, \quad (6)$$

$$s_{4i} = \sqrt{q_i^2 + j\omega\mu_4\mu_0\sigma_4}. \quad (7)$$

At the next stage, the magnetic vector potential A_ϕ , expressed in (1)-(4) by a series, was written for every region of the problem using matrix notation:

$$A_1(r, z) = J_1(\mathbf{q}^T r) e^{-\mathbf{q}z} \mathbf{C}_1, \quad (8)$$

$$A_2(r, z) = J_1(\mathbf{q}^T r) (e^{-\mathbf{q}z} \mathbf{C}_2 + e^{\mathbf{q}z} \mathbf{B}_2), \quad (9)$$

$$A_3(r, z) = J_1(\mathbf{q}^T r) (e^{-\mathbf{s}_3 z} \mathbf{C}_3 + e^{\mathbf{s}_3 z} \mathbf{B}_3), \quad (10)$$

$$A_4(r, z) = J_1(\mathbf{q}^T r) e^{\mathbf{s}_4 z} \mathbf{B}_4, \quad (11)$$

where $J_1(\mathbf{q}^T r)$ are Bessel functions in the form of row vectors, $\mathbf{q}, \mathbf{s}_3, \mathbf{s}_4, e^{\pm\mathbf{q}z}, e^{\pm\mathbf{s}_3 z}, e^{\mathbf{s}_4 z}$ are diagonal matrices, $\mathbf{C}_i, \mathbf{B}_i$ are column vectors of unknown coefficients.

The continuity of the B_r and H_z components on the interfaces between neighboring regions of the problem was ensured after satisfying the following conditions for the magnetic vector potential.

$$A_m(r, z) = A_{m+1}(r, z), \quad m = 1, 2, 3. \quad (12)$$

$$\frac{1}{\mu_m} \frac{\partial A_m}{\partial z} - \frac{1}{\mu_{m+1}} \frac{\partial A_{m+1}}{\partial z} = -\mu_0 I \delta(r - r_0), \quad m = 1, 2, 3. \quad (13)$$

where $\mu_0 I \delta(r - r_0)$ is current density.

By solving a system of six interface equations, the \mathbf{C}_i and \mathbf{B}_i coefficients were derived and, subsequently, they were used to write an expression for the magnetic vector potential of the filamentary coil with N turns.

$$A(r_0, h_0) = I \mu_0 r_0 N^2 \mathbf{q}^{-1} \begin{bmatrix} J_1(\mathbf{q} r_0) \\ J_0(\mathbf{q} b) b \end{bmatrix}^2 \begin{pmatrix} 1 + e^{\mathbf{q} h_0} \mathbf{C}_2 \\ \mathbf{B}_2 \end{pmatrix}, \quad (14)$$

where

$$\mathbf{C}_2 = \frac{1}{2} [\mathbf{C}_3 (1 + \frac{\mathbf{s}_3}{\mathbf{q} \mu_3}) + \mathbf{B}_3 (1 - \frac{\mathbf{s}_3}{\mathbf{q} \mu_3})], \quad (15)$$

$$\mathbf{B}_2 = \frac{1}{2} [\mathbf{C}_3 (1 - \frac{\mathbf{s}_3}{\mathbf{q} \mu_3}) + \mathbf{B}_3 (1 + \frac{\mathbf{s}_3}{\mathbf{q} \mu_3})], \quad (16)$$

$$\mathbf{C}_3 = \frac{1}{2} e^{-\mathbf{s}_3 l_1} e^{-\mathbf{s}_4 l_1} (1 - \frac{\mathbf{s}_4 \mu_3}{\mathbf{s}_3 \mu_4}), \quad (17)$$

$$\mathbf{B}_3 = \frac{1}{2} e^{\mathbf{s}_3 l_1} e^{-\mathbf{s}_4 l_1} (1 + \frac{\mathbf{s}_4 \mu_3}{\mathbf{s}_3 \mu_4}). \quad (18)$$

The general formula for coil impedance can be shown in the following form:

$$Z = \frac{j\omega 2\pi r_0 A(r_0, h_0)}{I}. \quad (19)$$

By setting (14) in (19), an expression describing the impedance of the filamentary coil placed above the two-layered conductive material was obtained:

$$Z = j\omega 2\pi\mu_0 r_0 N^2 \mathbf{q}^{-1} \left[\frac{J_1(\mathbf{q} r_0)}{J_0(\mathbf{q} b) b} \right]^2 \left(1 + e^{-2\mathbf{q} h_0} \frac{e^{-s_3 l_1} \mathbf{k}_1 \mathbf{k}_3 + e^{s_3 l_1} \mathbf{k}_2 \mathbf{k}_4}{e^{-s_3 l_1} \mathbf{k}_1 \mathbf{k}_4 + e^{s_3 l_1} \mathbf{k}_2 \mathbf{k}_3} \right), \quad (20)$$

where

$$\mathbf{k}_1 = \mathbf{s}_3 \mu_4 - \mathbf{s}_4 \mu_3, \quad (21)$$

$$\mathbf{k}_2 = \mathbf{s}_3 \mu_4 + \mathbf{s}_4 \mu_3, \quad (22)$$

$$\mathbf{k}_3 = \mathbf{q} \mu_3 + \mathbf{s}_3, \quad (23)$$

$$\mathbf{k}_4 = \mathbf{q} \mu_3 - \mathbf{s}_3. \quad (24)$$

The change in the filamentary coil impedance ΔZ due to the presence of the two-layered conductive material is represented by the second addend in (20) which can be written as:

$$\Delta Z = j\omega 2\pi\mu_0 r_0 N^2 \mathbf{q}^{-1} \left[\frac{J_1(\mathbf{q} r_0) e^{-\mathbf{q} h_0}}{J_0(\mathbf{q} b) b} \right]^2 \frac{e^{-2s_3 l_1} \mathbf{k}_1 \mathbf{k}_3 + \mathbf{k}_2 \mathbf{k}_4}{e^{-2s_3 l_1} \mathbf{k}_1 \mathbf{k}_4 + \mathbf{k}_2 \mathbf{k}_3}. \quad (25)$$

In the case shown in Fig. 3 in which the conductive material consists of one layer only, we obtain: $s_3 = s_4$, $\mu_3 = \mu_4$, $\sigma_3 = \sigma_4$, $l_1 = 0$ and equation (25) is reduced to the form:

$$\Delta Z = j\omega 2\pi\mu_0 r_0 N^2 \mathbf{q}^{-1} \left[\frac{J_1(\mathbf{q} r_0) e^{-\mathbf{q} h_0}}{J_0(\mathbf{q} b) b} \right]^2 \frac{\mathbf{k}_4}{\mathbf{k}_3}. \quad (26)$$

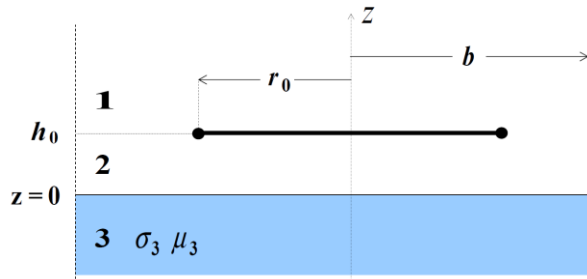


Fig. 3. Rectangular cross-sectional filamentary coil located above a conductive half-space.

III. COMPARISON WITH OTHER MODELS

The verification of obtained results was conducted by the aid of 3 mathematical models. The first one was created in the COMSOL Multiphysics package in which the finite element method is used in calculations. In region 2, between the coil and the surface of the investigated material, a mesh that consisted of around 20000 triangular elements and 400 edge elements was adaptively refined.

Calculations were made also by extending the mathematical model of a single turn coil proposed by Cheng [2]. Taking into consideration a finite number of

turns N and a conductive half-space consisting of two layers, a change in the impedance of such a coil was written in the following form:

$$\Delta Z = j\omega \pi \mu_0 r_0^2 N^2 \int_0^\infty J_1^2(q r_0) e^{-2q h_0} \quad (27)$$

$$\frac{e^{-2s_3 l_1} \mathbf{k}_1 \mathbf{k}_3 + \mathbf{k}_2 \mathbf{k}_4}{e^{-2s_3 l_1} \mathbf{k}_1 \mathbf{k}_4 + \mathbf{k}_2 \mathbf{k}_3} dq.$$

In the third mathematical model, described in [7], the infinite integration range was replaced with a sum of integrals whose boundaries were zeros of the Bessel function $J_1(x)$ normalized in relation to the β parameter. As a consequence, the integration in (28) is performed many times but only for relatively small intervals.

$$\Delta Z = j\omega \pi \mu_0 r_0 N^2 \beta \sum_{k=0}^{N_S} \int_{\lambda_k}^{\lambda_{k+1}} e^{-\alpha \beta q} J_1^2(\beta q) \quad (28)$$

$$\frac{(f_1 - f_2)(q + f_2) e^\Psi + (f_1 + f_2)(f_2 - q)}{(f_1 - f_2)(q - f_2) e^\Psi - (f_1 + f_2)(f_2 + q)} dq,$$

where

$$\alpha = \frac{2h_0}{r_0}, \quad (29)$$

$$\beta = r_0 \sqrt{\omega \mu_0 \sigma_3}, \quad (30)$$

$$f_1 = \sqrt{q^2 + j \frac{\sigma_4}{\sigma_3}}, \quad (31)$$

$$f_2 = \sqrt{q^2 + j}, \quad (32)$$

$$\lambda_k = \frac{q_k}{\beta}, \quad (33)$$

$$\Psi = -2l_1 f_2 \sqrt{\omega \mu_0 \sigma_3}. \quad (34)$$

Expressions (25), (27) and (28) were implemented in Matlab where the Newton-Raphson method was applied to determine the zeros of the Bessel function $J_1(x)$. The obtained values of coil impedance change were compared with the results from the COMSOL package. The relative difference of resistance δ_R and the relative difference of reactance δ_X were used for this purpose:

$$\delta_R = \frac{\Delta R_{COMSOL} - \Delta R_{MATLAB}}{\Delta R_{MATLAB}} \cdot 100\%, \quad (35)$$

$$\delta_X = \frac{\Delta X_{COMSOL} - \Delta X_{MATLAB}}{\Delta X_{MATLAB}} \cdot 100\%. \quad (36)$$

IV. RESULTS

The calculations of the coil impedance changes $\Delta Z = \Delta R + j \Delta X$ were carried out using expression (25) for 50 frequency values from the range 100 Hz to 100 kHz. The parameters of the coil and of the two-layered conductive material are presented in Table 1. Calculations were also made for the second coil of

radius $r_0 = 12$ mm. The results, normalized in relation to reactance X_0 and verified in the COMSOL package, are shown in Fig. 4 and 5. The difference between the ΔZ values obtained using the TREE and the FEM methods did not exceed in any case 0.2 %.

Table 1: Parameters of the coil and plate used in calculations

Number of turns	N	100
Coil radius	r_0	8 mm
Parameter	h_0	1 mm
Parameter	l_1	1.5 mm
Conductivity	σ_3	57 MS/m
Conductivity	σ_4	15.9 MS/m
Relative permeability	μ_3	1
Relative permeability	μ_4	1
Summation terms	N_s	150
Radius of the domain	b	$10 r_0$

The calculations for the filamentary coil of radius $r_0 = 8$ mm were performed also with expressions (27) and (28). In addition, for the TREE method, the second set of parameter values was applied, assuming $N_s = 25$ and $b = 5r_0$. The obtained ΔZ results for the frequency $f = 1$ kHz and $f = 100$ kHz are shown in Table 2 and the times of calculations for each of the mathematical models are included in Table 3. The changes in the filamentary coil impedance were derived for 1 and 10000 different frequency values, respectively, using a computer with an Intel Pentium E2220 2.4 GHz processor equipped with the 4 GB RAM.

It results from the data shown in Tables 2 and 3 that all the mathematical models that have been used make it possible to derive changes of the filamentary coil impedance with a very high degree of accuracy. In such a situation it is the fulfillment of the requirements regarding the time of obtaining the final results that is becoming the key aspect which determines the usefulness of a given mathematical model. The calculations led to the conclusion that the model created using the TREE method turned out to be by far the fastest one. Its advantage over the other solutions is

most visible with a large number of iterations. It is possible to obtain results in such a short time thanks to precomputations. In the first iteration all calculations are performed and in the subsequent ones only those that depend on the variable input parameter.

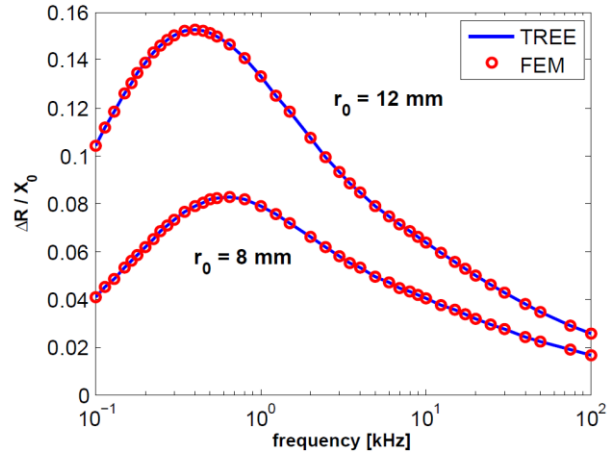


Fig. 4. Real part of the normalized impedance change as a function of frequency for filamentary coil.

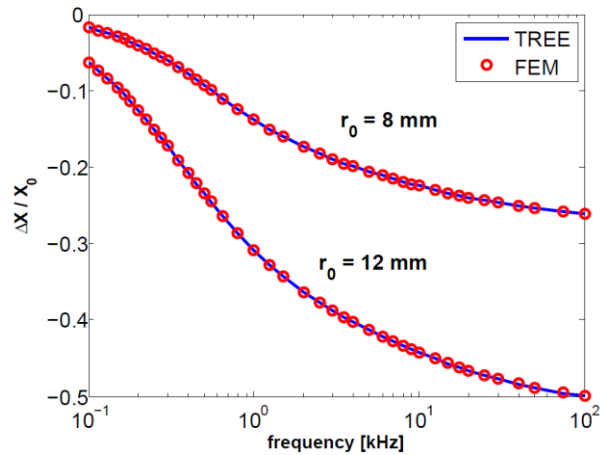


Fig. 5. Imaginary part of the normalized impedance change as a function of frequency for filamentary coil.

Table 2: Values of changes in the filamentary coil impedance

	ΔZ (Ω)					
	$f = 1$ kHz	δ_R [%]	δ_X [%]	$f = 100$ kHz	δ_R [%]	δ_X [%]
FEM	$0.267 - j 0.467$	---	---	$5.561 - j 88.596$	---	---
Eq. (27)	$0.267 - j 0.468$	-0.01	-0.18	$5.561 - j 88.680$	0.00	-0.10
Eq. (28)	$0.267 - j 0.468$	0.01	-0.18	$5.557 - j 88.676$	0.07	-0.09
TREE Eq. (25) $N_s = 150$ $b = 10r_0$	$0.267 - j 0.467$	-0.01	-0.01	$5.561 - j 88.601$	0.00	-0.01
TREE Eq. (25) $N_s = 25$ $b = 5r_0$	$0.267 - j 0.462$	0.03	1.21	$5.503 - j 87.936$	1.05	0.75

Table 3: Comparison of calculation times for different mathematical models

	Computation Time (s)	
	1 Iteration	10 000 Iterations
FEM	7	58148
Eq. (27)	0.06	233.8
Eq. (28)	0.07	70.1
TREE Eq. (25) $N_s = 150$ $b = 10r_0$	0.04	10.2
TREE Eq. (25) $N_s = 25$ $b = 5r_0$	0.03	3.2

In all the mathematical models being compared it is possible to shorten the time of making calculations at the expense of the result accuracy. In the COMSOL package the computations may be accelerated by reducing the number of mesh elements and in expressions (27) and (28) by diminishing the accuracy of the numerical integration procedure. In both cases errors in the derivation of impedance will be significantly greater. In case when the FEM software is used the computation time can be reduced as well by execution of preliminary calculations, e.g., by means of the perturbation method. In the TREE method the time of obtaining results depends primarily on the matrix size specified by the parameter N_s . The number of matrix elements, indeed, determines the number of arithmetic operations carried out in the computer program. Increasing the N_s value makes the calculations longer but at the same time it reduces the error and requires a larger solution domain defined by the parameter b . Both when the N_s value is too large and when it is too small with regard to the parameter b , the results are affected by significant error. The way how these parameters are selected, being usually a compromise between the computation time necessary to achieve the desired results and the acceptable error, is described in [8] more in details.

V. CONCLUSION

The paper presents a mathematical model of the ideal filamentary coil with N turns situated above a two-layered conductive material. An expression that describes the change in the impedance of such a coil due to the presence of the investigated material was derived by means of the TREE method. The ΔZ values calculated by applying the proposed solution were verified by means of the finite element method and the difference did not exceed in any case 0.2%. The time of obtaining the final results was compared with another 3 mathematical models. The application of precomputation and the replacement of integration with matrix operations made it possible to derive impedance changes in a significantly shorter time than using the other solutions. Such a difference was particularly visible in the case

of the most relevant calculations composed of many iterations. The mathematical model shown in the present paper can be implemented directly in an eddy current device. It can be used to create a scale of the measuring device as an equivalent for real coils of any structure, too.

REFERENCES

- [1] L. Dzikowski, "Elimination of coil liftoff from eddy current measurements of conductivity," *IEEE Trans. Instrum. Meas.*, vol. 22, no. 12, pp. 3301-3307, 2013.
- [2] D. H. S. Cheng, "The reflected impedance of a circular coil in the proximity of a semi-infinite medium," *IEEE Trans. Instrum. Meas.*, vol. IM-14, pp. 107-116, 1965.
- [3] C. V. Dodd and W. E. Deeds, "Analytical solutions to eddy-current probe-coil problems," *J. Appl. Phys.*, vol. 39, pp. 2829-2838, 1968.
- [4] A. J. M. Zaman, S. A. Long, and C. G. Gardner, "The impedance of a single-turn coil near a conducting half-space," *J. Nondestruct. Eval.*, vol. 1, no. 3, pp. 183-189, 1980.
- [5] S. K. Burke, "A perturbation method for calculating coil impedance in eddy-current testing," *J. Phys. D Appl. Phys.*, vol. 18, pp. 1745-1760, 1985.
- [6] L. Simankova, "Mathematical presentation of impedance variation of a coil cause by the measured object," *TESLA Electronics*, vol. 4, no. 4, pp. 112-118, 1971.
- [7] L. Dzikowski, "Enhancement of conductometer functions with the measurements of surface roughness," *Int. J. Appl. Electrom.*, vol. 41, no. 3, pp. 237-249, 2013.
- [8] T. P. Theodoulidis and E. E. Kriezis, *Eddy Current Canonical Problems (With Applications to Nondestructive Evaluation)*. Tech Science Press, Duluth Georgia, pp. 93-135, 2006.
- [9] G. Tytko and L. Dzikowski, "An analytical model of an I-cored coil with a circular air gap," *IEEE Trans. Magn.*, vol. 53, no. 4, pp. 6201104, 2017.
- [10] T. P. Theodoulidis and J. R. Bowler, "The truncated region eigenfunction expansion method for the solution of boundary value problems in eddy current non-destructive evaluation," *Rev. Progr. Quant. Non-Destruct. Eval.*, vol. 24A, pp. 403-408, 2004.
- [11] G. Tytko and L. Dzikowski, "An analytical model of an I-cored coil located above a conductive material with a hole," *Eur. Phys. J. Appl. Phys.*, vol. 82, no. 21001, pp. 1-7, 2018.
- [12] T. P. Theodoulidis and J. R. Bowler, "Interaction of an eddy-current coil with a right-angled conductive wedge," *IEEE Trans. Magn.*, vol. 46,

no. 4, pp. 1034-1042, 2010.

- [13] G. Tytko and L. Dzikowski, "I-cored coil probe located above a conductive plate with a surface hole," *Meas. Sci. Rev.*, vol. 18, no. 1, pp. 7-12, 2018.



Grzegorz Tytko (born 1984) received his M.S. degree in Telecommunication from Silesian University of Technology, Gliwice, Poland in 2010 and his Ph.D. degree in Nondestructive Testing by the same institution in 2016. His main research areas include electromagnetic testing, analytical modeling, measuring devices and eddy current techniques.



Leszek Dzikowski received the Ph.D. degree in Non-destructive Examinations of Metals from the Silesian University of Technology, Gliwice, Poland. He is with the Silesian University of Technology. He deals with engineering of telecommunication systems and equipment as well as protection systems for power engineering. His current research interests include engineering and construction of eddy-current conductometers and induction furnaces.

Analytical Modeling of Magnetic Field Considering the Saturation in Switched Reluctance Motor

Shenglong Hu and Shuguang Zuo*

Clean Energy Automotive Engineering Center
Tongji University, Shanghai, 201804, China
slhu825@163.com, sgzuo@tongji.edu.cn*

Abstract — This paper aims at accurately predicting the severe magnetic saturation of a switched reluctance motor (SRM). Firstly, Method I based on the solution of the Laplacian or Poissonian field equation is used to predict the magnetic field in the air gap, but this method is only applicable to the mildly saturated magnetic field. Secondly, Method II based on the winding function theory (WFT) considering the saturation is utilized to predict the magnetic field, which can precisely compute the severely saturated magnetic field. Nevertheless, the tangential magnetic flux density is not considered by Method II. Finally, the synthetic method based on the advantages of Method I and Method II is proposed, which can predict the air-gap magnetic field in SRM having any number of stator slots and rotor poles for any rotor positions. The results indicate that the error of the air-gap magnetic field obtained by the synthetic method is within 5%. Moreover, the radial electromagnetic force and torque obtained by the Maxwell Stress equation are compared with the results computed by the FEM, verifying the effectiveness of the synthetic method. It lays the groundwork for the optimization of torque ripple, vibration and noise of SRM.

Index Terms — Analytical modeling, magnetic field, saturation and switched reluctance motor.

I. INTRODUCTION

In recent years, SRMs are widely used in the aerospace, high-speed centrifugal compressor, electric vehicle, mine and so on due to its strong robustness, simple structure, high temperature resistance and low cost [1-3]. Nevertheless, SRM compared with other motors has a much larger torque ripple, vibration and noise, which limits its broader application [4-6]. Therefore, it is necessary to establish an analytical model that can accurately reflect the parameters of motor, which lays the foundation for the optimization of torque ripple, vibration and noise.

At present, there is much literature on the analytical modeling of the motor magnetic field, which mainly includes the analytical method based on the solution of

the Laplacian or Poissonian field equation and the other analytical method based on WFT. In [7-9], the method based on the solution of the Laplacian or Poissonian field equation has been applied to predict the air-gap magnetic field of surface mounted permanent magnetic brushless DC motors. In [10-12], the magnetic field distribution of flux-switching machine, surface mounted permanent-magnet synchronous motor and disc-type permanent generator was also predicted respectively through the above analytical method. In [13], the analytical modeling based on the solution of the Laplacian or Poissonian field equation considering the magnetic saturation has also been implemented, which was a semi-analytical method depending on the results of FEM. In [14], the method based on the solution of Laplacian or Poissonian field equation has been also applied and an iterative algorithm of saturation according to the working principle of induction motor has been proposed, however, the iterative algorithm about saturation was not applicable for SRM on account of the particular working principle. In [15], the above analytical method has been utilized to predict the magnetic field distribution in SRM and the magnetic saturation was also considered. However, it was not appropriate for the severe magnetic saturation but the mild magnetic saturation.

There are also lots of references on analytical modeling based on WFT. In [16-18], the air-gap magnetic field of interior permanent magnetic (IPM) motor has been predicted by the analytical method based on WFT, but the magnetic saturation was not taken into account. In [19], the magnetic field distribution of flux-switching machine has been computed with the above analytical method. However, the saturation problem has also been neglected. In [20], the magnetic field distribution considering the saturation of rotor in fractional-slot concentrated-wound IPM motor has been computed with the analytical method based on WFT. Nevertheless, the method based on WFT in the above literature only predicts the radial magnetic flux density, neglecting the tangential magnetic flux density. However, the slot width of SRM is larger than that of other motors, which results in severe magnetic flux leakage at the tooth

backlash, so that the magnetic flux density has a larger tangential component. Therefore, the tangential magnetic flux density cannot be ignored.

From the above, there is little literature about the analytical modeling of air-gap magnetic field considering the saturation in SRM. Moreover, the analytical modeling of magnetic saturation results from the doubly salient structure has been difficult. This paper aims at accurately predicting the severe magnetic saturation of SRM with the analytical method.

The originality in this paper includes two main points. Firstly, based on the idea of the distributed equivalent circuit with the series reluctance, a new algorithm of magnetic saturation is proposed, which combines the specific relationship between the permeability and the magnetic flux density of the iron core material. Secondly, the synthetic analytical method of the air-gap magnetic field of SRM based on the solution of the Laplacian or Poissonian field equation and WFT is presented, which can be applied to predict the air-gap magnetic field in SRM having any number of stator slots and rotor poles for any rotor positions.

II. THE MAIN PARAMETERS OF SRM

The proposed motor is a three-phase 6/4 SRM. Moreover, the main parameters are shown in Table 1.

Table 1: Main parameters of three-phase 6/4 SRM

Parameter	Symbol	Value
Number of stator poles	N_s	6
Number of rotor poles	N_r	4
Number of slot coil	N_c	66
Width of stator slot	θ_{ss}	0.524 rad
Width of one slot coil	d	0.154 rad
Air gap length	g	4 mm
Internal radius of stator	R_s	41.4 mm
External radius of rotor	R_r	41.0 mm
Internal radius of rotor slot	R_1	30.0 mm
External radius of stator slot	R_4	62.5 mm
Length of stator pole	h_s	21.1 mm
Length of rotor pole	h_r	11 mm
Length of rotor core	h	91.5 mm

III. METHOD I

Method I is used to predict the air-gap magnetic field of SRM by solving the Laplacian or Poissonian field equation. In [15], although the magnetic field of SRM was computed with Method I, the solution of the inverse matrix was unstable and difficult due to the large matrix dimension. Based on the analytical model in [15], Method I makes the following modifications to the column vector consisting of the coefficients of current density, the convolution matrixes of radial and tangential magnetic permeability.

According to [15], the complex Fourier series

expansion of current density in the three-phase 6/4 SRM in Fig. 1 is shown in Eq. (1):

$$J(\theta) = \sum_{n=-\infty}^{\infty} J_n e^{-jn\theta}, \quad (1)$$

The coefficients of J_n are computed as;

$$J_n = \sum_{i=1}^{N_s} \frac{1}{2\pi jn} \begin{bmatrix} J_{1,i} e^{-jn\theta_{ss}/2} (e^{jnd} - 1) + \\ J_{2,i} e^{jn\theta_{ss}/2} (1 - e^{-jnd}) \end{bmatrix} e^{jn\alpha_i}. \quad (2)$$

In Eq. (2), θ_{ss} is the slot width, d is the width of a single slot coil, the values $J_{1,i}, J_{2,i}, \alpha_i$ are defined as follows:

$$J_{1,i} = N_c/S \cdot [-i_a \ i_b \ -i_c \ i_a \ -i_b \ i_c]^T, \quad (3)$$

$$J_{2,i} = N_c/S \cdot [-i_b \ i_c \ -i_a \ i_b \ -i_c \ i_a]^T, \quad (4)$$

$$\alpha_i = 2\pi/N_s \cdot i - \pi/N_s. \quad (5)$$

In Eqs. (3) and (4), S is the area of the stator slot coil. \mathbf{J}_z is the column vector composed of the coefficients J_n , which is presented in Eq. (6). To acquire the inverse matrix more efficiently, the modified column vector of the coefficients of current density does not include J_0 because the DC component J_0 is equal to zero:

$$\mathbf{J}_z = [J_{-N} \ \cdots \ J_{-1} \ , \ J_1 \ \cdots \ J_N]^T. \quad (6)$$

In the same way, the complex Fourier series expansion of magnetic permeability can be obtained and the coefficients of radial magnetic permeability can compose one matrix $\boldsymbol{\mu}_r$. To make the dimension of $\boldsymbol{\mu}_r$ are consistent with that of \mathbf{J}_z , the matrix $\boldsymbol{\mu}_r$ needs to be revised, as shown in Eq. (7):

$$\boldsymbol{\mu}_r = \begin{bmatrix} \mu_0 & \cdots & \mu_{-n+1} & \mu_{-n-1} & \cdots & \mu_{-2n} \\ \vdots & \ddots & \vdots & \vdots & \ddots & \vdots \\ \mu_{n-1} & \cdots & \mu_0 & \mu_{-2} & \cdots & \mu_{-n-1} \\ \mu_{n+1} & \cdots & \mu_2 & \mu_0 & \cdots & \mu_{n+1} \\ \vdots & \ddots & \vdots & \vdots & \ddots & \vdots \\ \mu_{2n} & \cdots & \mu_{n+1} & \mu_{n-1} & \cdots & \mu_0 \end{bmatrix}. \quad (7)$$

Based on the matrix $\boldsymbol{\mu}_r$, the modified matrix $\boldsymbol{\mu}_t$ consisting of the coefficients of tangential magnetic permeability can be calculated, as shown in Eq. (8), where μ^{rec} can be obtained by replacing μ in the complex Fourier series expansion of radial magnetic permeability with $1/\mu$:

$$\boldsymbol{\mu}_t = \begin{bmatrix} \mu_0^{rec} & \cdots & \mu_{-n+1}^{rec} & \mu_{-n-1}^{rec} & \cdots & \mu_{-2n}^{rec} \\ \vdots & \ddots & \vdots & \vdots & \ddots & \vdots \\ \mu_{n-1}^{rec} & \cdots & \mu_0^{rec} & \mu_{-2}^{rec} & \cdots & \mu_{-n-1}^{rec} \\ \mu_{n+1}^{rec} & \cdots & \mu_2^{rec} & \mu_0^{rec} & \cdots & \mu_{n+1}^{rec} \\ \vdots & \ddots & \vdots & \vdots & \ddots & \vdots \\ \mu_{2n}^{rec} & \cdots & \mu_{n+1}^{rec} & \mu_{n-1}^{rec} & \cdots & \mu_0^{rec} \end{bmatrix}^{-1}. \quad (8)$$

According to the above analysis, the modified column vector \mathbf{J}_z , the convolution matrixes $\boldsymbol{\mu}_r$ and $\boldsymbol{\mu}_t$ can be captured. In the following, the air-gap magnetic field distribution will be computed based on the above

analysis. The air-gap magnetic field is determined by the magnetic field in the stator and rotor slots/teeth region due to the particular doubly salient structure of SRM, so the magnetic field in the stator and rotor slots/teeth region should be taken into account. According to [15], the magnetic vector potential in the air gap region and the stator slots/teeth region and the rotor slots/teeth region can be solved by corresponding Laplacian or Poissonian field equation.

The magnetic field calculated by the above method is linear. However, regional saturation is severe on account of the doubly salient structure and the particular working principle of SRM, especially the stator/rotor poles under excitation state. Therefore, the magnetic saturation of SRM must be taken into account. According to the iterative algorithm of magnetic saturation in [15], the air-gap magnetic flux density can be obtained, which is based on the accurate magnetic flux density in the stator and rotor slots/teeth region. Moreover, the magnetic flux densities in the air gap considering the saturation of three-phase 6/4 SRM at the unaligned and aligned position are shown in Fig. 1 and Fig. 2, respectively, which are calculated by Method I.

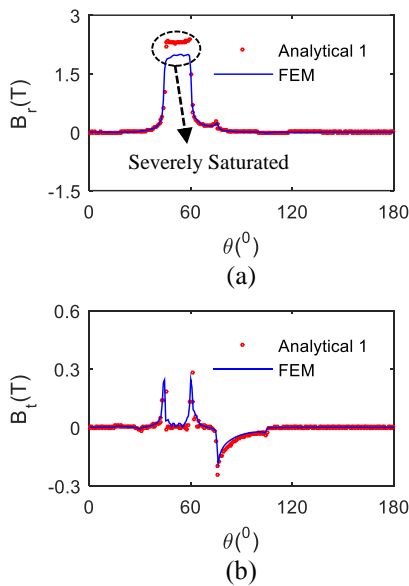


Fig. 1. The magnetic flux density at the unaligned position: (a) radial and (b) tangential.

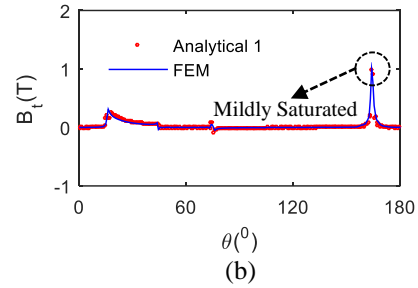
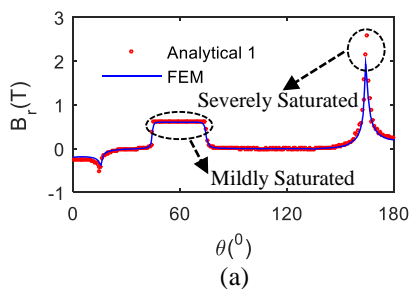


Fig. 2. The magnetic flux density at the aligned position: (a) radial and (b) tangential.

It can be observed in Fig. 1 and Fig. 2 that the magnetic flux density obtained by Method I is in good agreement with the result of FEM in the mildly saturated region. However, in the severely saturated region, especially in the stator/rotor poles under the excitation state, the error of Method I and FEM is significant and the maximum error is more than 20%. Besides, the tangential magnetic flux density obtained by Method I has a nice agreement with the FEM, but the radial magnetic flux density is not accurate. Because the tangential magnetic flux density is mildly saturated and the radial magnetic flux density is severely saturated. In addition, the iterative algorithm of air-gap magnetic saturation is based on the accurate magnetic flux density in the stator and rotor slots/teeth region. However, it is difficult to accurately calculate the magnetic flux densities in the stator and rotor slots/teeth region for severe magnetic saturation, so that the error of the air-gap magnetic field in the severely saturated region is enormous. Although the analytical magnetic field in [15] was in good agreement with the FEM, the selected motor worked under the mildly saturated condition, in which the maximum magnetic flux density is below 1.5 T. However, the magnetic saturation of SRM in this paper is severe and the maximum magnetic flux density is over 2 T, so the iterative algorithm considering the saturation is no longer working. In view of the knotty problem of magnetic saturation, this paper presents another analytical method, namely Method II, which will be introduced detailedly in the following.

IV. METHOD II

Method II is a kind of analytical modeling based on WFT and the specific modeling thinking is as follows.

A. The radial magnetic flux density without slot opening

The spatial distribution of magnetomotive force (MMF) of the q th-phase winding in SRM is shown in Fig. 3. Where $\alpha=N_r\theta$, N_c is the number of coil turns in one tooth, i_q the q th-phase current, β_s is the width of stator tooth, N_r is the number of rotor poles, N_t is the

number of stator pole pairs, $N_r = N_s / (2Q)$, Q is the number of phases and $1 \leq q \leq Q$.

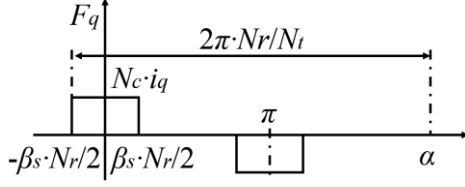


Fig. 3. The spatial distribution of MMF.

So, the Fourier series expansion of the q th-phase winding is given by Eq. (9) [16-18]:

$$F_q(\theta) = \sum_{v=1,3,5}^{\infty} F_v \cos(vN_r\theta). \quad (9)$$

The value of F_v is calculated through Eq. (10):

$$F_v = 4N_c i_q / (\pi v) \cdot \sin(N_r \beta_s v / 2). \quad (10)$$

Then, the Fourier series expansion of the q th-phase current is shown as:

$$i_q(t) = \sum_{i=0}^{\infty} I_i \cos(iN_r \omega t). \quad (11)$$

The value of I_i in Eq. (11) is given as follows, where θ_c is the conduction angle:

$$I_i = \begin{cases} I_0 \theta_c N_r / (2\pi), & i = 0 \\ 2I_0 / (\pi i) \cdot \sin(\theta_c N_r i / 2), & i = 1, 2, \dots \end{cases} \quad (12)$$

Equation (11) is substituted to Eq. (10); then, Eq. (10) is substituted to Eq. (9). Then, the Fourier series expansion of MMF of the q th-phase winding can be obtained, as shown in Eq. (13). Where $v=1,3,5,\dots$, $i=0,1,2,\dots$, K_{vi} is the coefficient associated with v, i :

$$F_q(\theta, t) = \sum_v \sum_i K_{vi} \cos(vN_r\theta \pm i\omega N_r t). \quad (13)$$

Assume $u = vN_r$; the Eq. (13) can be written as Eq. (14), where K_{ui} is the coefficient associated with u, i :

$$F_q(\theta, t) = \sum_u \sum_i K_{ui} \cos(u\theta \pm i\omega N_r t). \quad (14)$$

Based on the working principle of SRM, the MMF of different phase winding can be written as Eq. (15), where N_s is the number of stator poles:

$$\begin{cases} F_1 = \sum_u \sum_i K_{ui} \cos(u\theta \pm i\omega N_r t) \\ F_2 = \sum_u \sum_i K_{ui} \cos\left[u\left(\theta + \frac{2\pi}{N_s}\right) \pm i\omega N_r \left(t - \frac{2\pi}{q\omega N_r}\right)\right] \\ F_3 = \sum_u \sum_i K_{ui} \cos\left[u\left(\theta + \frac{4\pi}{N_s}\right) \pm i\omega N_r \left(t - \frac{4\pi}{q\omega N_r}\right)\right] \end{cases} \quad (15)$$

According to the literature [19], the radial magnetic flux density of the q th-phase winding without slot

opening can be given by Eq. (16), which is written as Eq. (17), where μ_0 is the air permeability, g is the length of the air gap:

$$B_{rq0}(\theta, t) = F_q(\theta, t) \cdot \Lambda_0, \quad (16)$$

$$B_{rq0}(\theta, t) = \frac{\mu_0}{g} \sum_u \sum_i K_{ui} \cos(u\theta \pm iN_r \omega t). \quad (17)$$

B. The influence of slot opening in stator and rotor

Suppose the coefficient of stator pole is 1 and the influence coefficient of the stator slot is ε_s .

Besides, the Fourier series expansion of the influence coefficient of the stator slot is given in Eq. (18) [18]:

$$\lambda_s(\theta) = \lambda_{s0} + \sum_{m=1}^{\infty} \lambda_{sm} \cos(mN_s\theta), \quad (18)$$

where the values of λ_{s0} and λ_{sm} are shown as follows:

$$\lambda_{s0} = \varepsilon_s + (1 - \varepsilon_s) \beta_s N_s / (2\pi), \quad (19)$$

$$\lambda_{sm} = 2 / (\pi m) \cdot (1 - \varepsilon_s) \sin(\beta_s N_s m / 2). \quad (20)$$

The analysis of the influence coefficient of the rotor slot is the same as stator slot. Suppose the coefficient of the rotor pole is 1 and the influence coefficient of the rotor slot is ε_r . The Fourier series expansion of the influence coefficient of the rotor slot is given in Eq. (21) [18]:

$$\lambda_r(\theta, t) = \lambda_{r0} + \sum_{n=1}^{\infty} \lambda_{rn} \cos(nN_r\theta - n\omega N_r t), \quad (21)$$

Moreover, the values of λ_{r0} and λ_{rn} are shown as follows:

$$\lambda_{r0} = \varepsilon_r + 1 / (2\pi) \cdot (1 - \varepsilon_r) \beta_r N_r, \quad (22)$$

$$\lambda_{rn} = 2 / (\pi n) \cdot (1 - \varepsilon_r) \sin(\beta_r N_r n / 2). \quad (23)$$

Furthermore, the product of the influence coefficient of stator and rotor slot is given in Eq. (24):

$$\begin{aligned} \lambda_{sr}(\theta, t) &= \lambda_s(\theta) \times \lambda_r(\theta, t) \\ &= \lambda_{s0} \lambda_{r0} + \sum_{m=1}^{\infty} \lambda_{r0} \lambda_{sm} \cos(mN_s\theta) + \\ &\quad \sum_n \lambda_{s0} \lambda_{rn} \cos(nN_r\theta - n\omega N_r t) + \\ &\quad \sum_m \sum_n \frac{1}{2} \lambda_{sm} \lambda_{rn} \cos\left[(mN_s \pm nN_r)\theta \mp n\omega N_r t\right]. \end{aligned} \quad (24)$$

C. The radial magnetic flux density with slot opening

Through the above analysis, the radial magnetic flux density of the q th-phase winding without slot opening, the influence coefficient of stator and rotor slot has been gotten, respectively. According to [16-18], the radial magnetic flux density of the q th-phase winding with slot opening can be obtained, which is given in Eq. (25) and Eq. (26):

$$B_{rq}(\theta, t) = B_{rq0}(\theta, t) \cdot \lambda_{sr}(\theta, t), \quad (25)$$

$$B_{rq}(\theta, t) = \mu_0/g \times \left\{ \begin{aligned} & \sum_u \sum_i K_{ui} \lambda_{s0} \lambda_{r0} \cos(u\theta \pm i\omega N_r t) + \\ & \sum_u \sum_i \sum_n \frac{1}{2} K_{ui} \lambda_{s0} \lambda_{rn} \cos\left(\frac{(u \pm nN_r)\theta \pm (i \mp n)\omega N_r t}{2}\right) + \\ & \sum_u \sum_i \sum_m \frac{1}{2} K_{ui} \lambda_{r0} \lambda_{sm} \cos\left(\frac{(u \pm mN_s)\theta \pm i\omega N_r t}{2}\right) + \\ & \sum_u \sum_i \sum_m \sum_n \frac{1}{2} K_{ui} \lambda_{sm} \lambda_{rn} \cos\left(\frac{(u \pm (mN_s \pm nN_r))\theta \pm (i \mp n)\omega N_r t}{2}\right) \end{aligned} \right\} \quad (26)$$

Because three-phase 6/4 SRM is selected in this paper, so $1 \leq q \leq Q=3$. Therefore, the linear magnetic flux density in the air gap is superimposed by the three-phase windings, as shown in Eq. (27):

$$B_{r,linear} = B_{r1}(\theta, t) + B_{r2}(\theta, t) + B_{r3}(\theta, t) = \mu_0/g \cdot (F_1 + F_2 + F_3) \cdot \lambda_s \cdot \lambda_r. \quad (27)$$

D. The algorithm of magnetic saturation

Based on the linear radial magnetic flux density obtained by Eq. (27), the magnetic saturation should be taken into account. In this paper, the distributed equivalent reluctance and dynamic permeability are used to solve the magnetic saturation. In the above linear model, the air gap reluctance was considered only. While the permeability of the stator and rotor core was considered infinite. So, the reluctance of the stator and rotor core was neglected. But the local magnetic saturation of SRM is serious, especially the stator and rotor poles under the excitation state.

The circle of motor is divided into n parts. The saturated magnetic field of a single part can be analyzed by the equivalent magnetic circuit, as shown in Fig. 4. The reluctance of one part is defined as R_m , which can be equivalent to the superposition of the air-gap reluctance R_2 and the stator and rotor core reluctance R_3 (defined as the series reluctance R_3). The local magnetic saturation of SRM is mainly in the front half of the stator and rotor poles, so the length l of the series reluctance R_3 is about half of the total length of stator and rotor poles, i.e., $(h_s+h_r)/2$. In addition, d_0 is the width of each equivalent reluctance in Fig. 4; g is the length of the air-gap reluctance; $h_s/2$ is the length of the stator core reluctance; $h_r/2$ is the length of the rotor core reluctance.

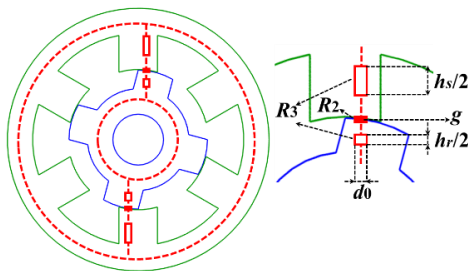


Fig. 4. The equivalent magnetic circuit.

The air gap reluctance R_2 and the series reluctance R_3 are shown in Eqs. (28) and (29). Where h is the effective length of the rotor core and μ_d is the dynamic permeability:

$$R_2 = g/(\mu_0 d_0 h), \quad (28)$$

$$R_3 = l/(\mu_d d_0 h). \quad (29)$$

Then, the equivalent reluctance R_m can be gotten by Eq. (30):

$$R_m = R_2 + R_3. \quad (30)$$

Besides, the magnetic flux and the magnetic flux density are calculated by Eqs. (31) and (32), respectively:

$$\phi = F/R_m, \quad (31)$$

$$B_r = \phi/(d_0 h). \quad (32)$$

Substituting Eqs. (28)-(31) into Eq. (32), the saturated magnetic flux density can be gotten, as shown in Eq. (33), where the MMFs can be obtained by Eq. (15):

$$B_{r,saturation} = (F_1 + F_2 + F_3) \cdot \lambda_s \cdot \lambda_r / (g/\mu_0 + l/\mu_d). \quad (33)$$

In Eq. (33), only the value of dynamic permeability μ_d is required. The μ_d is obtained by $\mu_d = B/H$ from the $B(H)$ curve, to draw the $\mu_d(B)$ curve, which is shown in Fig. 5.

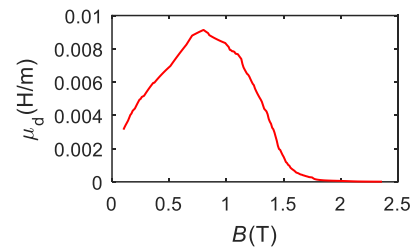


Fig. 5. The $\mu_d(B)$ curve.

Based on Eq. (33), combined with the $\mu_d(B)$ curve in Fig. 5 and the algorithm of magnetic saturation in Fig. 6, the dynamic permeability μ_d in the spatial circle at different rotor position can be captured. Therefore, the saturated magnetic density can be obtained. The radial magnetic flux density obtained by Method II in the three-phase 6/4 SRM is presented in Fig. 7, from which the radial magnetic density in the saturated region with Method II has a good agreement with the FEM. However, there is an enormous error between the analytical result and the FEM in the linear region, mainly because Method II can only calculate the radial magnetic flux density, neglecting the tangential magnetic flux density.

From the above, the radial magnetic density in the saturated region is accurate with Method II, which can be used to solve the magnetic saturation of SRM. However, the limitation of Method II is that the contribution of tangential magnetic density cannot be taken into account, which results in a significant deviation between the analytical result and the FEM in

the linear region. To obtain the saturated radial and tangential flux density, this paper presents a synthetic method based on Method I and Method II.

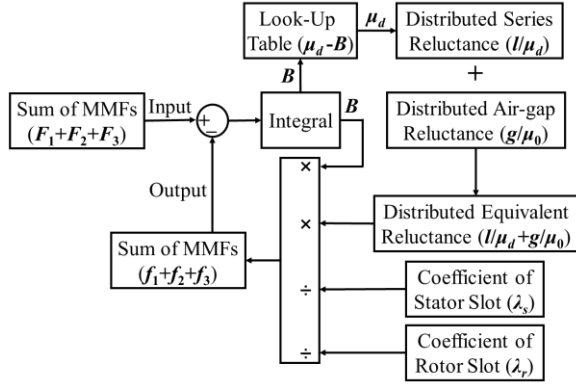


Fig. 6. The algorithm of magnetic saturation.

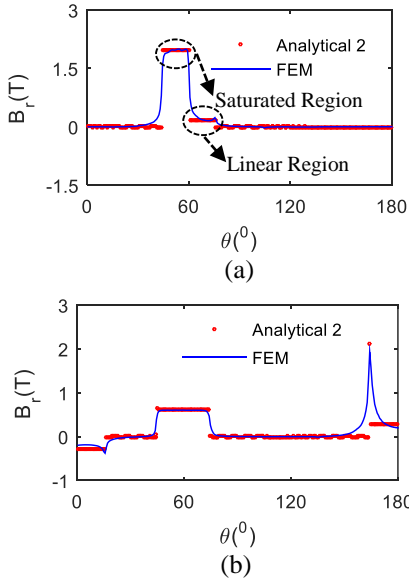


Fig. 7. The radial magnetic flux density: (a) unaligned position, and (b) aligned position.

V. THE SYNTHETIC METHOD

The main thinking of the synthetic method is shown as follows. The advantages of Method I and Method II are applied comprehensively. Because the tangential magnetic flux density which is mildly saturated is much less than the radial magnetic flux density, so Method I can be applied to predict the tangential magnetic flux density. Also, it can be seen from Fig. 5 that the magnetic over 1.5 T is severely saturated. So, for the radial magnetic flux density, it is calculated by Method I in the mildly saturated and linear region below 1.5 T; it is computed by Method II in the severely saturated region over 1.5 T. Therefore, the magnetic flux density considering the saturation in the air gap can be gotten by the synthetic

method.

A. The magnetic flux density verification

The air-gap magnetic flux densities obtained by the synthetic method at the unaligned and aligned position in the three-phase 6/4 SRM are shown in Fig. 8 and Fig. 9, respectively. It can be seen from Fig. 8 and Fig. 9 that the analytical result is in good agreement with the FEM and the error is within 5%, indicating that the synthetic method is working.

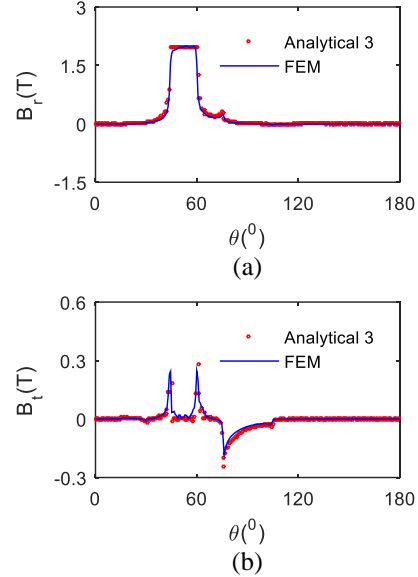


Fig. 8. The magnetic flux density at the unaligned position: (a) radial and (b) tangential.

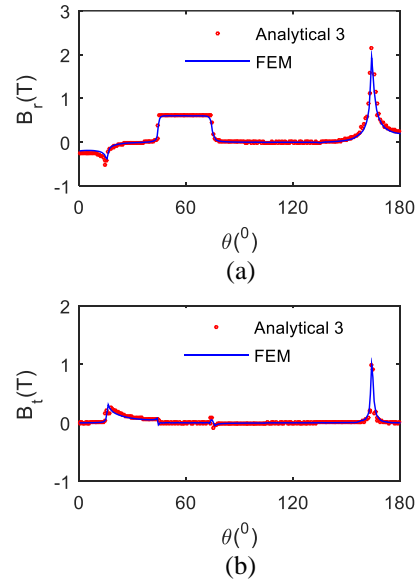


Fig. 9. The magnetic flux density at the aligned position: (a) radial and (b) tangential.

B. The radial electromagnetic force and torque verification

To further verify the above synthetic method, the radial electromagnetic force and torque are obtained by Maxwell Stress equation, which is compared with the FEM. The radial electromagnetic force at different rotor position is given in Fig. 10. Besides, the torque is presented in Fig. 11. Whether the electromagnetic force or the torque, the analytical results agree well with the FEM and the error is within 10%, which further indicates the accuracy of the synthetic method.

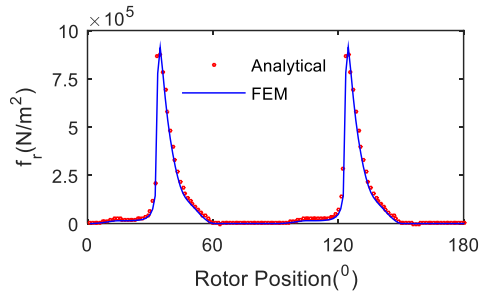


Fig. 10. The radial electromagnetic force at different rotor position.

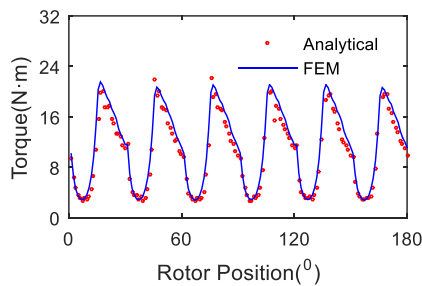


Fig. 11. The torque at different rotor position.

The computational time for the magnetic flux density calculation in all three-phase 6/4 SRMs in the aligned and unaligned position is given in Table 2. It can show in Table 2 that the speed of analytical computation is about twice that of finite element calculation. Therefore, the synthetic analytical method is much more time-efficient.

Table 2: Computational time

Rotor Position	Analytical /s	FEM /s
Aligned	3.95	8.09
Unaligned	3.67	7.56

VI. CONCLUSION

Although the finite element method always works well, it requires a huge amount of time and computational resources. By contrast, the analytical method is much more time-efficient and cost-effective. Therefore, it is

worthwhile to investigate the analytical method for calculating the magnetic field of SRM. Moreover, the proposed synthetic analytical method can be applied to analyze quickly the effect of structural and electromagnetic parameters on the magnetic field of motor. Besides, the proposed method can be used together with the torque and vibroacoustic calculation method to optimize motors' torque ripple and electromagnetic noise, which can improve the design of motor. Besides, Method I is only applicable to the mildly saturated magnetic field, in which the maximum magnetic flux density is below 1.5 T. Also, Method II can precisely predict the severely saturated magnetic field, but the tangential magnetic flux density is not taken into account. Finally, the synthetic method based on the advantages of Method I and Method II can predict the air-gap magnetic field in SRM with accuracy. Besides, the maximum relative error between the magnetic flux density obtained by the synthetic method and that by FEM is not more than 5%. In addition, the radial electromagnetic force and torque are compared with the FEM, verifying the effectiveness of the synthetic method. It lays the foundation for the optimization of torque ripple, vibration and noise of SRM.

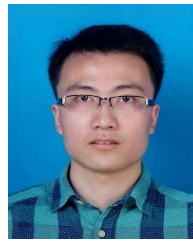
ACKNOWLEDGMENT

This work was supported by a Grant (Project 51875410) from the National Natural Science Foundation of China.

REFERENCES

- [1] X. Liang, G. Li, J. Ojeda, M. Gabsi, and Z. Ren, "Comparative study of classical and mutually coupled switched reluctance motors using multiphysics finite-element modeling," *IEEE Trans. Ind. Electron.*, vol. 61, no. 9, pp. 5066-5074, Sep. 2014.
- [2] H. Torkaman, N. Arbab, H. Karim, and E. Afjei, "Fundamental and magnetic force analysis of an external rotor switched reluctance motor," *Applied Computational Electromagnetics Society Journal*, vol. 26, no. 10, pp. 868-875, Oct. 2011.
- [3] H. Cheng, H. Chen, and Z. Yang, "Design indicators and structure optimisation of switched reluctance machine for electric vehicles," *IET Electr. Power Appl.*, vol. 9, no. 4, pp. 319-331, Apr. 2015.
- [4] T. Miller, "Optimal design of switched reluctance motors," *IEEE Trans. Ind. Electron.*, vol. 49, no. 1, pp. 15-27, Feb. 2002.
- [5] S. Corovic, R. Benedetic, and D. Miljavec, "Modal analysis of different stator configurations to mitigate electromagnetically excited audible noise and vibrations of switched reluctance motors," *Applied Computational Electromagnetics Society Journal*, vol. 32, no. 12, pp. 1089-1097, Dec. 2017.
- [6] L. Chen and W. Hofmann, "Speed regulation

- technique of one bearingless 8/6 switched reluctance motor with simpler single winding structure,” *IEEE Trans. Ind. Electron.*, vol. 59, no. 6, pp. 2592-2600, June 2012.
- [7] X. Wang, Q. Li, S. Wang, and Q. Li, “Analytical calculation of air-gap magnetic field distribution and instantaneous characteristics of brushless dc motors,” *IEEE Trans. Energy Convers.*, vol. 18, no. 3, pp. 424-432, Sep. 2003.
- [8] Z. Zhu, D. Howe, and C. Chan, “Improved analytical model for predicting the magnetic field distribution in brushless permanent-magnet machines,” *IEEE Trans. Magn.*, vol. 38, no. 1, pp. 229-238, Jan. 2002.
- [9] Z. Zhu and D. Howe, “Instantaneous magnetic field distribution in brushless permanent magnet DC Motors, Part II: Armature-reaction field,” *IEEE Trans. Magn.*, vol. 29, no. 1, pp. 136-142, Jan. 1993.
- [10] K. Boughrara, T. Lubin, and R. Ibtouen, “General subdomain model for predicting magnetic field in internal and external rotor multiphase flux-switching machines topologies,” *IEEE Trans. Magn.*, vol. 49, no. 10, pp. 5310-5325, Oct. 2013.
- [11] S. Mendaci, H. Allag, and M. Mekideche, “Multi-objective optimal design of surface-mounted permanent magnet motor using NSGA-II,” *Applied Computational Electromagnetics Society Journal*, vol. 32, no. 5, pp. 519-526, May 2015.
- [12] Y. Zhang, S. Ho, H. Wong, and G. Xie, “Analytical prediction of armature-reaction field in disc-type permanent magnet generators,” *IEEE Trans. Energy Convers.*, vol. 14, no. 4, pp. 1385-1390, Dec. 1999.
- [13] R. Sprangers, J. Paulides, B. Gysen, and E. Lomonova, “Magnetic saturation in semi-analytical harmonic modeling for electric machine analysis,” *IEEE Trans. Magn.*, vol. 52, no. 2, Feb. 2016.
- [14] R. Sprangers, J. Paulides, K. Boynov, E. Lomonova, and J. Waarma, “Comparison of two anisotropic layer models applied to induction motors,” *IEEE Trans. Ind. Appl.*, vol. 50, no. 4, pp. 2533-2543, July-Aug. 2014.
- [15] Z. Djelloul-Khedda, K. Boughrara, F. Dubas, and R. Ibtouen, “Nonlinear analytical prediction of magnetic field and electromagnetic performances in switched reluctance machines,” *IEEE Trans. Magn.*, vol. 53, no. 7, July 2017.
- [16] H. Chen, D. Li, R. Qu, Z. Zhu, and J. Li, “An improved analytical model for inductance calculation of interior permanent magnet machines,” *IEEE Trans. Magn.*, vol. 50, no. 6, June 2014.
- [17] Q. Li, T. Fan, and X. Wen, “Armature-reaction magnetic field analysis for interior permanent magnet motor based on winding function theory,” *IEEE Trans. Magn.*, vol. 49, no. 3, pp. 1193-1201, Mar. 2013.
- [18] G. Dajaku and D. Gerling, “Stator slotting effect on the magnetic field distribution of salient pole synchronous permanent-magnet machines,” *IEEE Trans. Magn.*, vol. 46, no. 9, pp. 3676-3683, Sep. 2010.
- [19] B. Gaussens, E. Hoang, O. de la Barriere, J. Saint-Michel, P. Manfe, M. Lecrivain, and M. Gabsi, “Analytical armature reaction field prediction in field-excited flux-switching machines using an exact relative permeance function,” *IEEE Trans. Magn.*, vol. 49, no. 1, pp. 628-641, Jan. 2013.
- [20] M. Farshadnia, M. Cheema, R. Dutta, and J. Fletcher, “Analytical modeling of armature reaction air-gap flux density considering the non-homogeneously saturated rotor in a fractional-slot concentrated-wound IPM machine,” *IEEE Trans. Magn.*, vol. 53, no. 2, Feb. 2017.



Shenglong Hu a Ph.D. candidate majoring in Vehicle Engineering at Tongji University, Shanghai, China. He received the Bachelor degree of Vehicle Engineering in 2016 from Dalian University of Technology, Dalian, China. His main research interests are in the control of vibration and noise of motor.



Shuguang Zuo a Professor at Tongji University, Shanghai, China. He received the B.S. degree in Mechanical Design from Hunan Agricultural University, Changsha, China, in 1990, and the M.S. and Ph.D. degrees in Automotive Engineering from Jilin University, Changchun, China, in 1993 and 1996, respectively. From 1996 to 1998, he was a Postdoctoral Researcher with the Aviation and Aerospace Technology Postdoctoral Research Station, Nanjing Aeronautics and Astronautics University, Nanjing, China. He is now a Professor with the College of Automotive Engineering, Tongji University. His research interests include vehicle system dynamics and control, vehicle vibration and noise control, and vibration and noise of electrical machines.

Characterizations of Magnetic Field Distributions inside Buckling Pipelines

Yu Zhang, Yameng Xue, Xinjing Huang*, Jian Li, and Shili Chen

State Key Laboratory of Precision Measuring Technology and Instruments
Tianjin University, Tianjin 300072, China

zhangyu@tju.edu.cn, xueyameng@tju.edu.cn, *huangxinjing@tju.edu.cn, tjupipe@tju.edu.cn, slchen@tju.edu.cn

Abstract — High internal temperature and pressure often induces the subsea pipelines to buckle and then crack. This paper exposes the magnetic field distribution characterizations inside buckling pipelines in order to detect the buckling via magnetic measurements. J-A force-magnetic coupling model is used to obtain the permeability μ_r as a function of the stress σ . Finite element method with multiphysics coupling is deployed to calculate the magnetic fields inside the buckling pipe with different magnetizations, temperatures, and pressures by importing the μ_r - σ curve. The results demonstrate that complicated stress fields cause the magnetic fields inside the buckling pipe to have many noticeable characteristics that can be deployed to reliably and precisely identify the buckling. The signs and magnitudes of the buckling stress vary significantly in different cross-sections, and even reverse at the buckling starts, where the axial and radial components have two peaks and two peak-valley-peaks symmetrically distributed about the middle plane, respectively. The magnetic fields can reveal tiny buckling with stress but without visible deformation.

Index Terms — Buckling, detection, magnetic field, magnetomechanical effect, subsea pipeline.

I. INTRODUCTION

Subsea pipelines are the most efficient method for continuously transporting offshore crude oil over a long distance. In order to prevent the internal crude oil from condensation, subsea pipelines are usually operated under high temperature and high pressure, having the subsea pipelines suffer great axial and hoop stresses [1]. When the axial stress exceeds the critical value, pipeline buckling occurs, as shown in Fig. 1.

Pipeline buckling deformation is very harmful and dangerous. It can directly lead to pipeline ruptures and leakages via causing the tensile stress over the ultimate yield strength at the outer side of the buckling section. It can also speed up the pipeline aging, as the buckled section suffers serious stress corrosion resulting from the existence of micro-cracks at the stress concentration area. Therefore, it is very significant to periodically, frequently, and timely detect the subsea pipeline buckling.



Fig. 1. Examples of vertical and lateral bucklings of subsea pipelines [1].

Underwater robot with sonar or underwater cameras, such as ROV (Remotely Operated Vehicle) and AUV (Autonomous Underwater Vehicle) [2-4], can be used for pipe buckling detections. Only very large bucklings can be detected, and the cost is very high. The difficulty and cost of deploying ROV and AUV will sharply increase with the increase of depth. Inner PIGs (Pipeline Inspection Gauges) [5-6] with inertial navigation can be used to measure the pipeline trajectory and is capable to identify the buckling sections based on the local abrupt change of the trajectory. However, sophisticated navigation systems and GPS [7-8] are required for PIGs to accurately measure the trajectory alone over a long distance so as to sensitively detect the buckling.

The magnetic fields inside pipelines with various directions have been measured and successfully employed to calculate pipeline orientations and geographical coordinates [9-11]. Since buckling pipelines have distinct geometric shape with non-constant directions, the inside magnetic fields should have some distinctive features. In addition, the stress distributions of the buckling sections are totally different from that of the straight sections. Due to the magnetomechanical effect that magnetization of ferromagnetic materials immersed in ambient magnetic fields can be changed by the stress [12], the magnetization or the equivalent permeability of the pipe wall can be changed by the pipeline buckling deformation. The magnetic fields inside the buckling sections may present special distribution characteristics, and are potential to be utilized for buckling detections.

The objective of this paper is to expose the magnetic field distribution characterizations inside buckling pipelines in order to detect the buckling via magnetic

measurements. First, the J-A force-magnetic coupling model [13], [14] is used to describe the magnetomechanical effect of the pipe steel, and calculate the permeability of the pipe steel under different stress. Second, finite element method is used to model temperature-force-magnetic multiphysics couplings existing in the buckling sections with different orientations, temperatures, and pressures, and calculate the inside magnetic field distributions by importing the calculated permeability. Third, magnetic characterizations of the buckling sections are extracted, discussed, and summarized for pipeline buckling detections, especially for the tiny bucklings, based on the magnetomechanical effect.

II. MAGNETIC PERMEABILITY CALCULATION PRINCIPLE

When an external magnetic field is applied to the ferromagnetic material, the free energy A of the material can be expressed as [13], [14]:

$$A = \mu_0 H M + \frac{\mu_0}{2} \alpha M^2 + \frac{3}{2} \sigma \lambda + T S, \quad (1)$$

where, $\mu_0 = 4\pi \times 10^{-7}$ H/m is the permeability of the air, H is the external magnetic field, M is the magnetization of the material, $\alpha = 0.001$ [15] is the coupling parameter, σ is the stress, λ is the magnetostrictive coefficient, T is the temperature, and S is the entropy. The effective magnetic field is expressed as the derivative of the energy to the external magnetic field [15]:

$$H_e = \frac{1}{\mu_0} \frac{dA}{dM} = H + \alpha M + \frac{3\sigma}{2\mu_0} \frac{d\lambda}{dM}. \quad (2)$$

As the magnetostrictive coefficient is experimentally demonstrated to be the even function of the magnetization M in the J-A force-magnetic coupling model [16], $\gamma = (\gamma_1 + \gamma_1' \sigma) M^2 + (\gamma_2 + \gamma_2' \sigma) M^4$, we can get:

$$H_e = H + \alpha M + \frac{3\sigma}{\mu_0} \left[(\gamma_1 + \gamma_1' \sigma) M + 2(\gamma_2 + \gamma_2' \sigma) M^3 \right], \quad (3)$$

where $\gamma_1 = 7 \times 10^{-18} \text{ A}^{-2} \text{ m}^2$, $\gamma_1' = -1 \times 10^{-25} \text{ A}^{-2} \text{ m}^2 \text{ Pa}^{-1}$, $\gamma_2 = -3.3 \times 10^{-30} \text{ A}^{-4} \text{ m}^4$, and $\gamma_2' = -2.1 \times 10^{-38} \text{ A}^{-4} \text{ m}^4 \text{ Pa}^{-1}$ [15] are the magnetostrictive parameters.

The non-hysteresis magnetizations are equivalent under the two conditions of the external magnetic field with non-zero stress and the equivalent magnetic field with zero stress [15]:

$$M_{an}(H, \sigma) = M_{an}(H_e, 0) = M_s \left[\coth\left(\frac{H_e}{a}\right) - \frac{a}{H_e} \right], \quad (4)$$

where the Langevin function is used for expressing the non-hysteresis magnetization curve; $M_s = 1.7 \times 10^6$ A/m and $a = 1000$ A/m are the planning constant and the saturation magnetization of the material, respectively.

The following relationships exist among the magnetization M , the non-hysteresis magnetization M_{an} , and, the irreversible magnetization M_{irr} [15]:

$$\begin{cases} M = c(M_{an} - M_{irr}) + M_{irr} \\ dM_{irr} = \frac{1}{\xi} \frac{\sigma}{E} (M_{an} - M_{irr}) d\sigma \end{cases}, \quad (5)$$

where $E = 200$ GPa and $\xi = 24.5$ kPa are the Young's modulus and the energy correlation coefficient of the ferromagnetic material, respectively; $c = 0.1$ is the ratio of the initial magnetic susceptibility and the initial non-hysteresis susceptibility.

Then the expression of J-A force-magnetic coupling model can be deduced from (5):

$$\frac{dM}{d\sigma} = \frac{\sigma}{\xi E} (M_{an} - M) + c \frac{dM_{an}}{d\sigma}. \quad (6)$$

The relationship between the magnetization M and the stress σ can be obtained from the force-magnetic coupling model by substituting (2) into (4) and then substituting (4) into (6). According to the definition as shown in (7) [17], the relative permeability μ_r as a function of the stress σ can be numerically calculated, and the result is shown in Fig. 2. This curve will be then imported into the finite element simulation model in the form of look-up table with a stress step of 0.1 MPa:

$$\mu_r = \frac{M}{H} + 1. \quad (7)$$

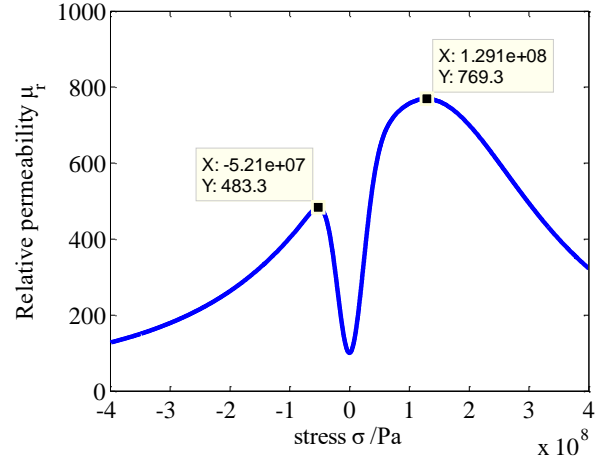


Fig. 2. Relative permeability vs. stress.

III. FINITE ELEMENT MODELING

This paper uses COMSOL software for simulation analyses as follows:

1) Establish the geometrical model, which consists of an air domain and a scaled down buckling pipe, the steel domain, as shown in Fig. 3. The length, width and height of the air domain are all 3m. The buckling pipe consists of two 700mm straight sections and a 1400mm long cosine buckling section. The buckling deflection is 200mm.

2) Set material properties. The relative permeability of the air domain is 1. For the steel domain, the thermal

conductivity is $44.5 \text{ Wm}^{-1}\text{K}^{-1}$; the thermal expansion coefficient is $1.23 \times 10^{-5} \text{ K}^{-1}$; the density is 7850 kg/m^3 ; the Young's modulus is 200 GPa ; the Poisson's ratio is 0.3 ; and the relative permeability at each point is obtained from Fig. 2.

3) Add physics field, including pressure load, thermal load, external magnetic field, and constraints, as shown in Fig. 3. Two ends of the pipeline are set as fixed constraints to accumulate thermal stress. Pressures are added onto the inner and outer surfaces to act as oil pressure and water pressure, respectively. When the heat transfer, from the crude oil to the pipe and then to the water, stabilizes, both the temperatures of the internal and external surfaces tend to be stable. Therefore, the temperatures of the pipe surfaces are configured as the stationary values in the simulation. The heat transfer model and the stationary temperatures of heated oil pipelines can be obtained from ref. [18]. The thermal stress is determined by the thermal expansion coefficient. The background magnetic field $H_b = (H_{xb}, H_{yb}, H_{zb})$ can be described as follows:

$$H_{xb} = H_b \cos I \sin D, H_{yb} = H_b \cos I \cos D, H_{zb} = -H_b \sin I, (8)$$

where I is the inclination angle between H_b and the x - y plane, and D is the angle between the component of H_b on the x - y plane and the y axis, as shown in the top right of Fig. 3. H_b is 40 A/m . The outer surfaces of the air domain are set as *External Magnetic Flux Density* boundary condition to force the total field to be equal to the background field on the external boundaries.

4) Carry on meshing, all the domains are meshed

into tetrahedral and triangular elements with an “Extra fine” mesh size configuration. Add steady state study to simulation before solving, then calculating, and post-processing the results.

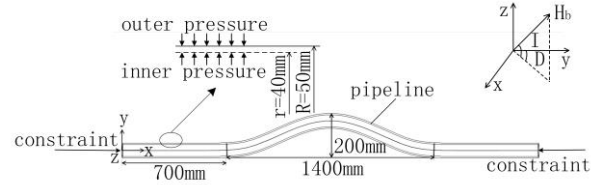


Fig. 3. Simulation model.

IV. RESULTS AND DISCUSSIONS

A. Magnetic field distributions inside the buckling pipe

One scenario with $I = 45^\circ$ and $D = 90^\circ$ is calculated for straight, deformed, and buckling pipes. Parametric sweeping will be carried out later. For the buckling pipe, a typical set of simulation parameters are chosen: the internal pressure is 10 MPa , the external pressure is 0.3 MPa , and the working temperature is 80°C . Calculation results are shown in Fig. 4. The magnetic fields inside the middle section are closer to that inside an actual infinitely long pipeline without magnetic sudden changes near the two ends. Therefore, the simulation results are trimmed off by 250 mm from the two ends with only the middle part preserved and presented in the following discussions.

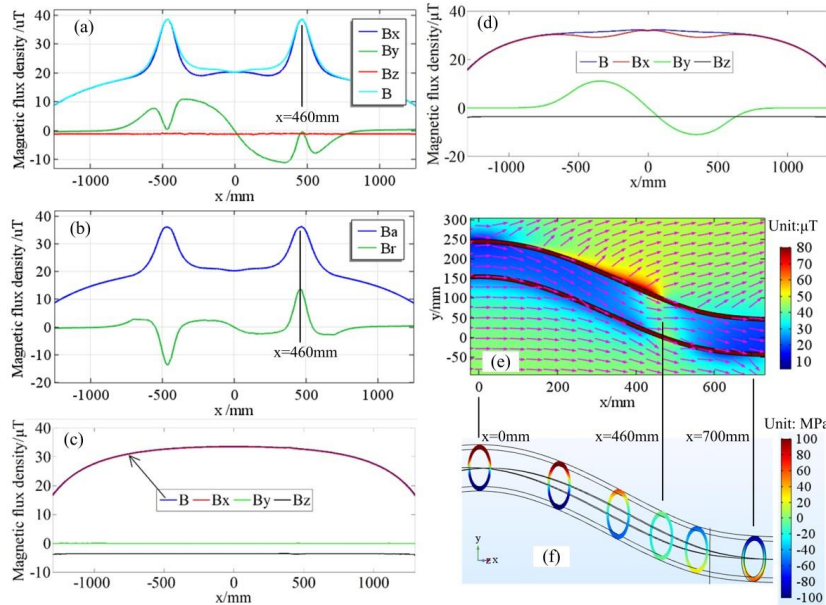


Fig. 4. Simulation results for a typical scenario with $I = 45^\circ$, $D = 90^\circ$, internal pressure of 10 MPa , and temperature of 80°C . Magnetic field distributions inside: (a) buckling, (c) straight, and (d) deformed pipes in the Cartesian coordinate system, and inside the (b) buckling pipe in the cylindrical coordinate system. (e) Intensity and normalized vector plot of the magnetic fields inside the buckling section. (f) Stress fields in different cross-sections.

The magnetic fields inside the three pipes are different. First, they have different distribution shapes. For the buckling pipe, as shown in Fig. 4 (a), B_x has two noticeable peaks at the position $x=\pm 460$ mm and B_y has four peaks and two valleys near the position $x=\pm 460$ mm symmetrically distributed about the $x=0$ plane, and each valley locates between two peaks. In the cylindrical coordinate system, as shown in Fig. 4 (b), the axial and radial magnetic components also have narrow and noticeable peaks. The magnetic fields inside the straight pipe are flat and smooth without any noticeable characteristics in terms of spatial distributions, as shown in Fig. 4 (c). For the deformed but not stressed pipe, as shown in Fig. 4 (d), B_x has two small valleys with one small peak between them, and B_y has two blunt peaks symmetrically distributed about the $x=0$ plane without valleys.

Second, the magnetic fields inside the three pipes have different intensities. The flat part of B curve is smaller than that inside the deformed but not stressed pipe and the straight pipe. In terms of the components, the amplitude of B_z reduces to $1\mu\text{T}$ from the original $4\mu\text{T}$ compared with the straight and deformed pipes. This indicates that when the pipe is buckling and stressed, the magnetic shielding of the pipe is enhanced as the equivalent permeability overall becomes larger due to the magnetomechanical effect.

It is pretty interesting that the B and B_x peaks and B_y valleys occur at $x=\pm 460$ mm, where the bend starts. The magnetic intensity and normalized vector plot, as shown in Fig. 4 (e), demonstrates that the magnetic intensity is larger near the buckling start than that at other areas inside the buckling pipe. The magnetic fields near the buckling start are parallel to the background magnetic fields or x axis, while the magnetic fields at other sections are parallel to the pipe axis. This is due to the complicated and special stress field distributions on different cross-sections, as shown in Fig. 4 (f). The polarity of the stress field is reversed at the bend start ($x=460$ mm), where the stress is almost zero. When $x>460$ mm, the stress is compressional and tensile in the upper and lower sides of the pipe, respectively; while when $x<460$ mm, the stress converts into being tensile and compressional in the upper and lower sides. Therefore, under the action of the magnetomechanical effect, the extreme existence of the stress makes B and B_x reach their maximum values.

Figure 5 shows the magnetic field distributions on different measurement lines with different distances from the pipe axis when the buckling pipe is loaded with high pressure and temperature. These measurement lines are parallel to the pipe axis. Figure 5 (a) shows the magnetic field distributions on different lines of $z>0$ in the x - z plane inside the pipeline, and Fig. 5 (b) shows the magnetic field distributions on different lines in the x - y plane inside the pipeline. Lift-off values have little

effects on the magnetic field distributions, in terms of both the distribution shape and amplitude. Therefore, in the following parts of this paper, we will use the magnetic fields on the central axis to analyze and discuss the magnetic field distribution characteristics inside buckling pipes under different parametric conditions.

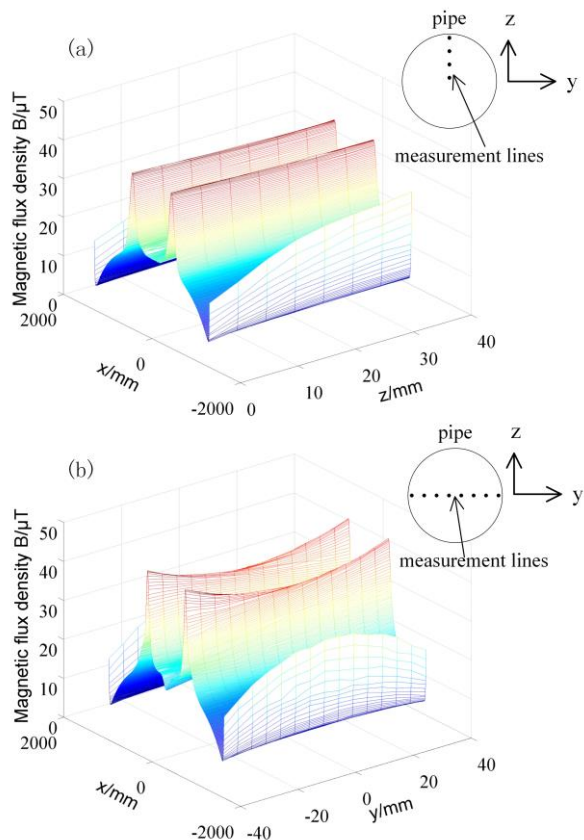


Fig. 5. Magnetic field distributions on different measuring lines parallel to the axis in the x - z (a) and x - y (b) planes.

B. Effects of ambient field direction

Parametric sweepings are performed for I and D with a range of $0\sim 90^\circ$ and a step of 10° in order to expose how ambient field direction affects the magnetic fields inside a buckling pipe. When $I = 0^\circ$ and $D = 0^\circ$, the ambient field is perpendicular to the pipe; when $I = 0^\circ$ and $D = 90^\circ$, the ambient field is parallel to the pipe. Due to there are too many combinations of I and D , here we only present the results of the scenarios with $I = 0^\circ$ and $D = 0\sim 90^\circ$, as shown in Fig. 6. The internal pressure is 10 MPa. The pipe temperature is 80°C .

B_x is much larger than B_y and B_z , so B_x and the norm B have similar distribution shapes, as shown in Figs. 6 (a) and (c), and both of them have two peaks at the two start points of the buckling section. B_y has four peaks and two valleys symmetrically distributed about the $x=0$ plane, as shown in Fig. 6 (b), and each valley locates between two

peaks. B_x and B_y are even and odd symmetrical around the $x=0$ plane, respectively. B_x and B_y for different D s have very similar distribution shapes, respectively. Their means have almost the same trend as their amplitudes, as shown in Fig. 6 (d). The amplitudes and means of B_x and B_y go up with the increase of D , demonstrating that smaller angle between the pipeline and the ambient field can cause more noticeable magnetic buckling characteristics.

C. Effects of temperature

Parametric sweeping is performed for the temperature 20 ~ 130°C. The background magnetic field

is with $I = 0^\circ$ and $D = 45^\circ$. The internal pressure is 10 MPa. The results are summarized and shown in Fig. 7. B_x and the norm B have similar distribution shapes, and both of them have two peaks at the two start points of the buckling section. When the temperature is lower than 50°C, B_y has two peaks symmetrically distributed about the $x=0$ plane; When the temperature is higher than 50°C, B_y has four peaks and two valleys symmetrically distributed about the $x=0$ plane, and each valley locates between two peaks. As the temperature exceeds 50°C and goes higher, characterizations of the pipe buckling by B_x and B_y become less and more noticeable, respectively.

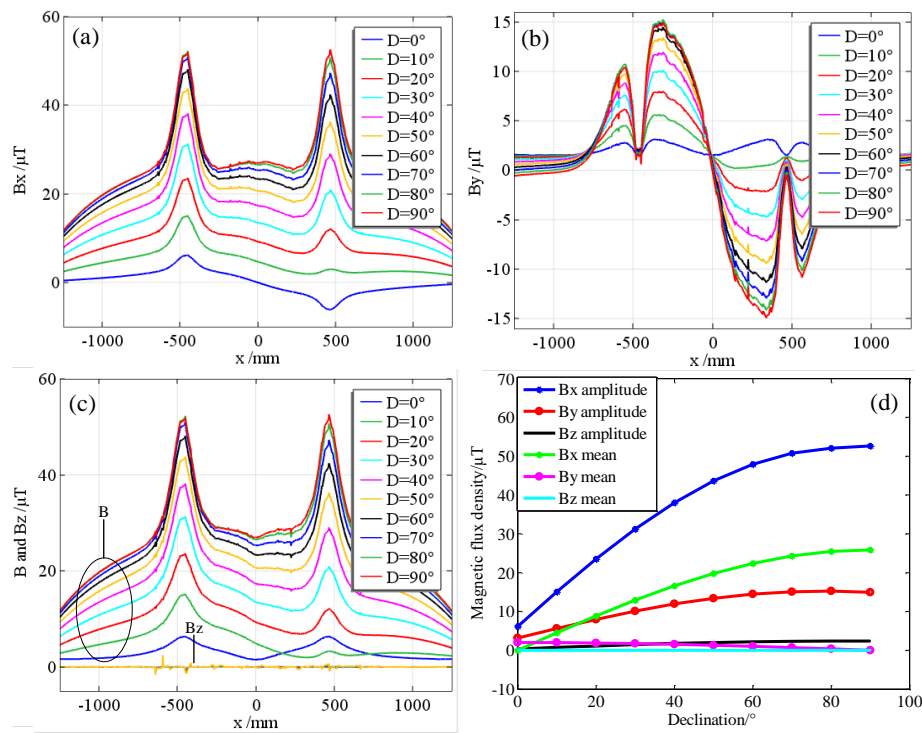


Fig. 6. Magnetic fields inside the buckling pipe under different directions of background magnetic fields: (a) B_x , (b) B_y , (c) B and B_z , and (d) amplitudes and means of the distributions of each component.

As shown in Fig. 7 (d), all the amplitudes and means of the magnetic components vary very slightly as the temperature increases except for B_x 's amplitude. This exception can be explained as follows. The internal pressure can cause hoop stress in the pipe wall and hence relieves the axial compressional stress resulting from the thermal expansion. At the two starts of the buckling section, the axial thermal stress is not easy to accumulate, so the axial and hoop expansions are comparable with each other. However, as the temperature is going higher and higher, the enhancing effects of the thermal expansion on the axial stress at first are smaller than and then exceed the weakening effects of the internal pressure. Therefore, the axial stress and the magnetic shielding at the buckling starts go down first and up then,

as the equivalent permeability goes down first and up then. The B_x component of the magnetic fields here therefore non-monotonically varies with the increase of D .

D. Effects of pressure

Parametric sweeping is performed for the internal pressure 0~20MPa with $I = 0^\circ$ and $D = 45^\circ$. The pipe temperature is 80°C. The results are summarized and shown in Fig. 8. B_x has two peaks at the two start points of the buckling section. B_y has four peaks and two valleys symmetrically distributed about the $x=0$ plane, and each valley locates between two peaks. B_x and B_y are even and odd symmetrical around the $x=0$ plane, respectively. The pressure only changes the overall magnetic intensity inside the buckling pipe, but does not change the magnetic

distribution modes along the axial line. That is because the stress in the pipe wall induced by the internal pressure is uniform and the permeability resulting from

the magnetomechanical effect is smoothly and evenly distributed.

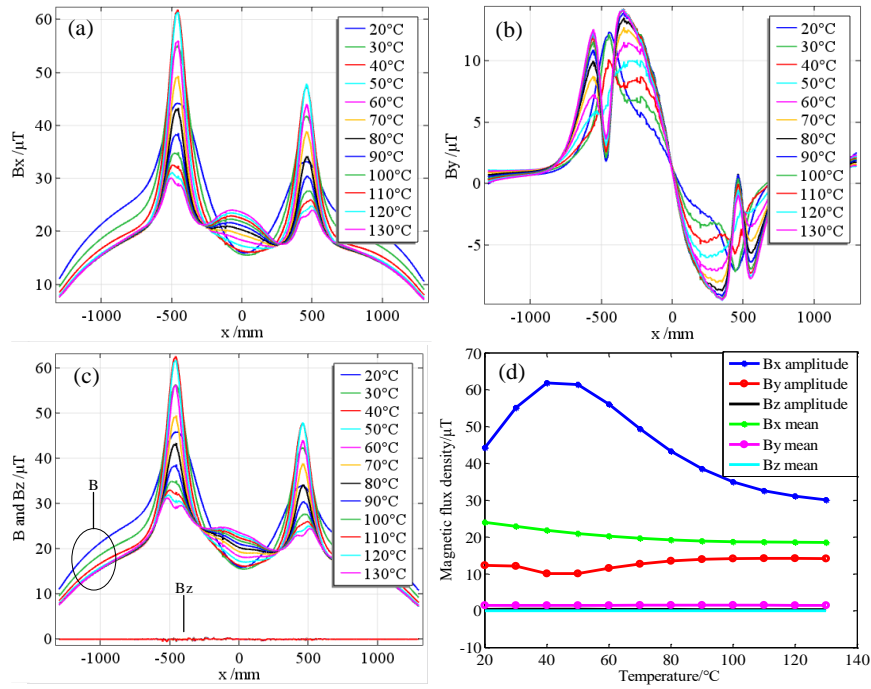


Fig. 7. Magnetic fields inside the buckling pipe with different temperatures: (a) B_x , (b) B_y , (c) B and B_z , and (d) amplitudes and means of the distributions of each component.

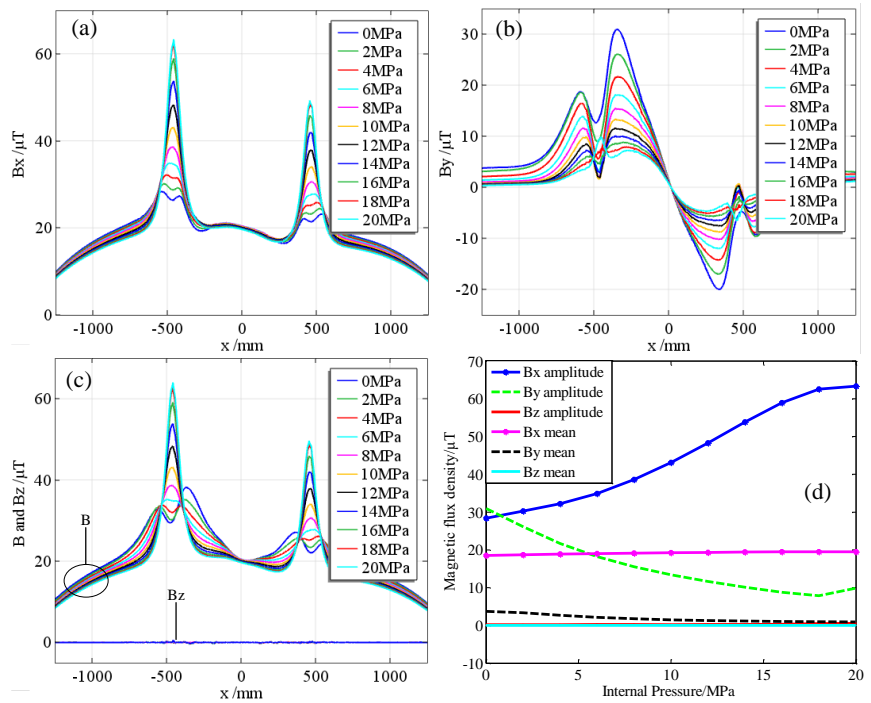


Fig. 8. Magnetic fields inside the buckling pipe with different internal pressures: (a) B_x , (b) B_y , (c) B and B_z , and (d) amplitudes and means of the distributions of each component.

Within this parameter configuration range, the weakening effect on the axial stress of the hoop expansion due to the internal pressure is always smaller than the enhancing effect of the thermal expansion. According to the stress calculation theory for thin-walled cylinder [19], the hoop strain monotonically increases with the increase of the internal pressure. Due to the Poisson effect, the axial stress is monotonically released. Therefore, the amplitude and mean of B_x and B_y components basically monotonously go up and down, respectively, with the increase of the internal pressure, as shown in Fig. 8 (d). In other words, if internal pressure is higher, the buckling characterization by B_x is better but worse by B_y .

E. Tiny buckling detection

In practice, a large pipeline buckling always starts from a tiny one that are very difficult to distinguish from their shape and appearance. It is preferable and very important to timely detect and predict the tiny buckling for early maintenance. Figure 9 shows the magnetic field distributions inside pipes under the same ambient field and pressure load, without and with considering the force magnetic effect, for the buckling deflections of 0 mm, 10 mm, 20 mm, and 30 mm.

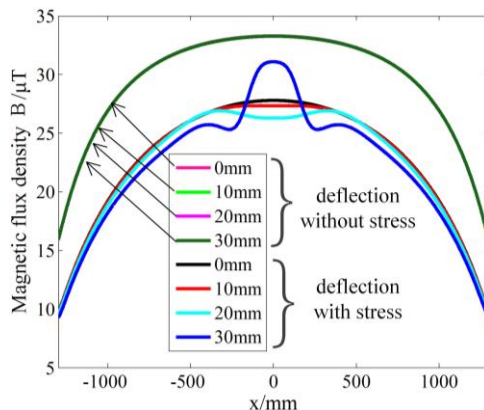


Fig. 9. Magnetic field distributions inside the tiny buckling pipes without and with stress considered.

When the magnetomechanical effect is not taken into account, all of the magnetic field distributions inside the pipes with deflections of 10mm, 20 mm, and 30 mm are the same to that of the straight pipe whose deflection is 0 mm. The tiny deformation without stress cannot be identified from the magnetic fields. When the permeability changes caused by the buckling stress are considered, the magnetic field distributions have noticeably local fluctuations in the middle of the buckling section, although the magnetic field values are a little smaller because the magnetic shielding becomes larger. Therefore, the results in Fig. 9 demonstrate that it is feasible to use the magnetic fields inside the pipelines to

detect the tiny buckling thanks to the magnetomechanical effect. This is very helpful for early diagnosis and prevention of pipeline bucklings.

V. CONCLUSIONS

(I) Magnetic fields inside the buckling pipe have many significant distribution characteristics that can be deployed to reliably and precisely identify the pipe buckling. B_x and B have similar even symmetric distribution shapes, and both have two peaks at the two start points of the buckling section. B_y has four peaks and two valleys odd symmetrically distributed about the middle vertical plane, and each valley locates between two peaks.

(II) These magnetic characteristics can be attributed to the complicated stress of the buckling section due to magnetomechanical effect. Internal pressure can cause hoop stress and hence relieve the axial compressional stress because of thermal expansion. The stress signs and magnitudes vary significantly in different cross-sections of the buckling pipeline, and reverse at the bend start. Higher internal pressures and temperatures seldom change the magnetic distribution shapes inside the buckling pipe, but indeed enhances the peak magnitudes. In addition, the results of each effect on magnetic behaviors/properties in the buckling pipe can be used as prior knowledges more reliably and precisely the pipe buckling by using these magnetic characteristics.

(III) It is feasible to use the magnetic fields inside the buckling sections to detect the tiny buckling with stress variances but without visible deformations thanks to the magnetomechanical effect. This is very helpful for early diagnosis and prevention of the pipeline bucklings.

ACKNOWLEDGMENT

This work was supported by National Natural Science Foundation of China (Nos. 51604192, 61773283, and 61473205).

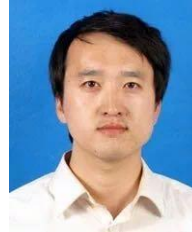
REFERENCES

- [1] Y. Liu, "Study on Transverse Thermal Buckling Mechanism and Control Measures of High Temperature/High Pressure Subsea Pipeline," *Ph.D. Thesis*, Dalian University of Technology, pp. 4-10, 2010.
- [2] N. F. Braathen and A. J. Sandford, *Pipeline Inspection by ROV*. Submersible Technology, Springer Netherlands, vol. 36, pp. 313-318, 1986.
- [3] W. Zeng, Y. Xu, L. Wan, and T. Zhang, "Optical vision pipeline inspection and tracking system for autonomous underwater vehicle," *Journal of Shanghai Jiao Tong University*, vol. 46, no. 2, pp. 178-183, 2012.
- [4] X. Huang, Y. Li, and S. Jin, "A control system based on data exchange using ethernet and CANBUS for deep water AUV," *IEEE: 9th Asian*

- Control Conference*, pp. 1-5, 2013.
- [5] J. Quarini and S. Shire, "A review of fluid-driven pipeline pigs and their applications," *Proceedings of the Institution of Mechanical Engineers, Part E: Journal of Process Mechanical Engineering*, vol. 221, no. 1, pp. 1-10, 2007.
- [6] H. S. Han, J. J. Yu, G. P. Chan, et al., "Development of inspection gauge system for gas pipeline," *Ksme International Journal*, vol. 18, no. 3, pp. 370-378, 2004.
- [7] M. S. Chowdhury and M. F. Abdelhafez, "Pipeline inspection gauge position estimation using inertial measurement unit, odometer, and a set of reference stations," *Sensors and Actuators B-Chemical*, vol. 2, no. 3, pp. 234-243, 2016.
- [8] M. Durali, A. Nabi, and A. Fazeli, "Design and simulation of an off-line internal navigation system for pipeline inspection applications," *ASME 2007 International Mechanical Engineering Congress and Exposition*, vol. 9, pp. 521-526, 2007.
- [9] W. Zhao, X. Huang, S. Chen, et al., "A detection system for pipeline direction based on shielded geomagnetic field," *International Journal of Pressure Vessels & Piping*, vol. 113, no. 1, pp. 10-14, 2014.
- [10] X. Huang, S. Chen, S. Guo, et al., "A 3D localization approach for subsea pipelines using a spherical detector," *IEEE Sensors Journal*, vol. 17, no. 6, pp. 1828-1836, 2017.
- [11] X. Huang, G. Chen, Y. Zhang, et al., "Inversion of magnetic fields inside pipelines: Modeling, validations, and applications," *Structural Health Monitoring-An International Journal*, vol. 17, no. 1, pp. 80-90, 2018.
- [12] J. Li, M. Xu, J. Leng, and M. Xu, "Metal magnetic memory effect caused by circle tensile-compressive stress," *Insight*, vol. 9, no. 25, pp. 142-145, 2011.
- [13] H. E. Stanley and V. K. Wong, "Introducing to phase transition and critical phenomena," *American Journal of Physics*, vol. 40, no. 6, pp. 927-928, 1972.
- [14] D. A. Kaminski, D. C. Jiles, S. B. Biner, M. J. Sablik, "Angular dependence of the magnetic properties of polycrystalline iron under the action of uniaxial stress," *Journal of Magnetism and Magnetic Materials*, vol. 291, pp. 382-384, 1992.
- [15] D. C. Jiles, "Theory of the magnetomechanical effect," *Journal of Physics D Applied Physics*, vol. 28, no. 8, pp. 1537-1546, 1995.
- [16] D. C. Jiles and L. Li, "A new approach to modeling the magnetomechanical effect," *Journal of Applied Physics*, vol. 95, no. 11, pp. 7058-7060, 2004.
- [17] G. Yicheng, *Ferromagnetic*. Peking University Press, pp. 8-11, 2014.
- [18] L. Peng, "Numerical analysis of buckling of high temperature and high pressure subsea pipelines

under coupling of pipe and soil," *Southwest Petroleum University*, pp. 57-59, 2014.

- [19] S. Zhifeng, "Gas pipeline special pipe section stress analysis and safety study," *China University of Petroleum (Hua Dong)*, pp. 18-19, 2009.



Zhang Yu received his B.E. and Ph.D. degrees in 2004 and 2009 from Tianjin University (TJU). He is now a Lecturer at TJU. His research interests cover detection technology and equipment.



Xue Yameng received her B.S. degree in 2016 in Taiyuan University of Technology. Now she is working toward her Master degree at TJU. Her research topics are pipeline localization.



Huang Xinjing received his B.S. and Ph.D. degrees in 2010 and 2016 at TJU. He is an Assistant Professor at TJU. His interests are magnetic analyses for pipeline damage detections. He is the corresponding author of this paper.



Li Jian received his B.E., M.E., and Ph.D. degrees in 1994, 1997 and 2000 from TJU. He is now a Professor at TJU. His research interests include pipeline leak detection and pipeline safety warning.



Chen Shili received his B.S. and Ph.D. degrees from TJU in 1997 and 2003. He is an Associate Professor at TJU. His research interests are novel online in-pipe detector.

A Novel Approach for Intruder Localization Based on Leaky Coaxial Cable Sensor with IQ Demodulation and Synchronous Subtraction

Qiao Guan^{1,2}, Hongmin Lu^{1,2}, Kunbo Wang², and Chongchong Chen¹

¹ School of Electronic Engineering

Xidian University, Xi'an, Shaanxi 710071, China

guanqiao@stu.xidian.edu.cn, hmlu@mail.xidian.edu.cn, ccchen@stu.xidian.edu.cn

² Key Lab of High-Speed Circuit Design and EMC

Xidian University, Xi'an, Shaanxi 710071, China

guanqiao@stu.xidian.edu.cn, hmlu@mail.xidian.edu.cn, 2849802702@qq.com

Abstract — Some aspects of the intruder detection system (IDS) based on the leaky coaxial cable (LCX) sensor are still unknown due to its complex propagation characteristics. In order to study the field disturbance mechanism of human intruder and to reduce the phase error caused by the initial state of the detection signal, a novel method of improving the localization accuracy is proposed. At the frequencies of 40MHz, 100MHz and 200MHz, the IDS based on the LCX sensor is proposed by analyzing the scattering characteristics of human intruder and using IQ demodulation method. According to the characteristics of the IDS, the electric field distribution is obtained by irradiating the human intruder from three typical radiation directions, which are front, side and low-side direction in the mentioned frequency range. Combined with the method of pulse accumulation and synchronous subtraction, the intruder localization can be easily realized by using pulse delay positioning method. The results demonstrate the improvement in localization accuracy and the decrement in false positive rate, and the positioning accuracy is less than 3 meter.

Index Terms — Intruder detection, LCX sensor, localization, phase error, synchronous subtraction.

I. INTRODUCTION

Leaky coaxial cable (LCX) has been intensively applied to various application scenarios for its receiving and emitting functions, such as the tunnel, the railway, the indoor communication and the positioning localization system [1~5]. The perimeter intrusion detection system (IDS) based on the LCX sensor has been widely studied because of its better concealment, flexible installation and all-weather conditions work [6~7]. Therefore, compared with other location systems, the characteristics and advantages of the IDS lie in its application scenario. The ordinary localization systems usually detect the target in the area of directional beam of the systems' antennas.

However, the IDS based on LCX sensor has some completely different characteristics. As the Fig. 1 shown, the apertures on the LCX's outer conductor are similar to the array antennas [8~9], which builds a wide-belt flexible detection area instead of the area of directional beam. The closer the aperture is to the targets, the more obvious reflection effect the aperture provides. The IDS can avoid the influence of the environment and the terrain. Because most of the power is transmitted in the LCX sensor, the IDS can reach a far distance to achieve the security guarding with the small attenuation in a specific area.

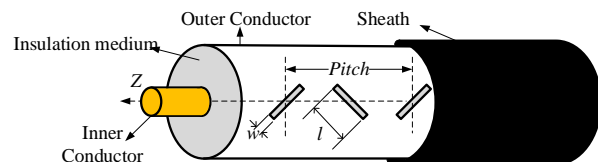
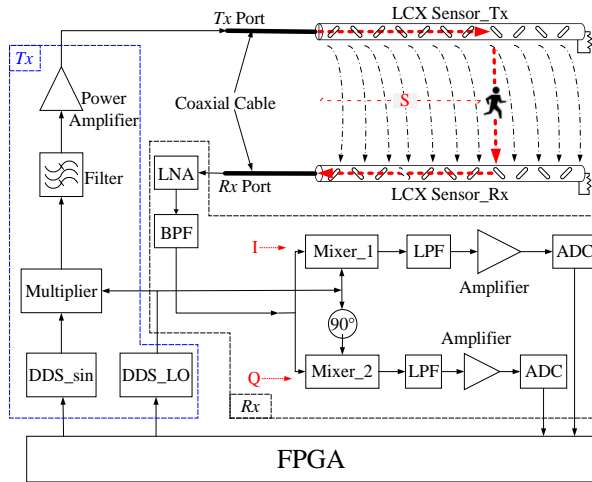


Fig. 1. Configuration of the leaky coaxial cable.

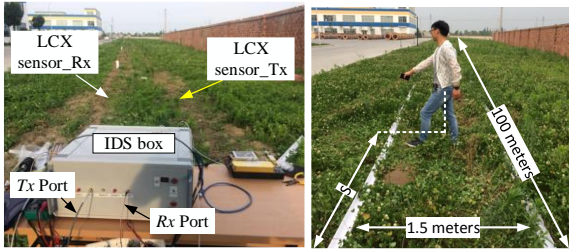
Although some IDS based on LCX sensor have been applied, there has few researches about the electromagnetic disturbance mechanism of the human intruders. Therefore, the disturbance of human body in electric field is studied, and the experiments in time-domain and frequency-domain echo signals are carried out in the radiation mode and coupling mode. Moreover, the experiment of the signal receive unit of IDS is conducted by means of the IQ-demodulation method and synchronous subtraction. On the basis of the amplitude stability of the V_{IQ} , the effects of the intruder positioning are evaluated at 40 MHz, 100 MHz and 200 MHz by referring to the time delay separately, which significantly reduces the phase error. In addition, the method of improving the positioning accuracy is further studied. Finally, the relation between echo signal quality and frequency is discussed.

II. INTRUDER DETECTION SYSTEM AND LOCALIZATION METHOD

The configuration of the IDS based on LCX sensor is shown in Fig. 2 (a), which is mainly composed of the signal generator unit T_x , the signal receives unit R_x , LCX sensor and field programmable gate array (FPGA) processor. The LCX sensor consists of the two same LCXs [10] in IDS. The LCX sensor_Tx is used to transmit and radiate the detection signals, and LCX sensor_Rx is used to receive the echo signals. Those two LCXs form the target monitoring area of the IDS. When there is a human intrusion in monitoring area, the original environmental medium become discontinuous, and the discontinuity of the medium leads to the amplitude attenuation and the path change of the signal transmission, which results in the significant fluctuations in the field distribution at the position of the intruder.



(a) Configuration of IDS



(b) IDS and human intruder

Fig. 2. Intruder detection system based on LCX sensor.

Figure 2 (b) is the test photo of the IDS and intruder, where the signal generator T_x and signal receive unit R_x are assembled in the IDS box. In the signal transmit unit, the method of direct digital synthesizer (DDS) is used to generate the signal. Compared with the traditional frequency synthesizer, DDS has the advantages of low cost, low power consumption, high resolution and fast switching time, which is widely used in the field of telecommunication and electronic equipment [11]. In

Fig. 2 (a), the signal for detecting intruder is a pulse signal with the carrier frequency f_0 . The signal is produced by the mixing in multiplier of the signal of DDS_SIN and the signal of DDS_LO, where DDS_SIN is a sine wave generator and DDS_LO is a square-wave pulse generator. The detection signal is transmitted in LCX sensor_Tx after passing through a filter and a power amplifier (PA). When an intruder enters the detection area, part of the signal is reflected and received by LCX sensor_Rx. The signal receive unit can detect the intruder by monitoring the fluctuation of this echo signals. The position information of the intrusion can be obtained through the propagation delay time τ_R . The distance S is calculated by [12]:

$$S = \frac{v \cdot \tau_R}{2}, \quad (1)$$

where v is the velocity of the signal transmitting in the LCX. When there is no intruder, this echo signal received by LCX sensor_Rx is called the system response. In general, the system response is unchanged, and it is only related to factors of the laying environment and the detection signal. The signal received by LCX sensor_Rx is called the intruder response when an intruder enters or walks near the warning area. In fact, the LCX sensor_Rx receives two kinds of signals, one is the system response, and the other is the reflection signal produced by the intruder in the detection area. By extracting the change of the echo signal, the location of the intruder can be determined.

As shown in Fig. 2 (a), the output of the Multiplier is defined as the detection signal:

$$S_T(t) = A_T \cdot \text{rect}\left(\frac{t - t_R/2}{t_R/2}\right) \cos(2\pi f_0 t + \varphi_0), \quad (2)$$

where A_T is the amplitude of the detection signal, t_R is the length of the pulse, f_0 is the carrier frequency. φ_0 presents the initial phase, which is a random value when the IDS starts to work. The detection signal transmits in the LCX sensor_Tx and radiates out through the apertures on the outer conductor of the LCX. The detection signal transmits back to signal receive unit when this signal meets the human intruder. The echo signal is given by:

$$S_R(t) = A_R \cdot \text{rect}\left(\frac{t - t_R/2}{t_R/2}\right) \cos(2\pi f_0 t + \varphi_0 + k_c v \cdot \tau_R), \quad (3)$$

where A_R is the amplitude of the echo signal, k_c is the number of the waves in the LCX. Then the echo signal is divided into I-signal and Q-signal for IQ-demodulation after passing through a low-noise amplifier (LNA) and a band-pass filter (BPF). Meanwhile, the high-order mode interference is reduced.

In signal analysis, the signal vector can be decomposed into two components of the same frequency and the amplitude but the phase difference of 90 degrees [13]. Amplitude, frequency and phase can be described completely by the description of the vector, it is really useful for IQ demodulation in this paper. The local

oscillator (LO) signals are $LO_{\sin} = A_{LO} \sin(2\pi ft + \phi_{LO})$ and $LO_{\cos} = A_{LO} \cos(2\pi ft + \phi_{LO})$ respectively, which are a pair of orthogonal signal vectors. After passing through Mixer_1 and Mixer_2, the signal demodulation was obtained by:

$$V_I(t) = \frac{A_R A_{LO}}{2} \cdot \text{rect}\left(\frac{t-t_R/2}{t_R/2}\right) \sin(\phi_{LO} - \phi_0 - 2k_c \cdot S), (4)$$

$$V_Q(t) = \frac{A_R A_{LO}}{2} \cdot \text{rect}\left(\frac{t-t_R/2}{t_R/2}\right) \cos(\phi_{LO} - \phi_0 - 2k_c \cdot S), (5)$$

where A_{LO} is the amplitude of LO signal. It is possible that $V_I(t)$ or $V_Q(t)$ can equal zero because of the appropriate phase $\phi_{LO} - \phi_0 - 2k_c \cdot S$ in (4) ~ (5). The value of the phase will directly affect the amplitude of the demodulated echo signal $V_I(t)$ and $V_Q(t)$. If there is a phase that makes the amplitude of zero or be lower than the alarm threshold value of IDS, then the intruder will be missed. So there is a blind area for the location of the intrusion, and the blind area is uncertain because the initial phase of the detection signal is uncertain when IDS works. The uncertainty of the phase will lead to the uncertainty of the position of the blind area. It will greatly reduce the accuracy of the location detection of the IDS if we consider $V_I(t)$ or $V_Q(t)$ as the only echo signal. In this case, when an intruder enters the detection area at some R that makes the appropriate phase, the intruder could not be found. Fortunately, $V_I(t)$ and $V_Q(t)$ are not both zero and orthogonal to each other. Therefore, the sum amplitude of the two signals vector can ensure a good result, which can be obtained by:

$$V_{IQ}(t) = \sqrt{(V_I(t))^2 + (V_Q(t))^2} = \frac{A_R A_{LO}}{2} \cdot \text{rect}\left(\frac{t-t_R/2}{t_R/2}\right). (6)$$

In (6), the amplitude of the echo signal $V_{IQ}(t)$ is a constant, it helps to reduce the alarm rate and provide a standard threshold value, which guarantees the accurate detection rate.

The distance S is only related to the delay time t_R of the echo signal in (1), and t_R can be calculated by the difference between system response $V_{IQ\text{-system}}(t)$ and intruder response $V_{IQ\text{-intruder}}(t)$. This processing method is called synchronous subtraction.

III. EXPERIMENTAL RESULTS

A. Analysis on the mechanism of the field disturbance caused by the human intruder

The parameters of the LCX sensor are defined as follows: the dielectric constant of the insulation medium is 1.247, dielectric loss angle tangent is 1.7×10^{-5} and the pitch is 1 meter. According to the classification method of LCX's working modes theory [12], the LCX is in the radiation mode when the frequency is higher than 142 MHz, or the LCX is in the coupling mode when the frequency is lower than 142 MHz. Figure 3 shows the human intruder model and the propagation characteristics

of electric field (E-field) when the frequency is at 40 MHz, 100 MHz and 200 MHz separately. The human intruder is irradiated from 3 typical directions by a source of plane wave, respectively. The normal vector of the side plane is $\vec{a}_s = \vec{a}_z$. Similarly, the normal vector of the front plane is $\vec{a}_f = -\vec{a}_y$, and the normal vector of the low-side plane is $\vec{a}_{ls} = \vec{a}_x + \vec{a}_z$.

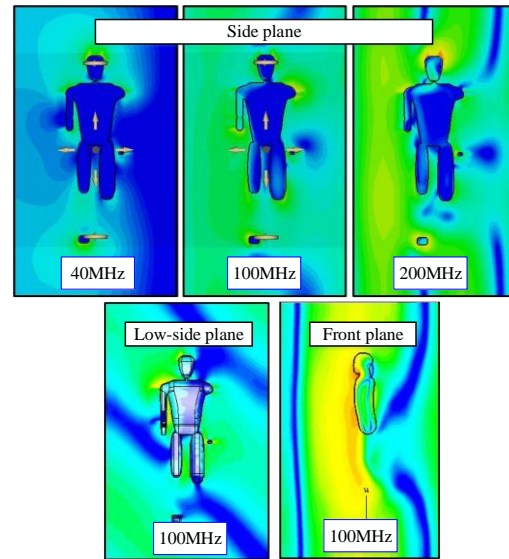


Fig. 3. Human intruder model and E-field distribution.

The simulation results show that the discontinuity of the electromagnetic wave is obvious in Fig. 3, and the scattering effect is more serious, especially in the complex part of the human intruder, such as the head and extremities of the arms and limbs. Besides, the E-field will quickly decay when the electromagnetic wave enters the trunk of the human intruder. The results indicate human intruder can disturb the electromagnetic field in mentioned frequency range. Therefore, the IDS based on LCX sensor proves to be a feasible method in practical.

The IDS based on LCX sensor is shown in Fig. 2 (b). The LCX sensor_Tx and LCX sensor_Rx are placed parallel on the ground. The detection range of the LCX sensor is 100 meters long, and the spacing between the two LCX is set to 1.5 meters. The Tx produces a single frequency pulse as the detection signal of the pulse period $T=2$ ms and the pulse width $\tau = 200$ ns. After amplified by a power amplify (PA), the detection signal is send into the LCX sensor_Tx. Signal receive unit is connected to the LCX sensor_Rx. Figure 4 shows the inside components of the IDS box.

The influence of the human intruder on the electromagnetic field established by LCX sensor can be analyzed by the changes of the echo signals in the time domain and the frequency domain. Figure 5 (a) shows

the comparison of the echo signal with intruder or without intruder in frequency spectrum, and it can be seen that their waveforms are basically the same. Moreover, the intensity of the echo signal with an intruder is slightly greater than that of no intruder. So the appearance of human affects the echo signal and reflection is obvious in the frequency range, and it is reasonable that human intruder is sensitive to the wavelength. Moreover, the normalization waveform records at different intrusion positions are shown in Figs. 5 (b) ~ (c) in the time domain.

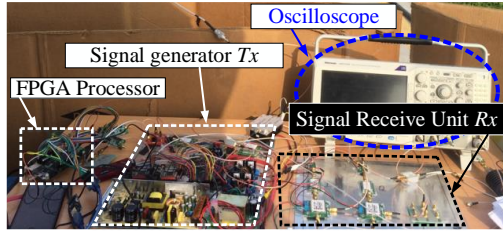


Fig. 4. The components in the IDS box.

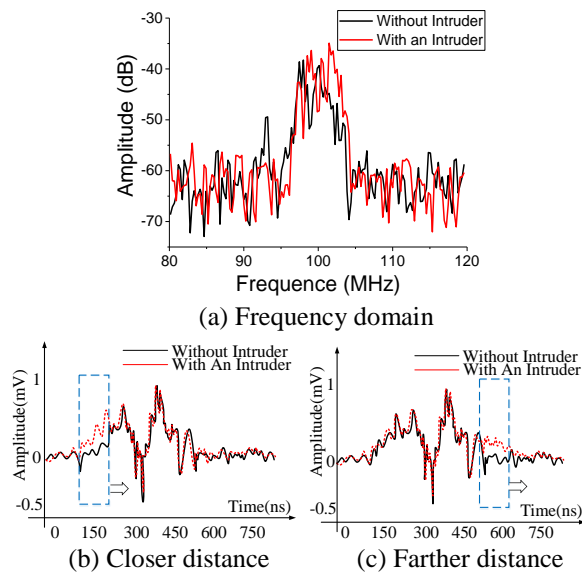


Fig. 5. Frequency domain and time domain with intruder or without intruder (detail of detection signal: the pulse period $T=2$ ms, the pulse width $t_R = 200$ ns, the carrier frequency $f_0=100$ MHz)

Figures 5 (b) ~ 5 (c) are related to three positions from near and far, the blue dashed box presents the difference of the system response and the intruder response. When an intruder moves along the LCX sensor, it can be observed that the different waveforms are in the time domain. It is obvious that the blue dashed box moves to right when the intruder is walking to the end of the LCX sensor. In other words, it proves that

intrusion position is also corresponding to the delay time of the intruder response.

In fact, as shown in Figs. 5 (b) ~ 5 (c), the waveforms of the system response or the intruder response in time domain is not an ideal smooth waveform, on the contrary, it composes of two peaks and one valley, the reason for such waveform is that the distribution of signal intensity is not uniform along the LCX sensor, where there are two areas with strong reflection and one area with relatively weak reflection. The number and amplitude of the peak are related to the environment around the LCX sensor, the type of LCX, or the climate conditions. Therefore, the system response is not always the same, and it is easy to be affected by the factors such as water content of soil, climate and vegetation status. In order to ensure the real and accurate results, it is very necessary to calibrate reference systems response regularly.

B. Experimental and calculated results of localization

As shown in Fig. 2 (b), the length of the LCX is 100 meters long, and the echo signal passes through the band-pass filter (BPF) after being amplified by the low-noise amplifier (LNA). The demodulated I-signal and Q-signal are obtained after the echo signal is mixed with LO_{sin} and LO_{cos} , respectively. The FPGA processor receives I-signal and Q-signal by the analog-digital converter (ADC).

The pulse accumulation and synchronous subtraction are very important signal processing in this paper, and those two methods can eliminate the interference of the environmental changes, which is a very flexible signal processing in IDS. The pulse accumulation is used to reduce the noise by adding the finite echo signals repeatedly, and the synchronous subtraction is used to locate the intruder accurately by calculating the difference between system response and intruder response.

The difference of the system response and the intruder response is shown in Fig. 6 (a). When an intruder enters the detection area at 30 meters, 50 meters, and 70 meters separately, the subtraction results of I-signal are 30m_I, 50m_I and 70m_I, the subtraction results of Q-signal is 30m_Q, 50m_Q and 70m_Q. The sum represents the subtraction result of IQ-signal by equation (6). Obviously, a pulse is obtained from the subtraction results, which indicates the position of the human intruder.

It can be seen that the peak value of the I-signal or Q-signal is small in some results. It is not accurate only to consider the subtraction result of I-signal or the subtraction result of Q-signal as the intruder’s position, because the subtraction results of I-signal are not always better than the Q-signal in all positions by (4) ~ (5). As shown in Fig. 6 (a), the difference of I-signal and Q-

signal becomes large from 30 meters to 70 meters. Therefore, it is possible to avoid this error and improve the detection probability by calculating the square root of the subtraction results of I-signal and Q-signal according to (6). The curves of square root are 30m_sum, 50m_sum and 70m_sum. It can be seen that the positioning accuracy is ± 3 meter from Fig. 6 (b), the statistics data indicates that there are 48 alarms in 50 intrusions, including a false alarm (red star marker) at 100 meters, two missed intrusions (blue star marker). Therefore, the false positive rate of IDS is $2/50 \times 100\% = 4\%$, and the false positive rate is lower than $(1+2)/50 \times 100\% = 6\%$.

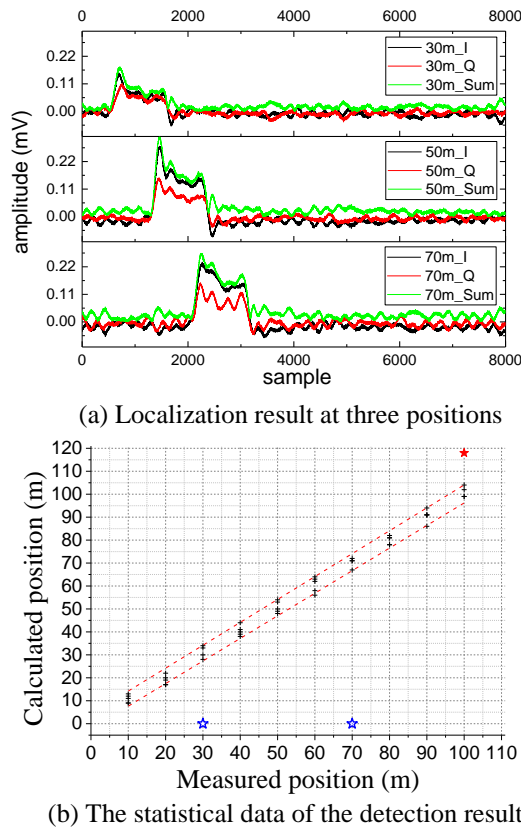


Fig. 6. Localization result (Detection signal: the pulse period $T=2$ ms, the pulse width $t_R=200$ ns, frequency $f_0=100$ MHz).

Figure 7 is the localization results of 40 MHz and 200 MHz.

The results of square root are obvious, while the amplitudes of 200 MHz and 40MHz are all less than that of 100MHz. Besides, compared with carried frequency of 200MHz, 40 MHz has a higher noise, though the amplitude of 40 MHz is less than that of 200MHz. It shows that 100 MHz has the best localization effect.

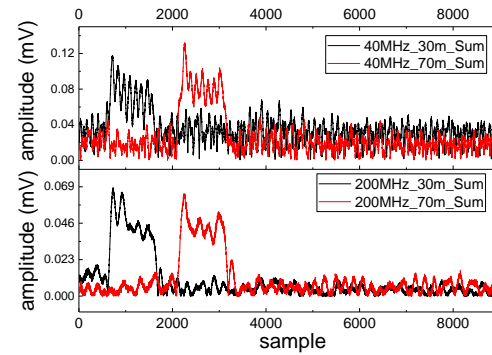


Fig. 7. Localization result of two positions with the method (Detection signal: the pulse period $T=2$ ms, the pulse width $t_R=200$ ns, frequency $f_0=40$ MHz/200MHz).

IV. CONCLUSION

A novel and effective general method for intruder localization using the IQ demodulation and synchronous subtraction is proposed in this paper, and it is suitable for the frequencies of 40 MHz, 100MHz and 200 MHz. In the studied frequency range, the scattering characteristics of human intruder is significant, which confirms the possibility of human detection and localization. Among those carrier frequencies, there is the largest reflection when the carrier frequency is 100MHz. The mechanism of the field disturbance caused by the human intruder can be measured by analyzing the field and the time domain or the frequency domain of the echo signal. In sum, the method of using IQ demodulation and synchronous subtraction can achieve high precision positioning of intrusion and avoid the inaccurate localization caused the phase error. The IDS positioning accuracy is improved effectively, and the results satisfy the calculated results, which is less than 3 meters.

ACKNOWLEDGMENT

This work was supported by the Fundamental Research Funds for the Central Universities (JB160205).

REFERENCES

- [1] J. R. Wait and D. Hill, "Propagation along a braided coaxial cable in a circular tunnel," *IEEE Trans. Microw. Theory & Tech.*, vol. 23, no. 5, pp. 401-405, 1975.
- [2] S. Okada, T. Kishimoto, K. Akagawa, et al., "Leaky coaxial cable for communication in high speed railway transportation," *Radio & Electronic Engineer*, vol. 45, no. 5, pp. 224-228, 2010.
- [3] A. S. Syed, "Posture recognition to prevent bedsores for multiple patients using leaking coaxial cable," *IEEE Access*, vol. 4, no. 99, pp. 8065-8072, 2016.

- [4] Q. Guan, C. C. Chen, and C. X. He, "A novel sensor using VHF zigzag-slotted leaky coaxial cable for intruder localization," *Microwave and Optical Technology Letters*, no. 60, pp. 634-639, 2018.
- [5] Q. Guan, X. F. Fan, Y. Liu, et al., "Research on VHF buried sensor using leaky coaxial cable techniques," *Journal of Microwaves*, no. 04, pp. 16-20, 2017.
- [6] E. Foley, K. Harman, and J. Cheal, "Improving intrusion detection radar," *IEEE Aerosp. & Electr. Syst. Maga.*, vol. 17, no. 8, pp. 22-27, 2002.
- [7] K. I. Nishikawa, T. Higashino, K. Tsukamoto, et al., "Two dimensional position detection method using bi-directional leaky coaxial cable based on TDOA," *IEEE, Intern. Sympo. Personal, Indoor Mobi. Radio Commu.*, pp. 2167-2170, 2009.
- [8] J. H. Wang and K. K. Mei, "Design of leaky coaxial cables with periodic slots," *Radio Science*, vol. 37, no. 5, pp. 1-10, 2016.
- [9] Q. Guan, H. M. Lu, K. B. Tan, et al., "Design of electromagnetic coupling sensor based on double leaky coaxial cables," *Journal of Xidian University*, vol. 45, no. 2, pp. 40-45, 2018.
- [10] C. Zhang, J. Wang, M. Chen, et al., "Radiation characteristic of the leaky circular waveguide with periodic slots," *IEEE Anten. & Wirel. Propag. Lett.*, vol. 11, no. 11, pp. 503-506, 2012.
- [11] Y. Du, W. Li, Y. Ge, et al., "A high-frequency signal generator based on direct digital synthesizer and field-programmable gate array," *Review of Scient. Instru.*, vol. 88, no. 9, pp. 96-103, 2017.
- [12] D. K. Barton, "Radar system analysis and modeling," *IEEE Aerosp. Electr. Syst. Maga.*, vol. 20, no. 4, pp. 23-25, 2005.
- [13] D. Qian, Z. Ping, H. Qi, et al., "Bandpass sampling and quadrature demodulation in synthetic aperture radar," *Interna. Confer. Radar. IEEE*, pp. 1-4, 2007.



Hongmin Lu, Professor, Ph.D. of Xi'an Jiaotong University, Postdoctoral Fellow of Xidian University of Electronic Science and Technology. Now he is a Professor at Xidian University, Chairman of Telecommunications Engineering Department, a Professor of National Key Laboratory of Antenna and Microwave Technology. His current research interests include the theory of high speed circuit and electromagnetic compatibility.



Kunbo Wang studied at Qingdao University from 2013 to 2017. She was admitted to Xidian University in 2017. And she is currently pursuing a master's degree. Her current research interest is electromagnetic compatibility. And she has been working in the Electromagnetic Compatibility, Xidian University.



Chongchong Chen was born in Xi'an, China, in 1994. He received his B.E. degree in Electronic Information Engineering from the School of Electronic Engineering of Xidian University, Xi'an, China, in 2015. He has been studying as a graduate student in the school of Electronic Engineering of Xidian University since 2015. His current research interests include electromagnetic compatibility and lightning protection.



Qiao Guan received the B.S. and M.S. degrees from the School of Electronic Engineering, Xidian University, Xi'an, China, in 2013 and 2015. He is currently pursuing his Ph.D. degree of the Electromagnetic and Microwave Technology in Xidian University. His research interest in the electromagnetic sensor, radar signal detection and estimation, electronics, and RF circuits.

Calculation and Analysis of an Analytical Model for Magnetic Field Monitoring Based on TREE in Eddy Current Testing

Feng Jiang^{1,2} and Shulin Liu¹

¹ School of Mechatronics Engineering and Automation
Shanghai University, Shanghai, 200072, China
lsl346@shu.edu.cn

² School of Mechatronics Engineering
Jiangsu College of Information Technology, Wuxi, 214153, China
jiangf@jsit.edu.cn

Abstract — In this work, theoretical model for magnetic field monitoring rather than traditional detection of coil impedance is investigated and analyzed. The truncated region eigenfunction expansion (TREE) method [1] offers analytical expressions by truncating the solution region to a finite length, so magnetic field can be derived in a series of proper eigenfunctions instead of the integral form, as it traditionally happens. The influences of truncation interval h , the number of summation n and excitation current frequency f on magnetic field above conductive plate for the model accuracy are estimated. The comparison of the results obtained between theoretical calculation and the finite element method shows excellent agreement under certain conditions. An applicative example is presented to assess the proposed theory to different conductor problem using the eddy current field derived by the analytical solution. The analytical model can be beneficial for analysis, parametric studies and development of eddy current testing system.

Index Terms — Analytical model, eddy current testing, finite element method, magnetic field.

I. INTRODUCTION

The eddy current testing (ECT) has been used for a wide variety of applications such as the detection of cracks and residual stresses, measurement of coating or metal thickness, determination of the alloy composition and hardness of tested object and so on [2-8]. Previous work has mainly focused on practical applications such as crack detection using the various types of coil and the exciting current [9,10]. In contrast, there are relatively few literature reports on theoretical and behavioural modeling. Modeling is a powerful tool for design optimization, enhancing a better understanding of the relevant physics and improving the reliability of defect analysis.

ECT can be studied by applying the electric circuit theory and the electromagnetic field theory [11-14]. However, electric circuit method is only approximate and it predicts signals that differ greatly from the measured signals. It is more suitable for analysis to use electromagnetic field theory. The electromagnetic field can be solved by analytical method or numerical method. Now, the numerical method such as the finite element method is widely used to predict signals in ECT [15-17]. The analytical method is more advantageous to obtain the general solution in the form of closed mathematical expression and need fewer computation resources as well as a useful starting point for some numerical optimization. So the analytical solution makes it possible to solve the inverse problem where the unknown geometric shape of a defect is to be reconstructed [18,19]. Moreover, analytical solution can easily be used for quantitative analysis, parametric estimation and calibration of the measurement device. Dodd and Deeds [20] proposed the “closed-form” solution for two different geometries: a rectangular cross-section coil above a plane and a rectangular cross-section coil encircling a two-conductor rod. The solutions were given in terms of integrals of Bessel functions. Measured values of coil impedance have been compared with calculated values and they have shown excellent agreement. On the basis of previous achievements made by Dodd and Deeds in analytical modeling, the TREE method has been employed to express magnetic vector potential as a series of proper eigenfunctions by truncating the domain of the problem instead of the integral form, as it traditionally happens [1]. As for the author’s knowledge, until now, the TREE method has been successfully employed only for prediction of coil impedance to a conductive plate with a cylindrical hole or a slot, conductive wedge and so on [21-23].

All eddy current problems above are usually detected as an impedance change of the pick coil [24,25].

The sensitivity of pick coil is reduced in detecting deep buried flaws because of low excitation frequency. Thus, it is more beneficial to measure the magnetic field rather than coil impedance variation. Magnetic field sensors based on Hall effect, giant magnetoresistance effect or superconducting quantum interference device have been used for ECT successfully [26,27]. Unfortunately, in this case, the measured signals from magnetic field sensors needed to be verified by theoretical methods. If compared with experimental studies, only a few theoretical analyses were conducted for magnetic field detecting in ECT.

In this paper, we extend the TREE method to the magnetic flux density, rather than the coil impedance. The formulas of two-dimensional magnetic field including source field and eddy current field above the conductor surface are deduced. Then, efforts have been made to determine the optimal value for the parameters that appear in equations.

II. SECTION ANALYTICAL MODELING

A. Formulation of magnetic vector potential

The mathematical model for eddy current problem at low frequencies is described by Maxwell's equations. Maxwell's equations in differential form are:

$$\begin{cases} \nabla \times \mathbf{H} = \mathbf{J} + \frac{\partial \mathbf{D}}{\partial t} \\ \nabla \times \mathbf{E} = -\frac{\partial \mathbf{B}}{\partial t} \\ \nabla \cdot \mathbf{D} = \rho \\ \nabla \cdot \mathbf{B} = 0 \end{cases}, \quad (1)$$

where some quantities above are defined as: \mathbf{H} -the magnetic field intensity, \mathbf{J} -the current density, \mathbf{D} -the electric flux density, \mathbf{E} -the electric field intensity, \mathbf{B} -the magnetic flux density, ρ -the volume electric charge density. The additional relations are the material constitutive relations:

$$\begin{cases} \mathbf{D} = \varepsilon \mathbf{E} \\ \mathbf{B} = \mu \mathbf{H} \\ \mathbf{J} = \sigma \mathbf{E} \end{cases}, \quad (2)$$

where ε is the permittivity, μ is the magnetic permeability, σ is the electric conductivity.

Excitation frequency is low and consequently the displacement current is neglected. Since the displacement currents can be neglected and sinusoidal excitation current is assumed, Maxwell's equations can be rewritten as follows:

$$\begin{cases} \nabla \times \mathbf{H} = \mathbf{J}_s + \mathbf{J}_e \\ \nabla \times \mathbf{E} = -j\omega \mathbf{B} \\ \nabla \cdot \mathbf{D} = \rho \\ \nabla \cdot \mathbf{B} = 0 \end{cases}. \quad (3)$$

The current densities given in Eq. (3) include source current density \mathbf{J}_s and eddy current density \mathbf{J}_e . In order

to simplify the equations for calculation, the magnetic vector potential \mathbf{A} is defined as $\nabla \times \mathbf{A} = \mathbf{B}$ with provision for $\nabla \cdot \mathbf{A} = 0$. The electric scalar ϕ is defined as $-\nabla \phi = \mathbf{E} + j\omega \mathbf{A}$. Substituting these definitions above into Eq. (3), we will have:

$$\nabla^2 \mathbf{A} = -\mu \mathbf{J}_s + \mu (\nabla \phi + j\omega \mathbf{A}). \quad (4)$$

Combined with Eq. (1) and definition of ϕ , the other equation can be obtained:

$$\nabla \cdot (\nabla \phi + j\omega \mathbf{A}) = 0. \quad (5)$$

We consider a cylindrical coil with rectangular cross-section, placed above a conductive plate. The dimension of conductive plate is assumed big enough compared to the size of coil. The axisymmetric model is shown in Fig. 1. The region above conductive plate is region 0 and conductive plate is region 1. The coil is assumed to be air-cored with N turns, inner radius r_1 , outer radius r_2 , thickness $z_2 - z_1$. The distance z_1 is called "lift-off". The coil is excited by a sinusoidal current of angular frequency ω .

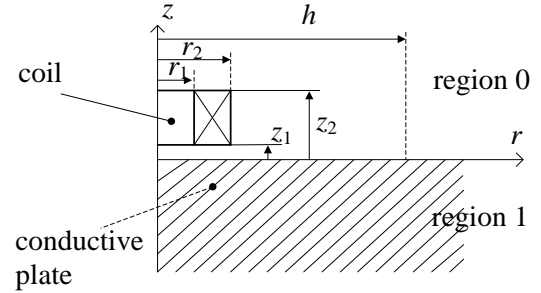


Fig. 1. 2D axisymmetric view of model.

We use cylindrical coordinates in solving the problem due to the axial symmetry. Then the magnetic vector potential A has only circumferential component as a function of r and z . Thus, the Eq. (5) is identically satisfied and the Eq. (4) can be simplified into:

$$\frac{\partial^2 A}{\partial r^2} + \frac{1}{r} \frac{\partial A}{\partial r} + \frac{\partial^2 A}{\partial z^2} - \frac{A}{r^2} = -\mu \mathbf{J}_s + k^2 A, \quad (6)$$

where $k^2 = j\omega\mu\sigma$.

B. Integral solution of the magnetic vector potential

Equation (6) can be solved by the separation of variables and the general solution has the following form [20]:

$$A(r, z) = \int_0^\infty [A(\alpha) J_1(\alpha r) + B(\alpha) Y_1(\alpha r)] \times [C(\alpha) e^{\lambda z} + D(\alpha) e^{-\lambda z}] d\alpha, \quad (7)$$

where $\lambda = \sqrt{\alpha^2 + k^2}$. J_1 denotes the Bessel function of the first kind and first order. Y_1 denotes the Bessel function of the second kind and first order. A , B , C and D are unknown coefficients.

Because the function Y_1 tends to infinity, we set

$B(\alpha) = 0$. The potential in the air ($k = 0$) below the coil assumes the following expression:

$$A_0(r, z) = \int_0^{\infty} J_1(\alpha r) [C_s e^{\alpha z} + D_{ec} e^{-\alpha z}] d\alpha. \quad (8)$$

Moreover, in order to remain finite of the potential, we set $D(\alpha) = 0$ in region 1. Thus, the potential in the conductive plate assumes the following expression:

$$A_1(r, z) = \int_0^{\infty} J_1(\alpha r) C_1(\alpha) e^{\lambda z} d\alpha. \quad (9)$$

The unknown coefficients in Eqs. (8) and (9) are determined by imposing the interface conditions between the two regions:

$$\left. \begin{aligned} A_0 &= A_1 \\ \frac{\partial A_0}{\partial z} &= \frac{1}{\mu_r} \frac{\partial A_1}{\partial z} \end{aligned} \right|_{z=0}. \quad (10)$$

After substituting Eqs. (8) and (9) into Eq. (10) we get the equations for the two unknown coefficients:

$$\begin{cases} C_1 = C_s \frac{2\alpha\mu_r}{\alpha\mu_r + \lambda} \\ D_{ec} = C_s \frac{\alpha\mu_r - \lambda}{\alpha\mu_r + \lambda} \end{cases}. \quad (11)$$

The term C_s is a source coefficient which has a form:

$$C_s = \frac{\mu_0 i}{2} \frac{\chi(\alpha r_1, \alpha r_2)}{\alpha^3} (e^{-\alpha z_1} - e^{-\alpha z_2}), \quad (12)$$

where $i = NI / [(r_2 - r_1)(z_2 - z_1)]$ is the source current density of the coil. The term $\chi(\alpha r_1, \alpha r_2)$ can be expressed as follows [20]:

$$\chi(x_1, x_2) = \int_{x_1}^{x_2} x J_1(x) dx. \quad (13)$$

Thus, we obtain the integral expression for the potential in the air below the coil:

$$\begin{aligned} A_0(r, z) &= \frac{\mu_0 i}{2} \int_0^{\infty} J_1(\alpha r) e^{\alpha z} \frac{\chi(\alpha r_1, \alpha r_2)}{\alpha^3} (e^{-\alpha z_1} - e^{-\alpha z_2}) d\alpha \\ &+ \frac{\mu_0 i}{2} \int_0^{\infty} J_1(\alpha r) e^{-\alpha z} \frac{\chi(\alpha r_1, \alpha r_2)}{\alpha^3} (e^{-\alpha z_1} - e^{-\alpha z_2}) \frac{\alpha\mu_r - \lambda}{\alpha\mu_r + \lambda} d\alpha, \quad (14) \\ &= A^s + A^e \end{aligned}$$

where A^s stands for the source potential, A^e corresponds to the one due to the eddy current.

C. Analytical solution of magnetic flux density

Equation (14) has been derived by assuming an infinite solution region. In the TREE method, the solution region is assumed finite in the radial direction ($0 \leq r \leq h$). Following the separation of variables and the imposition of Dirichlet boundary condition at $r = h$, the general expression for the magnetic vector potential in region 0 is given as [1]:

$$A_0(r, z) = \sum_{i=1}^{\infty} J_1(\alpha_i r) (C_i e^{\alpha_i z} + D_i e^{-\alpha_i z}). \quad (15)$$

The term C_i is a source coefficient which has a form [1]:

$$C_i = \mu_0 i \frac{\chi(\alpha_i r_1, \alpha_i r_2)}{\alpha_i^4 [hJ_0(\alpha_i h)]^2} (e^{-\alpha_i z_1} - e^{-\alpha_i z_2}). \quad (16)$$

The coefficient D_i is calculated using the same method as D_{ec} above. Thus the potential can be expressed as follow:

$$\begin{aligned} A_0(r, z) &= \mu_0 i \sum_{i=1}^{\infty} [J_1(\alpha_i r) e^{\alpha_i z} \frac{\chi(\alpha_i r_1, \alpha_i r_2)}{\alpha_i^4 [hJ_0(\alpha_i h)]^2} (e^{-\alpha_i z_1} - e^{-\alpha_i z_2}) + \\ &J_1(\alpha_i r) e^{-\alpha_i z} \frac{\chi(\alpha_i r_1, \alpha_i r_2)}{\alpha_i^4 [hJ_0(\alpha_i h)]^2} (e^{-\alpha_i z_1} - e^{-\alpha_i z_2}) \frac{\alpha_i \mu_r - \lambda_i}{\alpha_i \mu_r + \lambda_i}] \end{aligned} \quad (17)$$

Once the potential is calculated, the magnetic flux density can be derived from:

$$B = -\frac{\partial A}{\partial z} \mathbf{r}_0 + \frac{1}{r} \frac{\partial (rA)}{\partial r} \mathbf{z}_0. \quad (18)$$

Substituting the Eq. (17) into Eq. (18), we will have:

$$\begin{aligned} B_0(r, z) &= \mu_0 i \sum_{i=1}^{\infty} \left[J_1(\alpha_i r) \left(-e^{\alpha_i z} + e^{-\alpha_i z} \frac{\alpha_i \mu_r - \lambda_i}{\alpha_i \mu_r + \lambda_i} \right) \frac{\chi(\alpha_i r_1, \alpha_i r_2)}{\alpha_i^3 [hJ_0(\alpha_i h)]^2} (e^{-\alpha_i z_1} - e^{-\alpha_i z_2}) \right] \mathbf{r}_0 \\ &+ \mu_0 i \sum_{i=1}^{\infty} \left[J_0(\alpha_i r) \left(e^{\alpha_i z} + e^{-\alpha_i z} \frac{\alpha_i \mu_r - \lambda_i}{\alpha_i \mu_r + \lambda_i} \right) \frac{\chi(\alpha_i r_1, \alpha_i r_2)}{\alpha_i^3 [hJ_0(\alpha_i h)]^2} (e^{-\alpha_i z_1} - e^{-\alpha_i z_2}) \right] \mathbf{z}_0 \end{aligned} \quad (19)$$

Finally, we have the analytical expressions of magnetic flux density at $0 \leq z \leq z_1$:

$$\begin{cases} B_0(r) = \mu_0 i \sum_{i=1}^{\infty} J_1(\alpha_i r) \left(-e^{\alpha_i z} \right) \frac{\chi(\alpha_i r_1, \alpha_i r_2)}{\alpha_i^3 [hJ_0(\alpha_i h)]^2} (e^{-\alpha_i z_1} - e^{-\alpha_i z_2}) \\ \Delta B_0(r) = \mu_0 i \sum_{i=1}^{\infty} J_1(\alpha_i r) \left(e^{-\alpha_i z} \frac{\alpha_i \mu_r - \lambda_i}{\alpha_i \mu_r + \lambda_i} \right) \frac{\chi(\alpha_i r_1, \alpha_i r_2)}{\alpha_i^3 [hJ_0(\alpha_i h)]^2} (e^{-\alpha_i z_1} - e^{-\alpha_i z_2}) \\ B_0(z) = \mu_0 i \sum_{i=1}^{\infty} J_0(\alpha_i r) \left(e^{\alpha_i z} \right) \frac{\chi(\alpha_i r_1, \alpha_i r_2)}{\alpha_i^3 [hJ_0(\alpha_i h)]^2} (e^{-\alpha_i z_1} - e^{-\alpha_i z_2}) \\ \Delta B_0(z) = \mu_0 i \sum_{i=1}^{\infty} J_0(\alpha_i r) \left(e^{-\alpha_i z} \frac{\alpha_i \mu_r - \lambda_i}{\alpha_i \mu_r + \lambda_i} \right) \frac{\chi(\alpha_i r_1, \alpha_i r_2)}{\alpha_i^3 [hJ_0(\alpha_i h)]^2} (e^{-\alpha_i z_1} - e^{-\alpha_i z_2}) \end{cases}, \quad (20)$$

where the eigenvalues of α_i are the positive roots of $J_1(\alpha_i h) = 0$. $B_0(r)$ and $B_0(z)$ represent the radial and axial magnetic field, respectively, above the conductive plate generated by the excitation coil. $\Delta B_0(r)$ and $\Delta B_0(z)$ respectively stand for the radial and axial magnetic field caused by eddy current. We can get accurate solution of magnetic field easily using several summation operations from Eq. (20).

III. FE MODELING

We will obtain the magnetic field distributions using ANSOFT Maxwell [28] to verify the analytical model above. ANSOFT Maxwell is a finite element analysis software that can automatically adjust areas of the finite element mesh exhibiting large errors. Table 1 shows the main dimensions of the coil and conductive plate. The parameters L and T in Table 1 represent the length and

thickness of conductive plate respectively. The 2D model is shown below using the 2D RZ axisymmetric solver. Coils are wound with copper enameled wires, belonging to the stranded wires. The amplitude of the sinusoidal excitation current is 40 ampere-turns and its phase is 0 degree. Boundary conditions are balloon (upper and lower boundary), symmetry (left boundary) and vector potential = 0 (right boundary) respectively. The excitation current frequency is set at 1 kHz.

Table 1: Coil and conductive plate parameters

Coil	Conductive Plate
$r_1 = 2 \text{ mm}$	$\sigma = 3.6 \times 10^7 \text{ S/m}$
$r_2 = 4 \text{ mm}$	$\mu_r = 1$
$z_2 - z_1 = 3 \text{ mm}$	$L = 160 \text{ mm}$
$z_1 = 1 \text{ mm}$	$T = 20 \text{ mm}$
$N = 800$	

The distribution cloud of magnetic field intensity is shown in Fig. 2 through the analysis of model above. Figure 3 is the distribution of magnetic field lines. As the figures show, the magnetic flux density of the coil is close to the maximum and the lines are crowded together. Inside the conductor, magnetic field near the surface of the detection coil is strong. This shows that eddy current is concentrated in the surface and near the surface of the conductor.

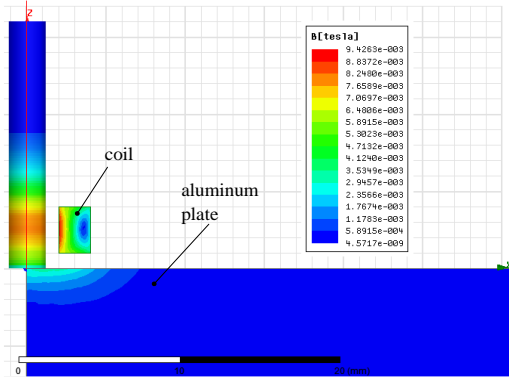


Fig. 2. 2D simulation model and distribution cloud of magnetic field intensity.

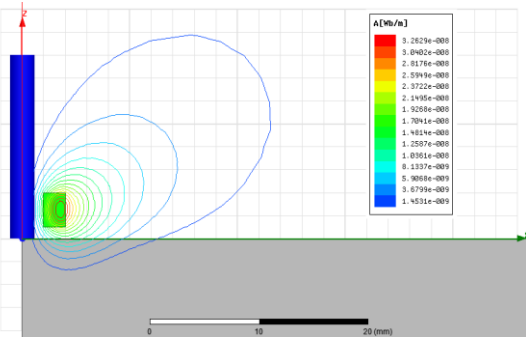


Fig. 3. Distribution of magnetic field lines.

IV. ANALYSIS AND DISCUSSION

A. Effects of the length of the truncation interval h

We compute magnetic field between the conductor and coil and show how the modeling error is influenced by the length of the truncation interval h . We choose $h = r_2, h = 20r_2, h = 40r_2, h = 80r_2$ respectively and the number of the summation $n = 50$.

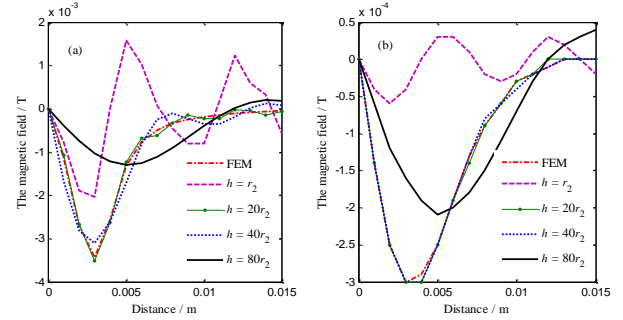


Fig. 4. (a) The real part and (b) imaginary part of radial magnetic field as a function of distance under different truncation interval at $z = 0.5 \text{ mm}$.

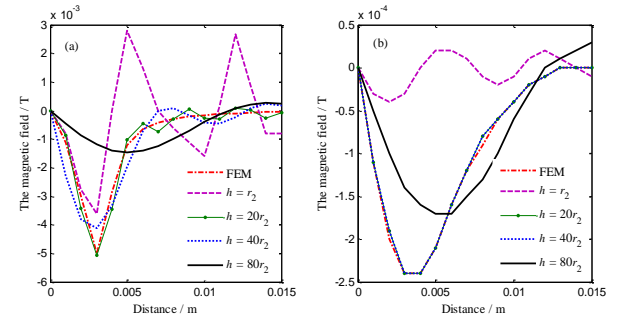


Fig. 5. (a) The real part and (b) imaginary part of radial magnetic field as a function of distance under different truncation interval at $z = 1 \text{ mm}$.

Figures 4 (a), 4 (b) show the real and imaginary parts of radial magnetic field calculated at $z = 0.5 \text{ mm}$ respectively. The real part and imaginary part of radial magnetic field calculated at $z = 1 \text{ mm}$ are shown in Figs. 5 (a) and 5 (b) respectively. Compared with finite element analysis, the results can be found from figures as follows: (1) The fact is not that h value is the bigger the better as theoretical analysis. Its impact on the calculation result is very large and h value cannot be too large or too small. Hence, the value of h should be in a certain range. Calculation results can infinitely approach the simulation results by selecting the appropriate h value. It proves that the eddy current concentrates only in a very narrow area. This is physically consistent because the electromagnetic field does not extend to great distance from the excitation coil. Therefore, the value of h is chosen only in relation to the outer radius

of the coil. (2) The calculated values fluctuate greatly when $0 < h < 2r_2$. Results have no obvious regularity, so we do not recommend h value within this range. With the increase of the value of h , the error increases slightly when $2r_2 \leq h \leq 40r_2$. As the error can be maintained within 10%, the calculation results can basically reflect the magnetic field distribution. The error is only 0.87% at $r = 3$ mm when $h = 2r_2$. Table 2 lists the calculation results at $h = 5r_2$, $h = 10r_2$, $h = 15r_2$ and simulation results at $z = 0.5$ mm. It can be seen that error is very small within this range. The difference between the calculated results and the simulation results becomes larger when $h \geq 40r_2$. The error is 70% at $r = 3$ mm when $h = 80r_2$. Therefore, too large h values will cause larger error obviously. It is not recommended to adopt the h value in the range of $h \geq 40r_2$ (3) The results also show that the real and imaginary part of radial magnetic field reaches the maximum at $r = 3$ mm which is the center of the coil width. The radial magnetic field is zero at $r = 0$ mm and $r > 15$ mm. These results are in accord with what we expected completely.

Table 2: Calculated and simulated results as a function of distance under different truncation interval (unit: 10^{-5} T)

	FEM		$h = 5r_2$		$h = 10r_2$		$h = 15r_2$	
	Re	Im	Re	Im	Re	Im	Re	Im
0	0	0	0	0	0	0	0	0
1	-116	-14	-116	-14	-115	-14	-110	-14
2	-269	-25	-271	-25	-270	-25	-274	-25
3	-344	-30	-351	-30	-353	-30	-350	-30
4	-258	-29	-255	-30	-254	-30	-256	-30
5	-132	-25	-131	-25	-131	-25	-131	-25
6	-76	-19	-76	-19	-76	-19	-75	-19
7	-49	-13	-49	-14	-49	-14	-51	-14
8	-34	-9	-34	-9	-34	-9	-33	-9
9	-25	-6	-24	-5	-25	-6	-26	-6
10	-19	-3	-18	-3	-18	-3	-18	-3

B. Effects of the number of summation n

It is expected that the greater the number of summation should be, the greater the ability to approximate a real result. To validate this presumption, the calculation results are shown in Fig. 6 for $n = 5, 10, 80, 200$ and 1000 keeping $z = 0.5$ mm and $h = 5r_2$. Figures 6 (a) and 6 (b) are the real part and imaginary part of radial magnetic field respectively.

It is easy to see that the results are quite different from our presumption. (1) When $n \geq 10$, it can basically meet the requirements with the error $< 5\%$ (at the point of maximum radial magnetic field). This is a strong proof of the biggest advantage for this mathematical model, that is, it can replace the theoretical needs of infinite summation through several summation operations, eliminating the need for the use of infinite integral calculation problem. (2) The number of summation is not the bigger the better as theoretical analysis. It is found that too many summation number results in lower

accuracy of the model. The calculation time will be very long at the same time. The error is 9.3% when $n = 1000$. The calculation time is about 70 seconds using Matlab. In contrast, the error is only 2.6% and the calculation time is only 3 seconds when $n = 20$. (3) The calculated data is also unstable when the number of summation is too large. The magnetic field presents abnormal increase as the distance is far enough. This does not conform to the actual situation obviously.

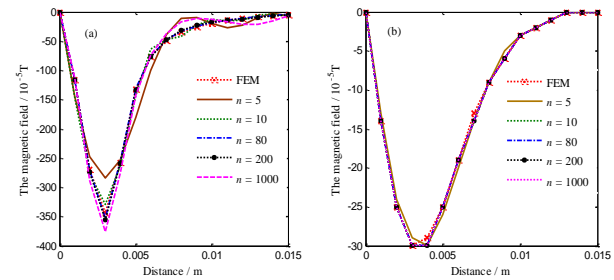


Fig. 6. (a) The real part and (b) imaginary part of radial magnetic field as a function of distance under different number of summation.

C. Effects of the excitation current frequency f

The excitation current frequency is a very important parameter in eddy current testing. Here we mainly analyze the error values of the radial magnetic field and the axial magnetic field calculated by the mathematical model under different frequencies compared with the simulation. The following frequencies are used: 50 Hz, 2 kHz, 10 kHz, 500 kHz, 1 MHz. According to the analysis results obtained above, we take $h = 5r_2$, $n = 20$. The magnitudes (real part and imaginary part) of the radial magnetic field B_r and the axial magnetic field B_z at $z = 0.5$ mm are calculated.

As shown in Fig. 7 (a), the error of $\text{Re}(B_r)$ decreases gradually as the frequency increases. The maximum error occurs at $r = 3$ mm when $f = 50$ Hz. The maximum error value is 9×10^{-5} T. In fact, the relative error is very small compared to the magnetic field value of 324×10^{-5} T at this time. Under the same frequency, the maximum error also occurs at $r = 3$ mm, because the magnetic field value is the largest. In Fig. 7 (b), the calculated values are in good agreement with the FEM values, except for very few points ($f = 50$ Hz, $r = 8$ mm; $f = 2$ kHz, $r = 3$ mm; $f = 500$ kHz, $r = 2$ mm). According to the further analysis, this error is not caused by the model itself. Since the imaginary part of the radical magnetic field is very small, the error is caused by data truncation during the calculation. Therefore, we believe that the calculation of the imaginary part of the radical magnetic field is consistent with the simulation results and the results are not affected by the frequency. The real part of the axial magnetic field is shown in Fig. 7 (c). The error occurs mainly at the starting position, especially $r = 0$. When

the frequency is less than or equal to 2 kHz, the error is obvious. The maximum error is 113×10^{-5} T with magnetic field of 517×10^{-5} T at $r = 0$ when $f = 2$ kHz. The error becomes very small at $r = 0$ when the frequency is greater than 2 kHz. Therefore, the error is greater only at a lower frequency and very close to zero point for the real part of the axial magnetic field. The imaginary part of the axial magnetic field is shown in Fig. 7 (d). The error is relatively large at $r = 0$ when $f = 2$ kHz. This result is similar to that obtained for the real part of the axial magnetic field. In the other frequency range, the calculation results are almost consistent with the simulation results.

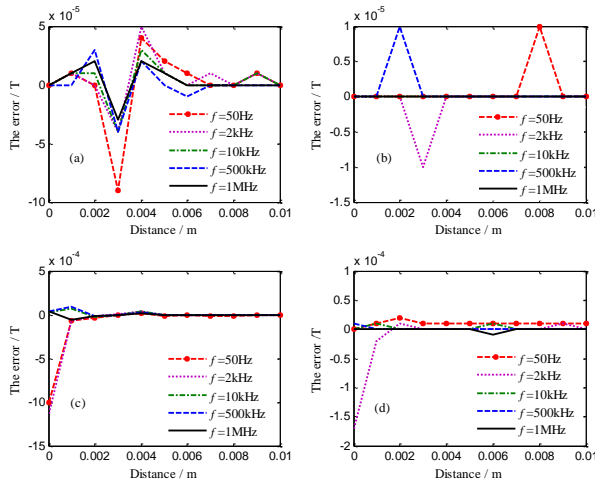


Fig. 7. Comparison of magnetic field between the calculation results and FEM under different frequencies. (a) The error of $Re(B_r)$; (b) the error of $Im(B_r)$; (c) the error of $Re(B_z)$; (d) the error of $Im(B_z)$.

In general, the results obtained by the mathematical model are not affected by the frequency. The model can maintain a high accuracy at any frequency. The error is smaller as the exciting current frequency increases. The larger frequency has no research value, because the skin depth is very small at this time and eddy current effect is not obvious.

V. APPLICATION

In this section we present an application example of the model to different conductor problems. Zinc and aluminum are widely used in the industrial field, and their integrity is very important for safety production. At present, their evaluation is mainly based on the principle of material conductivity change. In this section, zinc is first selected to analyze the distributions of source field and eddy current field. On this basis, zinc and aluminium are studied to analyze the eddy current field changes caused by different electrical conductivity. The electrical conductivities of zinc and aluminum are 1.86×10^7 S/m

and 3.6×10^7 S/m respectively. The relative permeability of both materials is approximately 1. We can only get the sum of the magnetic field using the finite element method which cannot distinguish between the source field generated by the excitation coil and the magnetic field caused by eddy current. But the two types of magnetic field can be clearly separated by Eq. (20). This is a very significant feature of the mathematical model distinguishing the finite element method.

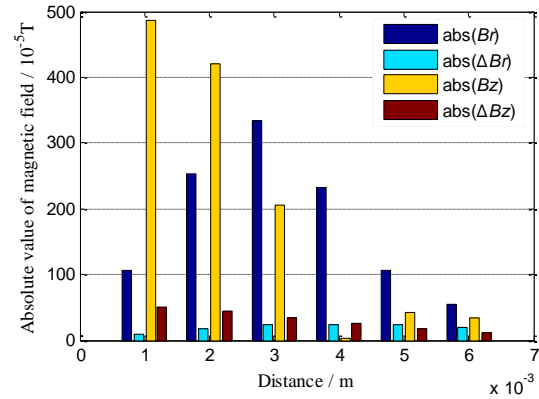


Fig. 8. The components of the magnetic field.

The components of the magnetic field are calculated for conductor zinc at $z = 0.5$ mm. The following values of the parameters are used: lift-off = 1 mm, $h = 5r_2$ and $n = 20$. According to the previous analysis, the error is 2.6% under these conditions. It can be seen from Fig. 8 that the radial and axial magnetic field above the conductor are greatly changed by eddy current. This is the basic principle that we adopt the magnetic sensor to measure the variation of magnetic field and realize the detection. From the height of the columns in Fig. 8, it is apparent that the magnetic field at different positions is not equal. The source field B_r and eddy current field ΔB_r increase firstly and then decrease with the increase of radial distance. The maximum B_r is 33.3 Gauss at $r = 3$ mm, which is the center of the coil width. The maximum ΔB_r is 2.4 Gauss at $r = 4$ mm, which is the outside radius of coil. The source field B_z and eddy current field ΔB_z are getting smaller and smaller with the increase of radial distance. The only difference is that source field B_z drops to zero suddenly at $r = 4$ mm. It is determined by the coil structure. In general, the changes of source field and eddy current field are similar with the increase of radius distance.

By means of the mathematical model, we can also analyze the magnetic field variations ΔB_r and ΔB_z caused by the conductivity or the permeability of detected object for eddy current nondestructive testing and thickness detection. The magnetic field variations ΔB_r and ΔB_z are calculated for the zinc and aluminum respectively in Fig. 9. It shows that the magnetic field

variations are very sensitive to the conductivity of the material being measured. This is a necessary precondition that we use the eddy current to detect cracks, corrosion and other defects. With the increase of conductivity of the material, the corresponding variation of the magnetic field increases. In general, the regularity of magnetic field variation caused by electrical conductivity is similar to that of magnetic field induced by eddy current.

According to Fig. 9, if we detect the magnetic field variations ΔBr , the maximum change of magnetic field variations $\Delta(\Delta Br)$ owing to the electrical conductivity takes place at $r = 3$ mm or $r = 4$ mm. If we detect the magnetic field variations ΔBz , the maximum change of magnetic field variations $\Delta(\Delta Bz)$ owing to the electrical conductivity takes place at $r = 0$ mm or $r = 1$ mm. That is to say, if sensitivity direction of sensor is radial, we can place the sensor at the outside radius of coil. If sensitivity direction of sensor is axial, we can place the sensor at the symmetry center of coil. The above analysis results have important implications for the arrangement of sensor position as well as to determine the sensitive direction of the magnetic sensor.

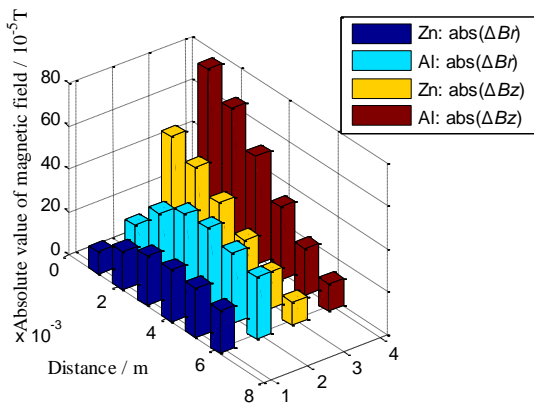


Fig. 9. Magnetic field variations for zinc and aluminum.

VI. CONCLUSION

(1) The analytical solution to mathematical model of eddy current problem is derived based on the magnetic field monitoring rather than traditional detection of coil impedance. The magnetic field can be decomposed into source field and eddy current field easily. This feature can be seen from an example of its application to different conductor problems.

(2) The value of the added distance for the computation, h , is not the bigger the better as theoretical analysis and should be in a certain range. The calculation results can infinitely approach the simulation results at $2r_2 \leq h \leq 40r_2$.

(3) It can basically meet the requirements that the error is less than 5% with the number of summation $n \geq 10$. There is no need to choose too many summation numbers as theoretical analysis. Not only does the error

increase correspondingly, but also the calculation time is very long. So we can only replace infinite summation or infinite integral calculation with several summation operations to obtain high accuracy.

(4) Model accuracy is almost not affected by the frequency. But it should be noticed that there is some error of the axial magnetic field for lower frequency at $r = 0$, which should be analyzed by further experiments.

ACKNOWLEDGMENT

This work was supported by the National Natural Science Foundation of China (51575331 and 51175316) and Shanghai Key Laboratory of Intelligent Manufacturing and Robotics (ZK1801).

REFERENCES

- [1] T. P. Theodoulidis and J. R. Bowler, "The truncated region eigenfunction expansion method for the solution of boundary value problems in eddy current nondestructive evaluation," *Review of Progress in Quantitative Nondestructive Evaluation*, Golden, Colorado, pp. 403-408, Apr. 2005.
- [2] A. Sophian, G. Tian, and M. Fan, "Pulsed eddy current non-destructive testing and evaluation: A review," *Chinese Journal of Mechanical Engineering*, vol. 30, no. 3, pp. 500-514, May 2017.
- [3] F. Jiang, S. L. Liu, and S. G. Xiao, "Quantitative estimation of rectangular surface crack based on the 2-D modeling of surface magnetic field with long straight rectangular wire," *IEEE Transactions on Magnetics*, vol. 54, no. 5, pp. 1-12, May 2018.
- [4] J. W. Wilson, G. Y. Tian, and S. Barrans, "Residual magnetic field sensing for stress measurement," *Sensors and Actuators A: Physical*, vol. 135, no. 2, pp. 381-387, Apr. 2007.
- [5] L. Yong, Z. Chen, Y. Mao, et al., "Quantitative evaluation of thermal barrier coating based on eddy current technique," *NDT & E International*, vol. 50, pp. 29-35, Sept. 2012.
- [6] M. S. Amiri and M. Kashefi, "Application of eddy current nondestructive method for determination of surface carbon content in carburized steels," *NDT & E International*, vol. 42, no. 7, pp. 618-621, Oct. 2009.
- [7] D. Mercier, J. Lesage, X. Decoopman, et al., "Eddy currents and hardness testing for evaluation of steel decarburizing," *NDT & E International*, vol. 39, no. 8, pp. 652-660, Dec. 2006.
- [8] B. Helifa, M. Féliachi, I. K. Lefkaier, et al., "Characterization of surface cracks using eddy current NDT simulation by 3D-FEM and inversion by neural network," *Applied Computational Electromagnetics Society Journal*, vol. 31, no. 2, pp. 187-194, Feb. 2016.
- [9] A. Sophian, G. Y. Tian, D. Taylor, et al., "Electromagnetic and eddy current NDT: A review," *Insight-*

- Non-Destructive Testing and Condition Monitoring*, vol. 43, no. 5, pp. 302-306, May 2001.
- [10] D. Rifai, A. N. Abdalla, K. Ali, et al., "Giant magnetoresistance sensors: A review on structures and non-destructive eddy current testing applications," *Sensors*, vol. 16, no. 3, pp. 1-30, Mar. 2016.
- [11] H. Ammari, A. Buffa, and J.-C. Nédélec, "A justification of eddy currents model for the maxwell equations," *SIAM Journal on Applied Mathematics*, vol. 60, no. 5, pp. 1805-1823, May 2000.
- [12] J. R. Nagel, "Fast finite-difference calculation of eddy currents in thin metal sheets," *Applied Computational Electromagnetics Society Journal*, vol. 33, no. 6, pp. 575-584, June 2018.
- [13] R. K. Murphy, H. A. Sabbagh, and E. H. Sabbagh, "A multiscale algorithm for eddy-current nondestructive evaluation based on volume-integral equations: Initial concepts," *Applied Computational Electromagnetics Society Journal*, vol. 31, no. 4, pp. 333-339, Apr. 2016.
- [14] C. Huang, X. Wu, Z. Xu, et al., "Ferromagnetic material pulsed eddy current testing signal modeling by equivalent multiple-coil-coupling approach," *NDT & E International*, vol. 44, no. 2, pp. 163-168, Mar. 2011.
- [15] H. Tsuboi, N. Seshima, I. Sebestyen, et al., "Transient eddy current analysis of pulsed eddy current testing by finite element method," *IEEE Transactions on Magnetics*, vol. 40, no. 2, pp. 1330-1333, Mar. 2004.
- [16] Y. Yu, X. Li, A. Simm, et al., "Theoretical model-based quantitative optimisation of numerical modelling for eddy current NDT," *Nondestructive Testing and Evaluation*, vol. 26, no. 2, pp. 129-140, Apr. 2011.
- [17] M. Tanaka and H. Tsuboi, "Finite element model of natural crack in eddy current testing problem," *IEEE Transactions on Magnetics*, vol. 37, no. 5, pp. 3125-3128, Sep. 2001.
- [18] Y. Li, L. Udpa, and S. S. Udpa, "Three-dimensional defect reconstruction from eddy-current NDE signals using a genetic local search algorithm," *IEEE Transactions on Magnetics*, vol. 40, no. 2, pp. 410-417, Mar. 2004.
- [19] F. Jiang and S. L. Liu, "Evaluation of cracks with different hidden depths and shapes using surface magnetic field measurements based on semi-analytical modelling," *Journal of Physics D: Applied Physics*, vol. 51, no. 12, pp. 125002, Mar. 2018.
- [20] C. V. Dodd and W. E. Deeds, "Analytical solutions to eddy-current probe-coil problems," *Journal of Applied Physics*, vol. 39, no. 6, pp. 2829-2838, May 1968.
- [21] T. Theodoulidis and J. R. Bowler, "Eddy-current interaction of a long coil with a slot in a conductive plate," *IEEE Transactions on Magnetics*, vol. 41, no. 4, pp. 1238-1247, Apr. 2005.
- [22] T. P. Theodoulidis and J. R. Bowler, "Eddy current coil interaction with a right-angled conductive wedge," *Proceedings of the Royal Society A: Mathematical Physical and Engineering Sciences*, vol. 461, no. 2062, pp. 3123-3139, Oct. 2005.
- [23] Y. J. Bai, X. Z. Zhang, L. Jiang, et al., "3-D eddy currents analysis in orthotropic materials using truncated region eigenfunction expansion method," *Applied Mechanics and Materials*, vol. 239-240, pp. 258-263, Dec. 2013.
- [24] J. García-Martín, J. Gómez-Gil, and E. Vázquez-Sánchez, "Non-destructive techniques based on eddy current testing," *Sensors*, vol. 11, no. 3, pp. 2525-2565, Feb. 2011.
- [25] B. A. Auld and J. C. Moulder, "Review of advances in quantitative eddy current nondestructive evaluation," *Journal of Nondestructive Evaluation*, vol. 18, no. 1, pp. 3-36, Mar. 1999.
- [26] J. Kim, G. Yang, L. Udpa, et al., "Classification of pulsed eddy current GMR data on aircraft structures," *NDT & E International*, vol. 43, no. 2, pp. 141-144, Mar. 2010.
- [27] C. Voulgaraki, N. Poulakis, and T. Theodoulidis, "Theoretical simulations and quantitative magnetic field measurements for Eddy-current testing with an HTS SQUID system," *IEEE Transactions on Applied Superconductivity*, vol. 23, no. 4, pp. 1603012-1603012, Aug. 2013.
- [28] Maxwell 2D User's Guide, ver. 15, ANSYS Inc., Southpointe, PA, 2012.



Feng Jiang was born in Yancheng, China, in 1981 and received the M.Sc. degree in the School of Mechanical Engineering from Jiangsu University, Zhenjiang, China, in 2006. He is currently pursuing the Ph.D. degree in the School of Mechatronics Engineering and Automation, Shanghai University, Shanghai, China. He is working as an Associate Professor in Mechatronics Engineering at Jiangsu College of Information Technology. His research interests include electromagnetic nondestructive evaluation, sensor techniques and fault diagnosis.



Shulin Liu was born in 1963 and received the M.Sc. degree in the School of Mechanical Engineering from Yanshan University, Qinhuangdao, China, in 1989 and received his Ph.D. degree from Harbin Institute of Technology, Harbin, China, in 2003. Since 2008, he is a Professor and Doctoral Supervisor at School of Mechatronics Engineering and Automation, Shanghai University, China. His major research direction is complex equipment fault diagnosis.